

NASA CR-159,200



NASA-CR-159200
19800016609

NASA Contractor Report 159200

INTERIOR NOISE CONTROL PREDICTION STUDY FOR HIGH-SPEED PROPELLER-DRIVEN AIRCRAFT

D.C. Rennison
J.F. Wilby
A.H. Marsh *
E.G. Wilby

BOLT BERANEK AND NEWMAN INC.
Canoga Park, California 91303

(*DYTEC ENGINEERING INC.
Long Beach, California 90806)

Contract No. NAS1-15426

September 1979



National Aeronautics and
Space Administration

Langley Research Center
Hampton, Virginia 23635
AC 804 827-3966

NASA Contractor Report 159200

INTERIOR NOISE CONTROL PREDICTION STUDY FOR HIGH-SPEED PROPELLER-DRIVEN AIRCRAFT

D.C. Rennison
J. F. Wilby
A.H. Marsh *
E.G. Wilby

BOLT BERANEK AND NEWMAN INC.
Canoga Park, California 91303

(*DYTEC ENGINEERING INC.
Long Beach, California 90806)

Contract No. NAS1-15426

September 1979



National Aeronautics and
Space Administration

Langley Research Center
Hampton, Virginia 23665
AC 804 827-3966

N80-25102 #

7

7

1

1

1

1



10

1

1

1

1

;

TABLE OF CONTENTS

<u>Section</u>	<u>Page</u>
1.0 SUMMARY	1
2.0 INTRODUCTION	3
2.1 Noise Control Study	3
2.2 General Characteristics of Analytical Model	4
2.3 Application of the Model to Propeller Aircraft	5
2.4 Study Aircraft Computations	8
2.5 Experimental Verification	10
3.0 ANALYTICAL MODEL	12
3.1 Power Balance Approach	12
3.2 General Formulation	13
3.3 Representations for the External Pressure Field	23
3.4 Tonal Power Flow Equation	31
3.5 Power Flow Statistics	33
3.6 Joint Acceptances	44
3.7 Internal Coupling	51
3.8 Test Conditions on Allowed Structural Wavenumbers	56
3.9 Sidewall Representation	59
3.10 Interior Acoustics	69
3.11 Computational Procedures	73
4.0 BASELINE AIRCRAFT	75
4.1 Study Requirements	76
4.2 Choice of Existing-Design Aircraft	77
4.3 Propfan Sizing Analysis	78
4.4 Characteristics of Baseline Aircraft	84
4.5 Baseline Fuselage Designs	92
4.6 Propeller Noise Field	107
5.0 MODEL OF STRUCTURE	116
5.1 General Representation	116
5.2 Structural Representations	122
5.3 Modal Density	125
5.4 Joint Acceptances	130
5.5 Radiation Efficiency	134
5.6 Loss Factors	135
5.7 Structural Idealization for Computational Purposes	138

<u>Section</u>	<u>Page</u>
6.0 NOISE LEVELS IN BASELINE AIRPLANES	147
6.1 Hamilton Standard Excitation Spectrum	147
6.2 Alternative Excitation Spectra	161
6.3 Conclusions	164
7.0 ADD-ON NOISE REDUCTION METHODS	165
7.1 General	165
7.2 Maximizing the Interior Absorption Coefficients	166
7.3 Increased Structural Damping	169
7.4 Double-Wall Sidewall Configurations	171
7.5 Summary	179
8.0 ADVANCED NOISE REDUCTION METHODS	181
8.1 Variations in Frame Parameters	182
8.2 Variation in Fuselage Skin Thickness	187
8.3 Honeycomb Skin Panels	189
8.4 Summary	192
9.0 REQUIREMENTS FOR EXPERIMENTAL VERIFICATION OF ANALYTICAL MODEL	196
9.1 Introduction	196
9.2 Sensitivity Studies	197
9.3 Candidate Noise Sources	227
9.4 Validation Experiments with a Model Fuselage	240
9.5 Aircraft Tests	255
10.0 CONCLUSIONS	267
REFERENCES	269
APPENDIX A - JOINT ACCEPTANCE EXPRESSIONS FOR NON-HOMOGENEOUS PRESSURE FIELDS	274
APPENDIX B - EXPECTED VALUE OF THE MODAL ADMITTANCE FUNCTION $g(\omega_b, \omega_n)$	280
APPENDIX C - RELATIONSHIP BETWEEN $\text{Im}[I^{rr}(\omega)]$ AND $f^2(n, r)$, $j_r^2(\omega)$	283
APPENDIX D - FINAL SIDEWALL DESIGN UTILIZING ADD-ON TREATMENTS	285
APPENDIX E - LIST OF SYMBOLS	290

LIST OF FIGURES

<u>Figure</u>	<u>Page</u>
1. Periodic Source Located Adjacent to (x,y) Plane . . .	26
2. Variation in Joint Acceptance with k_x/k_m and Amplitude Decay Constant a_x , for $m=4$, and $c_x=0$	47
3. Variation in Modal Joint Acceptance with k_x/k_m and m for Amplitude Decay Constant $a_x=0.5$	49
4. (a) Parallelepiped with Three Deformed Surfaces to illustrate representation of Fuselage Cabin	52
(b) Simplified Representation of Relationship between Vibrating Structure and Cabin	52
5. Mikulas' Frequency Equation for a Simply-Supported Stiffened Cylinder	58
6. Power Balance Representation of Sidewall Acoustics . . .	60
7. External Geometry of Panel-Pressure Field Con- figuration	64
8. Sidewall Representation for Porous Layer Bounded by Impervious Septa Mounted over Airgap	65
9. Cross-Section View of Image Array for Point Source (S) located in Wall and Centerline Observer (O)	72
10. Flow Diagram for Computation of Internal Noise Levels for Study Airplanes	74
11. Performance Parameters for 10-Bladed Propfan; Free Stream Mach Number $M_0 = 0.80$	83
12. Baseline Wide-Bodied Airplane	89
13. Baseline Narrow-Bodied Airplane	90
14. Baseline Small-Diameter Airplane	91
15. Typical Passenger Cabin Arrangements for the Study Airplanes	93
16. Typical Skin-Stringer-Frame Construction for Conventional Fuselages	94
17. Structural Details for Baseline Wide-Body Fuselage. . .	96
18. Structural Details for Baseline Narrow-Body Fuselage. .	97
19. Structural Details for Baseline Small-Diameter Fuselage	98
20. Baseline Transmission Loss for Add-On Sidewall	103

LIST OF FIGURES (Contd)

<u>Figure</u>	<u>Page</u>
21. Comparison of Measured and Model Absorption Coefficients	105
22. Sound Absorption Spectra Assumed for Furnishing Components	106
23. Directivity as a Function of Tip Clearance	108
24. Variation of External Sound Pressure Level Along the Cabin	109
25. Circumferential Trace Velocity and Amplitude Variation for Inboard Propeller of Wide Body Airplane.	111
26. Harmonic Levels of External Sound Field	112
27. Longitudinal Trace Velocity for Inboard Propeller of Wide Body Airplane	115
28. Representation of Fuselage Structural Element	119
29. Acceleration Coherence Measured on Adjacent Panels of Boeing 737 Fuselage ($M = 0.78$, Jet and Boundary Layer Noise)	123
30. Variation of Modal Density with Panel Area (Typical Narrow Body Fuselage Element, Low Frequency Structural Model)	126
31. Variation of Modal Density with Panel Element Area: Low Frequency Structural Models	127
32. Variation of Modal Density with Frequency	129
33. Effect of Panel Area on Band-Averaged Progressive Wave Joint Acceptance (Typical Narrow Body Fuselage Element, Low Frequency Structural Model)	131
34. Effect of Panel Area on Band-Averaged Progressive Wave Joint Acceptance: Low Frequency Structural Models	132
35. Effect of Panel Area on Band-Averaged Reverberant Field Joint Acceptance (Typical Narrow Body Fuselage Element, Low Frequency Structural Model)	133
36. Variation of Loss Factor with Frequency	137
37. Sketch Showing Locations of Structural Elements and Propellers: Wide Body Airplane	139

LIST OF FIGURES (Contd)

<u>Figure</u>	<u>Page</u>
38. Sketch Showing Locations of Structural Elements and Propellers: Narrow Body Airplane	140
39. Sketch showing Location of Structural Elements and Propeller: Small Diameter Airplane	141
40. Variation of Power Flow into the Cabin Along Cabin Length	148
41. Calculated Power Flow Through Fuselage Structures . . .	150
42. Axial Variation in Sound Level for Different Interior Absorption Coefficients (Narrow Body)	152
43. Comparison of Calculated and Measured Variation of Sound Level Along Cabin of a Small Diameter Propeller-Driven Aircraft	153
44. Axial Variation of Cabin A-Weighted Sound Level for Different Sidewall Treatments (Hamilton Standard Excitation [6])	154
45. Cabin Spectra at Location of Maximum dBA Levels for Bare and Baseline Treated Fuselages	156
46. Comparison of Calculated Baseline Noise Reductions with Empirical Data for Narrow-Bodied Fuselages	159
47. Expected Error Limits for the Acoustic Power Flow into the Airplane Cabins	160
48. Axial Variation of Cabin A-Weighted Sound Level for Different Excitation Spectra (Baseline Structure, Transmission Loss and Absorption)	162
49. Cabin Spectra at Location of Maximum Sound Level for Different Excitation Spectra	163
50. Sound Absorption Spectra assumed for Furnishing Components	167
51. Effect of Cabin Absorption on Cabin A-Weighted Sound Levels	168
52. Airplane Test Data on the Effect of Damping Treatments on Airplane Interior Noise Levels [35].	170
53. Effect of Structural Damping at Location of Maximum A-Weighted Sound Levels	172

LIST OF FIGURES (Contd)

<u>Figure</u>	<u>Page</u>
54. Additional Sidewall Transmission Loss (Double Wall Configuration Without Flanking)	174
55. Effect of Flow Resistance and Trim Surface Density on Add-On Sidewall Transmission Loss for Double Wall Sidewall (No Flanking)	177
56. Variation of Sidewall Treatment Surface Density along Cabin Length to Achieve 80 dBA Maximum Cabin Sound Level	178
57. Cabin Spectra at Location of Maximum Sound Levels, for Changes in Frames	183
58. Cabin Spectra at Location of Maximum Sound Levels, for Changes in Skin	188
59. Representation of Frame-Stiffened Honeycomb Fuselage Shell	191
60. Effect of Structural Changes on Space-Averaged Cabin A-Weighted Sound Levels	194
61. Effect of Structural Scaling on $\langle j_r^2 \rangle$, $n(\omega_b)/R$, and $\langle \sigma \rangle$	200
62. Predicted Additional Sidewall Transmission Loss, Full and Half-Scale Fuselage Models	208
63. Effect of Changes in Frame Stiffness and Skin Thickness and of Pressure Difference on $\langle j_r^2 \rangle$, $n(\omega)$, and σ for Wide Body Aircraft (Element 4).	211
64. Effect of Changes in Frame Stiffness and Skin Thickness and of Pressure Difference on $\langle j_r^2 \rangle$, $n(\omega_b)$ and σ for Narrow-Body Airplane (Element 4).	212
65. Effect of Changes in Frame Stiffness and Skin Thickness and of Pressure Difference on $\langle j_r^2 \rangle$, $n(\omega_b)$ and σ for Small-Diameter Airplane	213
66. Effect of Variations in Amplitude Decay Rate and Coherence on Band-Averaged Joint Acceptance: Wide-Body Airplane (Element 4): Low Frequency Structural Model.	215
67. Dependence of $\langle j_r^2 \rangle$ on Changes in $(a_x a_y)$, showing Constraints on $(a_x a_y)$ as determined by Required Accuracy in $\langle j_r^2 \rangle$	216
68. Effect of Variations in Trace Wave Speed on Band-Averaged Joint Acceptance: Wide Body Airplane (Element 4): Low Frequency Structural Model.	217

LIST OF FIGURES (Contd)

<u>Figure</u>	<u>Page</u>
69. Effect of Variations in Frame Properties for Wide Body Airplane - Variation in Frame Bending Stiffness	219
70. Effect of Variations in Frame Properties for Wide Body Airplane - Variation in Frame Membrane Stiffness.	220
71. Effect of Variations in Stringer Properties for Wide Body Airplane - in Stringer Bending Stiffness	221
72. Effect of Variations in Stringer Properties for Wide Body Airplane - in Stringer Membrane Stiffness.	222
73. Effect of Variations in Skin Thickness for Wide Body Airplane	224
74. Effect of Panel Curvative on $\langle j_r^2 \rangle$, $n(\omega_b)$ and σ for Wide Body Aircraft (Element 4)	225
75. Sketch of Possible Arrangement of Model Propfan and Fuselage Within the Anechoic Flow Facility, NSRDC, Carderock [44].	231
76. Spatial Variation of Propeller Overall Sound Level in Longitudinal Direction: Comparison of Propfan Predictions and General Aviation Measurements.	232
77. (a) Variation of Axial Trace Velocity with X/D for 3 Study Airplanes (Ray Acoustics Model with Source Location at 0.7 Propeller Radius) -X-Aero Commander Data [8]	234
(b) Variation of Circumferential Trace Velocity. Propfan Predictions Based on 'Rigid Body' Rotation of Hydrodynamic Propeller Pressure Field	234
78. Required Axial Directivity & Spherical Spreading Losses for Each Study Aircraft (Inboard Propeller). . .	236
79. Required Directivity for Acoustic Source (Inboard Propeller) Showing Panel Location for Narrow Body Aircraft	237
80. Comparison of Acoustic Source Spherical Spreading Losses with Propfan Airplane Predictions - Circumferential Direction	239
81. Schematic End View of Test Configuration	242
82. Schematic Diagram of Signal Generation and Data Acquisition Systems	251
83. Schematic Diagram of Data Reduction System	253
84. Differences Between Predicted and Measured Payload Bay Levels for Space Shuttle Validation Tests	256

LIST OF FIGURES (Contd)

<u>Figure</u>	<u>Page</u>
85. Use of Small Diameter Fuselage to Scale Model Wide Body Fuselage	261
86. Use of Small Diameter Fuselage to Scale Model Wide Body Fuselage	262

LIST OF TABLES

<u>Table</u>	<u>Page</u>
1. Performance Parameters for Propfan-Powered Baseline Study Airplanes	86
2. Performance Parameters Common to Each Baseline Study Airplane	88
3. Characteristics of Baseline Fuselages	99
4. Structural Segmentation Details: Wide-Body	143
5. Structural Segmentation Details: Narrow-Body	144
6. Structural Segmentation Details: Small-Diameter.	145
7. Structural Data for Typical Element of Baseline Airplanes.	146
8. Minimum Additional Noise Reduction Required for Baseline Structure	157
9. Calculated error limits for the acoustic power flow into airplane cabins	161
10. Predicted Weight Increase, relative to Baseline Aircraft, to achieve 80 dB A-Weighted Sound Level Criterion	179
11. Fuselage Details for Advanced Noise Control Structures: Wide Body	184
12. Fuselage Details for Advanced Noise Control Struc- tures: Narrow Body	185
13. Fuselage Details for Advanced Noise Control Struc- tures: Small Diameter	186
14. Dimensions for Honeycomb Structures	190
15. Summary of Noise Reductions Achieved with Advanced Concepts	193
16. Comparison of Study and Existing Aircraft	257

[illegible]

1.0 SUMMARY

An analytical model has been developed to predict the transmission of propeller noise into the cabin of a high-speed propeller-driven airplane. The model is then used to determine the noise control treatments required to achieve a goal of an interior A-weighted sound level of 80 dB for three study airplanes with different fuselage diameters but with a common cruise Mach number of 0.8 at an altitude of 30,000 ft.

The analytical model describes the excitation in terms of a propagating pressure field with a pressure amplitude which decays rapidly with distance. The fuselage structure is represented as a series of curved, orthotropic plates with in-plane loads, the orthotropic characteristics resulting from the effects of smearing out the stiffness and mass of the longitudinal and circumferential stiffeners. Finally, the receiving cavity or cabin is basically a rectangular parallel-piped with 'deformed' curved surfaces. Sound transmission into the cabin is then calculated using the concept of acoustic power flow with allowance being made for resonant and non-resonant response. The influence of the cabin sidewall treatment is introduced as an additional transmission loss experienced by the transmitted power. Sound absorption in the cabin results in power dissipation losses which balance the net inflow of acoustic power.

Three baseline aircraft with wide-body, narrow-body and small-diameter fuselages, respectively, are selected based on existing airplane designs, and the analytical model is used to calculate the propeller noise levels in the passenger cabin. It is found that noise reductions of about 25 dB, in the frequency range of 130-230 Hz, are required to achieve the goal of

80 dBA. Noise reduction methods are investigated in the form of either add-on treatments, which can be applied to existing fuselage structures, or advanced techniques, which require changes to the primary structures. For the add-on methods, only a double-wall sidewall with a heavy, limp trim panel isolated from the fuselage structure is found to give the required noise reduction. No advanced technique is found which, on its own, can provide the required additional 25 dB transmission loss over the frequency range of interest.

The elements of the analytical model are presented without direct validation. Such validation is, of course, highly desirable and the design and performance of validation experiments is discussed. All the test methods considered have disadvantages but laboratory tests using a loud speaker with a directional horn and a model fuselage structure in the form of a cylinder are recommended for validation of the basic analytical model and its use in predictions for add-on noise control treatments. Tests on present-day propeller-powered aircraft could be performed but they would not be directly applicable in terms of validating the predictions for the high-speed aircraft powered by the high-speed propfan concept for a propeller.

2.0 INTRODUCTION

2.1 Noise Control Study

As part of an overall program to develop aircraft with improved fuel efficiency, consideration has been given to the design of high-speed propeller-driven aircraft. Preliminary studies [1, 2, 3] have shown that significant fuel savings can be achieved by these aircraft but, at the same time, several problem areas were identified. One potentially severe problem is that of high interior noise levels in the passenger compartments. In order to explore this problem more fully, a study was initiated to develop an analytical model for the transmission of propeller noise into an airplane fuselage. The model is then to be used to explore potential noise control methods for three study aircraft of different fuselage diameters. The noise control techniques could be add-on treatments which would be applied to current day conventional fuselage structures, or advanced noise control methods which involve design changes to the primary structure.

The development and application of such an analytical model is presented in this report. A general overview of the study is provided in this section, while in Section 3 the development of the analytical model is described. The model is applied to three study aircraft whose aerodynamic, structural, and acoustic characteristics are presented in Section 4. Then the analytical idealization used to describe the structure of the fuselages for the three aircraft is presented in Section 5. The following three sections discuss the application of the analytical model to the baseline airplanes (Section 6) and explore the potential of add-on (Section 7) and advanced noise control treatments (Section 8). Finally, Section 9 considers

the feasibility and design of experiments to validate the analytical model and the predictions for the baseline airplanes.

The title of this study refers to high-speed propeller-driven aircraft. However, the implicit assumption is that a specified propeller, called a "propfan" in the relevant technical literature (see, for example, [1]) will be considered as the propulsive agent. The name propfan will be used in this report to identify the high-speed propeller.

2.2 General Characteristics of Analytical Model

The basic concept of the analytical model is that of power flow, and the cabin noise levels are estimated by means of a series of power balance equations which equate transmitted and dissipated acoustic energy. The model uses as a starting point the analytical study performed for the acoustic environment in the payload bay of the space shuttle orbiter vehicle at lift-off [4] and the analytical model considers both resonant and non-resonant response in one-third octave frequency bands. Resonant response occurs when the transmitting structural modes, or the receiving cavity acoustic modes have resonance frequencies in the frequency band of interest. Non-resonant response is associated with modes whose resonance frequencies lie outside the frequency band of interest. The relative importance of resonant and non-resonant response in a given frequency band will depend on a number of factors, one of the most important being the number of modes with frequencies within that band. For example, if there are few or no acoustic modes with resonance frequencies within the band of interest, then non-resonant acoustic response may be an important factor

in determining the total acoustic power flow in that band. Thus it might be anticipated that non-resonant response might be of particular importance at low frequencies. On the other hand, power flow from non-resonant structural modes may control the fuselage noise reduction when the radiation efficiency of resonant structural modes is very low.

The analytical model incorporates various simplifications and assumptions in order to provide an engineering prediction tool which does not require too extensive computation requirements. One such simplification involves the division of structural and acoustic response into low and high frequency regimes. At very low frequencies there are few modes in a given frequency band and individual modes must be considered when calculating structural response and coupling between structure and acoustic cavity. Then as modes in a given frequency bandwidth accumulate as frequency increases, some approximations can be made for the expressions for modal coupling. Finally, at high frequencies it is impractical to consider modal response on a mode-by-mode basis and recourse is had to a modification of the method of statistical energy analysis.

2.3 Application of the Model to Propeller Aircraft

The analytical model has been developed in a general sense so that it can be applied to propeller noise fields where the excitation is discrete frequency in character and has strong spatial decay of the pressure amplitude, as well as to cases where the excitation is broad-band and homogeneous, such as the space shuttle. However when the model is applied to the present study aircraft certain assumptions are made to reduce

the computational requirements without causing significant adverse effects on the accuracy of the calculations. These assumptions will be discussed at the appropriate place in this report, but some of the more important ones are mentioned in this section.

In the analytical model for noise transmission into a propeller-driven airplane, resonant and non-resonant response is considered in both low and high frequency regimes. However, as will be discussed later, it is found that the acoustic power flow is dominated by resonant response. Furthermore, because the modal density is high, only the high frequency idealization is used for power flow calculations.

One assumption concerns the size of the structural unit to be considered as a noise transmitting element. While it is possible that the fuselage structure can be considered as a single unit, it is feasible to break the fuselage down into several smaller units. Parametric studies in Section 4 will show that above a certain size, the calculated acoustic power flow will be essentially independent of the dimensions of the structural unit. This is due, to a large extent, to the rapid spatial decay of the amplitude of the excitation pressure field. Several advantages are obtained by this segmentation of the structure, including the ability to estimate the spatial variation of sound level inside the passenger cabin. Utilizing the concept of structural units, the fuselage is divided into several elements in the longitudinal direction. In the circumferential direction it is assumed that noise transmission through the floor can be neglected and that the transmitting structure can be considered as a floor-to-floor or a floor-to-ceiling unit, depending on fuselage diameter.

In terms of frequency regime, it is assumed that, when the modal bandwidth is greater than the separation between modes for the (cabin) acoustic volume, the various high frequency approximations can be used. Then the acoustic radiation into the volume can be described using a modified statistical energy analysis approach.

The basic analytical model estimates noise transmission through a single wall structure into a receiving cavity. However a typical airplane fuselage contains a sidewall treatment which will provide thermal and acoustic control. This sidewall treatment can be idealized as a double wall system, the outer panel being the skin of the fuselage structure. The space between the two panels is filled with insulation material such as glass fiber batts. The assumption is made in this analytical model that the additional transmission loss provided by the noise control treatment can be modeled as an extra transmission coefficient which is applied directly to the calculated power flow through the untreated fuselage structure. Whilst this assumption is not strictly valid [5], the errors associated with the assumption are not large and the simplifications to the analytical model are significant.

In applying the analytical model to an excitation field such as is generated by a propeller, consideration has to be given to the uncertainties which arise due to the dominance of discrete frequency components in the excitation spectrum. This is particularly important when the modal densities for the structure and receiving volume are low. In such cases the accuracy of the predicted resonance frequencies becomes critical in determining the accuracy of the predicted noise levels, and therefore statistical evaluations of the predicted noise

reduction are introduced. An approach which provides confidence limits for the predictions is presented in the description of the analytical model.

2.4 Study Aircraft Computations

Following development of the analytical model to predict propeller noise transmission into the interior of an airplane fuselage, various computations are made for the three study aircraft.

As a first step the external excitation pressure field has to be defined and this is accomplished on the basis of existing, albeit sparse, analytical and empirical information. This information refers to both high speed (propfan) and general aviation propellers. The propfan data were obtained from a prediction procedure for sound pressure level provided by the Hamilton Standard Division of United Technologies. This procedure [6] permits estimation of the spatial distribution of the sound pressure level under free field conditions, provided that the propfan performance characteristics are known or have been previously estimated. Propfan performance characteristics were estimated using Hamilton Standard procedures [7]. While there are several methods for predicting propfan noise, some of which predict higher levels [1], the Hamilton Standard procedure results from continuing investigation of propfan characteristics and thus it seemed appropriate to use it for this study. These free-field noise levels were converted to blocked surface pressures, as described in Section 4.6. General aviation propeller noise data [8,9] are used to infer trace velocity properties for the pressure field. It is recognized that the operating conditions for a general aviation

propeller are significantly different from those of a propfan but, in the absence of alternative data, the general aviation propeller measurements can be used as a preliminary model. When more data are forthcoming for the propfan, the analytical model can be brought up-to-date if need be.

Prior to calculating the noise transmission into the passenger cabin, the fuselage structure is idealized into equivalent orthotropic panels by smearing out the assumed structural characteristics for the different study aircraft. In addition, a transmission loss spectrum is provided for the baseline sidewall. Absorption spectra are assumed for the cabin interior. These acoustic absorption spectra are based on empirical data for conventional interior sidewall and trim configurations. With this information the longitudinal spatial variation of the cabin sound level can be calculated, and the noise reductions determined to reach the goal of a maximum level of 80 dB(A).

The next step in the computation process is to utilize the analytical model for a variety of add-on noise control methods to determine treatments which can provide the required noise reductions. These add-on treatments have to be such that they can be applied to existing conventional (baseline) fuselage structures without modification to the load-bearing characteristics of the structures. From the different concepts investigated, only the double wall with a heavy, limp interior trim panel appears to have the potential of achieving the large noise reductions required at the low frequencies associated with propfan excitation.

In order to perform computations for the advanced noise control concepts, where it is assumed that such concepts involve modifications to the fuselage primary structure, it is necessary

to calculate the structural response for each of the new structures. For each new structure, calculations are performed to determine the characteristics of the equivalent orthotropic panels and these characteristics are used to compute the noise transmission. Within the scope of the analysis, no primary structure was identified which could provide the noise reductions required to meet the 80 db(A) criterion.

2.5 Experimental Verification

In the development of any analytical model it is always advisable to perform experimental validation of the model. Such validation provides confirmation that the assumptions introduced into the analytical model are valid for the specific cases to which the model is applied. The validation also provides confidence in the accuracy of the analytical model.

Several validation experiments were performed on the analytical model for the space shuttle payload bay acoustic environment [10, 11]. Since that model provided a basis for the present analytical model for propeller-driven aircraft there is some confidence that the present model will provide reliable predictions. Even so, consideration should be given to obtaining direct verification of the propeller noise transmission model. Model verification did not form a part of the study reported herein, but the study did include an assessment of the important parameters in the model and recommendations for prospective verification experiments.

The choice of experiment depends to some extent on the actual objective of the tests. If the objective is to confirm the specific noise reductions predicted for the three study

airplanes, then the experiments should be designed to model the important parameters of those study aircraft. Alternatively, if the objective is to validate the analytical model under more arbitrary conditions, an existing propeller-driven airplane could be selected, the analytical model used to predict the noise transmission into that aircraft and an experiment devised to confirm those predictions. It should be borne in mind, however, that if the test conditions differ radically from those corresponding to the study aircraft, the validation of the analytical model may be performed for a situation unrepresentative of propfan operations.

The evaluation of potential test procedures discussed in Section 9 includes both of the above objectives although the emphasis is placed on the validation of the analytical model as applied to the study aircraft. This emphasis is chosen because it allows the analytical model to be tested under conditions appropriate to the subject under consideration -- high-speed, propeller-driven aircraft.

3. ANALYTICAL MODEL

3.1 Power Balance Approach

The basic concept of the analytical model is that of the balance of acoustic power flow from the exterior of a bounding surface to an interior-contained volume. This approach has recently been developed by Pope and Wilby [4] for application in the acoustic modeling of the payload bay of the Space Shuttle orbiter vehicle.

The first step in the analysis considers the vibrational response of the fuselage structure to the external pressure field. The model takes into account the external pressure field in terms of level distribution over the fuselage surface, spectrum shape, and spatial correlation. It describes the structure in terms of the mode shapes of equivalent orthotropic panels, including frequency-dependent effects of skin and stringer and frame stiffnesses and masses, pressurization, and curvature. The coupling between the external pressure field and the fuselage vibrational response is formulated in terms of modal joint acceptances.

The second step considers the power radiated by the fuselage structure into the cabin. Acoustic power is radiated into the volume by the structural modes, and the power is accepted by the acoustic modes of the volume. Resonant and nonresonant response of the structure and volume are considered in the analysis, resonant response being that for which the participating modes have resonance frequencies within the frequency band of interest. Nonresonant structural response can be either mass-controlled (resonance frequencies below the band of interest) or stiffness-controlled (resonance frequencies above the band). However, for present purposes, the stiffness-controlled response is excluded, as the

radiation efficiencies of stiffness-controlled modes are low compared with those of resonant and mass-controlled modes (Eq. (61)).

The final step determines the space-averaged sound pressure levels in the interior volume by equating the net inflow of acoustic power to that which is absorbed within the interior space. The model accounts for any transmission of acoustic power from the interior back to the exterior of the fuselage.

The following sections present a detailed derivation of these acoustic power flow equations, with particular emphasis placed on the following developments which have specific application to propeller noise:

1. Transmission of discrete tones through a structural element into a cavity;
2. Estimates for the mean and standard deviation of the acoustic power flow; and
3. Closed-form solutions for the coupling between a nonhomogeneous excitation and the fuselage vibration response.

3.2 General Formulation

In the general formulation, the transmitting structural system is assumed to cover a cavity which has absorbing walls as the interior surfaces. The frequency range considered is sufficiently wide to assure that the cavity possesses at least one mode which is resonant in the frequency band of interest. The transmitting structure is assumed to have modes resonant below and within (or simply within) the band of interest.

The transmitting structural system will respond to excitation by an external random pressure field according to the relation

$$W_T(\bar{x}, \omega) = \int G(\bar{x}, \bar{x}'; \omega) [P_T^O(\bar{x}', \omega) - P_T^I(\bar{x}', \omega)] d\bar{x}' \quad (1)$$

$G(\bar{x}, \bar{x}'; \omega)$ is the Green's function for the structure, $P_T^O(\bar{x}')$ represents the external exciting pressure, and $P_T^I(\bar{x}')$ the induced interior pressure on the structure. Mathematically $W_T(\bar{x}, \omega)$, $P_T^O(\bar{x}; \omega)$, $P_T^I(\bar{x}', \omega)$ are Fourier transforms of truncated records (in time) of length T and are related to the spectral components of the random displacements and pressures.

The induced interior field is related to the displacement response of the structure by

$$P_T^I(\bar{x}', \omega) = -\rho_i \omega^2 \int G_p(\bar{x}, \bar{x}'; \omega) W_T(\bar{x}, \omega) d\bar{x} \quad (2)$$

where $G_p(\bar{x}, \bar{x}'; \omega)$ is the Green's function for the interior space.

The external driving field is given by

$$P_T^O(\bar{x}', \omega) = P_{b\ell_T}(\bar{x}', \omega) + \rho_e \omega^2 \int G_p^O(\bar{x}, \bar{x}'; \omega) W_T(\bar{x}, \omega) d\bar{x} \quad (3)$$

where $P_{b\ell_T}(\bar{x}', \omega)$ is the transform of the blocked pressure, $G_p^O(\bar{x}, \bar{x}'; \omega)$ is the exterior field Green's function (source point on the structure), and the integral represents the radiated pressure field. The ambient densities in the interior and exterior spaces are given by ρ_i and ρ_e , respectively, and the associated speeds of sound are c_i and c_e .

3.2.1 Structural Response

These coupled integral equations can be reduced to a system of simultaneous algebraic equations to obtain the modal response ξ_{rt} of the transmitting structure [12]:

$$[-Y_r M_r + \omega^2(\rho_i I^{rr} + \rho_e J^{rr})]\xi_{rT} + \omega^2 \sum_{s \neq r} (\rho_i I^{rs} + \rho_e J^{rs})\xi_{sT} = -\Gamma_{pb\ell_T}^r. \quad (4)$$

In Eq. (4) external and internal acoustical coupling of structural modes is described by the intermodal coupling coefficients defined as [13]

$$\left. \begin{aligned} J^{rs}(\omega) &= \iint G_p^O(\bar{x}, \bar{x}'; \omega) \psi^r(\bar{x}') \psi^s(\bar{x}) d\bar{x}' d\bar{x}, \\ I^{rs}(\omega) &= \iint G_p(\bar{x}, \bar{x}'; \omega) \psi^r(\bar{x}') \psi^s(\bar{x}) d\bar{x}' d\bar{x}. \end{aligned} \right\} \quad (5)$$

$\Gamma_{pb\ell_T}^r(\omega)$ is the generalized blocked force

$$\Gamma_{pb\ell_T}^r = \int P_{b\ell_T}(\bar{x}', \omega) \psi^r(\bar{x}') d\bar{x}', \quad (6)$$

$\psi^r(\bar{x})$ is the eigenfunction of mode r , M_r is the modal mass, and Y_r is a receptance given by

$$Y_r = \omega_r^2 [1 - (\omega/\omega_r)^2 - i\eta_r], \quad (7)$$

where η_r and ω_r are the modal loss factor and resonance frequency, respectively.

The matrix form of Eq. (4) is

$$[a_{rs}]\{\xi_{rT}\} = \{-\Gamma_{pb\ell_T}^r\},$$

and has the solution

$$\{\xi_{rT}\} = [\bar{\alpha}_{rt}]\{-\Gamma_{pb\ell_T}^r\},$$

from which the displacement response of the structure is obtained:

$$W_T(\bar{x}, \omega) = - \sum_{r,t} \psi^r(\bar{x}) \bar{\alpha}_{rt} \Gamma_{pb\ell_T}^t(\omega). \quad (8)$$

The one-sided cross-power spectral density for the displacement at points \bar{x}, \bar{x}' is given by the relation

$$S_w(\bar{x}, \bar{x}'; \omega) = \lim_{T \rightarrow \infty} (2/T) (1/2\pi) W_T(\bar{x}) W_T^*(\bar{x}'), \quad (9)$$

and, from Eq. (8)

$$\begin{aligned} S_w(\bar{x}, \bar{x}'; \omega) = & \sum_{r,t,\ell,n} \bar{\alpha}_{rt} \bar{\alpha}_{\ell n}^* \psi^r(\bar{x}) \psi^\ell(\bar{x}') \iint S_p(\bar{x}'', \bar{x}'''; \omega) \\ & \times \psi^t(\bar{x}'') \psi^n(\bar{x}''') d\bar{x}'' d\bar{x}''', \end{aligned} \quad (10)$$

where $S_p(\bar{x}'', \bar{x}'''; \omega)$ is the one-sided cross-power spectral density of the exterior blocked pressure, i.e.

$$S_p(\bar{x}'', \bar{x}'''; \omega) = \lim_{T \rightarrow \infty} (2/T) (1/2\pi) P_{b\ell_T}(\bar{x}'', \omega) P_{b\ell_T}^*(\bar{x}''', \omega). \quad (11)$$

3.2.2 Power Radiated into the Cavity

The one-sided cross-power spectral density between pressure at position \bar{x} and velocity at \bar{x}' is

$$Sp_1 v(\bar{x}, \bar{x}'; \omega) = \lim_{T \rightarrow \infty} (2/T)(i\omega/2\pi) P_T^1(\bar{x}, \omega) W_T^*(\bar{x}', \omega). \quad (12)$$

Equation (2) yields

$$Sp_1 v(\bar{x}, \bar{x}'; \omega) = -i\rho_1 \omega^3 \int G_p(\bar{x}, \bar{x}''; \omega) S_w(\bar{x}'', \bar{x}'; \omega) d\bar{x}''.$$

Let $\bar{x}' \rightarrow \bar{x}$. Then, the spectral density of power radiated is obtained by integrating $Sp_1 v(\bar{x}, \bar{x}; \omega)$ over the transmitting area; i.e.

$$W_{rad}^{int}(\omega) = \int Sp_1 v(\bar{x}, \bar{x}; \omega) d\bar{x}. \quad (13)$$

This quantity is complex, and the real part is the real power. From above,

$$W_{rad}^{int}(\omega) = -i\rho_1 \omega^3 \iint G_p(\bar{x}, \bar{x}'; \omega) S_w(\bar{x}', \bar{x}; \omega) d\bar{x}' d\bar{x}. \quad (14)$$

Using Eq. (10), this becomes

$$\begin{aligned} W_{rad}^{int}(\omega) = & -i\rho_1 \omega^3 \sum_{r,t,\ell,n} \bar{\alpha}_{rt} \bar{\alpha}_{\ell n}^* \int_{\bar{x}} \int_{\bar{x}'} G_p(\bar{x}, \bar{x}'; \omega) \psi^r(\bar{x}) \\ & \times \psi^\ell(\bar{x}') d\bar{x} d\bar{x}' \int_{\bar{x}''} \int_{\bar{x}'''} S_p(\bar{x}'', \bar{x}'''; \omega) \psi^t(\bar{x}'') \\ & \times \psi^n(\bar{x}''') d\bar{x}'' d\bar{x}'''. \end{aligned} \quad (15)$$

Now introduce the intermodal coupling coefficients $I^{r\ell}(\omega)$ to obtain

$$W_{\text{rad}}^{\text{int}}(\omega) = -i\rho_1\omega^3 \sum_{r,t,\ell,n} \bar{\alpha}_{rt} \bar{\alpha}_{\ell n}^* I^{r\ell}(\omega) \iint S_p(\bar{x}, \bar{x}'; \omega) \psi^t(\bar{x}) \psi^n(\bar{x}') d\bar{x} d\bar{x}'. \quad (16)$$

If the cross terms for the external and internal acoustic coupling coefficients for the structural modes can be neglected, Eq. (16) reduces to:

$$W_{\text{rad}}^{\text{int}}(\omega) = -i\rho_1\omega^3 \sum_r \frac{I^{rr}(\omega)}{|M_r Y_r - \omega^2(\rho_e J^{rr} + \rho_1 I^{rr})|^2} \iint S_p(\bar{x}, \bar{x}'; \omega) \psi^r(\bar{x}) \psi^r(\bar{x}') d\bar{x} d\bar{x}'. \quad (17)$$

The assumption of negligible coupling of the structural modes by the radiated sound field (i.e., $I^{rs} = 0$ for $r \neq s$) is equivalent to the assumption of weak coupling between the structure and the cavity. Justification for this assumption is given in [4], where it is pointed out that the assumption does not preclude well-coupled modes that occur when acoustic and structural modes have resonance frequencies closely spaced relative to the modal bandwidths. The assumption that the cross terms for the external coupling coefficient can be neglected (i.e., $J^{rs} = 0$ for $r \neq s$) is adopted in [4] for a homogeneous excitation field. It is assumed now that the cross terms will also be negligible for the present inhomogeneous pressure field.

The cavity Green's function is

$$G_p(\bar{x}, \bar{x}'; \omega) = \sum_n \frac{\bar{\phi}_n(\bar{x}) \bar{\phi}_n(\bar{x}')}{(\bar{k}_n^2 - k^2) \iiint \bar{\phi}_n^2(\bar{x}) d\bar{V}} \quad (18)$$

where $\bar{\phi}_n(\bar{x})$ is the complex mode shape, and the complex eigenvalue is

$$\bar{k}_n = k_n - i\kappa_n. \quad (19)$$

The acoustic surface admittance of the cavity walls is

$$\beta = \xi - i\sigma = \rho_1 c_1 / z$$

where ξ is the normalized conductance and σ is the normalized susceptance of the wall. z is the inner surface's specific acoustic impedance, that is, the ratio of pressure to normal velocity at the wall,

$$z = p/v.$$

Analysis is confined to the case $|\beta| \ll 1$. Then

$$\bar{\phi}_n(\bar{x}) \approx \phi_n(\bar{x}),$$

which is real. With the normalization such that

$$\int \phi_n^2 d\bar{V} = V/\epsilon_n,$$

where V is the volume of the cavity and ϵ_n is mode dependent, the joint intermodal coefficient in Eq. (18) becomes

$$I^{rr}(\omega) = \iiint \sum_n \frac{\epsilon_n \phi_n(\bar{x}) \phi_n(\bar{x}')}{V(\bar{k}_n^2 - k^2)} \psi^r(\bar{x}) \psi^r(\bar{x}') d\bar{x} d\bar{x}',$$

which reduces to the form

$$I^{rr}(\omega) = \frac{A^2}{V} \sum_n \frac{\epsilon_n}{(\bar{k}_n^2 - k^2)} f^2(n,r), \quad (20)$$

where the function $f(n,r)$ is the coupling factor between the structure and the cavity.

$$f(n,r) = \frac{1}{A} \int \phi_n(\bar{x}) \psi^r(\bar{x}) d\bar{x}.$$

The spectrum of real power flowing inwardly can now be written:

$$\begin{aligned} \text{Re}[W_{\text{rad}}^{\text{int}}(\omega)] &= \frac{2\rho_i \omega^3 A^2}{V} \sum_n \frac{\epsilon_n k_n \kappa_n}{|\bar{k}_n^2 - k^2|^2} \sum_r \frac{f^2(n,r)}{|M_{rY_r} - \omega^2(\rho_e J^{rr} + \rho_i I^{rr})|^2} \\ &\times \iint C_p(\bar{x}, \bar{x}'; \omega) \psi^r(\bar{x}) \psi^r(\bar{x}') d\bar{x} d\bar{x}', \end{aligned} \quad (21)$$

where $C_p(\bar{x}, \bar{x}'; \omega)$ is the real part of $S_p(\bar{x}, \bar{x}'; \omega)$; i.e. the co-spectrum or co-spectral density function of the exterior blocked pressure, and

$$|\bar{k}_n^2 - k^2|^2 = (k_n^2 - \kappa_n^2 - k^2)^2 + 4k_n^2 \kappa_n^2. \quad (22)$$

Now $k_n = \omega_n / c_i$ and $\kappa_n = \omega_n \eta_n / 2c_i$ [4] where η_n is the loss factor of the acoustic mode with resonance frequency ω_n . Thus,

$$k_n \kappa_n = \eta_n \omega_n^2 / 2c_i^2$$

and

$$|\bar{k}_n^2 - k^2|^2 \approx \frac{\omega_n^4}{c_i^4} \left[\left(1 - \frac{\omega^2}{\omega_n^2} \right)^2 + \eta_n^2 \right]. \quad (23)$$

The band-limited input power, for a bandwidth $\Delta\omega$, is

$$\text{Re} \left[W_{\text{rad}}^{\text{int}}(\omega) \right]_{\Delta\omega} = \text{Re} \int_{\Delta\omega} W_{\text{rad}}^{\text{int}}(\omega) d\omega .$$

Then, under the assumption that the radiation loss factor is relatively small [4], the term in I^{rr} can be neglected, and

$$\begin{aligned} |M_r Y_r - \omega^2(\rho_e J^{\text{rr}} + \rho_i I^{\text{rr}})|^2 &\approx M_r^2 |Y_r|^2 \\ &= M_r^2 \omega_r^4 \left[\left(1 - \frac{\omega^2}{\omega_r^2}\right)^2 + \eta_r^2 \right], \end{aligned}$$

where η_r is now defined as the sum of the structure's dissipative and external radiation loss factors.

The band-limited power flow into the volume becomes

$$\begin{aligned} \text{Re} \left[W_{\text{rad}}^{\text{int}}(\omega) \right]_{\Delta\omega} &= \frac{\rho_i c_i^2 \omega^3 A^2}{V} \int_{\Delta\omega} \left\{ \sum_n \frac{\epsilon_n \eta_n}{\omega_n^2 \left[\left(1 - \frac{\omega^2}{\omega_n^2}\right)^2 + \eta_n^2 \right]} \right. \\ &\quad \times \left. \sum_r \frac{f^2(n,r) \iint C_p(\bar{x}, \bar{x}'; \omega) \psi^r(\bar{x}) \psi^r(\bar{x}') d\bar{x} d\bar{x}'}{M_r^2 \omega_r^4 \left[\left(1 - \frac{\omega^2}{\omega_r^2}\right)^2 + \eta_r^2 \right]} \right\} d\omega . \quad (24) \end{aligned}$$

It is clear then that, in general, calculation of the band-limited power flow into the volume requires estimates of both acoustic and structural resonance frequencies and mode shapes and their respective loss factors, together with a model for the excitation co-spectral density function.

3.2.3 Power Absorbed by Cavity Walls

When calculating the acoustic power absorbed by the interior surfaces of the fuselage cabin, it will be assumed that the surfaces are locally reacting. Then, the motion at one portion of the surface is dependent only on the acoustic pressure incident on that portion. This assumption is valid for the limp, absorptive surfaces envisaged for the cabin sidewall treatments.

From [4], the acoustic power absorbed by the walls is given by the general relationship

$$W_{abs}^{int} = \frac{1}{\rho_1 c_1} \sum_n \sum_w \epsilon_{wn} A_w \xi_w \langle p_n^2 \rangle$$

where A_w is the absorbing area of wall w , ξ_w is the wall conductance, $\langle p_n^2 \rangle$ is the space-averaged, mean square pressure in the volume V due to the response of the n th acoustic mode, and ϵ_{wn} is a modal factor. On an acoustic mode-by-mode basis, this becomes [4]

$$W_{abs}^{int} = \frac{V}{\rho_1 c_1} \sum_{n=p,q,r} \langle p_n^2 \rangle \left(\epsilon_p \frac{\xi_{x+} + \xi_{x-}}{a} + \epsilon_q \frac{\xi_{y+} + \xi_{y-}}{b} + \epsilon_r \frac{\xi_{z+} + \xi_{z-}}{c} \right) \quad (25)$$

where it is assumed that the volume is approximately rectangular in shape, with dimensions (a,b,c) . The wall conductances are now denoted by ξ_{x+} , ξ_{x-} , etc; and ϵ_p , ϵ_q , ϵ_r are modal participation factors with values of 1 or 2 depending on mode order.

Equation (25) requires a knowledge of the wall conductances before the absorbed power can be calculated. Such information is not readily available in practice, although values of the

absorption coefficients are often known or can be estimated. Therefore, it is necessary to convert Eq. (25) into a form that incorporates the absorption coefficient α rather than the conductance ξ . Following the approach used in [4], the conversion has been accomplished by modeling the low-frequency absorption characteristics of the volume in such a manner that the relationship maps into the correct form at high frequencies. The rate at which the formulation approaches the high frequency value is comparable to the accumulation of modes in the volume. The resulting equation is

$$W_{\text{abs}}^{\text{int}} \approx \frac{\langle p_f^2 \rangle}{2\rho_1 c_1} [(\alpha_{x+} A_{x+} + \alpha_{x-} A_{x-}) \Gamma_{\epsilon}^x + (\alpha_{y+} A_{y+} + \alpha_{y-} A_{y-}) \Gamma_{\epsilon}^y + (\alpha_{z+} A_{z+} + \alpha_{z-} A_{z-}) \Gamma_{\epsilon}^z]. \quad (26)$$

where $\Gamma_{\epsilon}^x = \frac{1}{N_n} \sum_n \frac{\epsilon_{p_n}}{\epsilon_{q_n} \epsilon_{r_n}}$, N_n is the number of acoustic modes, and

the assumption is made that the exterior input and interior coupling are complex enough to assure that the modal responses differ little from the mean, so that $\langle p_1^2 \rangle = N_n \langle p_n^2 \rangle$. In the high-frequency regime, where there are many oblique modes, the average conductance is about one-eighth of the average absorption coefficient [13].

3.3 Representations for the External Pressure Field

A joint acceptance function $j_r^2(\omega)$ can be introduced to quantify the the coupling between the external pressure field and the r th structural mode. The function can be defined as

$$j_r^2(\omega) = \frac{1}{A^2 S_{p_{XO}}(\omega)} \int_{\bar{x}} \int_{\bar{x}'} S_p(\bar{x}, \bar{x}', \omega) \psi^r(\bar{x}) \psi^r(\bar{x}') d\bar{x} d\bar{x}' \quad (27)$$

where $S_{p_{X_0}}(\omega)$ is the one-sided power spectral density of the exterior blocked pressure field at a reference location X_0 . As before, $S_p(\bar{x}, \bar{x}'; \omega)$ is the cross-power spectral density of the exterior blocked pressure, defined by Eq. (11) or by

$$S_p(\bar{x}, \bar{x}'; \omega) = \frac{1}{\pi} \int_{-\infty}^{\infty} R_p(\bar{x}, \bar{x}'; \tau) e^{-i\omega\tau} d\tau$$

where $R_p(\bar{x}, \bar{x}'; \tau)$ is the average cross-correlation of the blocked pressure over the exterior.

$$R_p(\bar{x}, \bar{x}'; \tau) = \lim_{T \rightarrow \infty} \frac{1}{T} \int_{-T/2}^{T/2} p_{bl}(\bar{x}, t) p_{bl}(\bar{x}', t + \tau) dt.$$

3.3.1 Homogeneous Exterior Pressure Field

For a homogeneous pressure field, such as is normally observed beneath a turbulent boundary layer or in the far field of a jet (provided the structural element considered is not too large), the following form of $S_p(\bar{x}, \bar{x}'; \omega)$ is found to represent the measured data quite accurately.

$$S_p(\bar{x}, \bar{x}'; \omega) = S_p(\bar{\xi}; \omega) = S_p(\omega) e^{-ck|\bar{\xi}|} e^{ik\bar{\xi}} \quad (28)$$

where $\bar{\xi} = \bar{x}' - \bar{x}$, c is the correlation decay parameter, k is the excitation trace wavenumber, and reference location X_0 is arbitrary because of the assumption of homogeneity.

The co-spectrum is

$$C_p(\bar{\xi}; \omega) = S_p(\omega) e^{-ck|\bar{\xi}|} \cos k\bar{\xi}. \quad (29)$$

Both the cross-spectral density function and the co-spectrum can be assumed to be separable in directions parallel and perpendicular to the direction of propagation.

3.3.2 Non-homogeneous Exterior Pressure Fields

White [14] has shown that estimates of the joint acceptance can be made for a pressure field whose power spectral density varies smoothly over the structural mode shape. The assumptions that the co-spectrum is homogeneous and that the spectral density is moderately uniform over the surface were made.

In general, strong variations in excitation co-spectrum can occur over the surface of the transmitting structure. Consider the situation where a periodic point source is located at P, adjacent to the (x,y) plane as shown in Figure 1. An expression is required for the cross-power spectral density of the pressure field over the two-dimensional (x,y) plane. (X₀,Y₀) is located at a distance d from P, such that the line joining (X₀,Y₀) to P is perpendicular to the (x,y) plane.

The pressure at points away from P varies inversely with r, the radial distance from P; i.e.

$$p(\bar{x}, t + \tau_0^x) = \frac{d}{r_x} p(\bar{X}_0, t)$$

$$\text{where } \tau_0^x = (r_x - d)/c = \left[(|\bar{x} - \bar{X}_0|^2 + d^2)^{1/2} - d \right] / c,$$

$$\tau_0^{x'} = (r_{x'} - d)/c, \text{ and}$$

$$|\bar{x} - \bar{X}_0|^2 = (x - X_0)^2 + (y - Y_0)^2.$$

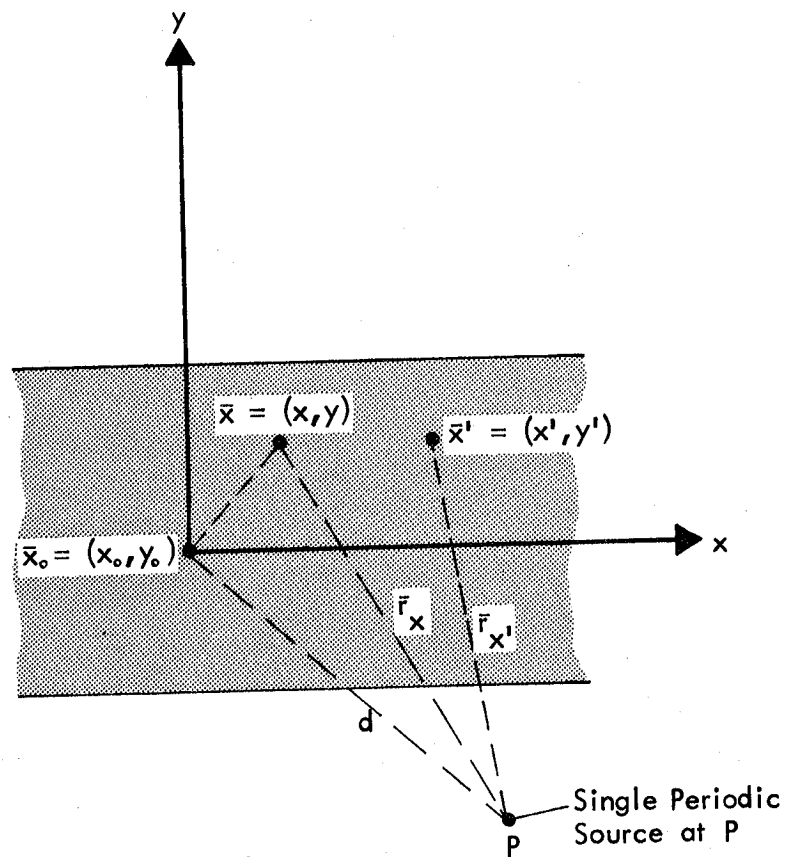


FIGURE 1. PERIODIC SOURCE LOCATED ADJACENT TO (x, y) PLANE

The cross-correlation of the pressures at \bar{x} and \bar{x}' can be written

$$R_p(\bar{x}, \bar{x}'; \tau) = \lim_{T \rightarrow \infty} \frac{1}{T} \int_{T/2}^{T/2} p(\bar{x}, t) p(\bar{x}', t + \tau) dt$$

$$\text{where } p(\bar{x}, t) = \frac{d}{(|\bar{x} - \bar{x}_0|^2 + d^2)^{1/2}} p(\bar{x}_0, t - \tau_0^x)$$

$$\text{and } p(\bar{x}', t + \tau) = \frac{d}{(|\bar{x}' - \bar{x}_0|^2 + d^2)^{1/2}} p(\bar{x}_0, t + \tau - \tau_0^{x'}).$$

If $p(\bar{x}_0, t)$ is periodic with period T_0 and frequency $\omega_0 = 2\pi/T_0$, the above equations become

$$R_p(\bar{x}, \bar{x}'; \tau) = q(\bar{x}, \bar{x}') \frac{1}{T_0} \int_{-\frac{T_0}{2} - \tau_0^x}^{\frac{T_0}{2} - \tau_0^{x'}} p(\bar{x}_0, z) p(\bar{x}_0, z + \tau + \tau_0^x - \tau_0^{x'}) dz \quad (30)$$

$$\text{where } q(\bar{x}, \bar{x}') = d^2 / [(|\bar{x} - \bar{x}_0|^2 + d^2)(|\bar{x}' - \bar{x}_0|^2 + d^2)]^{1/2}.$$

$$\text{With } p(\bar{x}_0, z) = \sum_{b=-\infty}^{\infty} c_m e^{ib\omega_0 z}, \text{ we find}$$

$$c_b = \frac{1}{T_0} \int_{-\frac{T_0}{2}}^{\frac{T_0}{2}} p(\bar{x}_0, z) e^{-ib\omega_0 z} dz = \frac{1}{T_0} F_{P_{X_0}}(b\omega_0).$$

Then, on substitution into Eq. (30),

$$R_p(\bar{x}, \bar{x}'; \tau) = \frac{q(\bar{x}, \bar{x}')}{T_o^2} \sum_{b=-\infty}^{\infty} \left| F_{p_{Xo}}(b\omega_o) \right|^2 e^{ib\omega_o(\tau + \tau_o^x - \tau_o^{x'})}. \quad (31)$$

The cross-power spectral density follows, on transforming and substituting for τ_o^x and $\tau_o^{x'}$, as

$$S_p(\bar{x}, \bar{x}'; \omega) = \frac{2q(\bar{x}, \bar{x}')}{T_o^2} \sum_{b=-\infty}^{\infty} e^{ib\omega_o} [(|\bar{x} - \bar{X}_o|^2 + d^2)^{\frac{1}{2}} - (|\bar{x}' - \bar{X}_o|^2 + d^2)^{\frac{1}{2}}] / c \\ \times \left| F_{p_{Xo}}(b\omega_o) \right|^2 \delta(\omega - b\omega_o) \quad (32)$$

$$\text{where } \delta(\omega) = \frac{1}{2\pi} \int_{-\infty}^{\infty} e^{-i\omega t} dt.$$

The co-spectrum is

$$C_p(\bar{x}, \bar{x}'; \omega) = q(\bar{x}, \bar{x}') \sum_{b=1}^{\infty} \cos \left\{ \frac{b\omega_o}{c} \left[(|\bar{x}' - \bar{X}_o|^2 + d^2)^{\frac{1}{2}} - (|\bar{x} - \bar{X}_o|^2 + d^2)^{\frac{1}{2}} \right] \right\} \langle p_{Xo}^2(b\omega_o) \rangle \\ \times \delta(\omega - b\omega_o) \quad (33)$$

where $\langle p_{Xo}(b\omega_o) \rangle$ is the mean square pressure at X_o attributable to the b th harmonic.

The co-spectrum (Eq. (33)) is a complicated function of observer positions relative to source position but depends on the amplitude of the pressure field relative to that at reference position X_o .

The function $q(\bar{x}, \bar{x}')$ expresses the spatial decay of the power spectral density between the observer positions \bar{x} and \bar{x}' and the reference point \bar{x}_0 .

Considerable effort has been expended in the literature to define the function $q(\bar{x}, \bar{x}')$ and coherence and phase relationships (correlation functions) for such excitations as jet noise [15,16]. In general, an approximation approach has been followed using the homogeneous cross power spectral density function of Sec. 3.3.1, where $S_p(\omega)$ has been obtained by averaging the measured data over the structural area of concern and where average values of k and c have been selected. This is valid where the spatial variation in power spectral density is small, but it is likely to be increasingly inaccurate as the spatial variation becomes more severe. For example, contrast a point excitation with a homogeneous excitation. The inclusion of the spatial distribution function $q(\bar{x}, \bar{x}')$ permits a more realistic and precise modeling of the coupling between the nonhomogeneous excitation and the fuselage response to be performed.

On the other hand, few measurements have been made of the cross power spectral density function of tonal nonhomogeneous pressure fields. From the available data [8,9], it can be argued that the following is an appropriate general formulation of the cross power spectral density for use in near-field and far-field applications. The selected function is

$$S_p(\bar{x} - \bar{x}_0, \bar{x}' - \bar{x}_0; b\omega_0) = q_1(\bar{x} - \bar{x}_0)q_1(\bar{x}' - \bar{x}_0)R_p(\bar{\xi}; b\omega_0) \langle p_{x_0}^2(b\omega_0) \rangle$$

where $q_1(\bar{x} - \bar{x}_0)$ represents the spatial variation in tonal rms pressure over the structure surface; $R_p(\bar{\xi}; b\omega_0)$ is a homogeneous

correlation function for the excitation [see Section 3.3.1] and $\bar{\xi} = \bar{x}' - \bar{x}$; defined by

$$R_p(\bar{\xi}; b\omega_0) = e^{-ck(b\omega_0)|\bar{\xi}|} \cos[k(b\omega_0)\bar{\xi}];$$

and $k(b\omega_0)$ is the excitation trace wavenumber at frequency $b\omega_0$, averaged over some appropriate spatial extent.

Often the excitation coherence will be close to unity (i.e. $c = 0$), as observed in the propagation direction in model tests for plane waves propagating over a structure [17] and on the Aero Commander fuselage [8,9] measuring circumferentially in the plane of rotation of the propeller.

At present, values of c and $k(b\omega_0)$, and the nature of $q_1(\bar{x} - \bar{x}_0)$, have to be estimated empirically. Ray acoustics, recent Hamilton Standard test data, and Hamilton Standard prediction methodology can be used to this end. For example, Hamilton Standard theoretical data [6] can be used to estimate the function $q_1(\bar{x} - \bar{x}_0)$: it is found that an exponential function describes the predicted spatial variation in power spectral density with fair accuracy in both the axial and circumferential directions. Then, considering for example

$$q_1(\bar{x} - \bar{x}_0) = e^{-a|\bar{x} - \bar{x}_0|},$$

a joint acceptance function for the nonhomogeneous field can be defined at frequency $b\omega_0$ in the form

$$j_r^2(b\omega_0) = \frac{1}{A^2} \int_{\bar{x}} \int_{\bar{x}'} e^{-a|\bar{x} - \bar{x}_0|} e^{-a|\bar{x}' - \bar{x}_0|} e^{-c|\bar{x}' - \bar{x}|} \cos[k(b\omega_0)(\bar{x}' - \bar{x})] \psi^r(\bar{x}) \psi^r(\bar{x}') d\bar{x} d\bar{x}'. \quad (34)$$

This expression is separable in the appropriate coordinate directions and may be evaluated for various mode shape functions. Furthermore, \bar{x}_0 may coincide with the edge of a structural member or it may be located at an arbitrary position on the structural surface. A general derivation is presented in Appendix A. The form of joint acceptance and the dependence on coherence, amplitude decay rate, and wavenumber matching between excitation and response is discussed in Section 3.6.

We note that, from say Eq. (27)

$$\int_{\bar{x}} \int_{\bar{x}'} c_p(\bar{x}, \bar{x}'; \omega) \psi^r(\bar{x}) \psi^r(\bar{x}') d\bar{x} d\bar{x}' = \sum_{b=1}^{\infty} A^2 j_r^2(\omega) \langle p_{x_0}^2(b\omega_0) \rangle \delta(\omega - b\omega_0). \quad (35)$$

3.4 Tonal Power Flow Equation

The preceding analysis of the power flow into a cavity has placed no restrictions on whether the structural or cavity response is resonant or nonresonant. Application of the analysis to typical baseline aircraft (to be discussed later in Section 6) indicates that the modal density of the acoustic cavity formed by the airplane cabin is sufficiently high that the power inflow is dominated by resonant response of the cavity. Thus, Eq. (24) for the power inflow can be simplified, from a computational standpoint, by considering only resonant response of the cavity. This is achieved in Eq. (24) by performing the summation for cavity modes of order n only over those modes that lie within the bandwidth $\Delta\omega$ of interest, as denoted by the summation limit $n\epsilon\Delta\omega$. Then Eq. (24) becomes, with substitution of Eq. (35),

$$\begin{aligned}
[W_{in}(\omega)]_{\Delta\omega} &= \int_{\Delta\omega} \frac{\rho_1 \omega^3 A^4 c_1^2}{V} \sum_{b=1}^{\infty} \langle p_{Xo}^2(b\omega_o) \rangle \sum_r \frac{j_r^2(\omega) \delta(\omega - b\omega_o)}{M_r^2 \omega_r^4 \left[\left(1 - \frac{\omega^2}{\omega_r^2}\right)^2 + \eta_r^2 \right]} \\
&\quad \times \sum_{n \in \Delta\omega} \frac{\epsilon_n \eta_n f^2(n, r)}{\omega_n^2 \left[\left(1 - \frac{\omega^2}{\omega_n^2}\right)^2 + \eta_n^2 \right]} d\omega \\
&\approx \frac{\rho_1 A^4 c_1^2}{V} \sum_{b \in \Delta\omega} \omega_b^3 \langle p_{Xo}^2(\omega_b) \rangle \sum_r \frac{j_r^2(\omega_b)}{M_r^2 \omega_r^4 \left[\left(1 - \frac{\omega_b^2}{\omega_r^2}\right)^2 + \eta_r^2 \right]} \\
&\quad \times \sum_{n \in \Delta\omega} \frac{\epsilon_n \eta_n f^2(n, r)}{\omega_n^2 \left[\left(1 - \frac{\omega_b^2}{\omega_n^2}\right)^2 + \eta_n^2 \right]} \quad (36)
\end{aligned}$$

where $\omega_b = b\omega_o$, $\omega_b \approx \omega_n$ since both lie in $\Delta\omega$, and

$$[W_{in}(\omega)]_{\Delta\omega} \equiv \text{Re}[W_{rad}^{int}(\omega)]_{\Delta\omega}.$$

The summation over excitation harmonics is also limited to those harmonics lying in $\Delta\omega$ (i.e. $b \in \Delta\omega$).

The bandwidth $\Delta\omega$ can be chosen such that only one harmonic of the excitation lies within $\Delta\omega$. Then Eq. (36) becomes

$$\begin{aligned}
\left[W_{in}(\omega) \right]_{\Delta\omega} &= \frac{\rho_i A^4 c_i^2 \omega_b^3}{V} \langle p_{Xo}^2(\omega_b) \rangle \sum_r \frac{j_r^2(\omega_p)}{M_r^2 \omega_r^4 \left[\left(1 - \frac{\omega_b^2}{\omega_r^2} \right)^2 + \eta_r^2 \right]} \\
&\times \sum_{n \in \Delta\omega} \frac{\epsilon_n \eta_n f^2(n, r)}{\omega_n^2 \left[\left(1 - \frac{\omega_b^2}{\omega_n^2} \right)^2 + \eta_n^2 \right]} \quad (37)
\end{aligned}$$

where $\omega_b \in \Delta\omega$.

3.5 Power Flow Statistics

The power flow equation presented in Eq. (37) is based on a mode-by-mode calculation of the response of the structure and cavity to an excitation at a given frequency. This is feasible from a computational point of view where there are relatively small numbers of structural and acoustic modes in the frequency band of interest, but the computational requirements become excessive when the number of modes is large. Thus, for the present study the power flow equations are considered for three frequency regimes. These regimes are defined in terms of modal overlap, which is essentially the ratio of modal bandwidth to modal separation for either the structure or the cavity as the case may be.

At low acoustic modal density and loss factor, such that the modal overlap is much less than unity, the cavity response depends intimately on the cavity resonance frequencies and loss factors and on the excitation frequency. The exact result given by Eq. (37) should be used for calculation of the power radiated into the volume; approximations for the modal admittance should not be made.

The high-frequency case is one in which the modal overlap is high for both the structure and the cavity. However, there can be intermediate frequency regimes where the modal overlap is high for either the structure or the cavity but not for both. Consider, for example, the case with a high acoustic modal overlap. This situation is one in which a tone of frequency ω_b drives a group of acoustic cavity modes contained in a narrow frequency band $\Delta\omega$. Then, with a modal overlap of approximately unity, it becomes appropriate, for computational efficiency and because of a lack of precision in mode shape and resonance frequency predictions, to seek solutions to the power flow analysis which are statistical in nature. Of particular interest is the expected value of the power radiated into the cavity $E[W_{in}(\omega_b)]$ and the corresponding variance $\sigma^2[W_{in}(\omega_b)]$.

3.5.1 Expected Value of Power Flow into Cavity with High Modal Overlap

The power radiated into the cavity depends on the acoustic modal admittances as well as the interior coupling parameters $f^2(n,r)$, mode normalization constants ϵ_n , and loss factors η_n . On assuming an average acoustic loss factor $\bar{\eta}_n$ and an average product of $f^2(n,r)$ and ϵ_n , $\langle \epsilon_n f^2(n,r) \rangle$, the expected value of the internally-radiated acoustic power may be written as

$$E[W_{in}(\omega_b)] = \frac{\rho_i A^4 c_i^4 \omega_b}{V} \langle p_{Xo}^2(\omega_b) \rangle \sum_r \frac{j_r^2(\omega_b)}{M_r^2 |Y_r(\omega_b)|^2} \bar{\eta}_n \langle \epsilon_n f^2(n,r) \rangle \times E[G(\omega_b, \omega_n)] \quad (38)$$

$$\text{where } G(\omega_b, \omega_n) = \sum_{n \in \Delta\omega} \left[\left(1 - \frac{\omega_b^2}{\omega_n^2} \right)^2 + \eta_n \right]^{-1}.$$

Thus, as the modal overlap increases, one seeks an estimate for the modal admittance which is independent of the precise modal details, so that the internal coupling becomes a function of modal overlap (and hence modal density and average loss factor) only. In the case of high acoustic modal overlap, there is interest in the expected value of the above modal admittance function $G(\omega_b, \omega_n)$ for fixed values of ω_n ($n \in \Delta\omega$) as ω_b samples in the band $\Delta\omega$. This is equivalent to the expected value of G for fixed ω_b , where the ω_n 's are distributed in frequency according to their distribution functions for an ensemble of (slightly) different cavities.

Now if

$$\begin{aligned}
 g(\omega_b, \omega_n) &= \left[\left(1 - \frac{\omega_b^2}{\omega_n^2} \right)^2 + \eta_n^2 \right]^{-1}, \\
 E[G(\omega_b, \omega_n)] &= E \left[\sum_{n \in \Delta\omega} g(\omega_b, \omega_n) \right] \\
 &= \sum_{n \in \Delta\omega} E[g(\omega_b, \omega_n)] \\
 &= N_{n \in \Delta\omega} E[g(\omega_b, \omega_n)] \tag{39}
 \end{aligned}$$

where $N_{n \in \Delta\omega}$ is the number of acoustic modes resonant in $\Delta\omega$. Then, assuming that ω_b and ω_n are statistically independent, that the probability density of ω_b in $\Delta\omega$ is $(\Delta\omega)^{-1}$, and that the probability density of ω_n in $\Delta\omega$ can be derived from the acoustic modal density, it can be shown that (see Appendix B)

$$E[g(\omega_b, \omega_n)] \approx \frac{\pi \omega_c}{2 \bar{\eta}_n \Delta \omega}$$

where ω_c is the center frequency of band $\Delta \omega$, and

$$E[G(\omega_b, \omega_n)] = n_n(\omega_b) \frac{\pi \omega_c}{2 \bar{\eta}_n} . \quad (40)$$

This expected value for the acoustic admittance of a group of resonant acoustic modes can be substituted into Eq. (38) to give

$$E[W_{in}(\omega_b)] = \frac{\pi \rho_i \omega_b^2 A^4 c_i^2}{2V} \langle p_{Xo}^2(\omega_b) \rangle \sum_r \frac{j_r^2(\omega_b)}{M_r^2 |Y_r(\omega_b)|^2} n_n(\omega_b) \langle \epsilon_n f^2(n, r) \rangle \quad (41)$$

$$\text{where } \langle \epsilon_n f^2(n, r) \rangle = \frac{1}{N_{n \in \Delta \omega}} \sum_n \epsilon_n f^2(n, r).$$

Thus, the expected value of the band-limited power flow into a group of acoustic modes from a tonal excitation depends only on the acoustic modal density of the acoustic modes and is independent of the acoustic loss factor.

It may be shown, see Appendix C, that

$$n_n(\omega_b) \langle \epsilon_n f^2(n, r) \rangle = \frac{\omega_b^2 V}{\pi^2 c_i^3} j_r^{2, \text{rev}}(\omega_b)$$

where $j_r^{2, \text{rev}}(\omega_b)$ is the joint acceptance for the structure exposed to a reverberant pressure field. On substitution, Eq. (41) becomes

$$E[W_{in}(\omega_b)]_{\Delta\omega} = \frac{\rho_i \omega_b^4 A^4}{2\pi c_i} \langle p_{Xo}^2(\omega_b) \rangle \sum_r \frac{j_r^2(\omega_b) j_r^{2,rev}(\omega_b)}{M_r^2 |Y_r(\omega_b)|^2} . \quad (42)$$

Additional results, for the power flow from resonant structural modes (i.e. modes whose resonant frequencies ω_r lie within the analysis bandwidth $\Delta\omega$) and the power flow from mass-controlled modes ($\omega_r < \Delta\omega$), may be easily derived. These are presented in Section 3.5.3.

3.5.2 Variance of Power Flow into Cavity with High Modal Overlap

Calculation of the variance for the internally-radiated acoustic power (with high modal overlap in the cavity) requires calculation of the average modal acoustic admittance function $G(\omega_b, \omega_n)$, where by definition [C.1]

$$\begin{aligned} \sigma^2[G(\omega_b, \omega_n)] &= E\left[\left\{G(\omega_b, \omega_n) - E[G(\omega_b, \omega_n)]\right\}^2\right] \\ &= E[G^2(\omega_b, \omega_n)] - E^2[G(\omega_b, \omega_n)] \end{aligned} \quad (43)$$

and $E[G(\omega_b, \omega_n)]$ has been already derived.

Now

$$\begin{aligned} E[G^2(\omega_b, \omega_n)] &= E\left[\left\{\sum_{\omega_n \in \Delta\omega} g(\omega_b, \omega_n)\right\}^2\right] \\ &= \sum_{n \in \Delta\omega} E[g^2(\omega_b, \omega_n)] \end{aligned}$$

as ω_b and ω_n are statistically independent.

$$E[g^2(\omega_b, \omega_n)] \approx \frac{\pi \omega_c}{8 \bar{\eta}_n^3 \Delta \omega} \quad (44)$$

Then, from Eqs. (40), (43), and (44)

$$\sigma^2[G(\omega_b, \omega_n)] = N_{n \in \Delta \omega} \left\{ \frac{\pi \omega_c}{8 \bar{\eta}_n^3 \Delta \omega} - \frac{\pi \omega_c}{2 \bar{\eta}_n \Delta \omega} \right\} \quad (45)$$

$$= n_n(\omega_b) \frac{\pi \omega_c}{8 \bar{\eta}_n^3} \quad \text{for } \bar{\eta}_n^2 \ll 1. \quad (45a)$$

Thus, the variance is inversely proportional to the cube of the band-averaged acoustic loss factor and directly proportional to the acoustic modal density.

Of interest is the normalized standard error ϵ_r or the coefficient of variation, defined as

$$\epsilon_r = \frac{\sigma[W_{in}(\omega_b)]}{E[W_{in}(\omega_b)]} \quad (46)$$

From Eqs. (38), (40), and (45a),

$$\epsilon_r = [2\pi \bar{\eta}_n n_n(\omega_b) \omega_b]^{-1/2}$$

where $\bar{\eta}_n n_n(\omega_b) \omega_b$ is the modal overlap term for the cabin acoustic field.

Thus, the standard error decreases as acoustic modal density and loss factor increase.

3.5.3 High Frequency Formulation

When the modal overlap is high for both acoustic and structural modes, a high-frequency solution can be found for the acoustic power inflow.

3.5.3.1 High-Frequency Acoustic Power Flow via Resonant Structural Modes

Adapting Eq. (42), the power inflow from resonant structural modes is given by

$$E[W_{in}(\omega_b)] = \frac{\rho_1 \omega_b^4 A^4}{2\pi c_1} \langle p_{Xo}^2(\omega_b) \rangle E \left[\sum_{r \in \Delta\omega} \frac{j_r^2(\omega_b) j_r^{2,rev}(\omega_b)}{M_r^2 \omega_r^4 \left[\left(1 - \frac{\omega_b^2}{\omega_r^2}\right)^2 + \eta_r^2 \right]} \right] \quad (47)$$

With $j_r^2(\omega_b)$ and $j_r^{2,rev}(\omega_b)$ set equal to band-averaged values $\langle j_r^2(\omega_b) \rangle_P$ and $\langle j_r^2(\omega_b) \rangle_R$, respectively, where the subscript P is used to denote that the joint acceptance is based on a progressive excitation field,

$$E[W_{in}(\omega_b)] = \frac{\rho_1 A^4}{2\pi c_1} \langle p_{Xo}^2(\omega_b) \rangle \frac{\langle j_r^2(\omega_b) \rangle_P \langle j_r^2(\omega_b) \rangle_R}{M_r^2} E \left\{ \sum_{r \in \Delta\omega} \left[\left(1 - \frac{\omega_b^2}{\omega_r^2}\right)^2 + \eta_r^2 \right]^{-1} \right\} \quad (48)$$

Using an approach similar to that used in Section 3.5.1,

$$E \left\{ \sum_{r \in \Delta\omega} \left[\left(1 - \frac{\omega_b^2}{\omega_r^2}\right)^2 + \eta_r^2 \right]^{-1} \right\} = n_r(\omega_b) \frac{\pi \omega_b}{2\bar{\eta}_r}$$

where $\bar{\eta}_r$ is the band-averaged structural loss factor and $n_r(\omega_n)$ is the structural modal density.

Hence,

$$E[W_{in}(\omega_b)] = \frac{\rho_i A^4 \omega_b}{4c_i} \langle p_{Xo}^2(\omega_b) \rangle \frac{n_r(\omega_b) \langle j_r^2(\omega_b) \rangle_P \langle j_r^2(\omega_b) \rangle_R}{M_r^2 \bar{\eta}_r} \quad (49)$$

It may be shown [4] that the band-averaged radiation resistance $\langle R_{rad}^{int} \rangle$ can be calculated as

$$\langle R_{rad} \rangle \approx \frac{2}{\pi} \frac{\rho_i \omega^2 A^2}{c_i} \langle j_r^2(\omega) \rangle_R \quad (50)$$

which leads, on substitution in Eq. (49), to the alternative representation for $E[W_{in}(\omega_b)]$ as

$$E[W_{in}(\omega_b)] = \frac{\pi A^2}{8\omega_b} \langle p_{Xo}^2(\omega_b) \rangle n_r(\omega_b) \frac{\langle j_r^2(\omega_b) \rangle_P \langle R_{rad}^{int} \rangle}{M_r^2 \bar{\eta}_r} \quad (51)$$

The normalized standard error is found to be the sum of the normalized standard errors inherent in the structural modeling and in the coupling to the cabin acoustic field, viz.

$$\epsilon_r = [2\pi \bar{\eta}_r n_r(\omega_b) \omega_b]^{-1/2} + [2\pi \eta_n \eta_n(\omega_b) \omega_b]^{-1/2}$$

where $\bar{\eta}_r n_r(\omega_b) \omega_b$ is the modal overlap term for the structure.

3.5.3.2 High-Frequency, Nonresonant Acoustic Power Flow

It is assumed here that, as there is a large number of modes with resonance frequencies below the band of interest, only these modes will be considered for nonresonant power flow calculation. This

restriction is made because, in general, these mass-controlled modes are more efficient acoustic radiators than are stiffness-controlled modes.

If it is further assumed that for these mass-controlled modes $\omega_b^2 \gg \omega_r^2$, then from Eq. (7)

$$|Y_r(\omega_b)|^2 \approx \omega_b^4.$$

Substituting in Eq. (42)

$$E[W_{in}(\omega_b)] = \frac{\rho_i A^4}{2\pi c_i} \langle p_{Xo}^2(\omega_b) \rangle \sum_{r < \Delta\omega} \frac{j_r^2(\omega_b) j_r^{2, rev}(\omega_b)}{M_r^2}. \quad (52)$$

The net acoustic power flowing from outside to inside from non-resonant, mass-controlled modes is then

$$E[W_{in}(\omega_b)] = \frac{\rho_i A^4}{2\pi c_i} \left\{ \langle p_{Xo}^2(\omega_b) \rangle \sum_{r < \Delta\omega} \frac{j_r^2(\omega_b) j_r^{2, rev}(\omega_b)}{M_r^2} - 2 \langle p_i^2(\omega_b) \rangle \sum_{r < \Delta\omega} \frac{[j_r^{2, rev}(\omega_b)]^2}{M_r^2} \right\}.$$

where the second term represents the acoustic power flow from the cavity to the exterior via nonresonant structural modes.

3.5.4 Net Power Flow

The high-frequency approximations developed in Section 3.5.2 and 3.5.3.1 provide estimates of the power flowing from the outside to the inside of the cavity. However, in order to obtain an estimate of the net inflow of acoustic power, the outward power flow from the cavity to the exterior has also to be taken into account.

It may be shown [4] that the analogous result for the acoustic power re-radiated from the fuselage due to excitation from the acoustic field inside the cavity is given by

$$E[W_{out}(\omega_b)] = \frac{\pi^2}{2} \frac{n_r(\omega_b)}{\rho_i \omega_b^2} \frac{\langle R_{rad}^{ext} \rangle}{M_r} \langle p_i^2(\omega_b) \rangle, \quad (53)$$

where $\langle p_i^2(\omega_b) \rangle$ is the induced interior space-averaged mean square pressure attributable to the b th harmonic.

The *net* acoustic power flowing from outside to inside from resonant structural modes is then obtained by combining Eqs. (51) and (53)

$$E[W_{net}(\omega_b)] = \frac{\pi A^2}{8\omega_b} \left\{ \langle p_{Xo}^2(\omega_b) \rangle \frac{n_r(\omega_b) \langle j_r^2(\omega_b) \rangle_P \langle R_{rad}^{int} \rangle}{M_r^2 \bar{n}_r} \right\} - \frac{\pi^2 n_r(\omega_b) \langle R_{rad}^{ext} \rangle}{2\rho_i \omega_b^2 M_r} \langle p_i^2(\omega_b) \rangle \quad (54)$$

or, similarly, by combining Eqs. (42) and (53).

3.5.5 Summary of Power Balance Equations

The preceding analysis has developed the acoustic power flow equations for a simple cavity in a rather general manner, although emphasis has been placed on high-frequency approximations that are appropriate to the baseline airplanes considered in this study. In addition, an excitation field with discrete frequency components and spatially-decaying amplitude has been included as a representation of a propeller noise field.

Power flow equations have been developed for three frequency regimes--a low-frequency regime where the modal overlap is low for both the structure and the cavity, a high-frequency regime where the modal overlap is high for structure and cavity, and an

intermediate regime where the modal overlap is low for the structure and high for the cavity. In the low-frequency regime, the power flow equation, Eq. (37), represents the net inflow into the cavity. However, when approximations are introduced for the high acoustic modal overlap case, power outflow has to be considered separately, Eq. (53), because Eqs. (42), (51), and (52) give estimates of the gross rather than net power inflow.

As shown in Section 2, the net power inflow has to be balanced by the power absorbed in the cavity. Equation (26) has been developed to provide an estimate of the power absorbed by the surfaces of the cavity (or cabin). In addition, acoustic power is absorbed by non-bounding surfaces such as seats, passengers, and service structures. The power absorbed by such items is

$$W_{\text{abs}} = \frac{\langle p_1^2 \rangle}{4\rho_1 c_1} \sum_j \alpha_j A_j$$

where α_j is the statistical absorption coefficient associated with area A_j and $\langle p_1^2 \rangle$ is the mean square pressure in the cabin interior. In a more general situation, the cabin volume might be composed of a series of subvolumes, either coupled directly or partitioned by barriers. Such a situation was followed in the analysis so that noise control methods such as partitioning of the cabin volume could be considered.

Equations (26), (37), (42), and (51) through (54) constitute the basic analytical model. However, these must be supplemented with information regarding cabin shape, excitation field, interior absorption, and sidewall configuration. The joint acceptances, interior coupling factors, and structure and volume resonance frequencies; allowed wavenumbers, structural loss factors, radiation resistances, and modal densities must be estimated for the

airplane configurations under study. The following sections address these items.

3.6 Joint Acceptances

3.6.1 General

The joint acceptance function describes the coupling between the excitation field and the structure, and in the present analysis it is defined, for a single harmonic at frequency ω_b , by Eq. (27)

$$j_r^2(\omega_b) = \frac{1}{A^2 \langle p_{X_0}^2(\omega_b) \rangle} \int_{\bar{x}} \int_{\bar{x}'} C_p(\bar{x}, \bar{x}'; \omega_b) \psi^r(\bar{x}) \psi^r(\bar{x}') d\bar{x} d\bar{x}'$$

where A is the panel area, $C_p(\bar{x}, \bar{x}'; \omega_b)$ and $\langle p_{X_0}^2(\omega_b) \rangle$, respectively, are the co-spectrum and mean square pressure at X_0 for the b th harmonic of the nonhomogeneous excitation field, and $\psi^r(\bar{x})$ is the shape of the r th structural mode.

In order to evaluate the joint acceptance, it is necessary to have representations for the excitation field and the structural mode shapes. For the present model, two excitation fields are encountered, one being a nonhomogeneous propagating acoustic field generated by the propeller and the other a diffuse acoustic field associated with the interior acoustic field of the cabin. The fuselage structure is composed of curved panels whose boundary conditions will probably lie between fixed and simply supported. Mode shapes are complicated by variations in skin thickness and the presence of stiffeners, windows, etc. As it is not possible to account for the detailed forms of the mode shapes, the simplifying assumption is made that the structural modes can be represented

by sine functions such as are associated with simply-supported boundary conditions and rectangular plates. Experimental and analytical data for stiffened cylinders [18] and for the Space Shuttle [4] support this approach. In any case, the precise mode shape used in the representation is probably not too critical. For example, joint acceptances have been calculated for rectangular panels using mode shapes associated with simply-supported and clamped boundary conditions. The excitation consisted of propagating waves in one case [19] and a subsonic turbulent boundary layer in another [20]. At coincidence, the joint acceptance was 0.5 to 2.5 dB higher for the simply-supported panel than for the clamped panel. Off-coincidence differences between the results were less than ± 2.5 dB. More significant is the representation for the excitation field.

3.6.2 Nonhomogeneous Propagating Acoustic Field

As discussed in Section 3.3.2 and in Appendix A, the strong spatial decay in mean square pressure away from the location of peak intensity is represented in this analysis by an exponential amplitude decay function in the expression for $C_p(\bar{x}, \bar{x}'; \omega_b)$ so that

$$C_p(\bar{x}, \bar{x}'; \omega_b) = e^{-a|\bar{x} - \bar{x}_0|} e^{-a|\bar{x}' - \bar{x}_0|} e^{-c|\bar{x}' - \bar{x}|} \cos[k(\bar{x}' - \bar{x})] \langle p_{X_0}^2(\omega_b) \rangle \quad (55)$$

where a is a pressure amplitude decay rate parameter,
 c is a correlation decay factor, and
 k is the wavenumber at frequency ω_b .

It is assumed that $C_p(\bar{x}, \bar{x}'; \omega_b)$ is separable in the longitudinal and transverse directions; i.e.

$$C_p(\bar{x}, \bar{x}'; \omega_b) = C_{px}(x, x'; \omega_b) C_{py}(y, y'; \omega_b) \langle p_{Xo}^2(\omega_b) \rangle$$

where

$$C_{px}(x, x'; \omega_b) = e^{-a_x |x - X_o|} e^{-a_x |x' - X_o|} e^{-c_x k_x |\xi|} \cos k_x \xi,$$

$$C_{py}(y, y'; \omega_b) = e^{-a_y |y - Y_o|} e^{-a_y |y' - Y_o|} e^{-c_y k_y |\eta|} \cos k_y \eta,$$

$$\xi = x' - x,$$

$$\eta = y' - y, \text{ and}$$

$$\bar{X}_o = (X_o, Y_o).$$

When a_x and a_y are zero, the pressure field corresponds to that of fully-developed turbulent flow (c_x and c_y both greater than zero). For such a case, the effects of variations in (c_x, c_y) on the joint acceptance have been investigated in detail elsewhere [17]. Of concern here is the dependence of the joint acceptance on variations in (a_x, a_y) , in particular for a coherent excitation, i.e. (c_x, c_y) close to zero. Some simple calculations have been performed to demonstrate the influence of (a_x, a_y) .

Figure 2 illustrates the effects of variations in a_x on the one-dimensional joint acceptance for the fourth mode of a 10m long beam when $c_x = 0$. The ratio of excitation to structural wave-number (k_x/k_m) varies from 10^{-1} (structure wavelength $\lambda_m \ll$ excitation wavelength λ_x) to 10^2 (excitation wavelength \ll structure wavelength). Maximum and minimum values of j_{mm}^2 occur for a_x and c_x both zero, corresponding to plane waves propagating over the beam length with no amplitude decay. However, as a_x takes

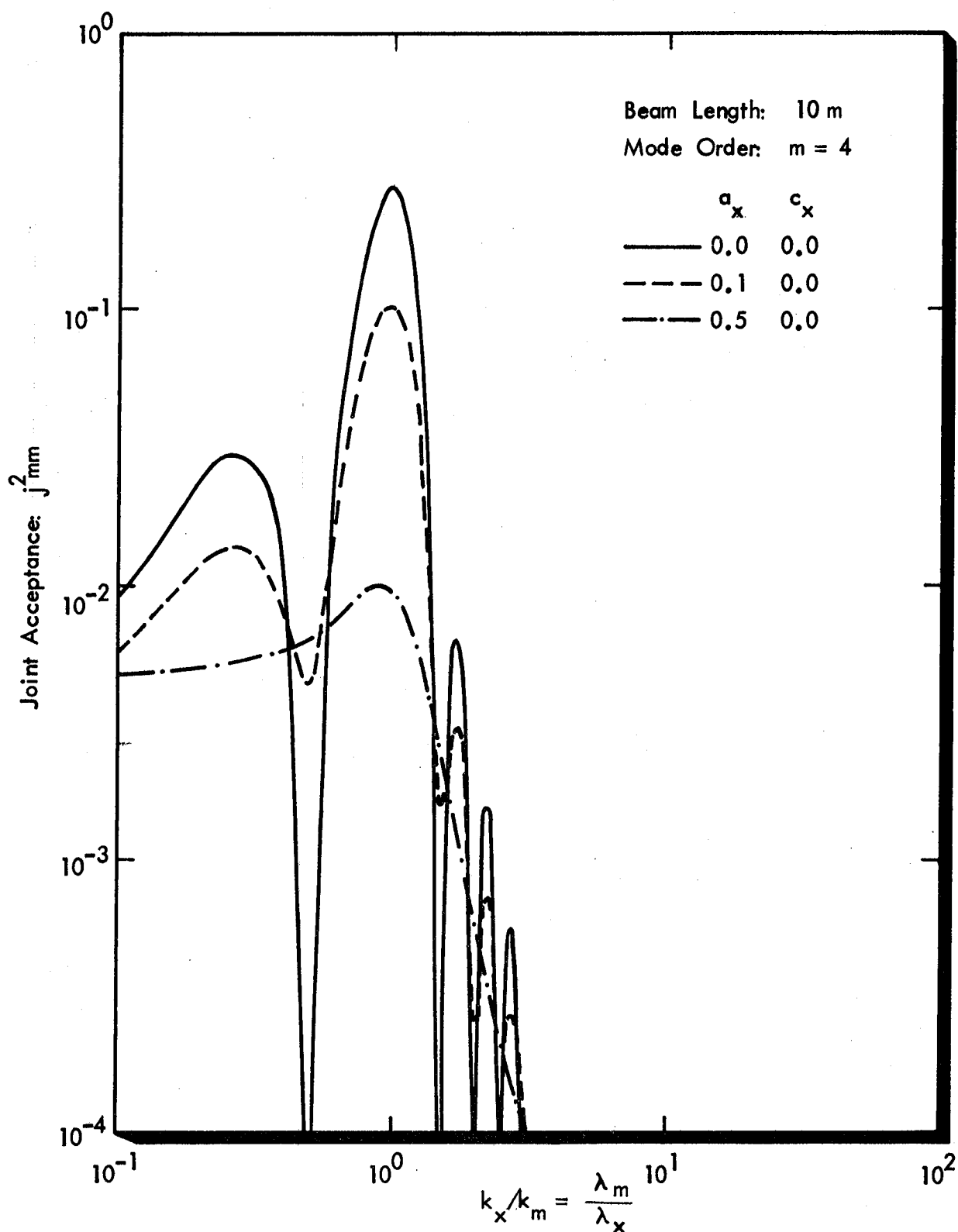


FIGURE 2. VARIATION IN JOINT ACCEPTANCE WITH k_x/k_m AND AMPLITUDE DECAY CONSTANT a_x , FOR $m=4$ AND $c_x=0$

increasingly higher values, the joint acceptance depends less strongly on the matching between structural and acoustic wavelengths: the strong oscillations in j^2 , as k_x/k_m varies, are damped by the presence of significant spatial amplitude decay. It is clear that neglect of this spatial amplitude decay may lead to significant errors in response predictions.

Figure 3 shows the dependence of the modal joint acceptance on k_x/k_m for various mode orders for a 10m long beam and for constant a_x . When the excitation wavelength is much greater than the structural wavelength ($k_x/k_m \ll 1$) in the presence of strong amplitude decay, j_{mm}^2 is inversely proportional to m^2 . When $k_x/k_m \gg 1$, j_{mm}^2 is proportional to $(k_m/k_x)^4$ and inversely proportional to m^2 . This is in agreement with the limits derived in Appendix A.

For the present study, values for the spatial decay coefficients (a_x, a_y), for the coherence coefficients (c_x, c_y), and for the average trace wavespeeds (U_x, U_y) [or, alternatively, trace wavenumbers (k_x, k_y)] were estimated from the Hamilton Standard prediction procedure [6], Aero-Commander tests [7,8], and ray acoustics, as is explained in more detail in Section 5.

3.6.3 Reverberant Acoustic Fields

The reverberant field joint acceptance is required both for calculation of the acoustic power flow from the reverberant acoustic field inside the cavity (cabin) out through the fuselage structure (Eq. (53)), and for calculation of the high-frequency internal radiation ratio [Eq. (52)].

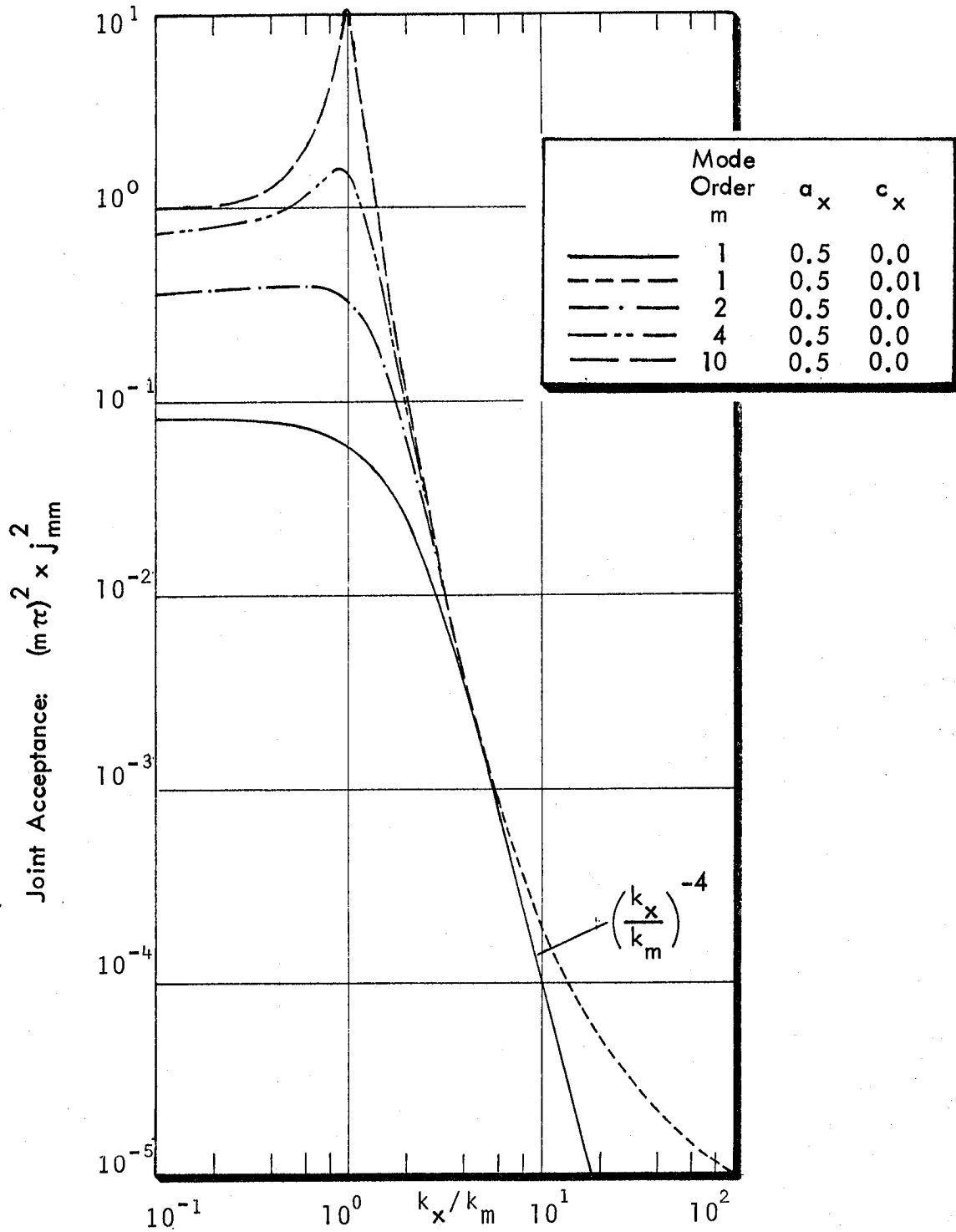


FIGURE 3. VARIATION IN MODAL JOINT ACCEPTANCE WITH k_x/k_m AND m FOR AMPLITUDE DECAY CONSTANT $a_x=0.5$

Equation (27) is again used to compute the reverberant field joint acceptance. The representation for the co-spectrum of pressure field, in this case considered to be homogeneous over the fuselage surface, is well established [21] and is given by

$$C_p(\bar{x}, \bar{x}'; \omega_b) = C_{px}(\xi, \omega_b) C_{py}(\eta, \omega_b) \langle p_{Xo}^2(\omega_b) \rangle \quad (56)$$

where $C_{px}(\xi, \omega_b) = \sin(k\xi)/k\xi$,

$$C_{py}(\eta, \omega_b) = \sin(k\eta)/k\eta,$$

and $\langle p_{Xo}^2(\omega_b) \rangle$ is independent of Xo for a homogeneous reverberant acoustic field.

Then, the joint acceptance for reverberant excitation is estimated with [22]:

$$j_m^{2\text{rev}}(\omega) = I_1(m) + I_2(m) + I_3(m)$$

$$I_1(m) = \frac{1}{2\pi m k L_x} [\text{Cin}(kL_x + m\pi) - \text{Cin}|m\pi - kL_x|]$$

$$I_2(m) = \frac{1}{2kL_x} [\text{Si}(kL_x + m\pi) - \text{Si}(m\pi - kL_x)]$$

$$I_3(m) = \frac{1 - (-1)^m \cos kL_x}{(m\pi)^2 - (kL_x)^2} \cdot \quad (57)$$

Similarly,

$$j_n^{2\text{rev}}(\omega) = I_1(n) + I_2(n) + I_3(n)$$

where $I_1(n)$, $I_2(n)$, and $I_3(n)$ are given by the above equations with n replacing m and L_y replacing L_x . Si and Cin are the sine and cosine integrals [23].

3.7 Internal Coupling

At very low frequencies, the acoustic power flow depends intimately on the modal characteristics of both fuselage structure and cabin volume. Then, detailed modal resonance frequencies and mode shapes are required to enable precise calculations to be carried out. In practice, computational efficiency requires the use of approximations in the description of both the cabin shape and its furnishings. For example, in the analytical model, the cabin volume is represented as a rectangular parallelepiped whose surfaces can be deformed as shown in Figure 4(a) to represent the curvature of the sidewall and ceiling trim panels.

This approach provides a more realistic model than either a cylindrical or an unmodified rectangular model, as can be judged by inspection of typical fuselage cabin cross sections (Figure 15). The analytical model assumes that the surfaces in the cabin are locally reacting, so that response of a given point on a surface will depend on the acoustic pressures at that point only. This is a reasonable assumption, since many surfaces in an airplane cabin are composed of materials such as carpets, thin plastic cloth backed by foam, and fiberglass-filled honeycomb with a perforated trim cover--which are locally reacting. The basic development of the perturbation method for the calculation of the cabin modes and resonance frequencies has been developed in [4].

The resulting power inflow is calculated via the internal coupling factor $f(n,r)$, which is discussed in detail below. At high

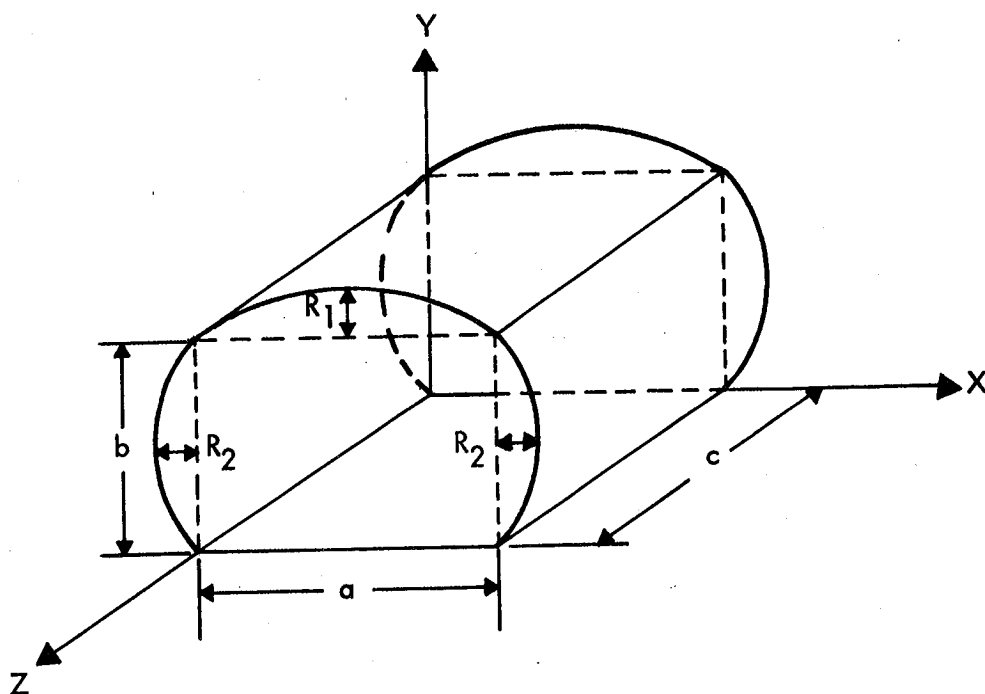


FIGURE 4(a). PARALLELEPIPED WITH THREE DEFORMED SURFACES TO ILLUSTRATE REPRESENTATION OF FUSELAGE CABIN

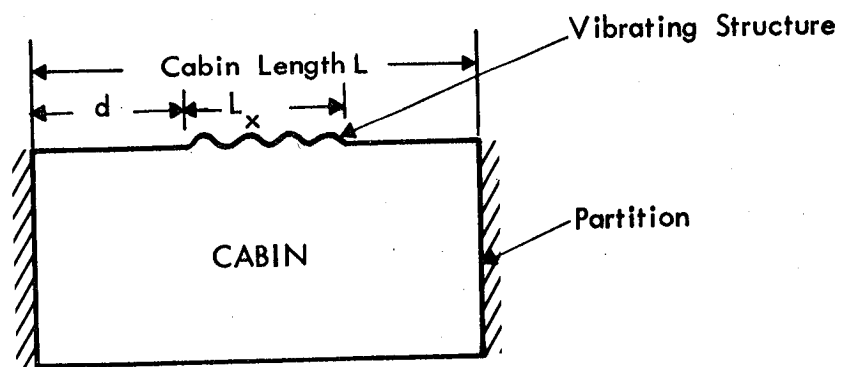


FIGURE 4(b). SIMPLIFIED REPRESENTATION OF RELATIONSHIP BETWEEN VIBRATING STRUCTURE AND CABIN

frequencies, where the power inflow depends only on acoustic modal density and where the cabin acoustic field tends to be diffuse, the internal coupling is formulated in terms of the radiation resistances of the fuselage structural elements, as demonstrated in Section 3.5.

3.7.1 Internal Coupling Factor

The coupling of the fuselage vibration modes is expressed by the internal coupling factor $f(n,r)$, defined in Eq. (21) as

$$f(n,r) = \frac{1}{A} \int \phi_n(\bar{x}) \psi^r(\bar{x}) d\bar{x} \quad (58)$$

where $\psi^r(\bar{x})$ represents the structural mode shape for mode of order r , and $\phi_n(\bar{x})$ is the cabin mode shape for mode of order n . The area of the structure that is radiating into the cabin is denoted by A .

The general situation considered in the analytical model is shown diagrammatically for the (x,z) plane in Figure 4(b). The figure shows a volume of length L exposed to a structural mode that extends over a small portion L_x of the structural length L . This represents the limited spatial extent of the structure response to a localized or nonhomogeneous excitation.

The associated values of the coupling parameter in the x direction are given by the following relations [4], where the structural mode shapes are modeled with $\psi^m(\bar{x}) = \sin k_m x$ and the acoustic mode shape is modeled by the zeroth order eigenfunction for the deformed volume viz. $\phi_p(x) = \cos k_p x$. The acoustic mode shapes and the coupling parameter are assumed separable in the x and y directions, as has been assumed for the structural mode shapes and the joint acceptance function. In particular,

$$f(n,r) = f(pq,mn) = f(p,m) f(q,n)$$

where, for the x direction,

$$f(p,m) = \frac{1}{L} \int_d^{L+d} \sin k_m x \cos k_p (x - d) dx \quad (59)$$

which yields

$$f(p,m) = \begin{cases} f_{pm} & \text{if } k_m \neq k_p \\ f_p & \text{if } k_m = k_p \end{cases} \quad (59a)$$

where

$$\begin{aligned} f_{pm} = \cos \pi c_d m & \left[\frac{\cos \pi c_d (m - \kappa) - \cos \pi (1 + c_d) (m - \kappa)}{2\pi (m - \kappa)} \right. \\ & + \frac{\cos \pi c_d (m + \kappa) - \cos \pi (1 + c_d) (m + \kappa)}{2\pi (m + \kappa)} \Big] \\ & - \sin \pi c_d m \left[\frac{\sin \pi (1 + c_d) (m - \kappa) - \sin \pi c_d (m - \kappa)}{2\pi (m - \kappa)} \right. \\ & + \frac{\sin \pi (1 + c_d) (m + \kappa) - \sin \pi c_d (m + \kappa)}{2\pi (m + \kappa)} \Big], \quad (59b) \end{aligned}$$

$$\begin{aligned} f_p^{pm} = \cos \pi c_d \kappa & \left[\frac{\sin^2 \pi (1 + c_d) \kappa - \sin^2 \pi c_d \kappa}{2\pi \kappa} \right] \\ & - \sin \pi c_d \kappa \left[\frac{1}{2} \left(1 + \frac{\sin 2\pi (1 + c_d) \kappa - \sin 2\pi c_d \kappa}{2\pi \kappa} \right) \right] \quad (59c) \end{aligned}$$

For the particular case of $d = 0$, then $c_d = 0$,

$$f_{pm} = \frac{1}{2\pi} \left[\frac{1 - \cos \pi(m - \kappa)}{(m - \kappa)} + \frac{1 - \cos \pi(m + \kappa)}{(m + \kappa)} \right]$$

and $f^{pm} = 0$. Also, $\kappa = k_p L_x / \pi$ and $c_d = d / L_x$.

For the transverse axis,

$$f(q, n) = \begin{cases} f_{qn} & \text{if } k_n \neq k_q \\ f^{qn} & \text{if } k_n = k_q \end{cases}$$

where f_{qn} and f^{qn} are given by Eqs. (59b) and (59c) for f_{pm} and f^{pm} , respectively, with appropriate variable changes [4].

The factor $f^2(n, r)$ is synonymous with the joint acceptance function that couples the external pressure field to the structure. Values of $f^2(n, r)$ are nondimensional, positive numbers that are less than unity. Typical results are presented in [4].

This internal coupling factor is used only at low frequencies. When the acoustic modal overlap is much greater than zero, the approximation (Section 3.5.1)

$$n_n(\omega_b) \langle \epsilon_n f^2(n, r) \rangle \approx \frac{\omega_b^2 V}{\pi^2 c_1^3} \langle j_r^2(\omega_b) \rangle_R$$

allows calculation of the interior coupling from band-averaged values of the joint acceptance of the structural modes. This is always the case for the study airplanes.

3.7.2 Radiation Resistances

The radiation resistance of a structural system is determined by the relationship

$$R_{\text{rad}} = \rho_i c_i A \sigma_{\text{rad}}, \quad (60)$$

where σ_{rad} is the radiation efficiency, and A is the surface area of the structure. Using reciprocity, it can be shown that [24]

$$\sigma_{\text{rad}} = \frac{2A}{\pi} \frac{\omega^2}{c_i^2} \langle j_r^2(\omega) \rangle_R \quad (61)$$

where $\langle \rangle$ indicates an average over the modes resonant in the band of concern.

3.8 Test Conditions on Allowed Structural Wavenumbers

To calculate the required joint acceptances and internal coupling factors, structural bending wavenumbers (or mode numbers) must be selected for each analysis frequency band $\Delta\omega$. The selection is simple in the case of isotropic flat rectangular panels since, for such panels, curves of constant frequency are (approximately) curves of constant bending wavenumber. If the structure is orthotropic or curved, or has pressurization stresses (as is the case for the study airplanes), the determination of allowable values of k_m and k_n must be done with a frequency test, either

$$\omega_{mn} \in \Delta\omega$$

or

$$\omega_{mn} < \Delta\omega,$$

whichever is required.

The effects of curvature and pressurization and of the orthotropic properties of a structure over a frequency band are translated into the model by a set of resonance frequencies and corresponding wave-numbers for that band. It is the composite set for each band $\Delta\omega$ which is important. Imprecision, in the sense that a few modes may be classified wrongly, is unimportant. The estimate for input power will depend on the properties of the whole group rather than the specifics of a few individual classifications. If the modes can be classified approximately correctly as a group, then the desired result will be obtained in the input power calculation. The simple joint acceptances and internal coupling terms are entirely supported by general classification of modes. Equations for the prediction of resonance frequencies for the fuselage structures are discussed in detail in Section 3.8.1 below.

The analysis bandwidth for calculation of resonant and nonresonant power flow is chosen to be sufficiently wide that at least several, but less than 100, structural modes are resonant within the computational bandwidth. At low frequencies, bandwidths are typically 1/2 or 1/3 octave, while as structural modes accumulate with increase of frequency, the bandwidth rapidly decreases (a 1/30 octave bandwidth is typical at high frequencies).

3.8.1 Resonance Frequency Equations

The basic resonance frequency equation used for prediction purposes was derived by Mikulas and McElman [25] and is shown in Figure 5 with the addition of a term due to pressurization. Figure 28 shows the representation of a typical structural element. Other changes to the formulation were made to allow for boundary conditions other than simply supported. Use of the equation is described in Section 4.1.

$$\frac{\omega^2 M L_x^4}{\pi^4 D} = \underbrace{m^4(1 + \delta^2)^2 + m^4 \left[\frac{E I_s}{D \ell_y} + \delta^2 \left(\frac{G J_s}{D \ell_y} + \frac{G J_r}{D \ell_x} \right) + \delta^4 \frac{E I_r}{D \ell_x} \right]}_{\text{Bending Stiffness}} + \underbrace{\frac{12 L_x^4 (1 - \nu^2)}{\pi^4 h^2 R^2} \left[\frac{1 + \bar{S} \Lambda_s + \bar{R} \Lambda_r + \bar{S} \bar{R} \Lambda_{rs}}{\Lambda} \right]}_{\text{Membrane Stiffness}} + \underbrace{\Delta p \frac{R}{2} \frac{m^2 L_x^2}{\pi^2 D} (1 + 2\delta^2)}_{\text{Pressurization Membrane Stiffness}}$$

Mass Reactance

where

$$\frac{E I_r}{D \ell_x} = \text{Ring Bending Parameter}$$

$$\bar{R} = \frac{E A_r}{E h \ell_x} = \text{Ring Membrane Parameter}$$

$$\frac{E I_s}{D \ell_y} = \text{Stringer Bending Parameter}$$

$$\bar{S} = \frac{E A_s}{E h \ell_y} = \text{Stringer Membrane Parameter}$$

$$\Lambda_s = 1 + 2\lambda^2 (\bar{z}_s/R) (\delta^2 - \nu) + \lambda^4 (\bar{z}_s/R)^2 (1 + \delta^2)^2$$

$$\Lambda_r = 1 + 2n^2 (\bar{z}_r/R) (1 - \nu \delta^2) + n^4 (\bar{z}_r/R)^2 (1 + \delta^2)^2$$

$$\Lambda = (1 + \delta^2)^2 + 2\delta^2 (1 + \nu) (\bar{R} + \bar{S}) + (1 - \nu^2) [\bar{S} + \delta^4 \bar{R} + 2\delta^2 \bar{R} \bar{S} (1 + \nu)]$$

$$\begin{aligned} \Lambda_{rs} = & n^2 \lambda^2 [\delta^2 (1 - \nu^2) + 2(1 + \nu)] (\bar{z}_s/R)^2 \\ & + n^4 [1 - \nu^2 + 2\delta^2 (1 + \nu)] (\bar{z}_r/R)^2 \\ & + 2n^2 (1 - \nu^2) (\bar{z}_s/R) + 2n^2 (1 - \nu^2) (\bar{z}_r/R) \\ & + 2n^4 (1 + \nu)^2 (\bar{z}_r/R) (\bar{z}_s/R) + 1 - \nu^2 \end{aligned}$$

\bar{z}_r and \bar{z}_s are the distance to the centroid from skin middle surface for ring and stringer, respectively.

$\lambda = m\pi R/L_x$ where m = number of axial half wavelengths. $D = Eh^3/12(1 - \nu^2)$, is the skin bending rigidity.

$\delta = \frac{nL_x}{m\pi R}$ where n = number of circumferential full wavelengths.

FIGURE 5. MIKULAS' FREQUENCY EQUATION FOR A SIMPLY-SUPPORTED STIFFENED CYLINDER

3.9 Sidewall Representation

3.9.1 General

The analytical model predicts the bare fuselage noise reduction by equating the net acoustic power inflow from resonant and non-resonant structural modes to the power that is absorbed within the cabin interior. The model examines the modal response of the fuselage structure and of the cabin and calculates the coupling between the two systems to arrive at the internal noise levels and hence the noise reduction for the bare fuselage. In [5], the additional transmission loss provided by the sidewall treatment was calculated assuming infinite panel conditions and the results showed reasonably good agreement with test data for finite panels. Although the present analytical model calculates the power flow through finite structural panels in order to include both resonant and nonresonant structural response, it is assumed, on the basis of the above evidence and for simplicity, that the infinite panel approach can be used to calculate the additional transmission loss provided by the sidewall treatments. The infinite panel model for the sidewall noise transmission is discussed in this section.

Figure 6 shows a simplified representation of the sidewall acoustic power flow. The external pressure field, characterized by incidence angle and intensity, acts on the airplane skin (element 1). The acoustic power flow W_{12} from the skin to the cabin interior (element 3) when no sidewall (element 2) exists, is calculated from a knowledge of the bare fuselage transmission coefficient, and the transmitted power is then equated to the power absorbed within the cabin W_{abs} to find the resulting internal diffuse acoustic pressure $\langle p_i^2 \rangle$. The presence of the add-on sidewall acoustic treatment acts to reduce the acoustic power inflow to an

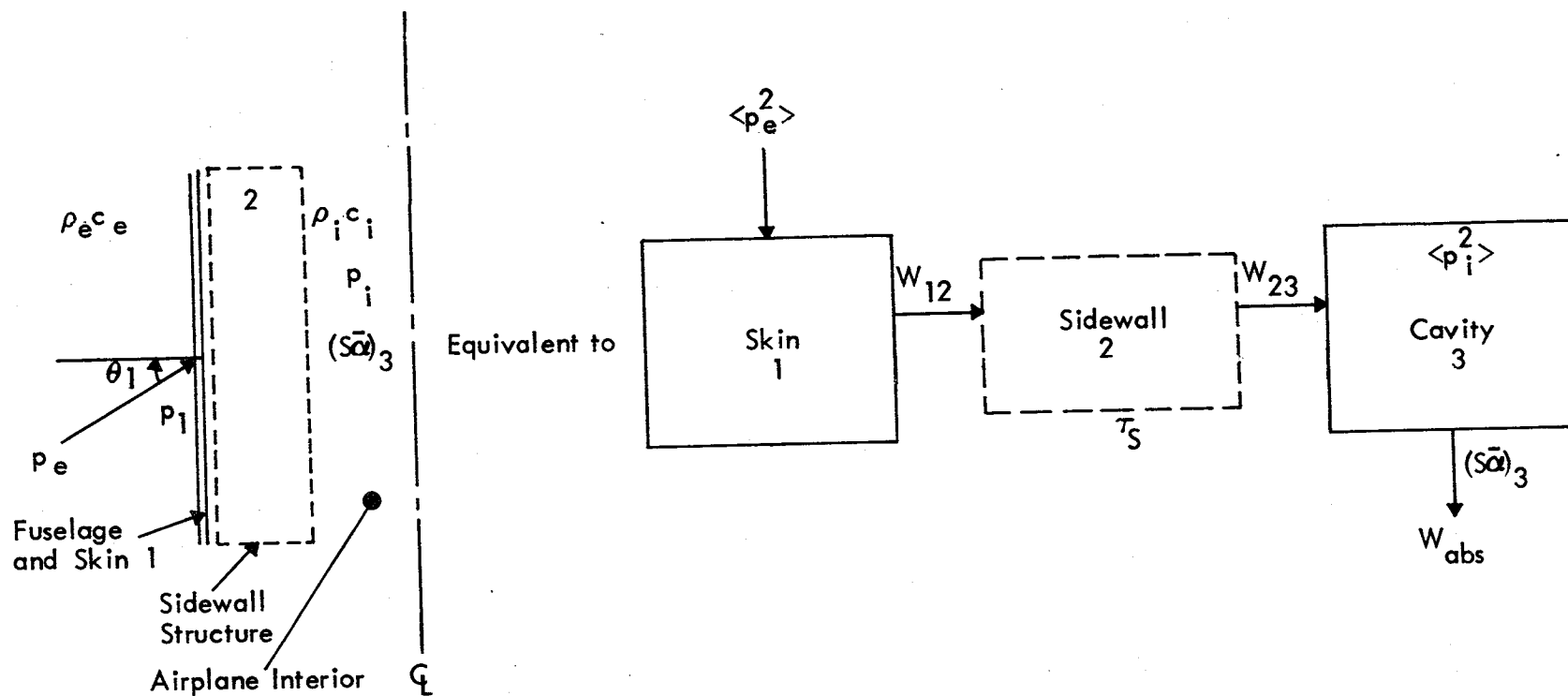


FIGURE 6. POWER BALANCE REPRESENTATION OF SIDEWALL ACOUSTICS

amount $\tau_s W_{12}$. In general, the transmission coefficient of the add-on sidewall acoustic treatment τ_s cannot be calculated from a consideration of the sidewall treatment in isolation, but rather a knowledge of the bare fuselage impedance is required as well.

Calculation of the additional noise reduction provided by the add-on sidewall structure consequently involves (1) calculation of the noise reduction of the bare (infinite panel) fuselage structure, (2) calculation of the noise reduction provided by the treated fuselage infinite panel representation, and (3) subtraction of the bare fuselage noise reduction from that of the treated fuselage to find the noise reduction for the add-on sidewall structure. Allowance must also be made for any changes in absorption coefficient, which may result from sidewall changes.

The noise reduction for the untreated bare fuselage, for a diffuse interior acoustic field, can be expressed as [5]

$$NR = 10 \log \frac{\langle p_e^2 \rangle}{\langle p_i^2 \rangle} \approx 10 \log_{10} \frac{(S\alpha)_U}{A\tau_p} \frac{\rho_e c_e}{\rho_i c_i} \quad (62)$$

where $\langle p_e^2 \rangle$ characterizes the level of the external blocked pressure field on the fuselage surface,

$\langle p_i^2 \rangle$ is the mean-square sound pressure in the cabin,

$(S\bar{\alpha})_U$ is the absorption in the untreated cabin, and

τ_p is the bare fuselage transmission coefficient.

Two symbols, S and A, are used for area to distinguish between transmitting area A and absorbing area S.

From a similar expression for the noise reduction for the treated fuselage (including the acoustic sidewall), the additional noise reduction provided by the add-on sidewall is [5]

$$\Delta NR = 10 \log \tau_s - 10 \log [(S\bar{\alpha})_U / (S\bar{\alpha})_T] \quad (63)$$

where $\tau_s = \tau_{s2} / \tau_p$ is the transmission coefficient of the add-on sidewall acoustic treatment,

τ_{s2} is the transmission coefficient of the treated fuselage structure, and

the subscript T refers to the treated cabin interior.

Expressions for calculation of the transmission coefficients τ_{s2} and τ_p and the interior absorption coefficients $\bar{\alpha}_T$ are, therefore, required. Sections (3.9.2) and (3.9.3) derive relations for τ_{s2} and τ_p , respectively, while empirical data are used for absorption coefficients $\bar{\alpha}_T$, although reliable analytical models are available [5].

3.9.2 Sidewall Transmission

The transmission coefficient τ of a structure can be defined with respect to the blocked pressure field as [5]

$$\tau_1 = \left| \frac{p_t}{p_1} \right|^2 \frac{\rho_1 c_1}{\rho_2 c_2} = \left| \frac{p_t}{p + p_r} \right|^2 \frac{\rho_1 c_1}{\rho_2 c_2} \quad (64)$$

where for massive structures and incident plane waves, the blocked pressure p_1 is approximately equal to the sum of the incident (p) reflected (p_r) pressures.

Figures 7 and 8 present the model of a double-wall sidewall structure whose transmission characteristics are of interest in this study. The untreated fuselage is shown also.

Acoustic plane waves are assumed incident on the exterior of the structure and reflected and transmitted as determined by the various impedances present. The medium on the interior side of the structure is assumed to extend to infinity with an acoustic impedance of p_0 . Of interest is the transmission coefficient τ and the noise attenuation across individual media or layered combinations of such media when aligned in series. From expressions for the pressure ratios across boundaries between adjacent media and the pressure ratios across the media themselves, it is possible to derive expressions for the transmission coefficient across a complex series of layered media. Fundamental to this analysis are expressions for the characteristic impedance of the various media and for the impedance looking into a finite depth medium whose propagation and attenuation characteristics may be simply defined.

It is now possible to derive expressions for the characteristic impedance Z_0 and propagation constant b of a porous medium and the impedance of a stiffened, pressurized and curved panel.

Following [5], expressions for Z_0 and b for a porous material are determined empirically from only the material flow resistivity. For example, empirical relationships exist for determining b for semi-rigid fibrous materials. Thus

$$Z_0 = - \frac{jK}{\omega Y} b, \text{ and } b = \alpha + j\beta \quad (65)$$

where, following [47]

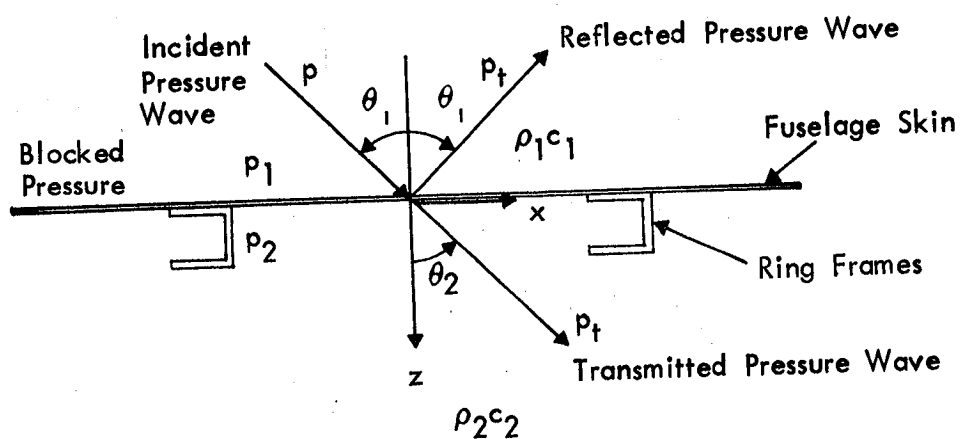
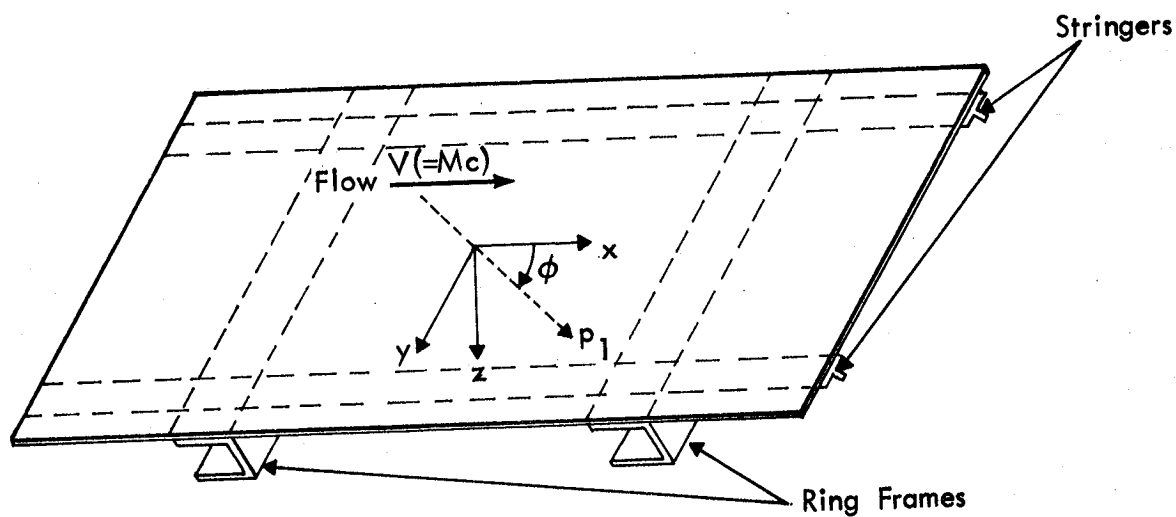
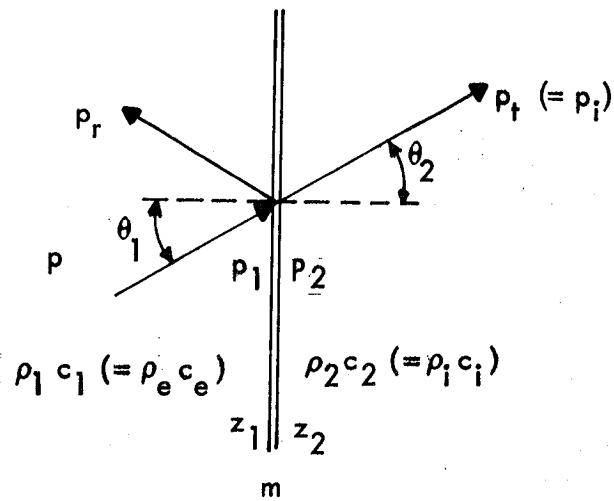
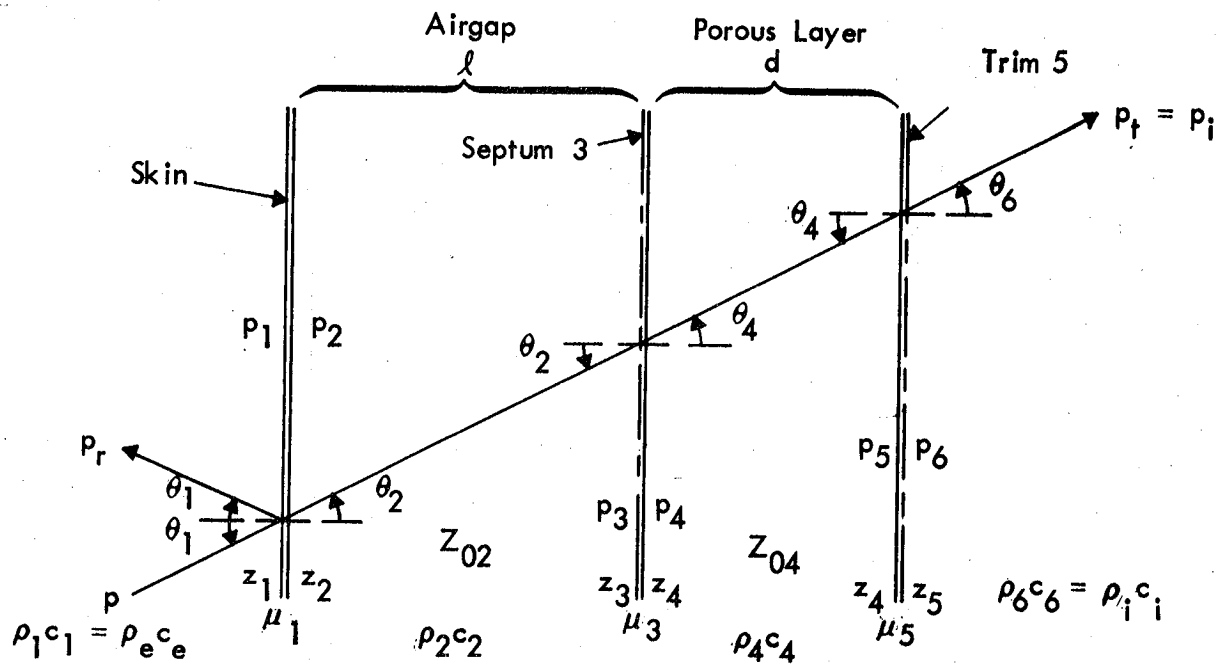


FIGURE 7. EXTERNAL GEOMETRY OF PANEL-PRESSURE FIELD CONFIGURATION



UNTREATED



TREATED

FIGURE 8. SIDEWALL REPRESENTATION FOR POROUS LAYER BOUNDED BY IMPERVIOUS SEPTA MOUNTED OVER AIRGAP

$$\alpha = (\omega/c)[0.189(\rho f/R_1)^{-0.595}] \quad (66)$$

$$\beta = (\omega/c)[1 + 0.0978(\rho f/R_1)^{-0.700}] \quad (67)$$

K is the complex compressibility of the gas in the porous material (\approx atmospheric pressure),
 f is the frequency ($\omega/2\pi$),
 Y is the porosity of the porous material,
 c is the speed of sound in the gas in the porous material,
 ρ is the density of the gas in the porous material, and
 R_1 is the flow resistivity of the porous material
 ($0.01 \leq \rho f/R_1 \leq 1$ in general).

The effects of variations in material density are reflected in changes in material flow resistivity. Bies and Hansen [26] have recently extended the empirical relationships for α and β to values of $\rho f/R_1$ much less than 0.01.

It should be noted that this model does not consider mechanical transmission through the material fibers, such flanking of the acoustic path providing a limit to the noise reduction of a double-wall sidewall.

From results such as [27], the impedance of an infinite stiffened, curved and pressurized fuselage structure for a sound wave incident at an angle θ relative to the normal and at azimuthal angle ϕ relative to the x-axis, as shown in Figure 7, can be written as

$$z_p(\theta, \phi) = \omega \mu_1 [\chi n + j(1 - \psi - \chi)] \quad (68)$$

where

$$\chi = \omega^2 \sin^4 \theta_2 \Delta / (c_2^4 \mu_1),$$

$$\Psi = N_x \sin^2 \theta_2 [\cos^2 \phi + 2 \sin^2 \phi] / (\mu_1 c_2^2), \text{ and}$$

$$N_x = \Delta p R/2 \text{ } (\Delta p \text{ acts positively outwards}).$$

$$\Delta = D_x \cos^4 \phi + 2D_{xy} \cos^2 \phi \sin^2 \phi + D_y \sin^4 \phi$$

η is the structural loss factor,

$$k = \omega/c,$$

D_x is the bending rigidity of the structure in section perpendicular to the x-axis, D_y is the y-axis bending rigidity, and D_{xy} the cross rigidity given by

$$D_{xy} = \frac{(D_x \nu_x + D_y \nu_y + 4D_k)}{2}.$$

ν_x and ν_y are the Poisson's ratios for the two axes, and

$$D_k = \frac{Gh^3}{12}$$

where G is the modulus of rigidity for shear stresses and h is the plate thickness.

The effect of η is only important near the coincidence frequency. Then, the transmission coefficient $\tau_p (= \tau_1)$ across the untreated panel is given by Eq. (64) as

$$\frac{1}{\tau_p} = \left(\frac{\rho_2 c_2}{\rho_1 c_1} \right) \left| \frac{p_1}{p_2} \right|_{\text{UNTREATED}}^2 = \left(\frac{\rho_2 c_2}{\rho_1 c_1} \right) \left| \frac{z_2 + z_p}{z_2} \right|^2 \quad (69)$$

where $z_2 = \rho_2 c_2 / \cos \theta_2$ and z_p is given by Eq. (68).

The transmission coefficient τ_{S2} across the treated sidewall is given by

$$\frac{1}{\tau_{S2}} = \left(\frac{\rho_6 c_6}{\rho_1 c_1} \right) \left| \frac{p_1}{p_2} \cdot \frac{p_2}{p_3} \cdot \frac{p_3}{p_4} \cdot \frac{p_4}{p_5} \cdot \frac{p_5}{p_6} \right|^2 \quad (70)$$

The terms in Eqs. (69) and (70) are given by

$$\frac{p_1}{p_2} = \frac{z_2 + z_p}{z_2}$$

$$z_2 = Z'_{02} \coth(jk_2 l \cos \theta_2 + \psi_2)$$

$$\psi_2 = \coth^{-1}(z_3/Z'_{02}) \quad \text{and} \quad Z'_{02} = \frac{\rho_2 c_2}{\cos \theta_2}$$

$$\theta_2 = \sin^{-1}(c_2 \sin \theta_1 / c_1) \quad (\text{Snell's Law})$$

$$\frac{p_2}{p_3} = \frac{\cosh(jk_2 l \cos \theta_2 + \psi_2)}{\cosh \psi_2}$$

$$\frac{p_3}{p_4} = \frac{z_3}{z_4}$$

$$z_3 = j\omega \mu_3 + z_4 \quad \text{and} \quad z_4 = Z'_{04} \coth(b_4 d \cos \theta_4 + \psi_4)$$

$$Z_{04} = -\frac{jKb_4}{\omega Y} \quad \text{and} \quad Z'_{04} = Z_{04} / \cos \theta_4$$

$$b_4 = \alpha_4 + j\beta_4 \quad \text{and} \quad c_4 = \omega / \beta_4$$

$$\theta_4 = \sin^{-1}(c_4 \sin \theta_2 / c_2) \quad \text{and} \quad \psi_4 = \coth^{-1}(z_5/Z'_{04})$$

$$\frac{p_4}{p_5} = \frac{\cosh(b_4 d \cos \theta_4 + \psi_4)}{\cosh \psi_4} \quad \text{and} \quad \frac{p_5}{p_6} = \frac{z_5}{z_6}$$

where $z_5 = j\omega\mu_5 + z_6$, $z_6 = \rho_6 c_6 / \cos \theta_6$, and $\theta_6 = \sin^{-1}(c_6 \sin \theta_4 / c_4)$.

Then, the transmission coefficient of the add-on acoustic treatment $\tau_s (= \tau_{s2} / \tau_{ML})$ is defined as

$$\tau_s = \frac{\tau_{s2}}{\tau_{ML}} = \left| \frac{\left(\frac{p_1}{p_2} \right)_{\text{UNTREATED}}}{\left(\frac{p_1}{p_2} \right) \cdots \left(\frac{p_{n-1}}{p_n} \right)_{\text{TREATED}}} \right|^2 \quad (71)$$

where $p_n = p_t$, and the added transmission loss of the sidewall is found from

$$\Delta TL = -10 \log_{10} \tau_s. \quad (72)$$

In summary, the *treated* fuselage acoustic power flow into the cabin interior is found by multiplying the *bare* fuselage acoustic power flow into the cabin, calculated from Eqs. (51) and (52), by the transmission coefficient of the add-on acoustic treatment τ_s , computed using the above equations. The flow diagram for computation, shown in Sec. 3.11, indicates the stage in the calculation procedure when this multiplication is carried out.

3.10 Interior Acoustics

3.10.1 Spatial Variation of Interior Noise Levels

In order to generate a nonhomogeneous structural response to the nonhomogeneous excitation pressure field, the computation method

divides the fuselage structure into various elements located along the fuselage length. Resulting computations of the net acoustic power inflow produce a nonhomogeneous distribution of power inflow varying in much the same way as the excitation level varies over the fuselage exterior surface. Since it is desired to calculate the maximum noise level developed inside the airplane cabin, account must be taken of this nonhomogeneity in structural response and power radiation in calculations of the internal noise levels.

An imaging technique is used to calculate the variation in interior noise levels. Each of the radiating structural elements is represented as a point source mounted in the fuselage, located at the element center, and considered to radiate into the cabin volume. The contribution of each point source to the local pressure level along the cabin centerline is calculated by adding to the direct radiation from the point source itself, the contributions from all the image sources that are associated with reflections from the various bounding surfaces of the airplane interior (walls, ceiling, floor).

The local intensity is the sum of the local intensities produced by each fuselage element (i.e., image-source array). The level variation along the fuselage interior is averaged to determine the space-average mean square pressure, which is also the basic output of analytical model already presented (Section 3.5). The local levels are adjusted at each frequency by adding the difference between the space-average noise levels calculated by the power flow and the image-source array models, respectively; thus, the space-average noise levels at each frequency calculated by the image array and the power flow model are equal. The differences in space-average spectrum levels between the two calculation schemes are less than 1.0 dB in most cases and result mainly from a certain coarseness in the representation of the image field.

3.10.2 Image Array Formulation

Figure 9 shows the image array used to model the radiation pattern from a point source located at S in the sidewall. For model simplicity, the cabin fuselage is assumed to be rectangular. For example, the image (1,1) shown in Figure 9 represents the contribution from that ray which travels via the indirect path involving two reflections, one each from opposite wall and ceiling. Equation (73) below expresses the dependence of the local center-line intensity on distance from the source, on the absorption coefficients of each of the bounding surfaces (the sidewalls are considered identical), and on the paths by which the sound waves can travel from source to observer position [28].

$$I_o = \frac{\langle p_o^2 \rangle}{\rho_1 c_1} = \sum_j^N W_j \left(\frac{1}{4\pi R^2} + \frac{1}{2\pi} \sum_{\substack{\beta, \gamma = -\infty \\ (\beta, \gamma \neq 0)}}^{\infty} \frac{(1 - \alpha_w)^p (1 - \alpha_c)^q (1 - \alpha_f)^r}{[R^2 + (\gamma H)^2 + (2|\beta|W - \frac{\beta}{|\beta|} \frac{W}{2})^2]} \right)_j \quad (73)$$

Here I_o is the acoustic intensity at observer position 0,

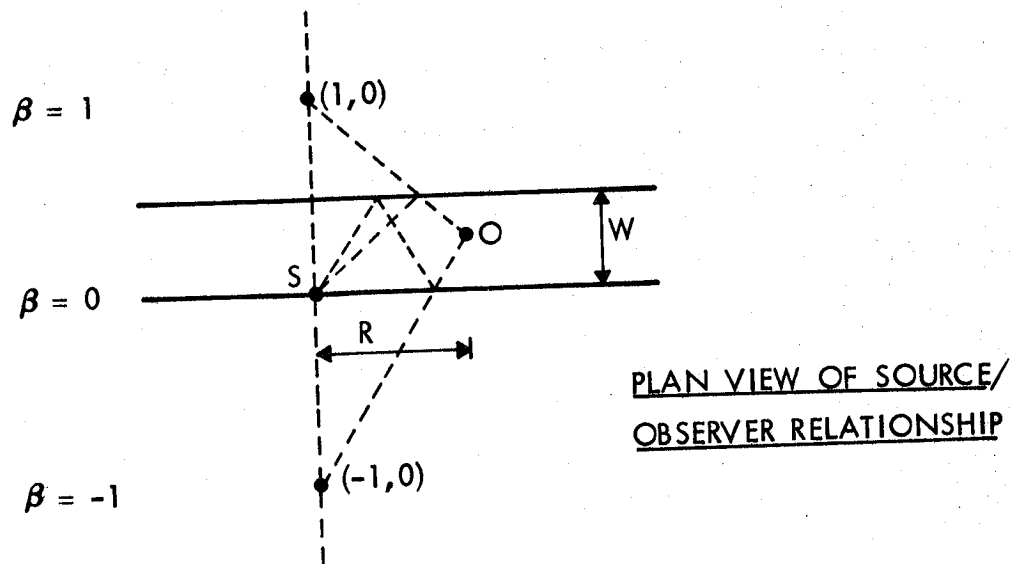
$\langle p_o^2 \rangle$ is the observed mean-square pressure at the observer position,

W_j is the power radiated by the j th structural element (considered to radiate as a point source),

$\alpha_w, \alpha_c, \alpha_f$ are absorption coefficient for sidewalls, ceiling, and floor, respectively,

R is the axial distance between observer 0 and j th source location S,

H, W are the mean height and mean width of the cabin,



Rays for $(-1,0)$ and $(1,0)$ Images

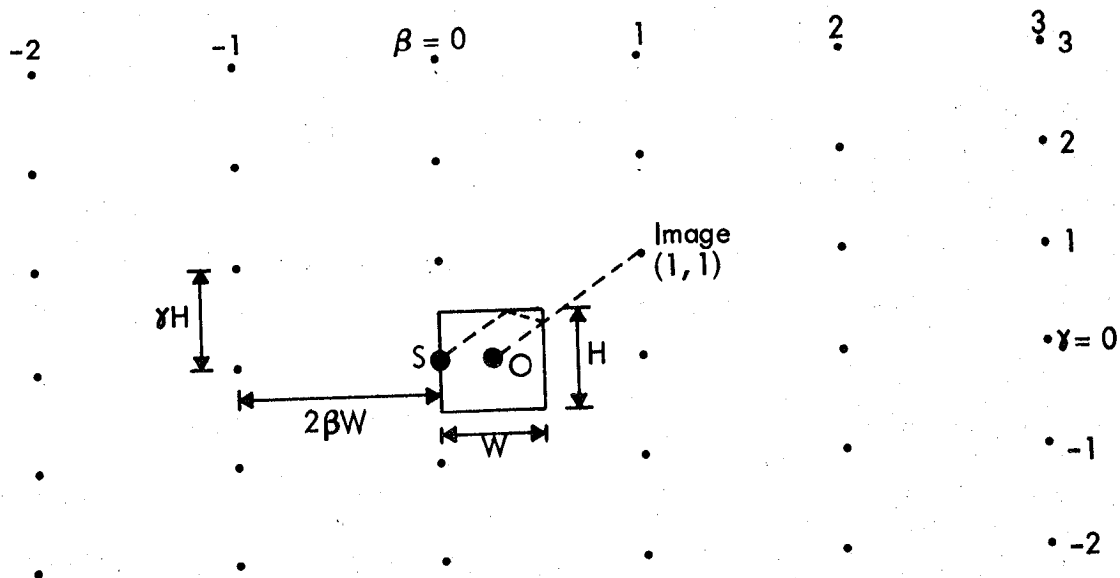


FIGURE 9: CROSS-SECTION VIEW OF IMAGE ARRAY FOR POINT SOURCE (S) LOCATED IN WALL AND CENTERLINE OBSERVER (O)

p,q,r are indices determining the path taken by acoustic ray from source to receiver, defined by

$$p = \begin{cases} 2\beta - 1 & \text{for } \beta > 0 \\ -2\beta & \text{for } \beta < 0 \end{cases} \quad \begin{matrix} q = (-1)^{\gamma}(\gamma + 1)/2 \\ r = (q - 1) \end{matrix} \quad \text{for } \gamma \text{ odd}$$

$$q = r = \gamma/2 \quad \text{for } \gamma \text{ even or zero.}$$

3.11 Computational Procedures

The analytical model was computerized to automate the calculations of the noise levels developed in propfan-powered study airplanes. An outline of the overall computational procedure, with details of how the various components of the analytical model are assembled together within the computer programs, is presented in this section.

Figure 10 presents a flow diagram of the computational processes. The various computational phases and the associated input requirements are linked together; references to appropriate sections of the report text and/or relevant equations are included; locations where important decisions must be made are indicated.

The computing prediction system in fact consists of five interdependent computer programs. Four of these organize acoustic and structural data and perform preliminary calculations, the results of which are used as input to a main computer program for final calculation of the cabin interior noise levels.

It should be noted that, while the effects of changes to the structure require that all programs be run, changes to the sidewall transmission characteristics and to the cabin interior can use data stored on existing input files generated by previous (baseline) computer runs.

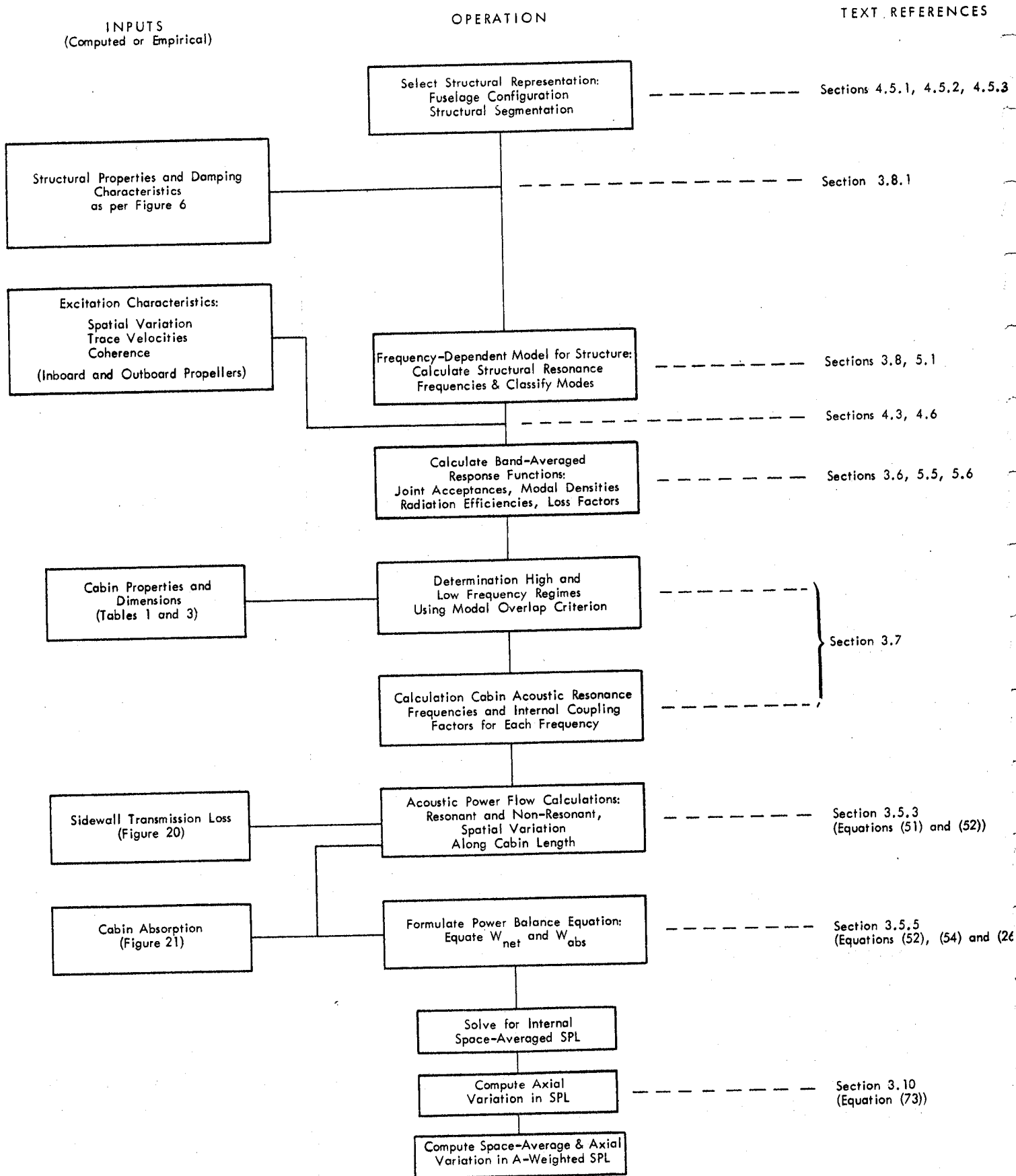


FIGURE 10. FLOW DIAGRAM FOR COMPUTATION OF INTERNAL NOISE LEVELS FOR STUDY AIRPLANES

4.0 BASELINE AIRCRAFT

The previous section described development of the analytical model which is to be applied to the design of fuselage sidewalls for the baseline propfan-powered study aircraft such that the interior noise levels will meet an 80-dB criterion for the average A-weighted sound level during cruise. The fuselage sidewalls of the study aircraft are to be designed to have minimum surface weight density and high sound transmission loss. Two concepts are to be considered for reducing low-frequency propfan noise through modification of the fuselage sidewall design: (1) add-on noise control features wherein nonstructural noise-control elements are to be added to the conventional sidewall structure, and (2) advanced noise control designs wherein the materials and the basic structural configuration of the baseline aircraft could be modified to obtain higher sound transmission loss and hence lower interior noise levels than could be obtained by add-on designs, possibly, at a lower total weight penalty.

Because the effectiveness of add-on or advanced acoustical treatment depends on the characteristics of the fuselage structure to which the additional acoustical treatment is applied, it was necessary to select baseline aircraft that would allow meaningful assessments of the application of the analytical method. The study required that three baseline aircraft be selected, namely a wide-body aircraft, a narrow-body aircraft, and a small-diameter aircraft. The fuselage diameters were to be as follows:

<u>Airplane</u>	<u>Fuselage Diameter</u>
Wide-body	4.88 to 6.10 m (16 to 20 ft)
Narrow-body	3.05 to 3.96 m (10 to 13 ft)
Small-diameter	1.83 to 2.44 m (6 to 8 ft)

It was considered desirable, as well as acceptable, that the baseline study aircraft should be derived from aircraft that were already designed or flying. This section presents the general requirements for the existing-design aircraft as well as the baseline study aircraft. The process of designing the propfans to power the baseline study aircraft is then described. This is followed by a description of the relevant structural characteristics of the baseline study aircraft, and a discussion of the acoustical characteristics of the fuselage sidewall and interior. Finally, the properties of the exterior noise field are presented.

4.1 Study Requirements

In addition to the requirement to have fuselage diameters in the range described above, the baseline aircraft were to have

- .wing-mounted engines,
- .an initial-cruise altitude of 9000 m (30,000 ft) and
- .a cruise Mach number of 0.8.

Also, the wide-body and narrow-body aircraft were to be able to carry at least 50 passengers over a range of at least 805 km (500 mi).

The propfans were to be designed using data developed by the Hamilton Standard Division of United Technologies Corporation, [7]. The fuselages of each of the three baseline study aircraft were to have structural characteristics compatible with cruising at the specified cruise altitude. The structures of the three baseline study aircraft were expected to have some differences because of the different design approaches used by the manufacturers of the existing design aircraft to achieve fail-safe structural requirements.

4.2 Choice of Existing-Design Aircraft

The following three aircraft were selected as being able to meet the general study requirements outlined above. They were the McDonnell Douglas DC-10-30 for the wide-body aircraft, the Boeing 707-320B for the narrow-body aircraft, and an aircraft having the fuselage of a Grumman Gulfstream I, but modified for high-speed subsonic cruise with a swept wing similar to that on a Gulfstream II instead of the unswept wing on the Gulfstream I.

Each of the three existing-design aircraft meet all the requirements for initial cruise altitude, cruise Mach number, payload, and range [48,49]. Also, each aircraft has a fuselage structure capable of carrying all design loads, which therefore forms a realistic fuselage design for a baseline study aircraft.

Each of the existing-design aircraft was modified, conceptually, to accept the propfan propulsion system. The DC-10 is powered by three turbofan engines - one on each wing, supported below the wing from a pylon, and one mounted through the vertical stabilizer. The aft fuselage of the DC-10 was modified to eliminate the center engine. The two wing engines were replaced by propfans, and an extra two propfans were added to the wings. The 707 had the four turbofan engines replaced by four propfans. The small-diameter airplane used two propfans located approximately at the spanwise wing station where the propellers are mounted on the straight wings used with the Grumman Gulfstream I aircraft. All aircraft are low wing designs. The propfans were installed such that the center of thrust was above the wing rather than below the wing as it is for the 707 and the wing-mounted engines on the DC-10.

Four propfans, two on each wing, were used to power the wide-body aircraft. Conceptually, it would have been feasible to have used more than four engines. That would have reduced the diameter of each of the propfans, and, if the inboard engine location had remained fixed, the propeller tip clearance would have increased. Then, the exterior noise field impinging on the outside of the widebody fuselage would have been reduced somewhat. However, more than four propfans was not considered practical.

4.3 Propfan Sizing Analysis

Previous studies [1, 2, 3] have considered the selection of propfans to optimize a given aircraft mission. In those studies, considerations were given to aerodynamic, mechanical and economic factors in producing an optimum propfan design for a specified mission. For the study here, however, it was not feasible to conduct such an analysis since the propfans were to be installed, conceptually, on existing-design aircraft. Therefore, the approach used to size the propfans for the three baseline study aircraft proceeded from a definition of the total thrust required to propel the aircraft at the desired cruise Mach number and initial cruise altitude. Values for total installed thrust per airplane, obtained on the basis of previous analyses, are listed below.

<u>Airplane</u>	<u>Installed Net Cruise Thrust Per Airplane</u>
Wide-body	133.45 kN (30,000 lb)
Narrow-body	71.17 kN (16,000 lb)
Small-diameter	22.24 kN (5,000 lb)

These values of total net thrust per airplane, coupled with the number of propfans per airplane, defined the net thrust to be produced by each propfan.

The Hamilton Standard data in [7] describe performance characteristics for propfans having 6, 8, or 10 blades. For a propfan producing a given net thrust, a study of the performance data in [7] indicated that the smallest-diameter propfan would be one having the largest number of blades. Since data were only available for 6, 8, or 10 blades, propfans designed for the three baseline study aircraft were based on propfans having 10 blades.

The next design parameter that was selected was the operating tip speed of the propfan. The tip rotational speed V_{rot} , was chosen to be 243.84 m/s (800 ft/s). This tip speed would be used during takeoff to minimize the noise level at the Appendix C noise-measurement location for noise certification under Part 36 of the Federal Aviation Regulations. That same tip speed would be used during cruise.

With specifications for (1) the installed net thrust per propfan, (2) the number of propfans per airplane, (3) the cruise tip speed, and (4) the number of blades per propfan, it was necessary only to select one more design parameter in order to calculate the rest of the propfan characteristics.

That design parameter was the cruise power loading P/D^2 where P is the power supplied to the propfan and D is the propfan diameter. From the studies that had been previously conducted of propfan installations (see Refs. 1, 2, 3), and from discussions with personnel at Hamilton Standard, it was

decided to select a P/D^2 ratio of 280 kW/m² or 35 SHP/ft² where SHP is the propfan shaft horsepower. The same value of power loading was assumed to apply to the propfans for each of the three baseline study aircraft; it would permit fuel-efficient cruise at the specified cruise altitude and cruise Mach number.

It was further assumed that the atmospheric conditions at the design cruise altitude would be those of an International Standard Atmosphere - namely a density ratio of $\rho_0/\rho = 2.6686$ and a speed of sound $c = 303.2$ m/s where ρ_0 is the density of the air at sea level and ρ is the density at 9014.4 m. For a cruise Mach number of 0.8, this assumption gave an airspeed, V_a , of 242.58 m/s. The helical tip Mach number was then

$$M_{hel} = \left(V_{rot}^2 + V_a^2 \right)^{1/2} / c = 1.13$$

Propfans on each study aircraft were powered by turbofan engines operated as turboshaft engines to provide shaft power through a reduction gearbox. The turboshaft engines produced some jet thrust to augment the thrust produced by the propfans. Previous analyses had indicated that the jet thrust was about 10 percent of the total propfan thrust. Those analyses had also indicated that the sum of the drag resulting from flow around the nacelle and the gearbox, and the drag resulting from interference effects between the wing and the nacelle and gearbox, was about 6 to 8 percent of the total propfan thrust. Therefore, it was assumed that the jet thrust was approximately equal to the sum of the nacelle drag and the wing/nacelle interference drag. With this assumption, the net installed thrust from the propfan equalled the net uninstalled thrust, $F_{n,u}$.

The propfan performance analyses in [7] are based on the generalized non-dimensional parameters used for analyzing the performance of propellers. The parameters are: the power coefficient, C_P , the advance ratio J , and the thrust coefficient C_F . A net efficiency parameter, η_{net} , is also defined.

The propfan design process consisted of the following steps:

1. Determine the advance ratio J ;
2. Determine the power coefficient C_P ;
3. From C_P and J , find the thrust coefficient C_F and the net efficiency η_{net} ;
4. From the thrust coefficient and the net thrust, find propfan diameter; and
5. Find propfan rotational speed from the ND product and propfan diameter.

The analysis was carried out only for the design cruise Mach number of 0.8 at the design cruise altitude, for propfans having 10 blades.

Advance ratio is defined as

$$J = V_a / (V_{rot} / \pi) = 3.13 \text{ for present conditions;}$$

Propfan power coefficient C_P is defined as

$$C_P = \text{power} / \rho n^3 D^5,$$

and can be related to propfan design parameters by

$$C_P = (P/D^2) (\rho_0/\rho) / [5.671 (ND/1000)^3]$$

where P is in kW, D is in m, N is in rev/min, and ρ_0 is 1.225 kg/m³.

The ND product is,

$$ND = 60V_{\text{rot}}/\pi = 4657 \text{ m/min. for present conditions.}$$

Using $P/D^2 = 280 \text{ kW/m}^2$, the power coefficient for the propfans is then

$$C_P = 1.30.$$

Propfan performance data from Table VII of [7(c)] were used to develop the design chart shown in Figure 11 which relates power coefficient, advance ratio, thrust coefficient, and net propulsive efficiency. Entering the design chart at a power coefficient of 1.30 and interpolating at the advance ratio of 3.13 gives an uninstalled net thrust coefficient of 0.355 with a net propulsive efficiency of 0.85, the efficiency parameter being defined as

$$\eta_{\text{net}} = J C_{F_{n,u}} / C_P$$

An efficiency parameter of 0.85 is compatible with values that were used in previous propfan design studies and is close to, but does not equal, the maximum-possible efficiency for the design advance ratio 3.13. The maximum net efficiency according to the data in [7] would be slightly higher than 0.85. To achieve more efficiency, however, would require operating the propfan at a lower power coefficient which would mean a lower thrust coefficient and hence a larger propfan diameter in order to provide the same net thrust.

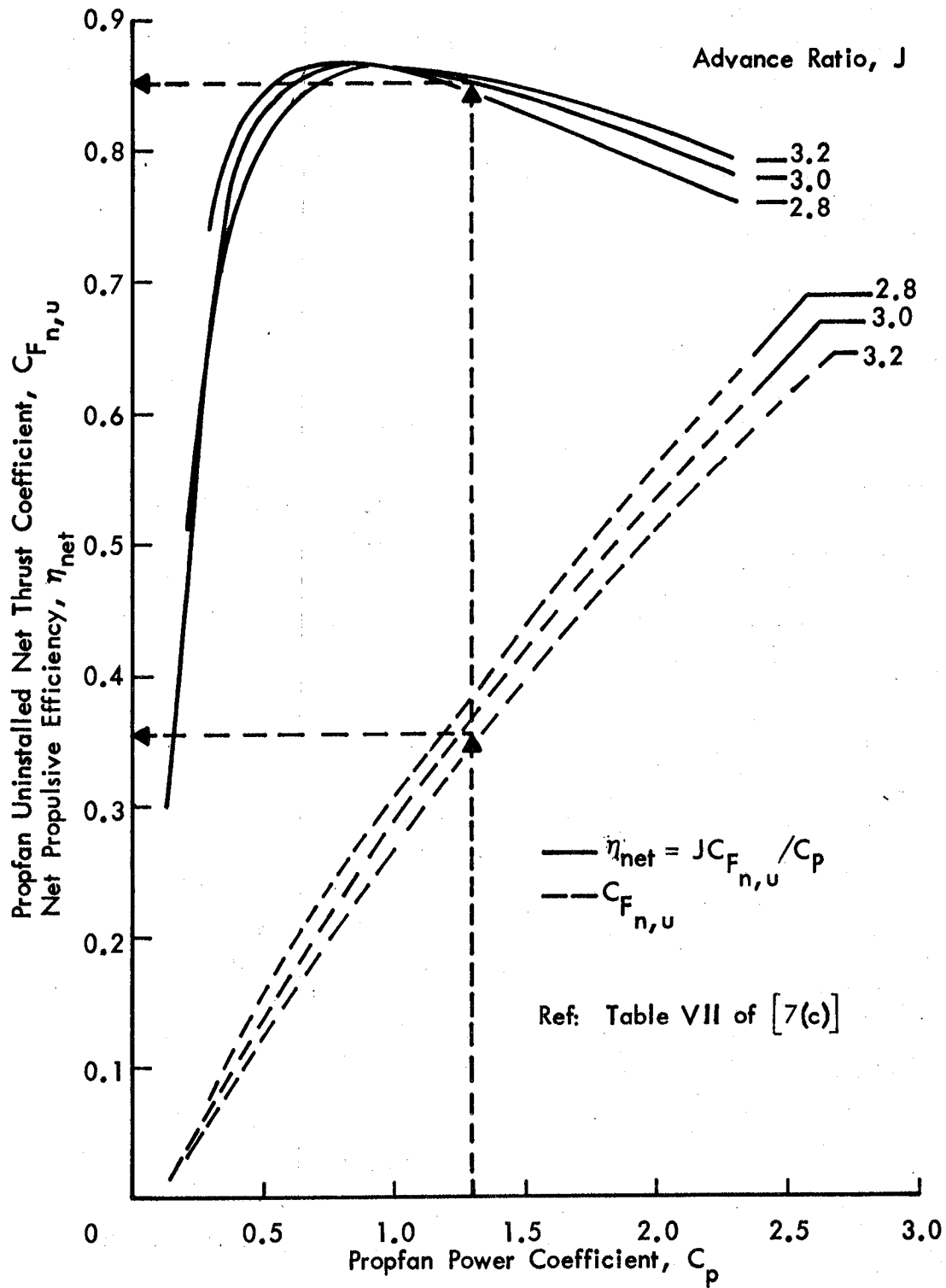


FIGURE 11. PERFORMANCE PARAMETERS FOR 10-BLADED PROPFAN; FREE STREAM MACH NUMBER $M_0 = 0.80$

Propfan diameter was determined from the net thrust coefficient C_{F_n} with

$$C_{F_n} = \text{net thrust} / \rho n^2 D^4$$

where net thrust is in newtons, and ρ , n , and D have the units stated above.

The equation for C_{F_n} can now be written as

$$C_{F_n} = (F_n) (\rho_0 / \rho) / [340.28 (ND/1000)^2 D^2]$$

where F_n is the net thrust in newtons required per propfan, and other parameters have units specified earlier.

From previously given net thrusts per aircraft, the installed net thrusts per propfan are:

Wide-body:	33,362 N (7500 lb)
Narrow-body:	17,793 N (4000 lb)
Small-diameter:	11,120 N (2500 lb)

Then, on substituting values for ρ_0 / ρ and the ND product, the propfan diameter D can be calculated for each value of net thrust. Rotational speed N is found from $ND/D = 4657/D$.

4.4 Characteristics of Baseline Aircraft

The baseline study aircraft were designed by placing the propfans on the wings at appropriate locations. For wide-body aircraft, the inboard propfans were placed at the same wing station at which the wing engines are currently installed on the DC-10-30. The outboard engines were placed at an

appropriate location farther outboard. For the narrow-body aircraft, the propfans were placed at the same stations as the existing locations for the wing engines. For the small-diameter aircraft, engines were installed approximately at the same wing stations that the propellers are installed for the Grumman Gulfstream I aircraft, but on the swept wing.

Results of the propfan sizing study for the three baseline study aircraft are shown in Table 1. Each of the aircraft meets the general study requirements described earlier. The data in Table 1 indicate that the ratio of propfan diameter to fuselage diameter is approximately equal to, or somewhat greater than, 1.

On the two larger airplanes, tip clearances range from 0.4 propfan diameters for the inboard propfan of the wide-body aircraft to 2.7 propfan diameters for the outboard propfan on the narrow-body airplane. Tip clearance for the small diameter airplane is 0.3 propfan diameters.

The sweep of the wings for the wide-body and narrow-body airplanes means that the outboard propfans, even though they are significantly farther outboard, could cause the exterior noise field to be spread over an extensive region of the fuselage and hence eliminate the option of using localized noise control methods in a particular area of the cabin (as is discussed in Section 7.0). Localized procedures used in the past on propeller-powered airplanes have located coat closets in the regions of the plane of the propeller in order to put a compatible cabin furnishing in the region of highest noise levels.

Table 1.
PERFORMANCE PARAMETERS FOR
PROPFAN-POWERED BASELINE
STUDY AIRPLANES

Parameter	Study Airplane		
	Wide-body	Narrow-body	Small-diameter
Design range, km (n. mi)	7400 (4000)	6900 (3700)	6670 (3600)
Maximum takeoff weight, kg (lb)	252,000 (555,000)	148,000 (327,000)	30,000 (66,000)
Typical number of psgr seats	270	145	18
Fuselage diameter, ϕ m (ft)	6.02 (19.75)	3.76 (12.33)	2.44 (8.0)
Fuselage length, m (ft)	52.0 (170.5)	45.7 (150.0)	21.7 (71.3)
Number of propfans	4	4	2
Net cruise thrust per propfan, F_n , N (lb)	33,362 (7500)	17,793 (4000)	11,120 (2500)
Propfan diameter, D, m (ft)	5.83 (19.1)	4.25 (14.0)	3.37 (11.1)
Propfan diam./fuselage diam.	0.97	1.13	1.38
Propfan rotational speed, N, rpm	799	1096	1384
Power required per propfan, P, kW (hp)	9517 (12,762)	5058 (6782)	3172 (4254)
Blade-passage frequency, f_b , Hz	133	183	231
Inboard tip clearance, r/D	0.4	1.3	0.3
Outboard tip clearance, r/D	1.8	2.7	---

The data in Table 1 also show the power required per propfan and indicate that it ranges from approximately 10 megawatts per propfan for the wide-body airplane to 3.2 megawatts for the small-diameter airplane. The table also lists the maximum takeoff gross weights and design ranges for the three airplanes. Typical numbers of passenger seats are given for mixed-class configurations for the wide-body and narrow-body airplanes; the small-diameter airplane would have 18 seats in a typical business/executive-jet arrangement.

Table 2 lists the values of performance parameters that are common to each of the three baseline study airplanes. The values in Table 2 were either derived as indicated above, or were specified as part of the study requirements. Figures 12, 13, and 14 show the three baseline study airplanes and illustrate the relative fuselage and propfan diameters, the placement of the propfans on the wings and the clearances between the fuselage and the propfans. Note that, although the design of the propfans and the installation on the aircraft is considered to be reasonably realistic, the airplane designs were not developed as a result of a detailed design study and thus are somewhat conceptual. However, the designs are considered realistic enough to provide suitable baseline aircraft for development and initial application of the analytical model.

Table 2.
PERFORMANCE PARAMETERS COMMON
TO EACH BASELINE STUDY AIRPLANE

Initial cruise altitude, m (ft)	9014.4 (30,000)
Cruise Mach number, M	0.80
Cruise airspeed, V_a , m/s (knots)	242.58 (471.6)
Speed of sound, c, m/s (knots)	303.23 (589.5)
Density ratio, ρ_0/ρ	2.6686
Number of propfan blades	10
Propfan tip rotational speed, V_{rot} , m/s (ft/s)	243.84 (800)
Propfan helical tip Mach number, M_{hel}	1.13
Propfan power loading, kW/D ² (SHP/D ²)	280 (35)
Propfan advance ratio, J	3.13
Propfan power coefficient, C_p	1.30
Propfan uninstalled net thrust coefficient, $C_{F_{n,u}}$	0.355
Propfan net propulsive efficiency, η_{net}	0.85

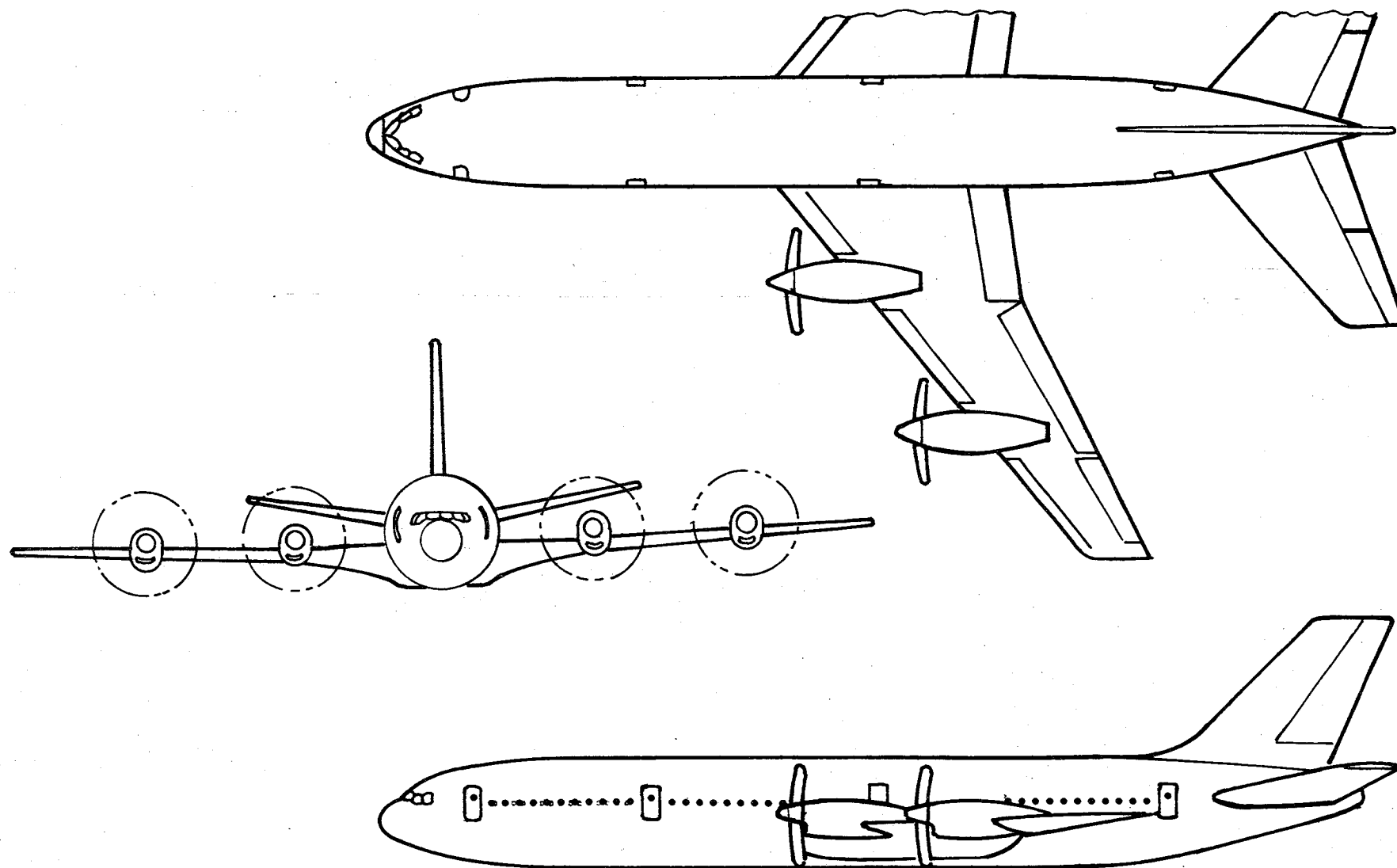


FIGURE 12. BASELINE WIDE-BODIED AIRPLANE

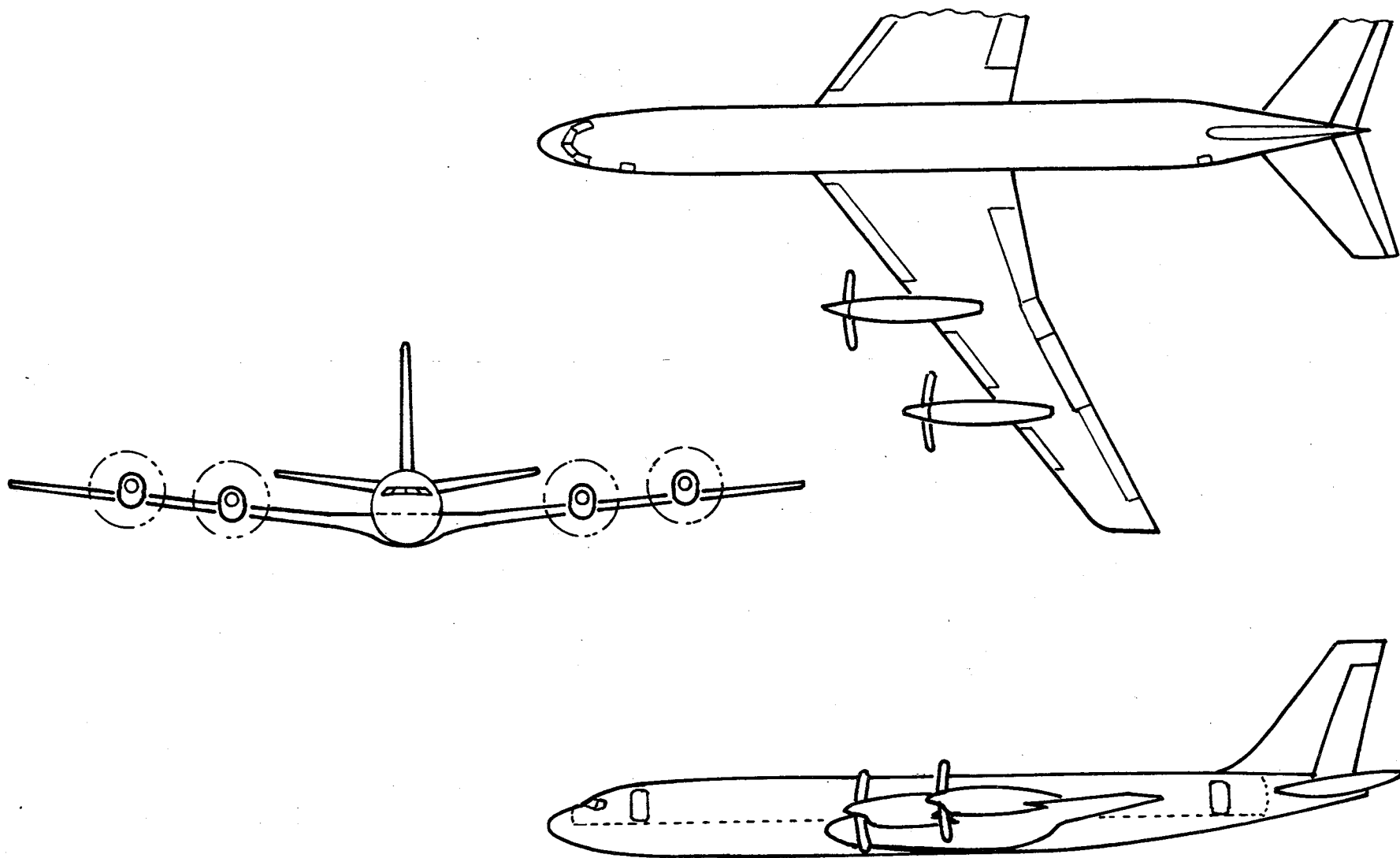


FIGURE 13. BASELINE NARROW-BODIED AIRPLANE

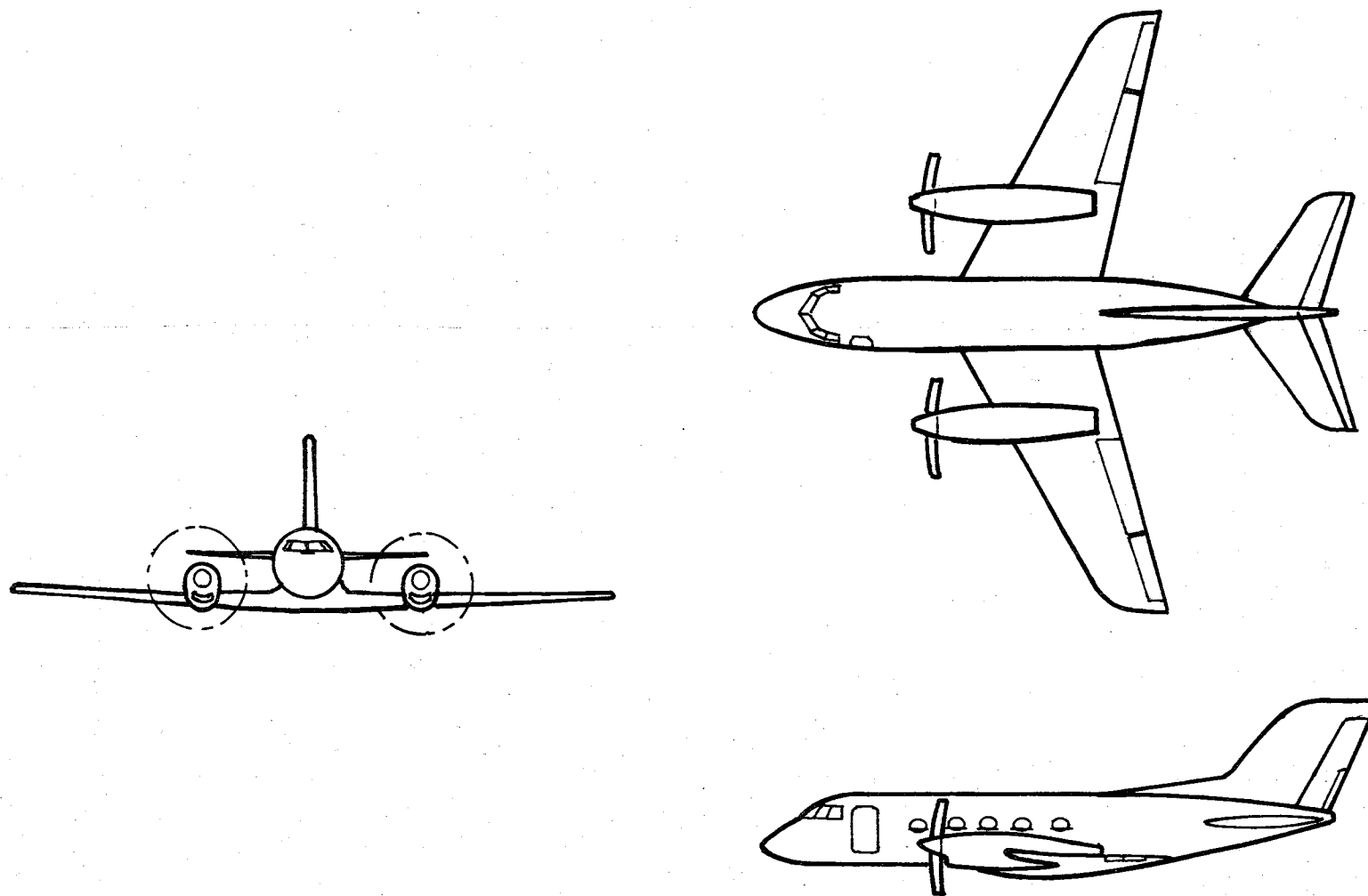


FIGURE 14. BASELINE SMALL-DIAMETER AIRPLANE

Figure 15 illustrates typical seat arrangements and cabin interior contours for the three study aircraft. The wide-body and narrow-body seating arrangements are fairly easy to define as there is little variation among commercial aircraft. The wide-body aircraft has two aisles in a first-class and coach-class configuration whereas the narrow-body aircraft has a single aisle.

Seating arrangements for the small-diameter fuselage are less easy to define as there are many configurations used in current business/executive jet aircraft. However, there will be a single aisle down the center of the aircraft, as shown in the fuselage cross-section.

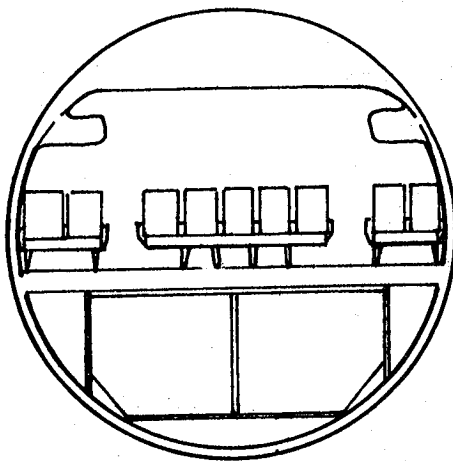
4.5 Baseline Fuselage Designs

4.5.1 General Considerations

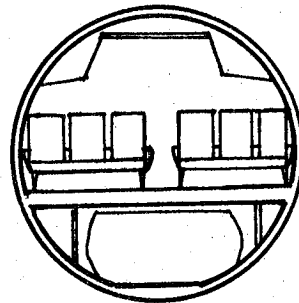
The fuselage structures of the three baseline aircraft are of conventional skin-stringer-frame construction, an example of which is given in Figure 16. The figure shows longitudinal stiffeners, or stringers, with hat sections and circumferential stiffeners, or frames, with zee sections. The frames are coupled to the skin by shear ties, and to the stringers by clips. Fail-safe straps or doublers are bonded to the skin at the frame locations to provide local reinforcing of the skin. These four structure elements -- skin, doubler, stringer, and frame -- are all taken into account in the descriptions of the baseline structures.

Other parameters to be considered are fuselage radius, cabin windows, and in-plane stresses in the skin. These stresses result from the cabin pressurization and fuselage bending

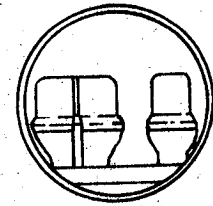
(a) CABIN CROSS-SECTION



WIDE-BODY



NARROW-BODY



SMALL BODY

(b) CABIN PLAN VIEW

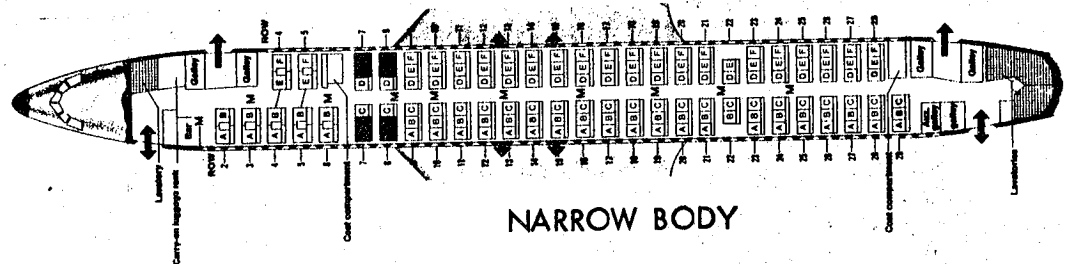
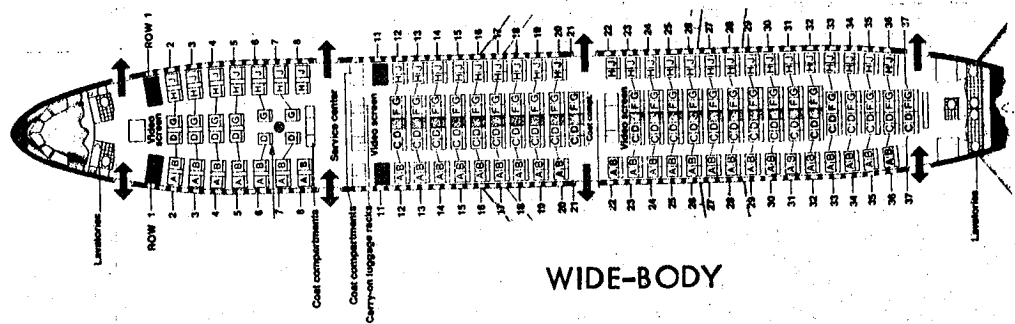


FIGURE 15. TYPICAL PASSENGER CABIN ARRANGEMENTS FOR THE STUDY AIRPLANES

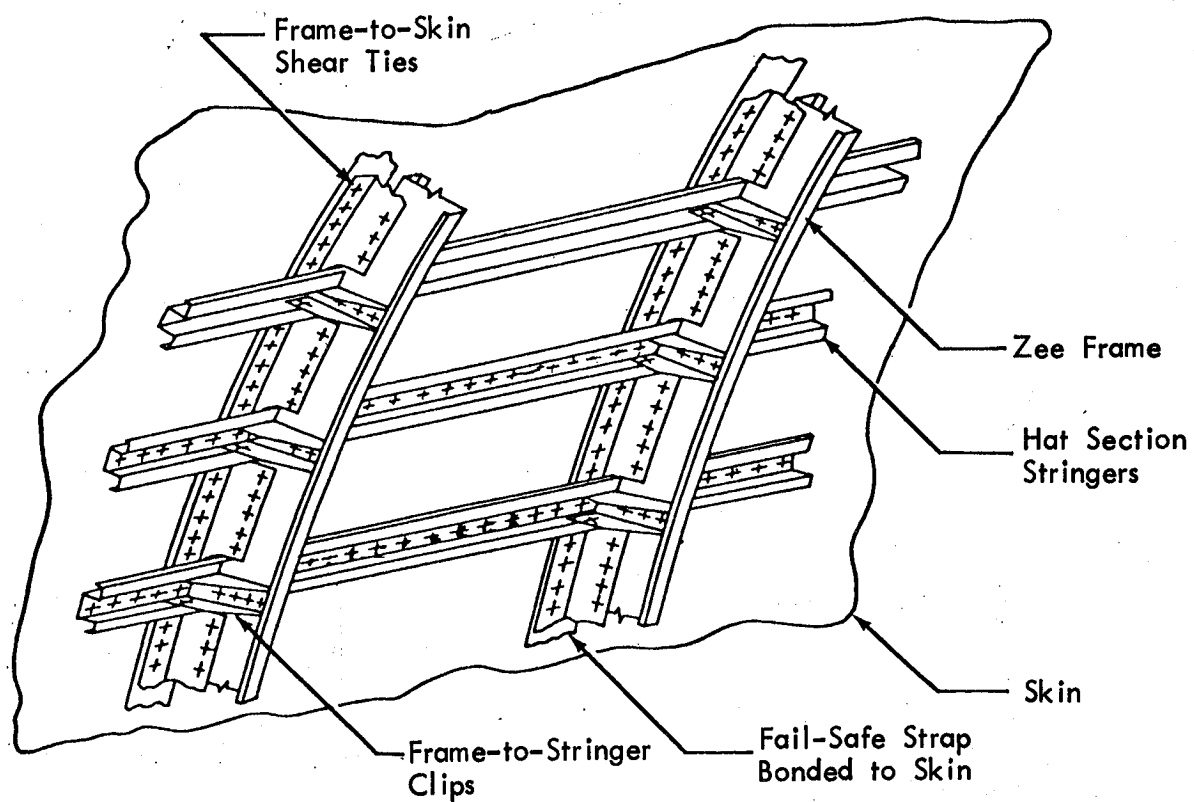


FIGURE 16. TYPICAL SKIN-STRINGER-FRAME CONSTRUCTION FOR CONVENTIONAL FUSELAGES

loads, and form a complicated distribution with tensile stresses on the upper portion of the fuselage and compressional stresses on the lower portion. An example of such a stress distribution is given in [29] for the Boeing 747.

4.5.2 Baseline Structures

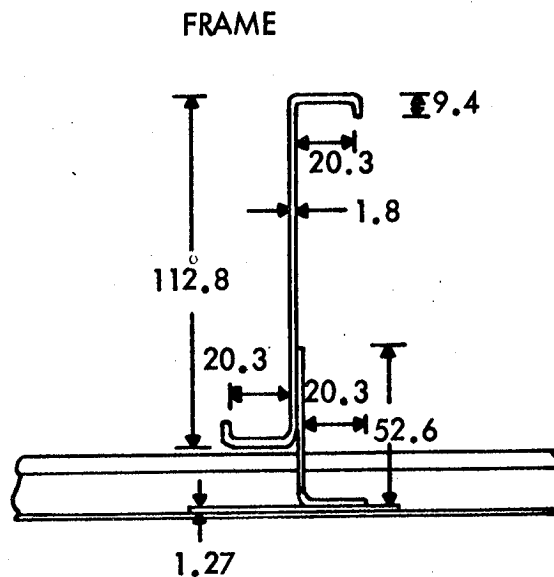
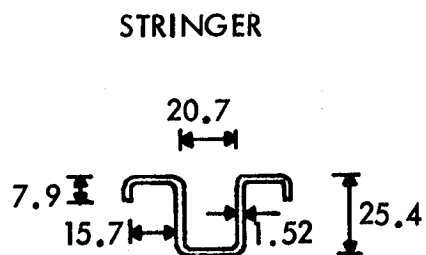
Baseline structures for the three study airplanes were defined on the basis of existing technology and typical characteristics of current-day aircraft of comparable size. Dimensions and shapes for the stringers, frames and doublers for the study aircraft are shown in Figures 17, 18, and 19 for the wide-body, narrow-body, and small-diameter fuselages respectively. All airplanes are assumed to have hat-section stringers. The two larger diameter fuselages have zee-section frames, and the small-diameter fuselage has cee-section frames. All fuselages are assumed to have doublers beneath the frames, although shear ties are included only in the wide-body fuselage. Skin thickness is assumed to be constant for the wide-body and small-diameter fuselages, but, since some aircraft have a skin whose thickness varies along the length of the cabin, a varying skin thickness was assumed for the narrow-body baseline structure.

Characteristics of the baseline fuselages, including skin thickness, frame and stringer spacing, cabin pressure differential, and material properties of the structure are listed in Table 3.

In order to reduce the complexity of the analytical model, the structure is assumed to be uniform in construction throughout the region above the cabin floor (acoustic power flow through

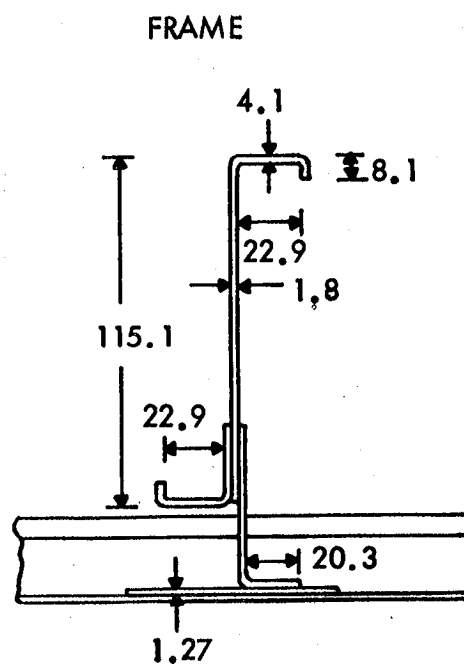
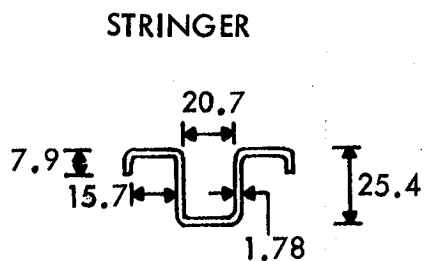
(a) FORWARD OF OUTBOARD PROPELLER

SKIN THICKNESS: 1.78 mm



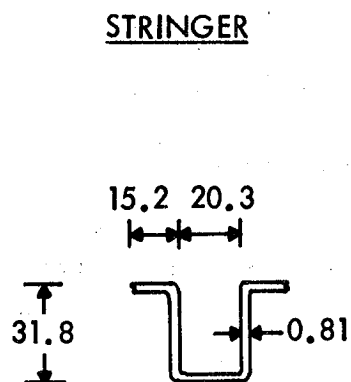
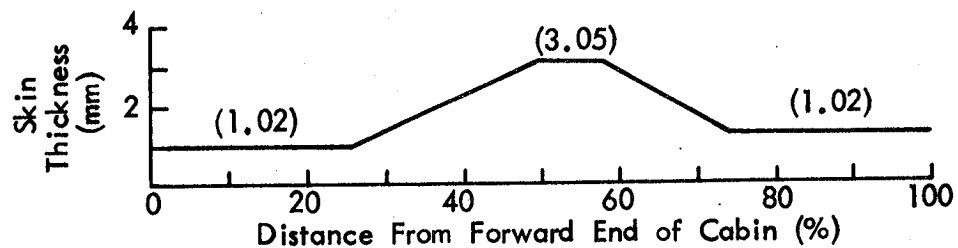
(b) AFT OF OUTBOARD PROPELLER

SKIN THICKNESS: 1.78 mm



All Dimensions in mm

FIGURE 17. STRUCTURAL DETAILS FOR BASELINE WIDE-BODY FUSELAGE



All Dimensions in mm

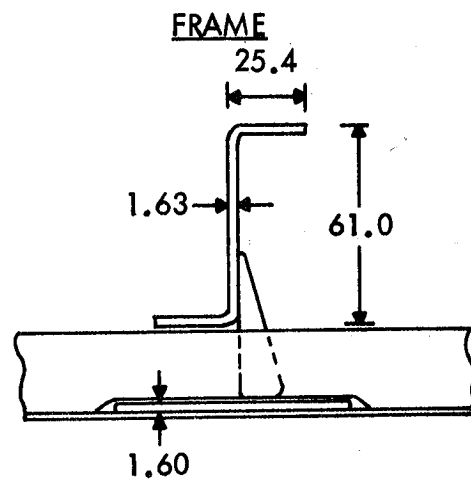
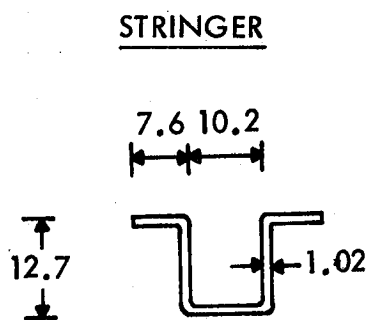


FIGURE 18. STRUCTURAL DETAILS FOR BASELINE NARROW-BODY FUSELAGE

SKIN THICKNESS = 1.02 mm



All Dimensions in mm

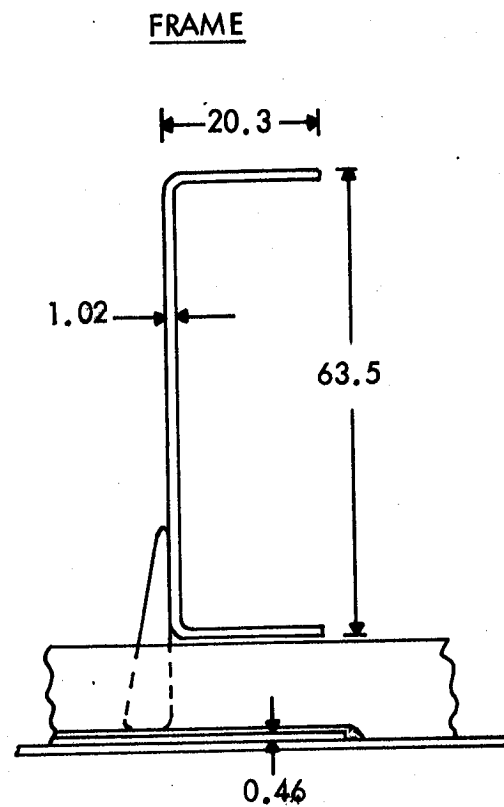


FIGURE 19. STRUCTURAL DETAILS FOR BASELINE
SMALL DIAMETER FUSELAGE

TABLE 3
CHARACTERISTICS OF BASELINE FUSELAGES

AIRPLANE		WIDE BODY	NARROW BODY	SMALL DIAMETER
FUSELAGE DIAMETER	(m)	6.02	3.76	2.44
CABIN LENGTH	(m)	41.45	34.00	10.06
CABIN WIDTH	(m)	5.72	3.55	2.18
CABIN HEIGHT	(m)	2.44	2.31	1.76
SKIN THICKNESS	(mm)	1.78	1.02 to 3.05	1.02
FRAME SPACING	(m)	0.508	0.508	0.330
STRINGER SPACING	(m)	0.183	0.229	0.127
CABIN PRESSURE DIFFERENTIAL	(N/m ²)	5.515×10^5	5.515×10^5	5.515×10^5
MATERIAL		Aluminum	Aluminum	Aluminum
YOUNG'S MODULUS E	(N/m ²)	7.2×10^{10}	7.2×10^{10}	7.2×10^{10}
DENSITY	(kg/m ³)	2770	2770	2770

the structure beneath the floor is assumed to be negligible in the analytical model). This means that the analytical model does not take into account circumferential variations in skin thickness, stringer spacing, or frame depth. Furthermore, the model excludes windows and window cut-outs. A more-detailed representation of the sidewall structure in the analytical model is not feasible within this study.

4.5.3 In-plane loads

The fuselage structure is subjected to in-plane tensile/compressional loads N_x and N_y , in the axial and circumferential directions respectively, and to shear loads N_{xy} . The two main contributors to these loads are pressurization and body-bending forces. If the fuselage radius is R and the pressure differential is Δp , then the cabin pressurization loads introduce contributions of $0.5 R \cdot \Delta p$ and $R \cdot \Delta p$ to N_x and N_y respectively, the shear load contribution being zero. In all calculations the fuselage pressure differential was chosen to be 55.1kPa (8 p.s.i.). Body-bending loads vary with airplane flight conditions and with axial and circumferential location on the fuselage. Also, they will be affected by the weight of the aircraft. At some locations the loads will be positive (tensile) whereas at other locations they will be negative (compressional).

Because of the variation in the magnitude of the body-bending loads, the influence of these loads on structural response has been neglected in the present analytical model. Pressurization loads have been included as being indicative of an average value throughout the fuselage structure. In any case, results presented in Section 6.0 indicate that in-plane loads are not

important at low frequencies, which are critical from a noise control point-of-view, because of the effects of the frames and stringers.

Circumferential pressurization stresses in the fuselage skin will be relieved to some extent by the frames and doublers. Typical average values for the percentage of nominal loop stress accepted by the skin lie in the range of 75 to 80%. However, the analytical model assumes that the full pressurization loads are carried by the skin since the effect on calculated panel resonance frequencies is small.

4.5.4 Noise Control Treatment

Two properties of the noise control treatment have to be defined for the baseline airplanes. The first is the transmission coefficient for the sidewall treatment and the second is the acoustic absorption in the cabin.

The baseline transmission loss spectrum was obtained from a review of empirical data for sidewall treatments typical of those in present-day use. These sidewalls consist mainly of glass fiber batts and a trim panel. In some cases damping tape may be used and in other cases lead-impregnated vinyl sheets may be installed, but such items are usually introduced for specific problems. These special treatments are excluded from the baseline sidewall.

Much of the suitable transmission loss data is associated with tests in laboratory facilities where the fuselage structure is represented by a stiffened flat or curved panel, and where the transmission loss of interest is the insertion loss provided by the add-on treatment. It is this insertion loss which is of

interest to the present study because the noise transmission of the basic fuselage structure is calculated by the analytical model.

The baseline sidewall is shown diagrammatically in Figure 20. It is assumed that acoustic insulation material is installed over the stringers and between the frames. Then a second layer of the material is placed as a continuous blanket over the top of the frames. Finally, the trim panel is installed such that there is a gap between the trim and the frame cap, the gap being filled by the glass-fiber batt. The glass fiber material is assumed to have a density of 9.61 kg/m^3 (0.6 lb/ft^3) and the trim panel a surface density of 1.76 kg/m^2 (0.3 lb/ft^2). The total thickness of the batts is assumed to be 10.2 cm (4 inches) for all three study airplanes. In the case of the narrow-body and small-diameter designs, the region between fuselage skin panel and trim panel will be completely filled with the glass fiber material. The wide-body airplane will have an airgap between the batts. Installations of this type are described in [30] for a small-diameter (Gulfstream II) airplane, in [31] for a narrow-body (Boeing 727) airplane and in [32] for a wide-body (DC-10) airplane. The associated insertion loss, or additional transmission loss, associated with the baseline installation is shown in Figure 20. The curve is based on data such as is given in [30] and [33].

Acoustic absorption in the passenger cabin is provided by the sidewall trim panels (including the ceiling), carpet, seats, and other surfaces. Absorption data for materials used in air-

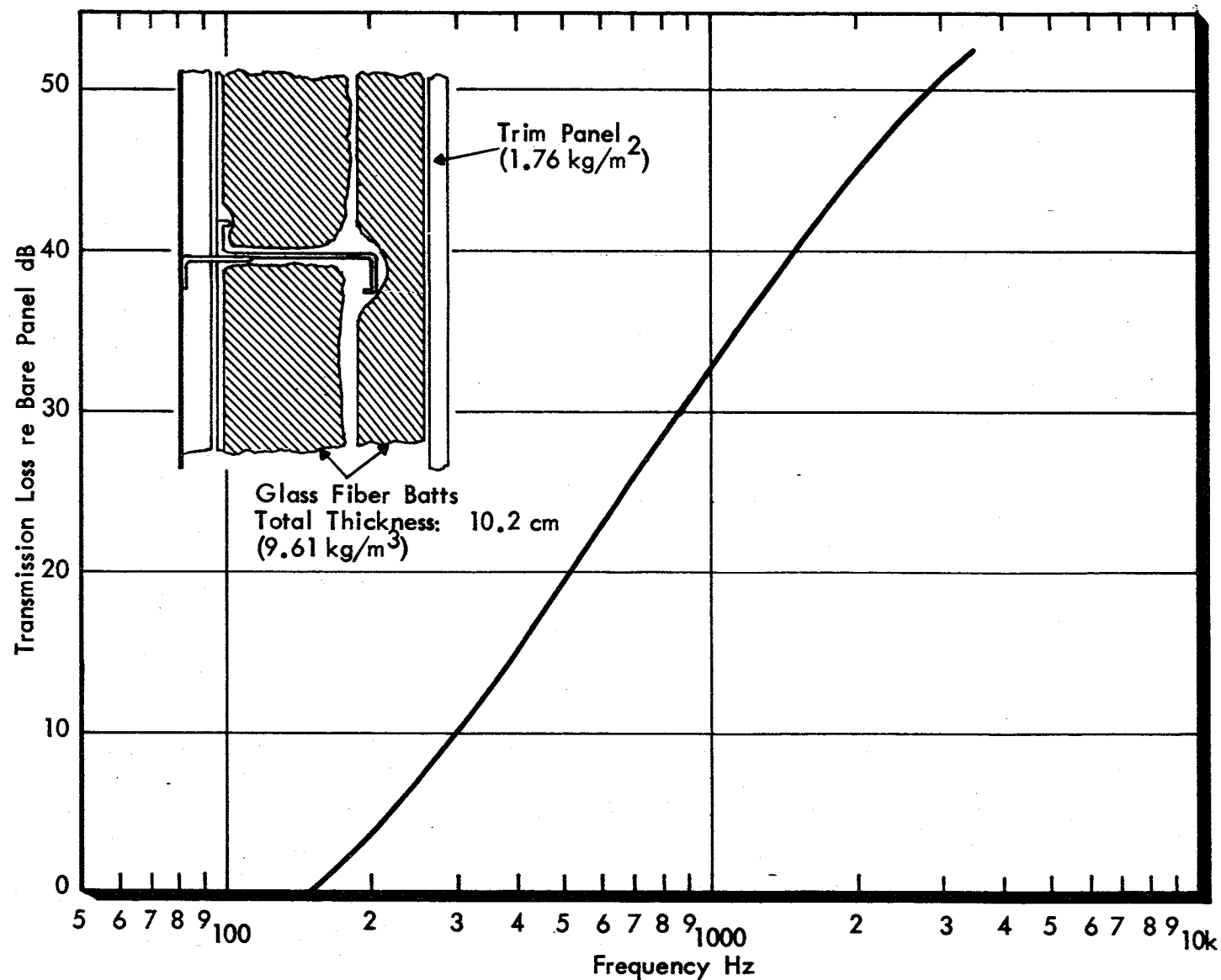


FIGURE 20. BASELINE TRANSMISSION LOSS FOR ADD-ON SIDEWALL

craft interiors are not readily available but estimates can be made of average absorption coefficients, or corresponding absorption units, provided by the different items. Estimated absorption coefficient spectra for typical sidewall, carpets, and seats are given in [34], where the coefficients for the seats are based on typical seat distributions as a function of wall area. The absorption coefficients in [34] were obtained from laboratory test data for the individual items rather than for measurements in furnished aircraft cabins. However, there are some unpublished data for measured space-averaged absorption coefficients in furnished cabins and these data provide the band of data presented in Figure 21.

Using the data in [34] and the band of measured data in Figure 21, a series of component absorption coefficient spectra were constructed and these are shown in Figure 22. The component spectra were chosen so that the space-averaged absorption coefficient $\bar{\alpha}$, for a typical airplane cabin, would lie roughly at the upper boundary of the measured data in Figure 21. The calculated $\bar{\alpha}$ spectrum is shown in Figure 21 for comparison with the measured values. The main difference between the data in Figure 22 and the data in [34], is in the assumed absorption coefficient for the sidewall trim. This spectrum was modified to incorporate results of Goss [30] and to bring the composite spectrum into agreement with the measured values of $\bar{\alpha}$.

Also shown in Figure 21 is an absorption coefficient spectrum based on reverberation measurements in a bare fuselage [35]. Since the absorption coefficient was obtained in this case using conventional reverberation equations the value includes the effect of noise transmission out of the fuselage interior.

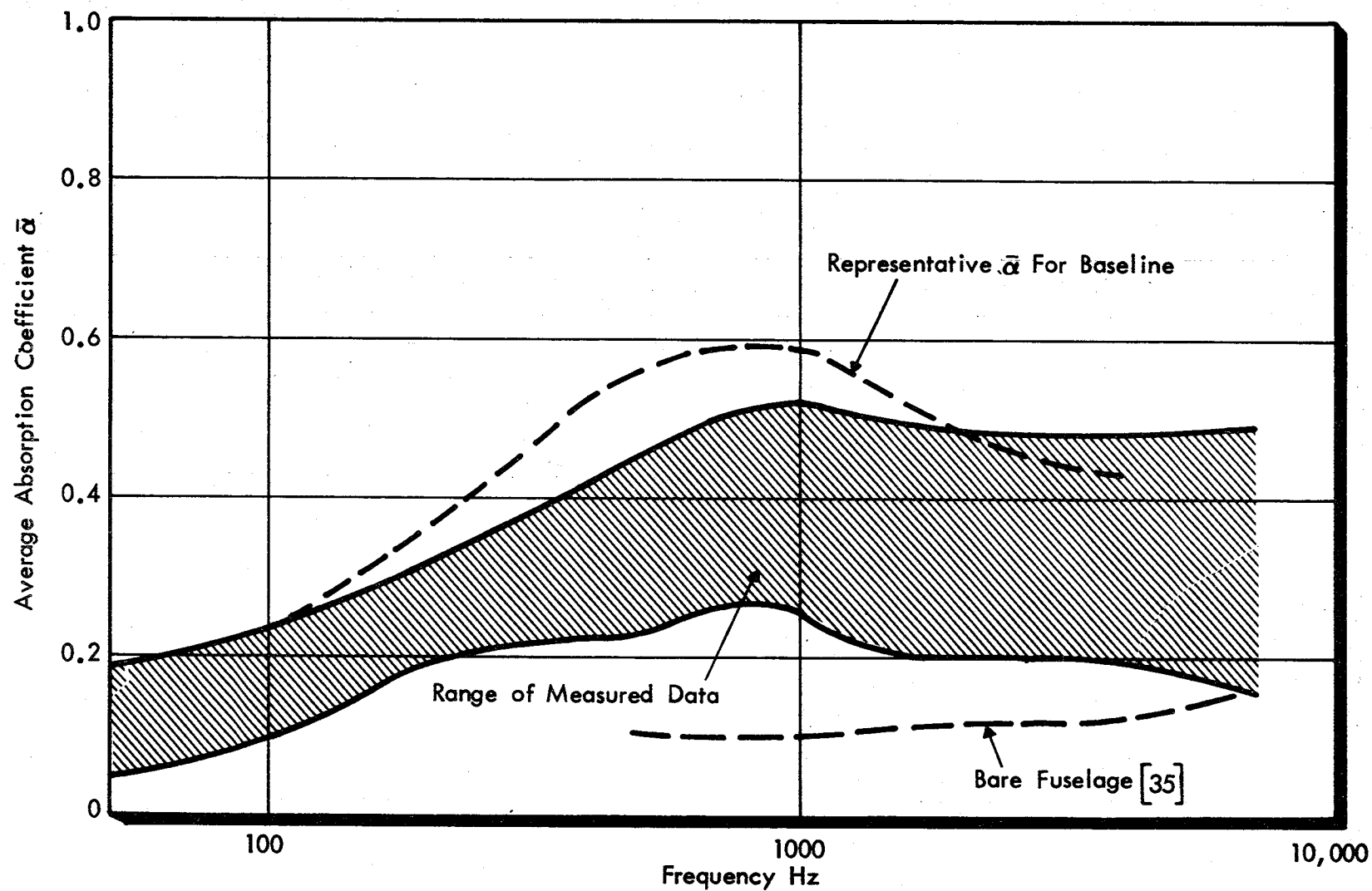


FIGURE 21. COMPARISON OF MEASURED AND MODEL ABSORPTION COEFFICIENTS

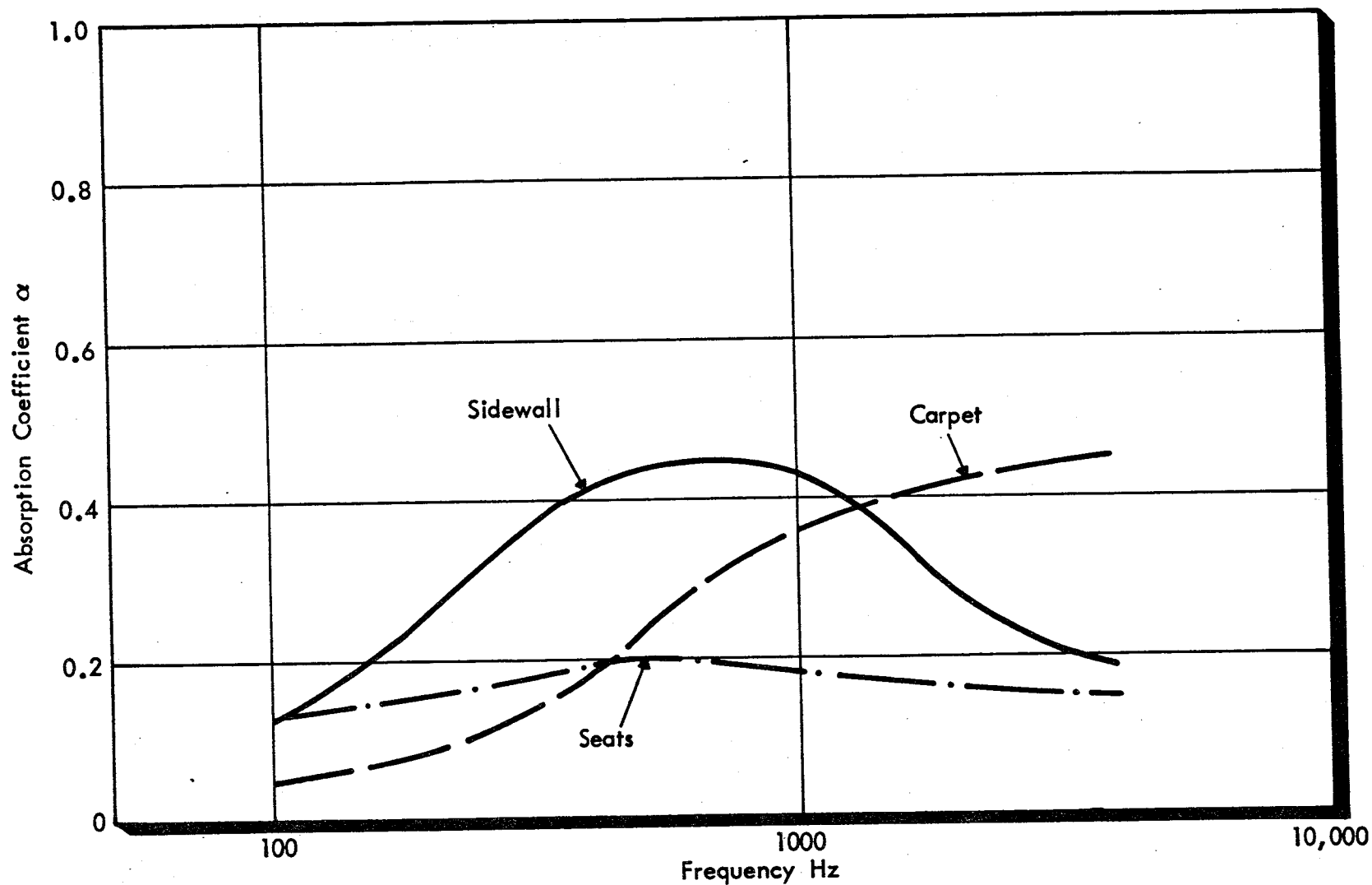


FIGURE 22. SOUND ABSORPTION SPECTRA ASSUMED FOR FURNISHING COMPONENTS

A typical value for the absorption coefficient for bare aluminum, excluding the effects of noise transmission is 0.05, as was used in [4].

4.6 Propeller Noise Field

In the development of the analytical model it was shown, in Section 3.3, that the inhomogeneous pressure field generated by the propeller can be described in terms of the spatial distribution of the pressure amplitude or level, the spatial decay of the coherence function, and the trace velocities of the pressure field in the axial and circumferential directions. This section will describe briefly the characteristics of the acoustic fields used to represent the exterior pressure fields on the three study aircraft.

The basis for calculation of the spatial distribution of the pressure level is the prediction procedure developed by Hamilton Standard [6]. Typical free-field directivity curves [6] for the near-field pressures are shown in Figure 23 for a range of tip clearances similar to those for the study airplanes. The available data refer to an 8-blade propeller with a tip rotational Mach number of 0.7, but the general trend of the data can be used for the selected 10-blade propeller with a tip rotational Mach number of 0.8.

Predicted variation of the overall sound level along the fuselage exteriors of the three baseline aircraft are shown in Figure 24. In calculating these surface pressure distributions, it was assumed that pressure doubling (+6dB) occurred in the neighborhood of the plane of rotation of the propellers and that the pressure increase was +3dB elsewhere. The curves in

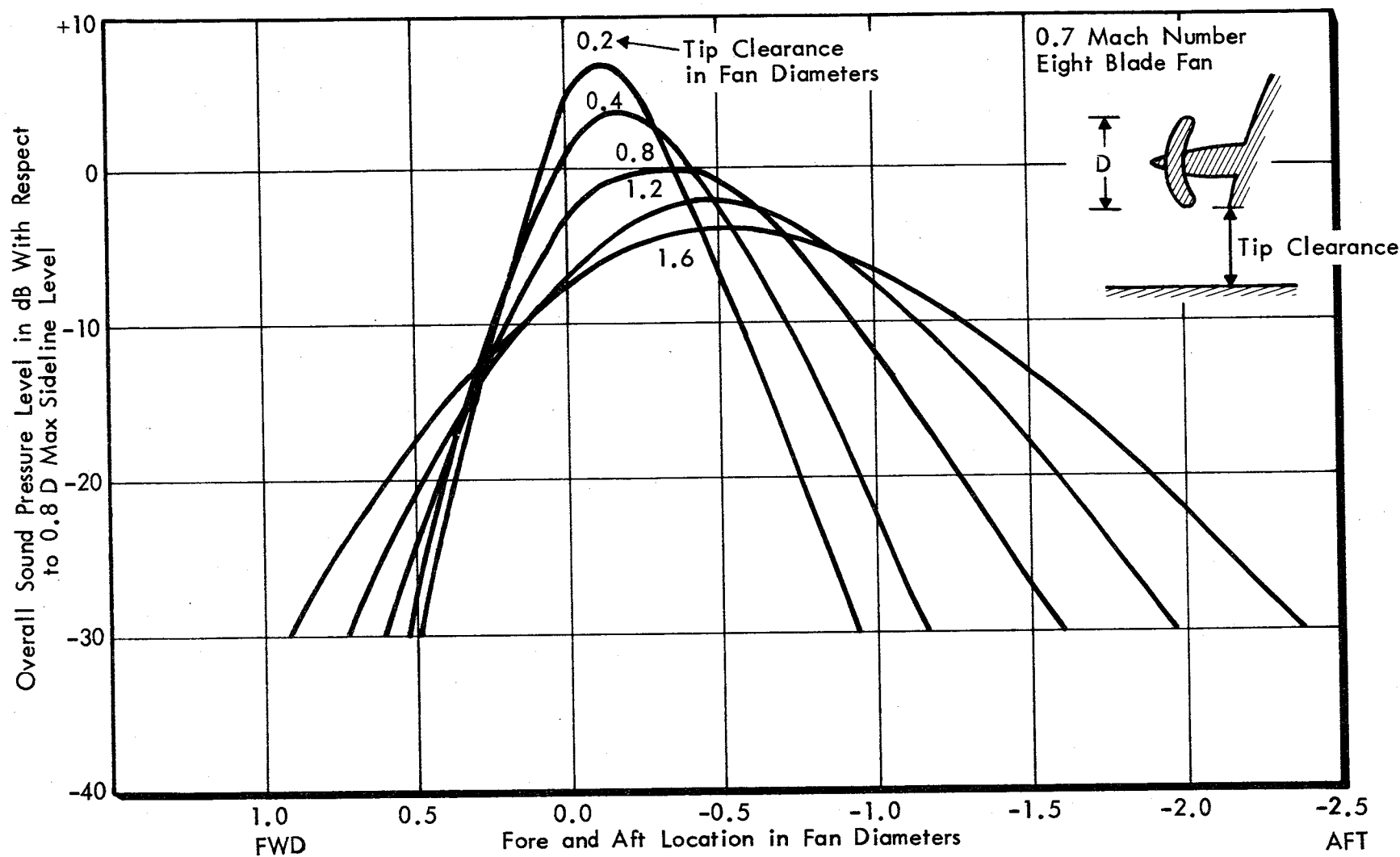


FIGURE 23. DIRECTIVITY AS A FUNCTION OF TIP CLEARANCE

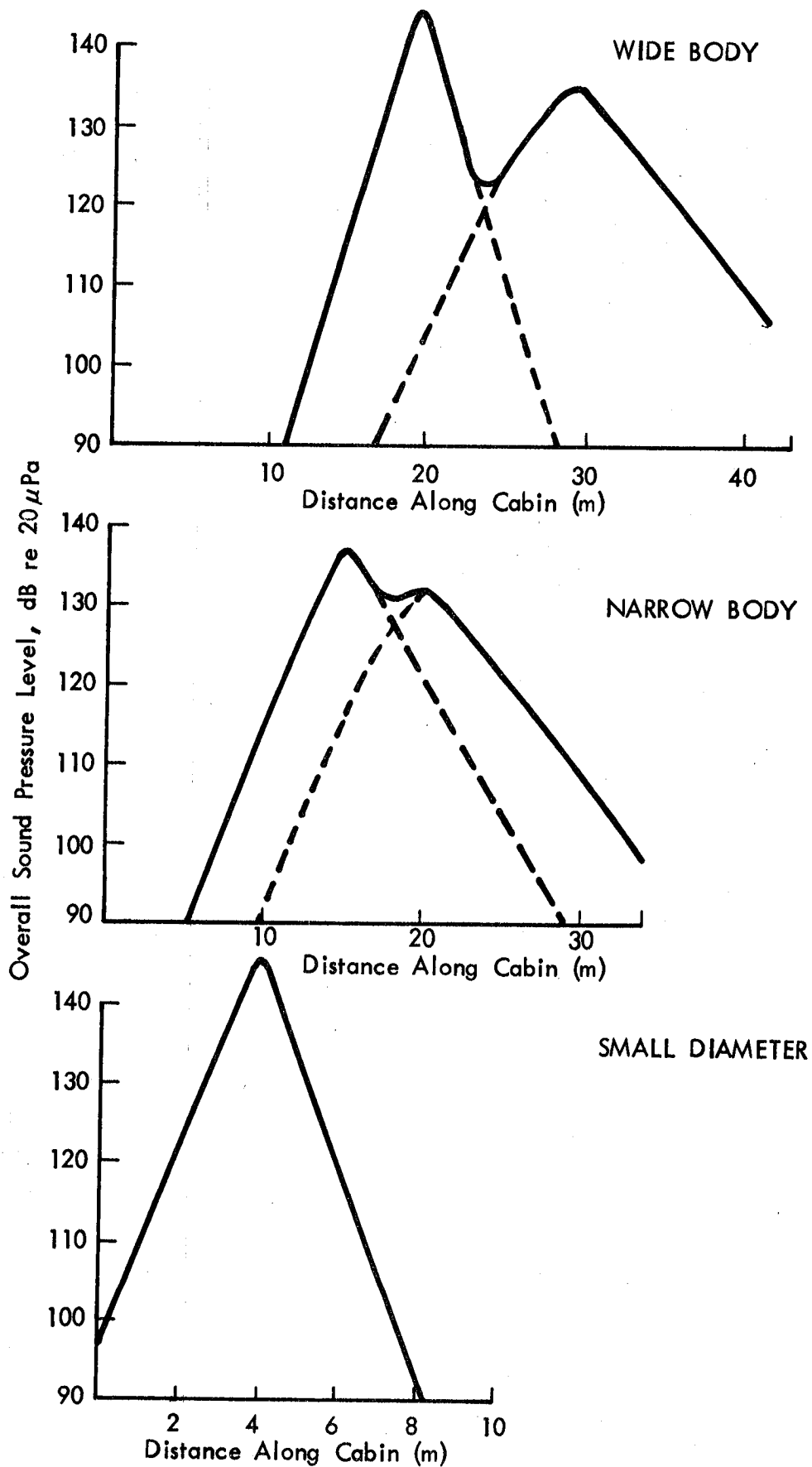


FIGURE 24. VARIATION OF EXTERNAL SOUND PRESSURE LEVEL ALONG THE CABIN

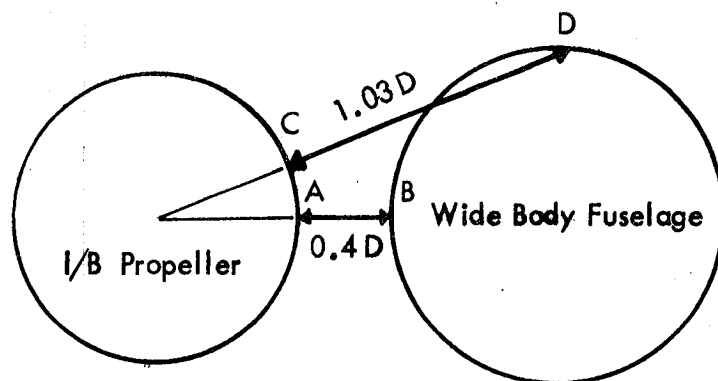
Figure 24 for the wide-body and narrow-body airplanes show the double-hump characteristic associated with the two propellers on each side of the fuselage. The small-diameter design shows only a single peak as there is only one propeller on each wing. The predicted peak pressure level is a function of propeller efficiency, tip rotational speed, cruise Mach number, tip clearance, altitude and number of blades. Since all these parameters, with the exception of tip clearance, are the same for all the study airplanes, the peak overall sound pressure levels shown in Figure 24 differs from airplane to airplane as a function of tip clearance only. The peak level is highest (146dB) on the small-diameter fuselage, where the tip clearance is smallest (see Table 1) and is lowest (137dB) on the narrow-body airplane where the tip clearance is greatest.

The data in Figure 24 show the rapid decrease in sound level as distance increases from a region of peak level. This spatial decay provides values for amplitude decay parameter a_x , these values varying with position along the fuselage.

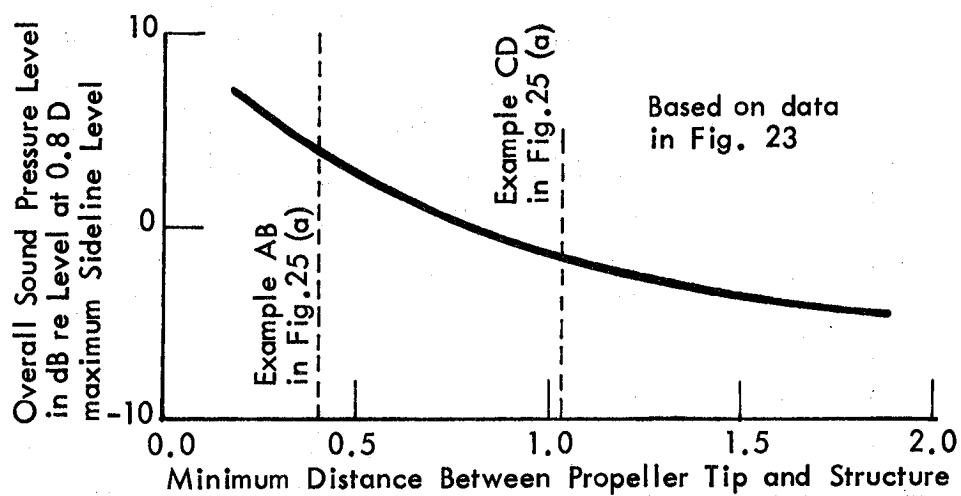
The spatial decay of sound pressure level in the circumferential direction was estimated by first calculating the free-field distribution using Figure 25(b). Then the influence of the fuselage structure was taken into account by adding 6 dB at the position of minimum tip clearance (location B in Figure 25(a)) decreasing to 3 dB at locations on the vertical centerline, for example, location D in Figure 25(a).

The analytical study was required to consider three different spectrum shapes for the excitation field on each of the study airplanes. These spectra, which refer to the relative levels of the different harmonic components of the propeller noise field, are shown in Figure 26. The first spectrum identified

(a)



(b)



(c)

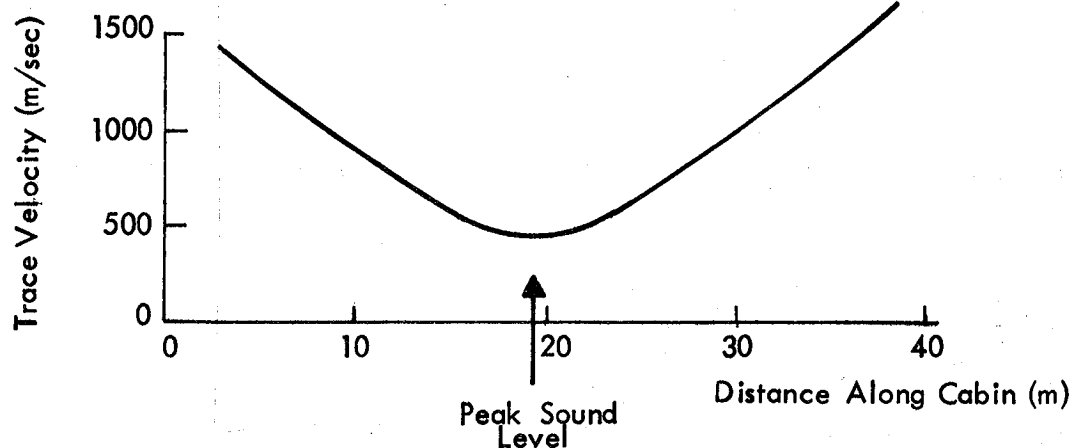


FIGURE 25. CIRCUMFERENTIAL TRACE VELOCITY AND AMPLITUDE VARIATION FOR INBOARD PROPELLER OF WIDE BODY AIRPLANE

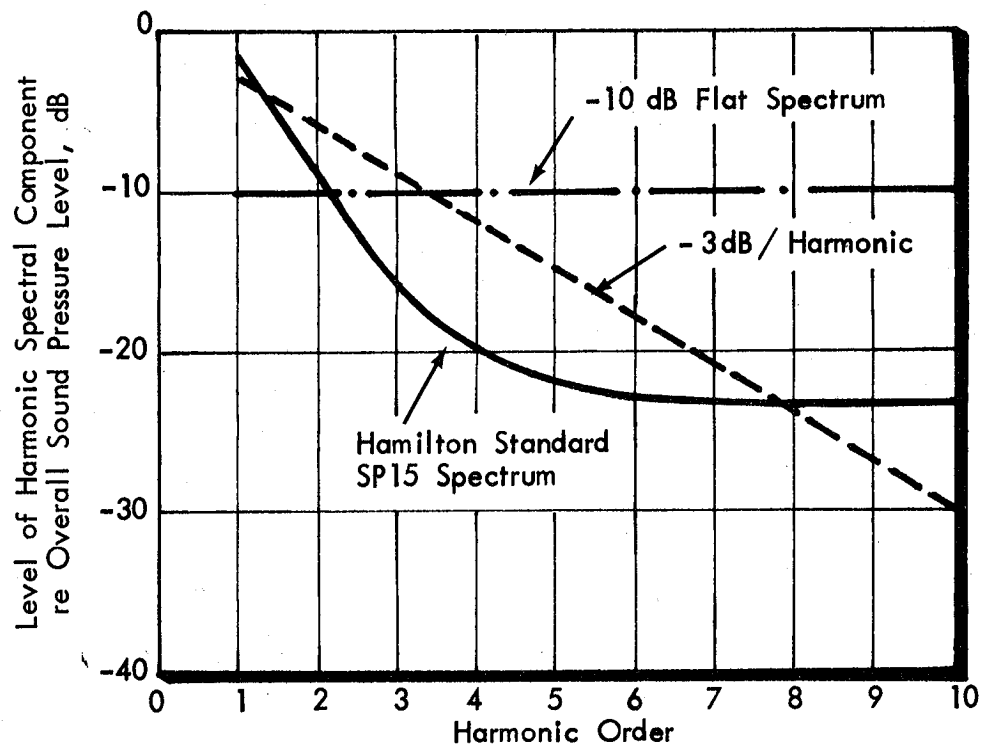


FIGURE 26. HARMONIC LEVELS OF EXTERNAL SOUND FIELD

as the Hamilton Standard SP15 Spectrum is obtained from [6]. The other two spectra show harmonic levels falling off much more slowly as harmonic order increases; in one case the change in harmonic level being -3dB per harmonic and in the other case all the harmonic levels are equal. For present purposes it was assumed that the constant harmonic level specification was applied to the ten lowest order harmonics only.

Pressure field coherence and trace (or phase) velocity were not covered by the Hamilton Standard prediction procedure [6], and other means had to be used to obtain the required information. One source of information was the data analysis [8, 9] performed on measurements from a test program on an Aero Commander airplane. The analysis included coherence and trace velocity results, although the test conditions (tip clearance approximately 0.05D, forward speed less than 40 m/s (120 ft/sec)) differed considerably from those associated with the study airplanes.

The Aero Commander data [9] show that, where there is forward velocity of the airplane, the decay of the pressure field coherence for the low order harmonics is very slow in both the longitudinal and circumferential directions. This is to be expected when the excitation consists of a series of discrete frequency components. Thus, a similar slow decay of pressure field coherence was assumed for the study airplanes, the coherence decay parameters c_x and c_y of Eq. (29) ($c \equiv (c_x, c_y)$) each being given a value of 0.01.

The trace velocity in the longitudinal direction was estimated on the basis of acoustic wave propagation from an effective

source location. The source was located at 70% of the propeller radius, in the effective plane of rotation of the propeller, as shown in Figure 27. The effective plane of rotation was used to take into account the forward motion of the airplane. Figure 27 shows the construction of the trace velocity relationship for the inboard propeller of the wide-body airplane. The net trace velocity for the pressure field includes the influence of flight velocity so that the trace velocity is subsonic on the forward region of the fuselage and about twice the speed of sound on the aft region. Close to the plane of rotation of the propeller, the acoustic field is modeled as plane waves incident normally to the fuselage, so that the axial trace velocity tends to an infinite value.

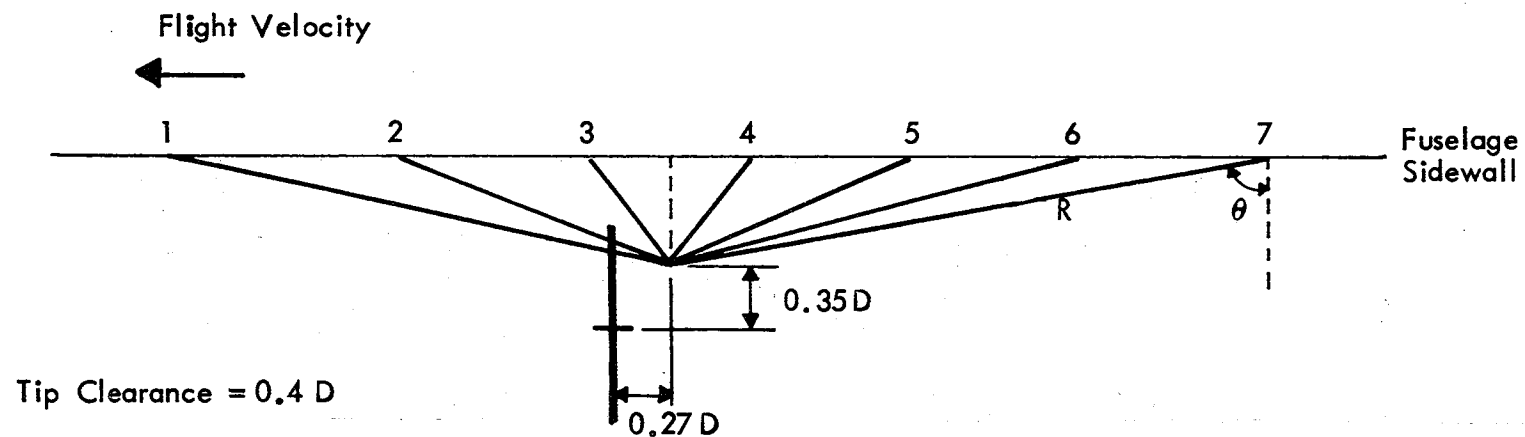
In the circumferential direction the trace velocity is obtained by assuming that the pressure field rotates with the propeller. Thus, for a constant tip rotational speed, the greater the tip clearance, the higher will be the circumferential trace velocity. The value of the trace velocity is supersonic for all conditions of interest, and, because of the model chosen, the circumferential velocity increases with distance from the propeller plane R, as is shown in Figure 25(c) for the inboard propeller of the wide-body airplane. The circumferential trace velocity in the region of the propeller plane (peak levels) is predicted from

$$U_y = \pi D f_o (1 + 2r/D)$$

where r/D is the tip clearance in fan diameters and f_o the blade passage frequency. Away from the propeller plane, U_y is calculated from

$$U_y = 2\pi f_o R$$

where R is identified in Figure 27 for the 7th element.



$$\text{Trace Velocity} = 242.6 \pm \frac{303.2}{\sin \theta} \quad (\text{m/sec})$$

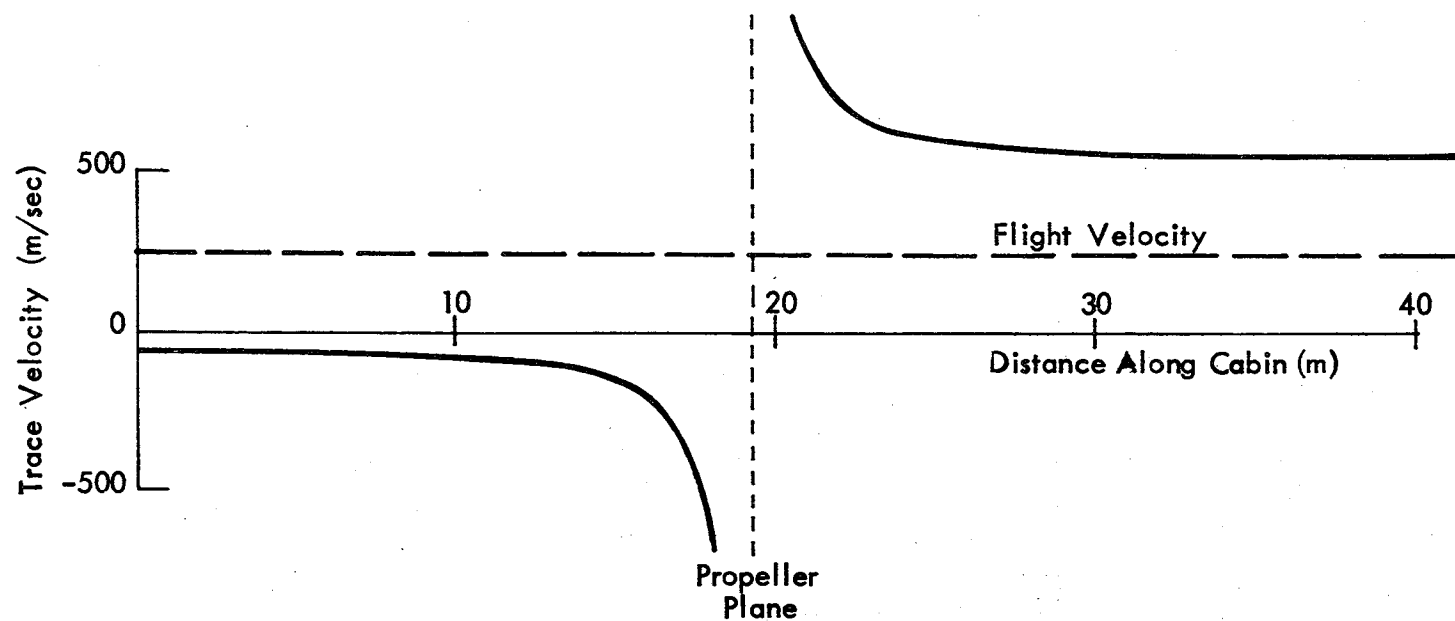


FIGURE 27. LONGITUDINAL TRACE VELOCITY FOR INBOARD PROPELLER OF WIDE BODY AIRPLANE

5.0 MODEL OF STRUCTURE

Calculation of the structural response to the propeller excitation pressure field requires the calculation or determination of several functions such as joint acceptance, modal density, radiation ratio and structural damping. These functions can, in turn, be determined only after a model has been constructed for the fuselage structure. As was discussed in Section 4, one of the basic assumptions about the baseline fuselage structure was that the construction would be the conventional skin-stringer-frame type used in current day aircraft. This section describes the steps taken to describe such a structure in a form suitable for computation in the analytical acoustic model presented in Section 3. The discussion centers on the resonant structural response, since, as will be shown in Section 6, the power flow associated with resonant response is significantly greater than that due to non-resonant response.

5.1 General Representation

The analytical formulation in Section 3.2.2 gives the total power flow from the external excitation field through the sidewall structure into the interior, and, in the process, predicts a homogeneous, average level for the structural response. To allow for non-homogeneous spatial distributions of the external pressure, the structural response and the interior noise levels, it is necessary to divide the fuselage structure into several segments along the fuselage length.

Then the total resonant power flow equation for N structural elements can be written in the approximated form

$$W_{in}(\omega_b) = \sum_{j=1}^N \frac{2\pi A_j \rho_i c_i}{\omega_b \mu_j^2} \langle p_{xo}^2(\omega_b) \rangle_j \frac{n_{r,j}(\omega_b)}{\bar{n}_{r,j}} \langle j_r^2(\omega_b) \rangle_j P_j \langle \sigma_{rad} \rangle_j \quad (74)$$

Eq. (74) is obtained by substitution of Eq. (60) into Eq. (51) and by replacement of the modal mass M_r by the resulting value appropriate to sinusoidal structural modes,

$$\text{i.e.} \quad M_r = \frac{\mu A}{4} \quad (75)$$

where A is the structural area and μ is the surface density. Eq. (74) applies to the frequency regime where structure and receiving cavity have sufficiently high values for the modal overlap. The summation is performed over structural elements j.

The choice of the size and number of the structural elements is influenced by the following points.

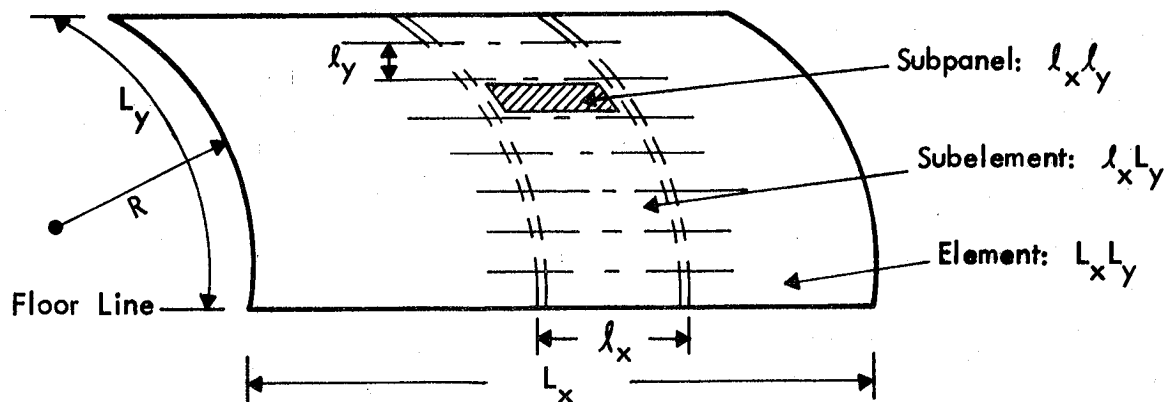
- (i) The element dimensions should be large enough that the amplitude of the external pressure field decays by at least 10 dB within the element.
- (ii) The elements chosen should have structural wave number-frequency distributions characteristic of the detailed overall fuselage modes.

- (iii) The total power flow into the interior must not depend on the sizes of the elements chosen.

The fuselage structure is idealized so that each structural element is assumed to be part of a pressurized cylinder, i.e. a cylindrical plate of uniform thickness with uniformly spaced ring stiffeners (or frames) and stringers (Figure 28). It is assumed that no power flows into the interior from below the cabin floor so that the element is not a complete cylinder. Furthermore, when calculating resonance frequencies, it is assumed that the structural element has clamped boundaries. The structural parameters used to describe the element will vary according to the wavelengths and frequencies of the modes of vibration [36].

At low frequencies, where the structural modal wavelengths, both axially and circumferentially, are greater than the frame and stringer separation distances respectively, both frames and stringers may be 'smeared-out' orthotropically over the skin surface. The frequency equation, derived by Mikulas and McElman [25] and presented in Figure 5 of Section 3.8.1 (with the addition of a term due to pressurization), was found during study calculations, to give reasonable estimates for the resonance frequencies of a simply-supported ring stiffened cylinder [36]. Mikulas' equation was then used for the resonance frequencies of an element of a stiffened cylinder with edges clamped by using the following changes and approximations:

- (1) For axial mode order m , the simply-supported wavelength is replaced by the smaller clamped-clamped wavelength [37], and m is replaced by $(m + 0.5)/1.05$



l_x = Frame Pitch

l_y = Stringer Pitch

R = Radius of Curvature

FIGURE 28. REPRESENTATION OF FUSELAGE STRUCTURAL ELEMENT

- (ii) For a complete cylinder, n is the number of circumferential full wavelengths. In this analysis, n is the number of circumferential half wavelengths, and

$$n \text{ is replaced by } \frac{1}{2} (n + 0.5)/1.05$$

- (iii) The ratio of circumferential to axial wavenumbers becomes

$$\delta = \frac{k_n R}{k_m R} = \frac{L_x (n + 0.5)}{L_y (m + 0.5)}$$

For modes of low order m in the axial direction and low order n in the circumferential direction, the resonance frequency equation is dominated by the membrane stiffness term due to curvature. Then, as n increases, the ring bending stiffness term becomes dominant. Mikulas' equation with frames and stringers represented as 'smeared-out' masses and stiffness, therefore covers regions I and II defined by Hu et al [36]. The modal density is dependent on both bending and membrane stiffnesses and is not very sensitive to changes in frame bending stiffness alone.

As frequency increases, the axial half-wavelength of the modes becomes less than the spacing between the frames, and the frame motion becomes small compared to the motion of the panel between the frames. Inclusion of the frame stiffness now results in overestimates of the panel resonance frequencies. Thus, in this mid-frequency region, the frame stiffness and mass are omitted from the analytical model, and only the stringers are 'smeared-out' over the surface. Mikulas' equations are again used to calculate the modal frequencies.

In the high frequency region, both the axial and circumferential half-wavelengths are less than the spacing between frames and stringers respectively, and subpanel resonances occur. Only the skin stiffness and mass are included now in the analytical model, as the panel motion is now effectively independent of the frames and stringers.

The frequencies at which the structural parameters are changed are given by

- (i) The minimum value of the resonance frequency of the subelement, of size ($l_x l_y$), clamped along two adjacent frames, for any circumferential mode order n with half-wavelengths greater than the stringer pitch, using (stringer + skin) structural parameters, and
- (ii) The fundamental frequency of subpanel with clamped edges, whose size ($l_x l_y$) is given by (frame pitch \times stringer pitch), using skin structural parameters only.

The first of the above frequencies defines the boundary between low and intermediate frequency regimes in the structural modeling, and the second frequency is the boundary between the intermediate and high frequency regimes. It should be noted that these panel sizes are used only in defining the frequency regimes for the structural modeling and are not used in calculating structural response. In calculating panel response, panel dimensions $L_x L_y$ are always used.

5.2 Structural Representations

The factors to be considered in selecting the size of the structural elements were given in Section 5.1. The discussion in this section identifies those parameters which are influenced by element area while Sections 5.3 to 5.5 investigate these parameters in more detail with the objective of choosing a minimum element size while maintaining the accuracy of the response calculation.

Empirical evidence suggests that, at low frequencies, the element size should be much larger than the frame and stringer spacings. For example, vibration data for a Boeing 737 fuselage structure [38] exposed to boundary layer and jet noise excitation show that acceleration coherence can remain high over several adjacent panels (see Figure 29). This is true even though the coherence coefficient of the excitation pressure field decays much more rapidly [38] than it does for the propeller pressure field considered in the present study.

In the circumferential direction, the coherence coefficient for propeller noise maintains a high value over large separation distances, and the amplitude decays little with distance [9]. The structural element should, therefore, extend at least from the cabin floor to the ceiling centerline or, preferably, from floor to floor. For a typical baseline airplane, the structural element would include 15 to 30 stringers. This idealization in the circumferential direction cannot give a spatial variation of sound level across the width of the cabin, but gives, instead, a local average value of structural response and interior noise level. This is considered adequate because measurements at appropriate frequencies in present day aircraft indicate that the lateral variation in cabin sound level is small (less than ± 2 dB on an octave band basis).

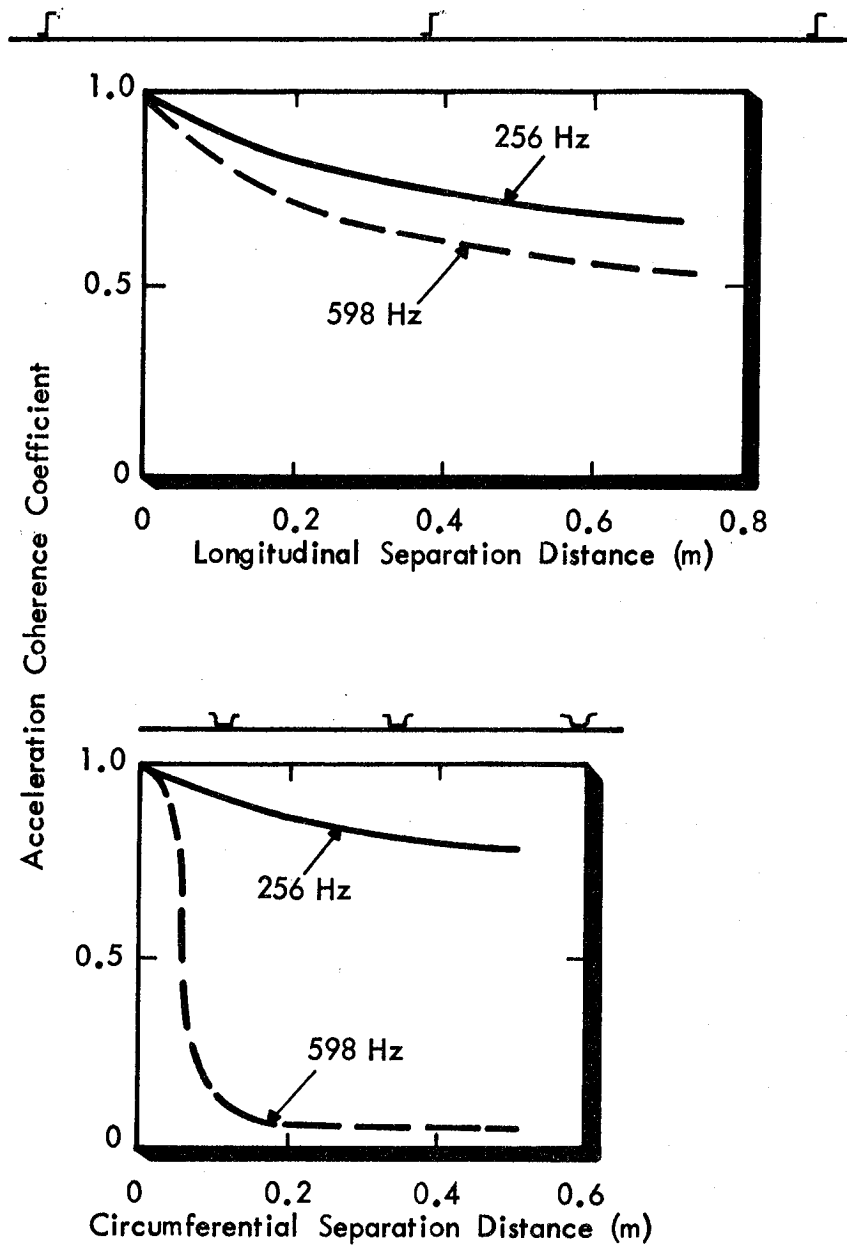


FIGURE 29. ACCELERATION COHERENCE MEASURED ON ADJACENT PANELS OF BOEING 737 FUSELAGE ($M = 0.78$, JET AND BOUNDARY LAYER NOISE)

In the longitudinal direction, coherence is again high at low frequencies, but the pressure amplitude decays rapidly with distance. For example, the amplitude of the pressure field predicted using [6] decreases by 20 dB or more over a distance of 10 frame spacings on the larger baseline aircraft.

For a non-homogeneous excitation, the acoustic power flow equation for N structural elements is given by Eq. (74). Assume that the elements are identical, with equal values of generalized mass M_{rj} and loss factor \bar{n}_{rj} . Furthermore for excitations involving strong spatial amplitude decay over the length of the structural element,

$$\langle p_{X0}^2(\omega_b) \rangle_{j=1} \gg \langle p_{X0}^2(\omega_b) \rangle_{j \neq 1} \quad (j = 1, 2, 3, \dots)$$

where $\langle p_{X0}^2 \rangle_j$ is the maximum pressure amplitude applied at the edge of element j. Therefore only the term involving element 1 will contribute significantly to the power inflow, if other factors such as excitation coherence, amplitude decay rate and trace velocity remain constant or vary only slightly. Hence the acoustic power flow equation may be written in the approximate form:-

$$W_{in}(\omega_b) = \frac{2\pi\rho_1 c_1}{\omega_b} \langle p_{X0}^2(\omega_b) \rangle_j \frac{A_j n_{r,j}(\omega_b)}{\mu_j^2 \bar{n}_{r,j}} \langle j_r^2(\omega_b) \rangle_{P_j} \langle \sigma_{rad} \rangle_j; j=1 \quad (76)$$

The effect of element size then reduces to a consideration as to whether

$$\Lambda_j = A_j n_{r,j} \langle j_r^2 \rangle_{P_j} \langle \sigma_{rad} \rangle_j \quad \text{for } j = 1 \quad (77)$$

is independent of A_j .

The term $\langle p_{X_0}^2 \rangle_j = 1$ is constant for different values of A_j , since as area A_j increases, the change is made such that the location \bar{X}_0 of the maximum pressure always lies on one edge of the element $j=1$. For convenience, Eq. (77) may now be written in the alternative form

$$A_j = \frac{n_{r,j}}{A_j} \langle \sigma_{rad} \rangle_j (A_j^2 \langle j_r^2 \rangle_{P_j}) \quad (78)$$

The various terms on the right hand side of this equation will now be considered in more detail in Sections 5.3-5.5.

5.3 Modal Density

For a flat plate, the modal density is given by

$$n_{r,j}(\omega_b) = \frac{\pi A_j}{\kappa_p c_l} \quad (79)$$

where κ_p is the radius of gyration of the panel. This equation will be approximately valid even for pressurized and stiffened panels, provided that the value of κ_p is determined for the equivalent (smeared-out) panel. From Eq. (78), it is required that $n_{r,j}/A_j$ for fuselage panels of various A_j , but constant surface density and stiffener arrangement, should be independent of A_j , at least when the modal density is sufficiently high so that several modes exist in the frequency band of interest.

Figures 30 and 31 present calculated values for $n(\omega)/A_j$ for typical narrow-body and wide-body fuselage elements. The curves in both figures, are associated with the low-frequency structural model which includes frames, stringers and skin. For the

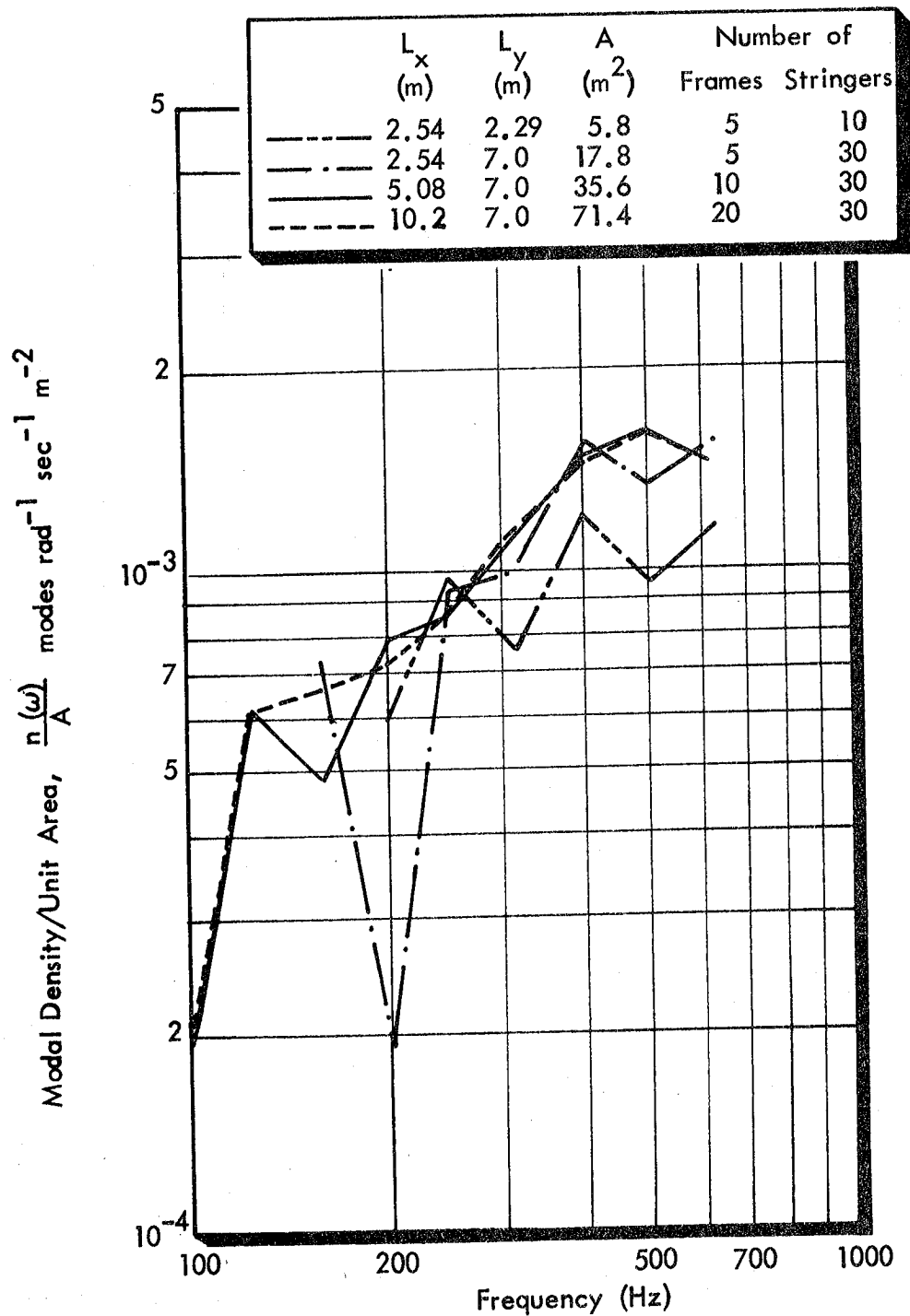


FIGURE 30. VARIATION OF MODAL DENSITY WITH PANEL AREA
(TYPICAL NARROW BODY FUSELAGE ELEMENT, LOW
FREQUENCY STRUCTURAL MODEL)

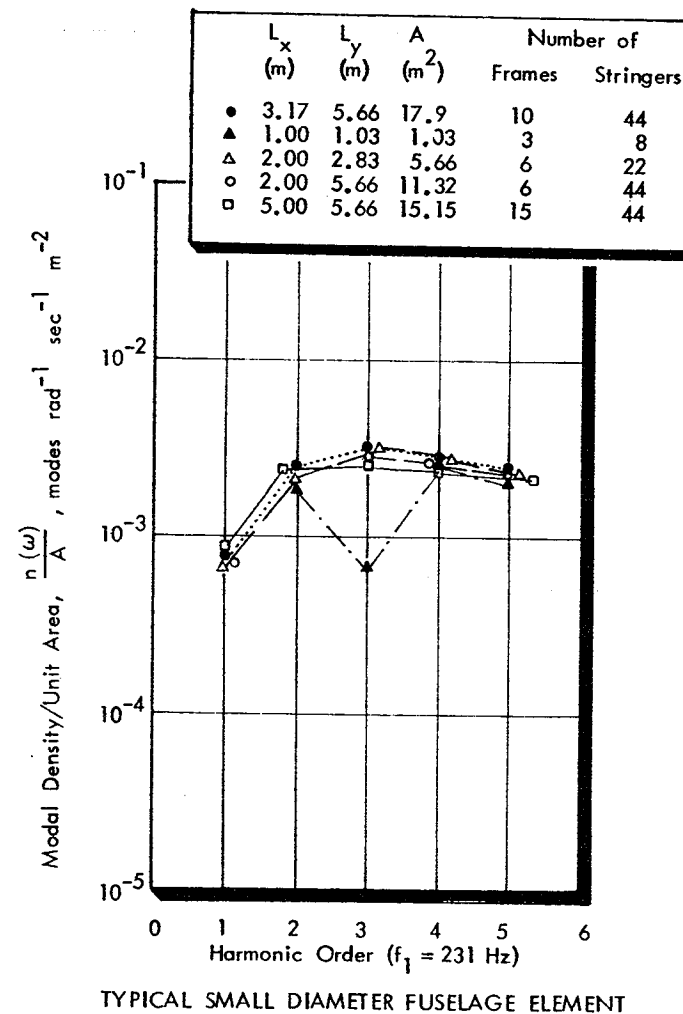
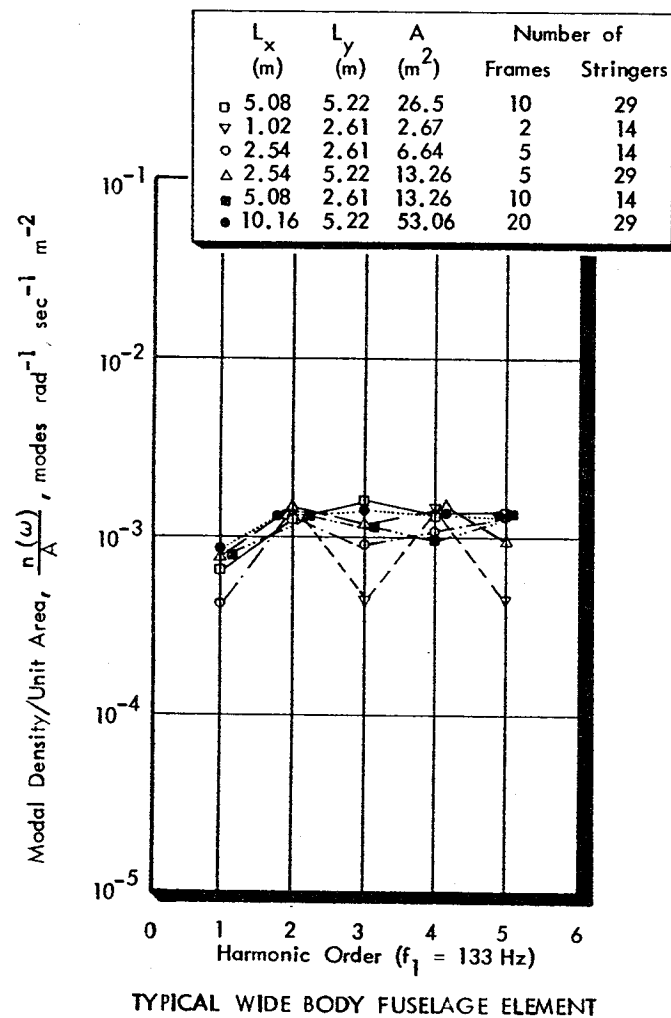
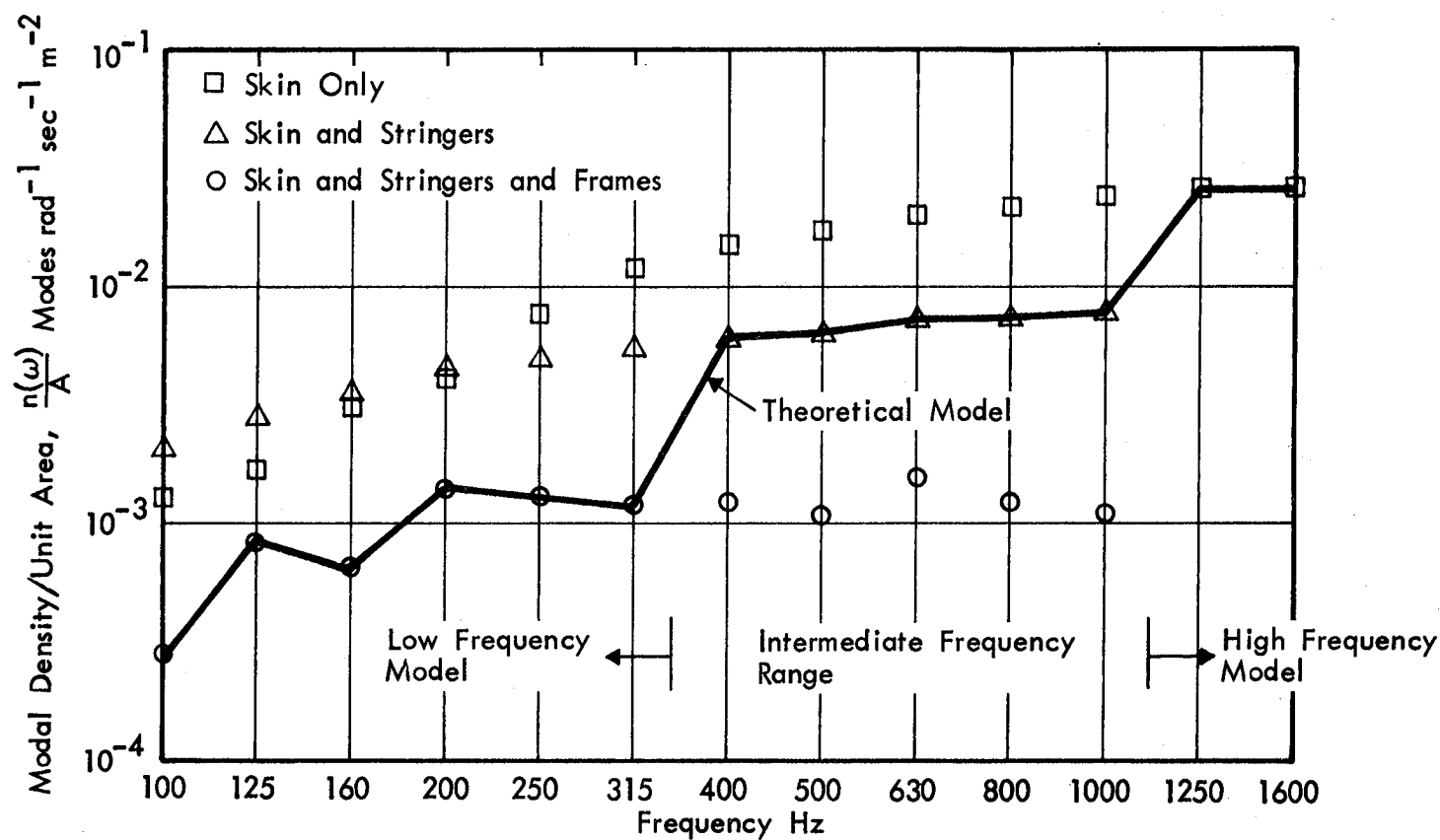


FIGURE 31. VARIATION OF MODAL DENSITY WITH PANEL ELEMENT AREA :
LOW FREQUENCY STRUCTURAL MODELS

narrow-body fuselage (Figure 30), when $L_y = 7.0\text{m}$ (i.e. element extends from floor to floor), the ratio $n(\omega)/A$ is independent of element length L_x when L_x is greater than approximately 4m (8 frames) for frequencies 100Hz and above. When $L_x = 2.54\text{m}$ (5 frames), $n(\omega)/A$ shows little change at frequencies above 200Hz , but at lower frequencies the differences can be as much as $\pm 5\text{dB}$.

For the wide-body fuselage, an element of width $L_y = 5.22\text{m}$ (i.e. extending from floor to ceiling centerline) and a length L_x of at least 2.5m (5 frames) is sufficient to give a value of $n(\omega)/A$ which is independent of area for frequencies of 125Hz and above (Figure 31). An element of dimensions $L_x = 3.17\text{m}$ and $L_y = 5.66\text{m}$ is satisfactory for the small-diameter fuselage (Figure 31).

The modal density of the structural elements varies with frequency (as shown in Figures 30 and 31), but it also depends on the structural representations used in the analysis. Figure 32 shows the modal density for a typical wide-body fuselage element calculated using the three different structural representations discussed in Section 5.1. It is seen that there is a large difference in modal density between the low-frequency structural representation of 'smeared-out' frames and stringers and the high-frequency structural representation where only the skin is considered. Differences of this type have been observed in practice [36].



Typical Wide Body Fuselage Element

Size: $L_x = 5.08 \text{ m}$ (10 Frames)

$L_y = 5.22 \text{ m}$ (28 Stringers)

FIGURE 32. VARIATION OF MODAL DENSITY WITH FREQUENCY

5.4 Joint Acceptances

The effect of element size on the product $A_j^2 \langle j_r^2 \rangle_p$ is shown in Figure 33 for typical narrow-body and in Figure 34 for wide-body and small diameter fuselage elements, the calculations having been performed for the low frequency structural models, which include frames, stringers and skin. For the narrow-body element lengths L_x greater than 4m, $A_j^2 \langle j_r^2 \rangle_p$ is independent of A_j . When the elements are much smaller than 4m, the approximate equation (Eq. (76)) for the power flow is no longer valid and the contribution from adjacent elements cannot be ignored. More importantly, $A_j^2 \langle j_r^2 \rangle_p$ is significantly underestimated in these situations due to the preclusion of long wavelength, well-coupled structural modes.

Figure 34 shows that $A_j^2 \langle j_r^2 \rangle_p$ is independent of A_j , for the wide-body fuselage, for an element of width $L_y = 5.22\text{m}$ and length L_x greater than 5.08m, and for the small diameter fuselage for an element $L_y = 5.66\text{m}$ and length L_x greater than 3.17m.

These conclusions regarding the effect of element size on the progressive wave joint acceptance are valid only for a strong decaying excitation pressure amplitude. If the excitation is a homogeneous, reverberant acoustic field*, the progressive wave joint acceptance is replaced by the reverberant field joint acceptance $\langle j_r^2 \rangle_R$. From Eq. (61),

$$A_j \langle j_r^2 \rangle_R = \pi c_i^2 \sigma_{\text{rad}} / 2\omega^2 \quad (61)$$

Now, as will be shown in Section 5.5, the structural element can be chosen such that σ_{rad} is independent of A_j . Then $A_j \langle j_r^2 \rangle_R$ will also be independent of A_j . This is shown in Figure 35.

* required for acoustic power flow calculations (See Section 3.6.3).

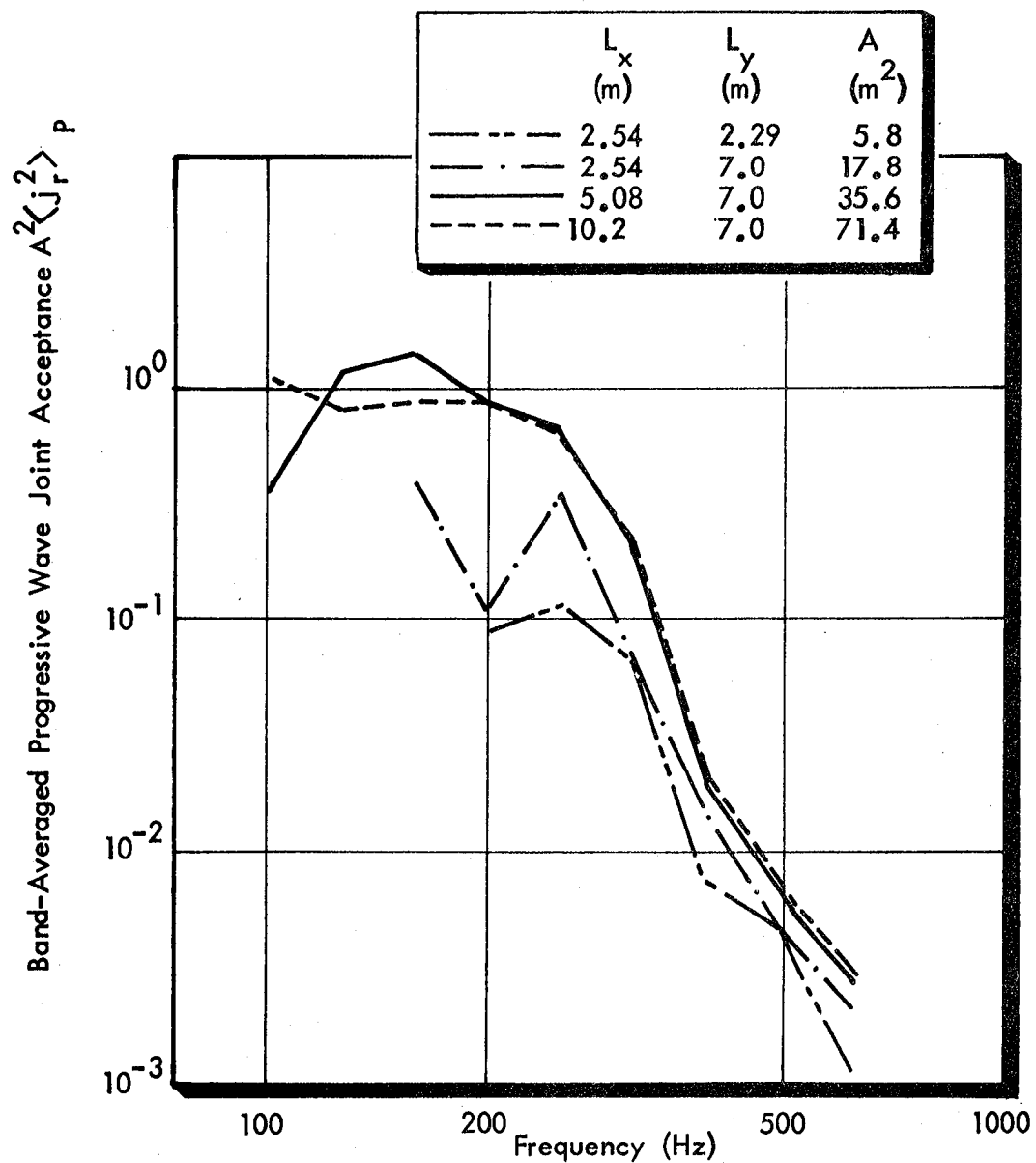


FIGURE 33. EFFECT OF PANEL AREA ON BAND-AVERAGED PROGRESSIVE WAVE JOINT ACCEPTANCE (TYPICAL NARROW BODY FUSELAGE ELEMENT, LOW FREQUENCY STRUCTURAL MODEL)

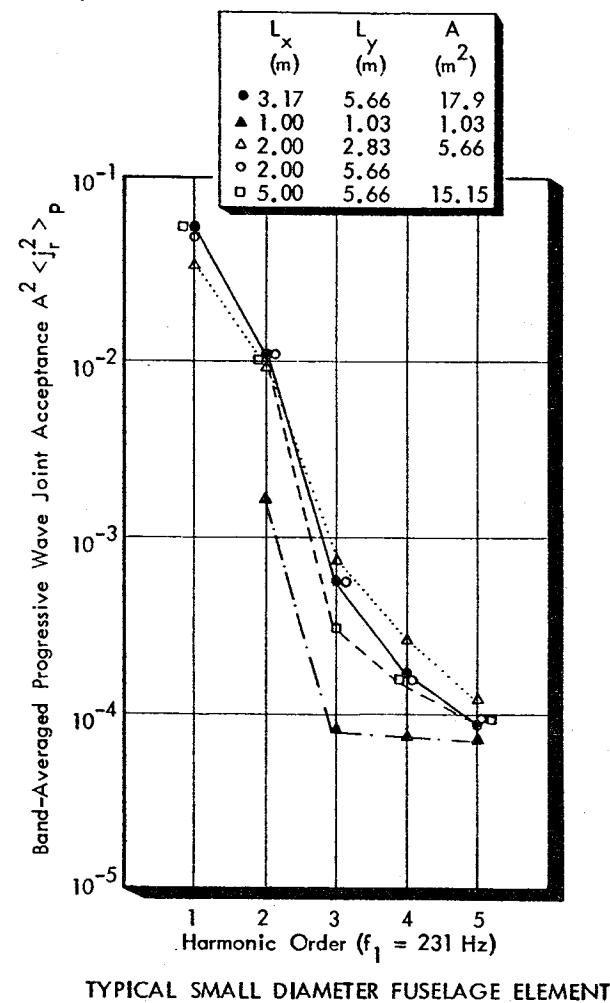
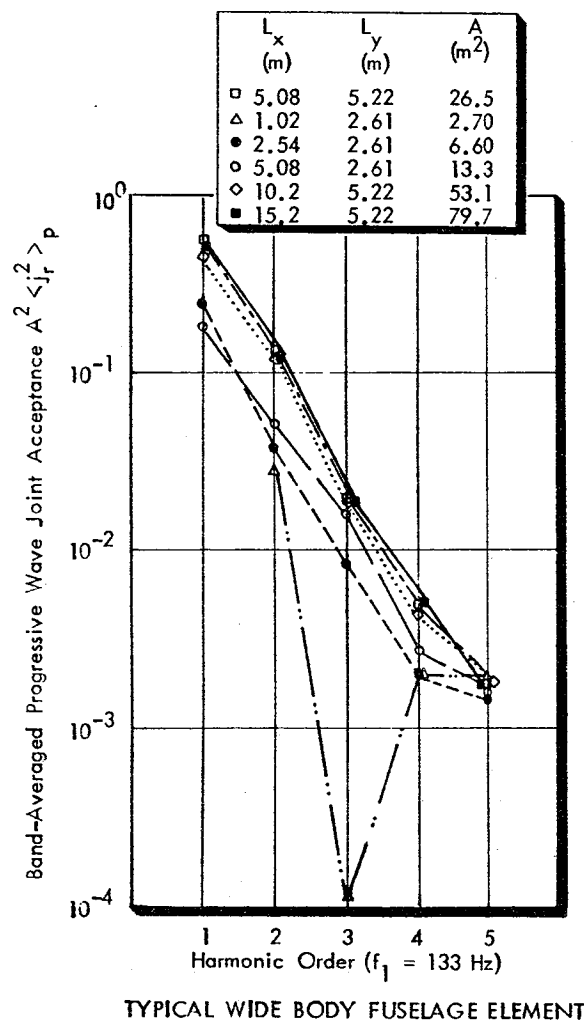
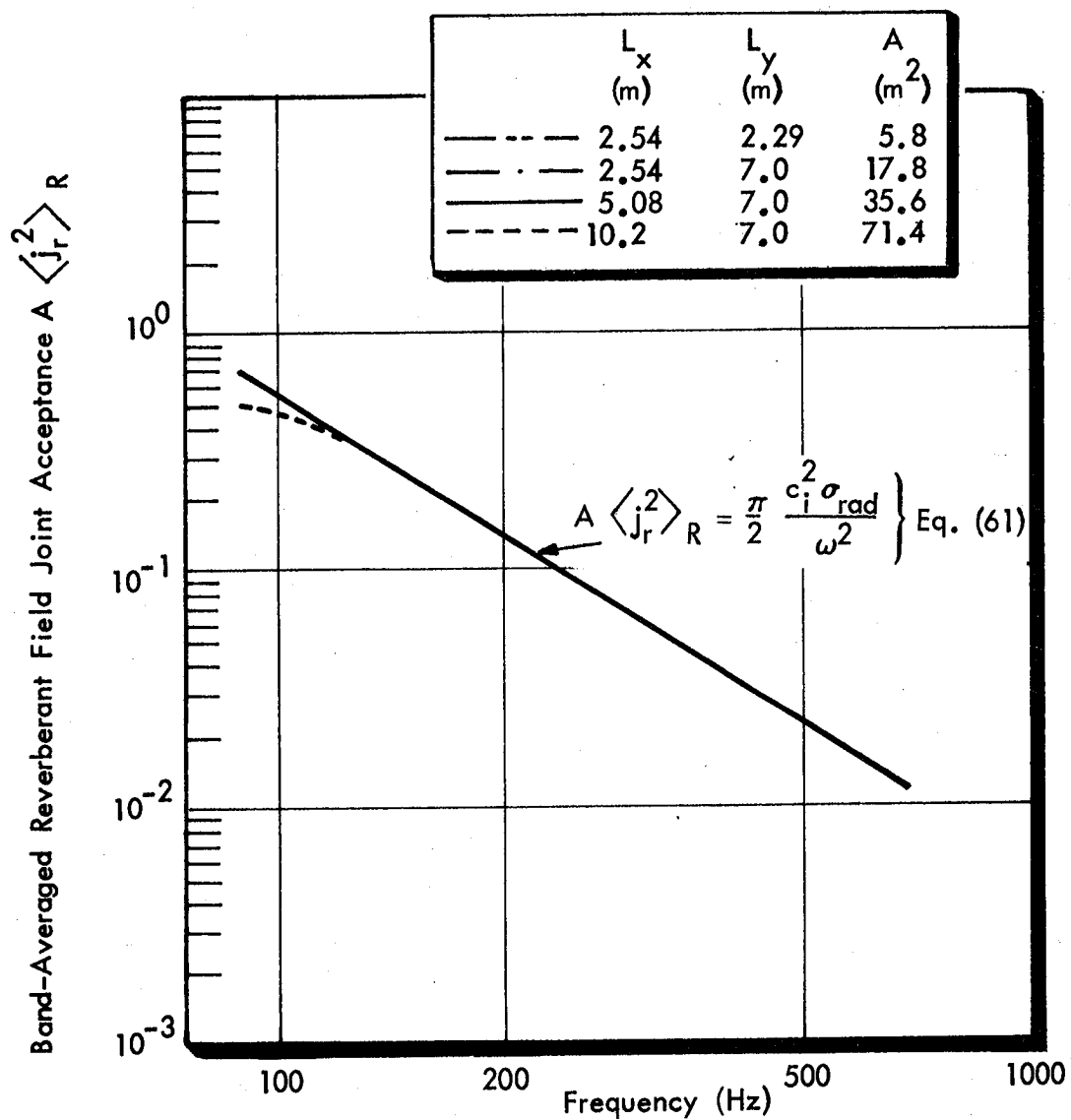


FIGURE 34. EFFECT OF PANEL AREA ON BAND-AVERAGED PROGRESSIVE WAVE JOINT ACCEPTANCE: LOW FREQUENCY STRUCTURAL MODELS



(Note: Except at Low Frequencies, All Curves Lie on the Same Graph)

FIGURE 35. EFFECT OF PANEL AREA ON BAND-AVERAGE REVERBERANT FIELD JOINT ACCEPTANCE (TYPICAL NARROW BODY FUSELAGE ELEMENT, LOW FREQUENCY STRUCTURAL MODEL)

5.5 Radiation Efficiency

At low frequencies, with structural elements of sizes previously discussed ($L_x \approx 2.5$ m, $L_y \approx 5$ m) so that they include several frames and stringers, the radiation efficiency σ_{rad} is unity for all modes, and hence is independent of the element area A_j . This occurs because at low frequencies the modes are acoustically fast (and hence efficient radiators) due to the effects of fuselage curvature, the 'smeared-out' stiffness of the frames and stringers and, to a lesser extent, cabin pressurization. Modal wavelengths at low frequencies are large compared to typical frame and stringer pitch, and the corresponding mode shapes are well represented by simple sinusoidal functions, even though the element boundaries are assumed clamped for resonance frequency calculation. The effect of stiffeners is to modulate the basic mode shape with a wavelength equal to twice the stiffener pitch. As frequency increases however, the stiffeners participate less in the fuselage motion. Then, mode shapes are determined more by subpanel properties with stiffeners acting as restraining edges. The radiation properties of such 'ribbed' structures may be estimated following Maidanik [39] or Barger et al [40]: the latter approach was adopted, from which it may be shown that, for an isotropic free vibration field

$$\sigma_{\text{rad}} = \frac{8}{\pi^2} \cdot \frac{L}{A} \cdot \lambda_c \cdot \epsilon \left[1 + \left(1 + \frac{4h}{A_r k_p} \right)^2 \right]^{-1} \quad (80)$$

where L is the sum of the total length of rib attachment to the skin surface and one-half the total length of ribs attached to the area edge. A is the plate area, $\lambda_c = 2\pi \kappa c_L / c_1$ is the skin critical wavelength, κ is the skin radius of gyration, h is the skin thickness, A_r is the cross-sectional area of the stiffeners, k_p is the structural wavenumber at frequency ω , and $\epsilon = \sin^{-1}(k_{c1}/k_p)$. Since L/A is constant for a uniform grid of arbitrary area the radiation ratio is independent of the area.

5.6 Loss Factors

For lightly damped aluminum structures, only structural damping and acoustic radiation will contribute significantly to the decay of vibrational energy levels. Structural energy dissipation will be associated both with material (internal) damping mechanisms, and with energy losses occurring at the structural boundaries; of the latter mechanisms, viscous damping arising from the pumping of gas within the joints can be important in non-rigid joints such as those occurring in bolted built-up structures [41]. Acoustic radiation damping can become a significant means of energy dissipation for lightweight structures whose radiation ratios are high.

The overall modal loss factor η_r may be expressed by the relation

$$\eta_r = \eta_i + \eta_j + \eta_{rad} = \eta_{struc} + \eta_{rad} \quad (81)$$

where η_i is the internal loss factor associated primarily with material damping (which for aluminum can be considered to be essentially independent of frequency), η_j is the loss factor associated with dissipation at structural joints and η_{rad} is the modal loss factor resulting from acoustic radiation damping. η_{rad} is given by

$$\eta_{rad} = R_{rad}/\omega A\mu = \rho c \sigma_{rad}/\omega\mu \quad (82)$$

where ω is the circular frequency, μ and A are the surface density and area of the structure, R_{rad} is the radiation resistance, ρ and c are respectively the density of, and speed of sound in, the fluid surrounding the structure and σ_{rad} is the radiation efficiency or radiation ratio.

For lightly damped structures, $\eta_i < 10^{-3}$, while for rigid joints allowing no relative motion between the component parts, $\eta_j < \eta_i$. For lightweight structures and supersonic modes, $\sigma \approx 1$, so that η_{rad} can be greater than both η_i and η_j . This can be particularly important for cylindrical structures as they have supersonic modes at frequencies well below the acoustic coincidence frequency of a flat plate with the same thickness as the skin. The same statements are assumed valid for band-averaged loss factors, $\bar{\eta}_r$, which represent the arithmetic mean of the modal loss factors in the frequency band of interest. The structural component η_{struc} of the loss factor for an undamped bare structure, with no applied damping treatments, is assumed to be 0.01 at 100 Hz and to vary inversely with frequency [4], i.e.

$$\eta_{\text{struc}} = 0.01 (2\pi \cdot 100 / \omega) \quad (83)$$

When the radiation loss factor (Eq. (82)) is included, it can be seen (see Figure 36) that the structural loss factor for an undamped structure is small compared with the radiation loss factor at most frequencies of current interest. Limited experimental data is available [42] to support the calculated values as seen in Figure 36. Also shown are the total loss factors for a highly-damped structure, assuming that η_{struc} has a constant value of 0.05, a value considered to approach the maximum achievable value in practical fuselage structures at low frequencies using proven techniques [42]. In this case the radiation loss factor is no longer the most significant contribution to the total loss factor at low frequencies.

$$\eta_r = \eta_{rad} + \eta_{struc} \quad \text{Eq. (81)}$$

$$\text{---} \cdot \text{---} \eta_r = \eta_{rad} + 0.05$$

$$\text{---} \eta_r = \eta_{rad} + 0.01 \left(\frac{100}{f} \right)$$

$$\text{---} \eta_{rad}$$

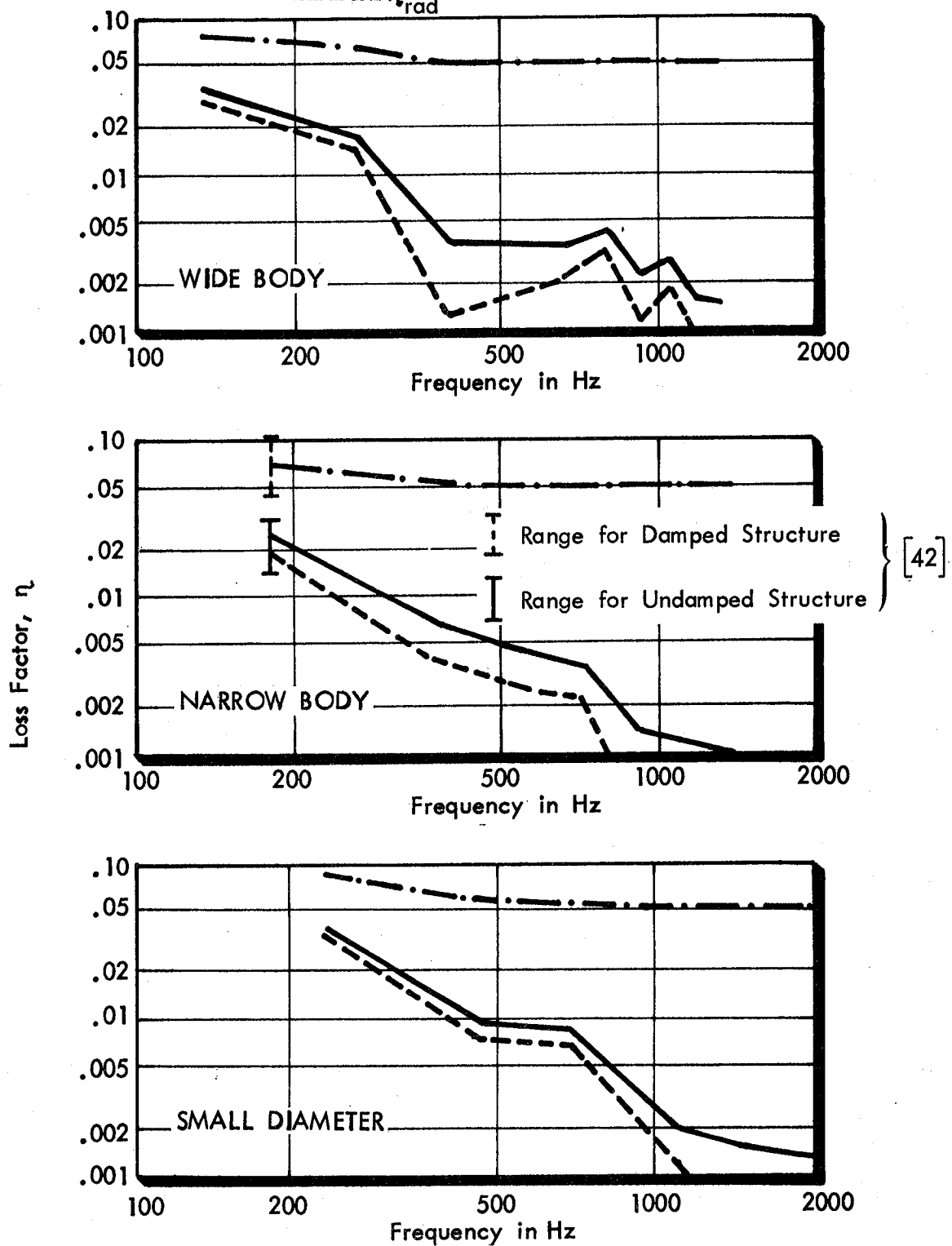


FIGURE 36. VARIATION OF LOSS FACTOR WITH FREQUENCY

5.7 Structural Idealization for Computation Purposes

The preceding discussion has described how the fuselage structure is represented as a series of structural elements (see, for example, Figure 28). The elements extend from floor-to-floor or floor-to-ceiling in the circumferential direction, and divide the fuselage into several segments in the longitudinal direction. The selection of these elements for the three study airplanes is discussed in this section. In addition, the dimensions and structural characteristics of the elements, and the excitation characteristics associated with each element are presented in tabular form for reference.

The division of the fuselage structure into a series of elements was determined to some extent by the amplitude decay of the excitation pressure field for each study airplane in both the longitudinal and circumferential direction. Element sizes were selected for each airplane on the basis of sensitivity calculations similar to those presented in Section 5.1 - 5.5 for the wide-body airplane.

Location of the boundaries between adjacent segments was selected in the first place on the basis of the location of peak sound level from the inboard propeller. For computation reasons it was desired to have this peak level occur on the boundary between two structure elements, as is indicated in Figures 37 through 39 which show schematic sideviews of the structural segmentation. Thus, for example, the peak sound level associated with the inboard propeller of the narrow-body airplane (Figure 38) occurs on the boundary between structure elements 3 and 4. Similarly, a second boundary between elements was selected to correspond with the peak sound levels associated with the outboard propeller (Figures 37 and 38).

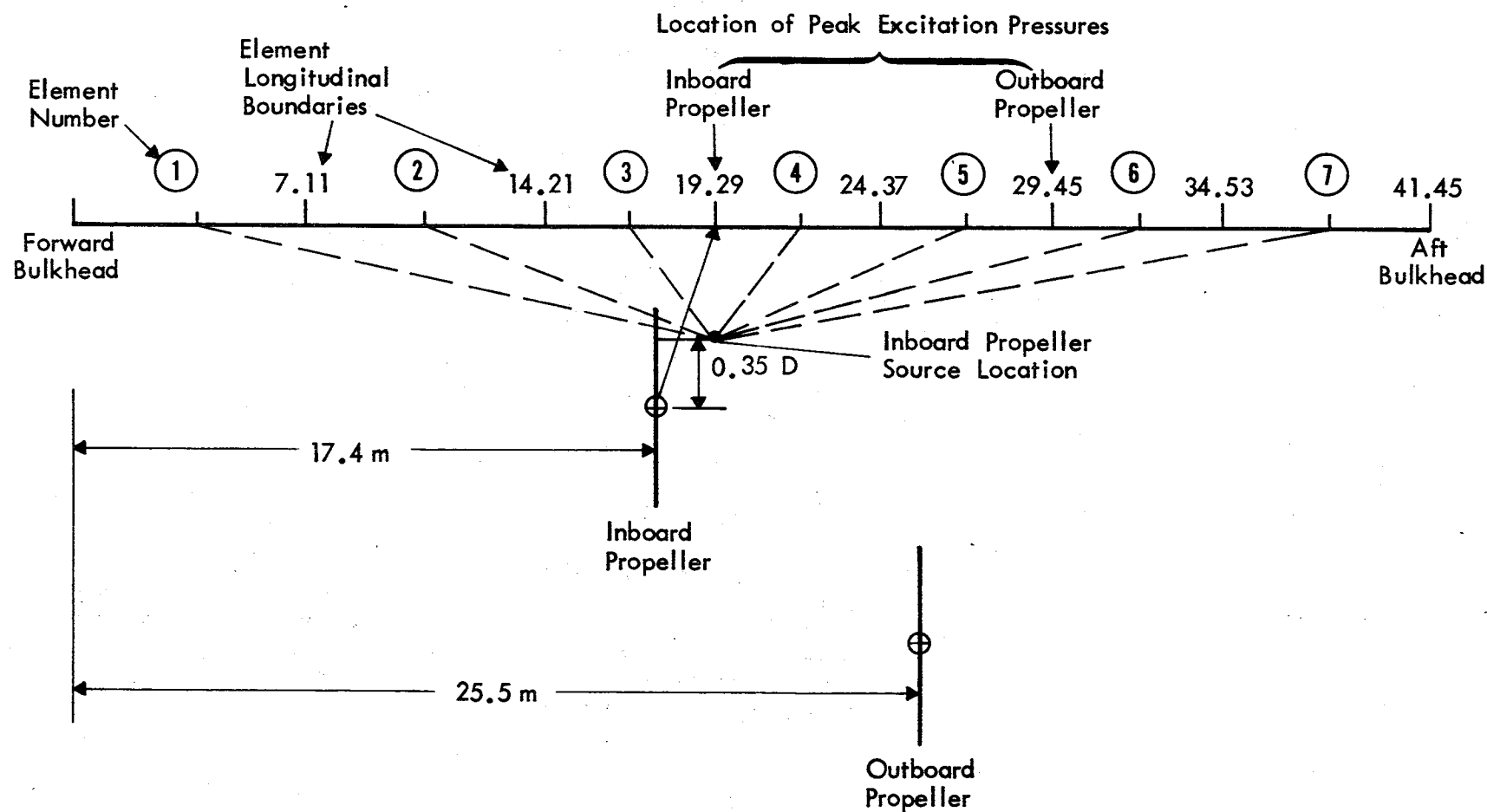


FIGURE 37. SKETCH SHOWING LOCATIONS OF STRUCTURAL ELEMENTS AND PROPELLERS: WIDE BODY AIRPLANE

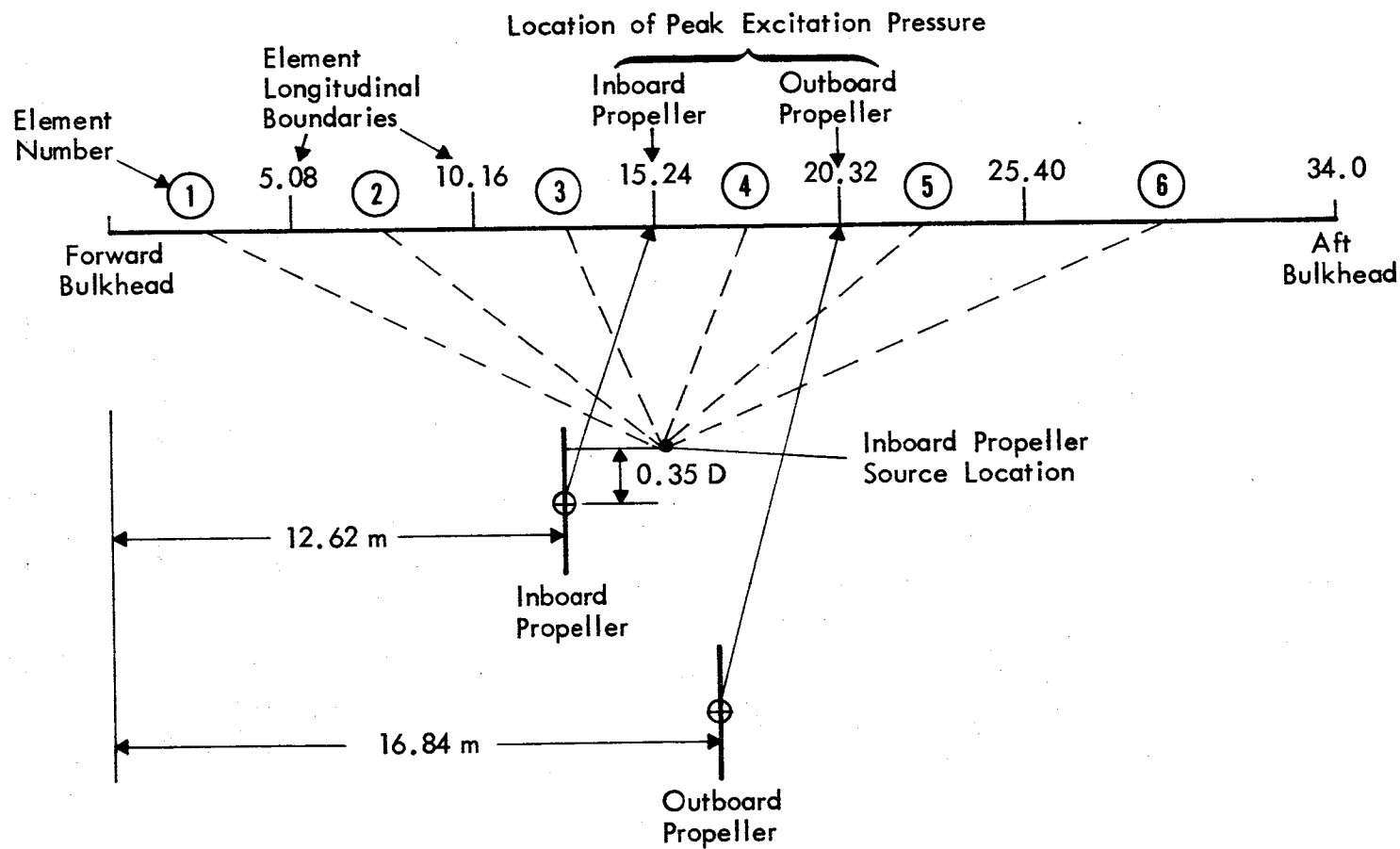


FIGURE 38. SKETCH SHOWING LOCATIONS OF STRUCTURAL ELEMENTS AND PROPELLERS: NARROW BODY AIRPLANE

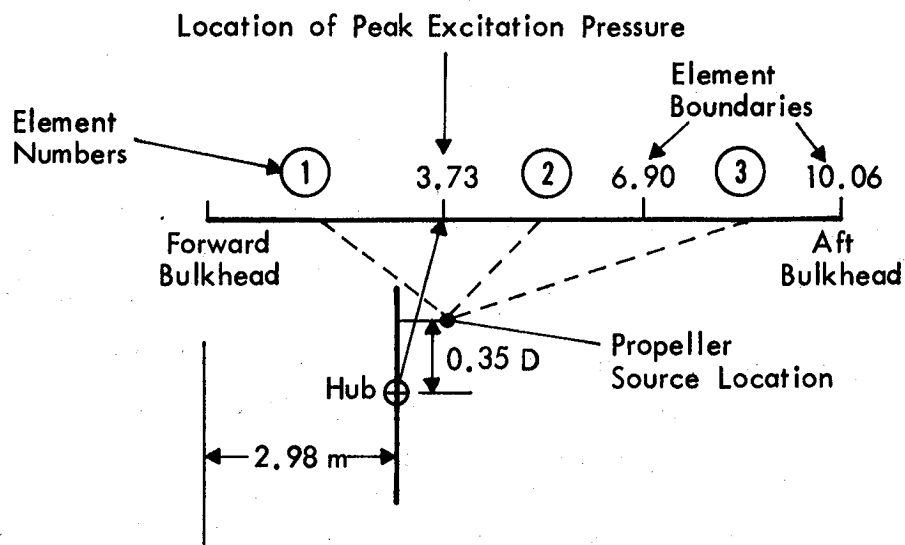


FIGURE 39. SKETCH SHOWING LOCATION OF STRUCTURAL ELEMENTS AND PROPELLER: SMALL DIAMETER AIRPLANE

Having defined these boundaries, and, having determined acceptable element sizes from parametric analyses in Sections 5.1 - 5.5, the segmentation of the fuselage could be completed. The resulting divisions for the three airplanes are shown in Figures 37 through 39 and associated segment locations, dimensions and excitation characteristics are given in Tables 4 through 6. For convenience, element locations are given in terms of the distance of the upstream edge of the element from the forward pressure bulkhead of the cabin.

The selection of the location of peak sound level as the factor determining element boundaries allows the excitation field for a given element to be described in terms of a monotonically-decaying pressure amplitude with a mean trace velocity either upstream or downstream. This representation reduces the complexity of the analytical model.

Structural data for the three baseline study airplanes, as required for the calculation of acoustic power flow into the fuselage interior, are presented in Table 7. These data are also applicable to the baseline airplanes with add-on noise control.

Table 4

Structural Segmentation Details: Wide-body

Element Descriptors	Element No.						
	1	2	3	4	5	6	7
Location of upstream edge of element, re forward bulkhead (m)	0.0	7.11	14.21	19.29	24.37	29.45	34.53
Element dimensions							
L_x (m)	7.105	7.105	5.08	5.08	5.08	5.08	6.92
L_y (m)	5.227	5.227	5.227	5.227	5.227	5.227	5.227
Location of maximum excitation level re forward bulkhead (m)			19.29				
Amplitude Decay Rates							
$a_x L_x$	5.77	5.87	3.77	3.56	3.50	3.50	4.77
$a_y L_y$	1.15	1.15	1.15	1.15	1.15	1.15	1.15
Trace Velocities (m/s)							
U_x	68.	83.	260.	745.	574.	556.	551.
U_y	1390.	851.	498.	498.	780.	1153.	1626.
Coherence Decays							
$c_x = c'_x k_x$	0.01	0.01	0.01	0.01	0.01	0.01	0.01
$c_y = c'_y k_y$	0.01	0.01	0.01	0.01	0.01	0.01	0.01

Table 5

Structural Segmentation Details: Narrow-body

Element Descriptors	Element No.					
	1	2	3	4	5	6
Location of upstream edge of element, re forward bulkhead (m)	0.0	5.08	10.16	15.24	20.32	25.40
Element dimensions						
L_x (m)	5.08	5.08	5.08	5.08	5.08	8.60
L_y (m)	7.00	7.00	7.00	7.00	7.00	7.00
Location of maximum excitation level re forward bulkhead (m)	15.24					
Amplitude Decay Rates						
$a_x L_x$	3.12	3.12	2.51	1.98	1.98	3.35
$a_y L_y$	0.70	0.70	0.70	0.70	0.70	0.70
Trace Velocities (m/s)						
U_x	95.	148.	553.	1038.	633.	572.
U_y	1703.	1241.	926.	926.	1241.	1880.
Coherence Decays						
$c_x = c'k_{xx}$	0.01	0.01	0.01	0.01	0.01	0.01
$c_y = c'k_{yy}$	0.01	0.01	0.01	0.01	0.01	0.01

Table 6

Structural Segmentation Details: Small diameter

Element Descriptors	Element No.		
	1	2	3
Location of upstream edge of element, re forward bulkhead (m)	0.0	3.73	6.90
Element dimensions			
L_x (m)	3.73	3.165	3.165
L_y (m)	5.66	5.66	5.66
Location of maximum excitation level re forward bulkhead (m)	3.73		
Amplitude Decay Rates			
$a_x L_x$	5.71	4.50	4.71
$a_y L_y$	1.79	1.79	1.79
Trace Velocities (m/s)			
U_x	145.	658.	560.
U_y	473.	451.	791.
Coherence Decays			
$c_x = c'_x k_x$	0.01	0.01	0.01
$c_y = c'_y k_y$	0.01	0.01	0.01

Table 7
Structural Data for Typical Element of
Baseline Airplanes

Baseline Aircraft	Wide	Narrow	Small
Element No. (in propeller plane)	4	4	4
Frame Spacing ℓ_x m	.5080	.5080	.3302
Stringer Spacing ℓ_y m	.1829	.2286	.1270
<u>Skin</u>			
Thickness h mm	1.7780	3.0	1.016
Mass/unit area ρh kg/m ²	4.8006	8.100	2.7432
Bending stiffness, D_x, D_y N.m	38.133	183.18	7.1151
Torsional stiffness, D_k N.m	12.584	60.45	2.3480
Wave speed, c_L m/sec	5491.1	5491.1	5491.1
<u>Stringer</u> (smeared out over width ℓ_y)			
Equivalent thickness, A_s/ℓ_y mm	.9882	.4006	.4064
Mass/unit area $\rho A_s/\ell_y$ kg/m ²	2.6680	1.0817	1.0973
Bending stiffness, $E I_s/\ell_y$ N.m	6510.05	4338.9	687.23
Torsional stiffness, $G J_s/\ell_y$ N.m	19.388	2.3164	3.8956
Centroid to skin middle surface \bar{z}_s	-.01583	-.01855	-.00744
Bending stiffness, D_x (skin & stringers) N.m	18,549	13,410	1,895.2
<u>Frame</u> (smeared out over width ℓ_x)			
Equivalent thickness A_r/ℓ_x m	1.0448	.6012	.3716
Mass/Unit area $\rho A_r/\ell_x$ kg/m ²	2.8209	1.6233	1.0034
Bending stiffness, $E I_r/\ell_x$ N.m	174,872	53,956	20,213
Torsional stiffness, $G J_r/\ell_x$ N.m	24.510	8.1609	1.2314
Centroid to skin middle surface \bar{z}_s	-.05468	-.03921	-.03911
Bending stiffness D_y (skin & frames) N.m	323,420	110,780	51,237
Stiffener Cross-sectional Area m ² $A_{rib} = (A_s \ell_x + A_r \ell_y)/(\ell_x + \ell_y)$	2734×10^{-3}	$.1579 \times 10^{-3}$	$.7136 \times 10^{-4}$

6.0 NOISE LEVELS IN BASELINE AIRPLANES

As a first step in the analysis of the interior noise levels in the three study airplanes, interior noise levels were calculated for the three airplanes with bare interiors and with baseline sidewall treatment. The results of the calculations are presented in this section for the three different excitation spectral shapes described in Section 4.6. Subsequent sections will present the results of applying the analytical model to add-on and advanced noise control concepts. The information presented in this section shows axial distributions of fuselage acoustic power in-flow, axial distributions of interior overall noise levels, resonant and non-resonant contributions to the total acoustic power flow, and low-order harmonic levels. Finally the required noise reductions for the baseline study airplane to achieve the criterion of 80 dB maximum interior A-weighted noise level are presented.

6.1 Hamilton Standard Excitation Spectrum

The major part of the discussion in this section will be concerned with analytical results obtained using the excitation spectrum defined in the Hamilton Standard prediction procedure [6], since this spectrum is associated with the highest predicted interior sound levels.

6.1.1 Acoustic Power Flow into Fuselage

The calculated acoustic power flow into the baseline airplane interior for the two lowest order harmonics and for each study airplane is shown in Figure 40: here the airplane fuselages

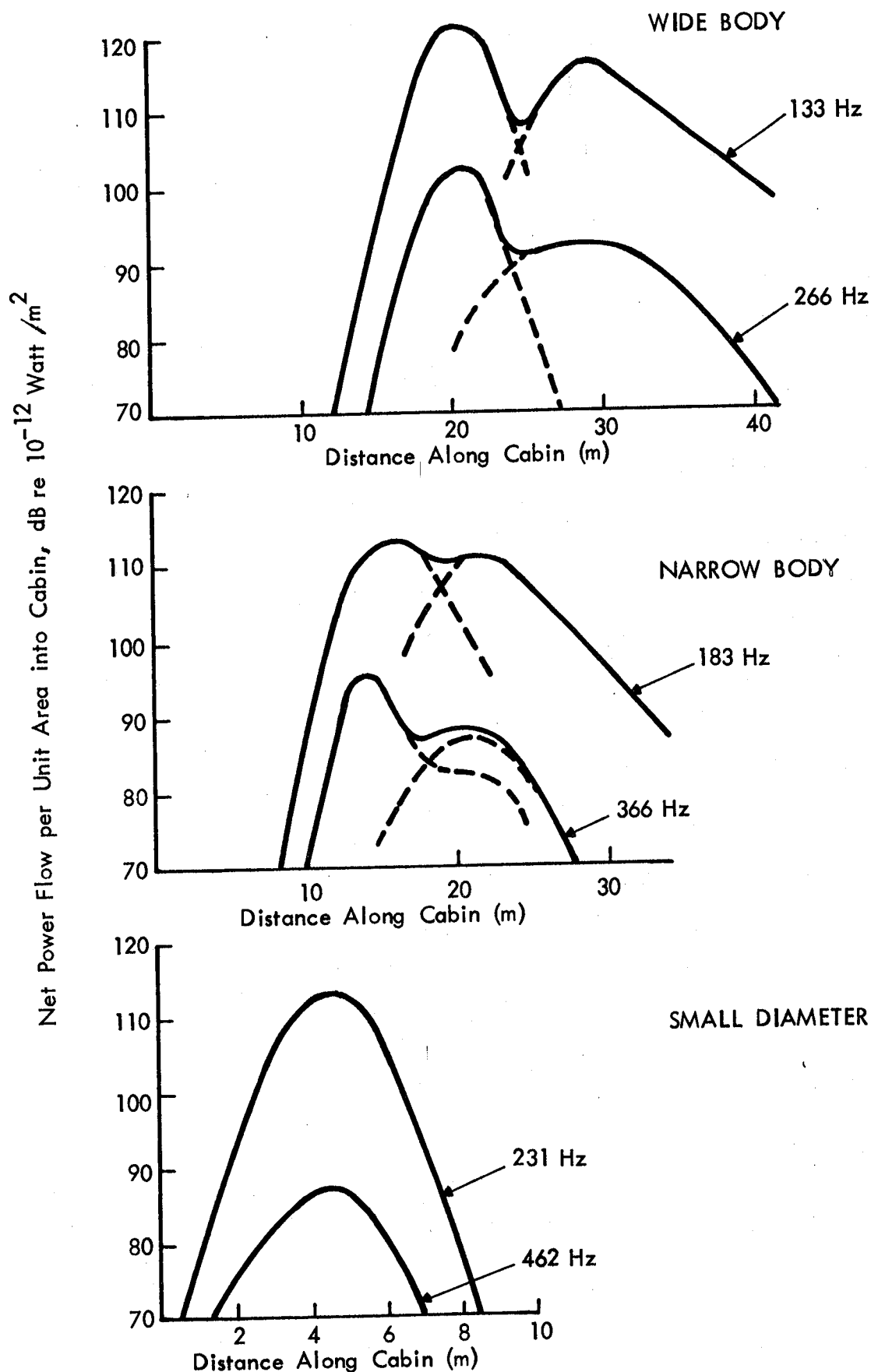


FIGURE 40. VARIATION OF POWER FLOW INTO THE CABIN ALONG CABIN LENGTH (Fuselages Furnished With Baseline Sidewall Treatments: Frequencies Correspond to Fundamental and Second Harmonic of Propfan Blade Fuselage Frequency)

are each lined with the baseline sidewall treatments. It is clear that, while maximum transmission occurs in the region of maximum excitation level, the power flow is distributed over a considerable portion of the fuselage length. This is due, for the wide-body and narrow-body fuselages, to the influence of the outboard propellers whose directivities have less pronounced effects than do the inboard propellers. The contributions of the inboard and outboard propellers are indicated separately. In general it is seen that fuselage sections extending from just forward of the inboard propeller plane of maximum excitation level to well-rear of the outboard propeller plane of maximum excitation level will require acoustic treatment to achieve significant reductions in acoustic power flow.

Further it will not be possible to confine the acoustic power flow to a small element of the enclosed cabin by partitioning the cabin space. This conclusion follows from the fact that the calculated power flow distribution is a direct indication of the noise transmission distribution through the sidewall irrespective of any subsequent distribution of energy within the cabin.

Spectra of the net calculated power flow through the baseline fuselage of each of the study airplanes (Eqs. (51) and (52)) are shown in Figure 41. Also shown in the figure are the contributions associated with resonant and non-resonant transmission through the fuselage structure. At higher frequencies where the effects of frames are not included in the structural representations, the structural resonant modes become less efficient radiators so that the resonant power approaches that of the mass-controlled non-resonant modes. The calculations clearly

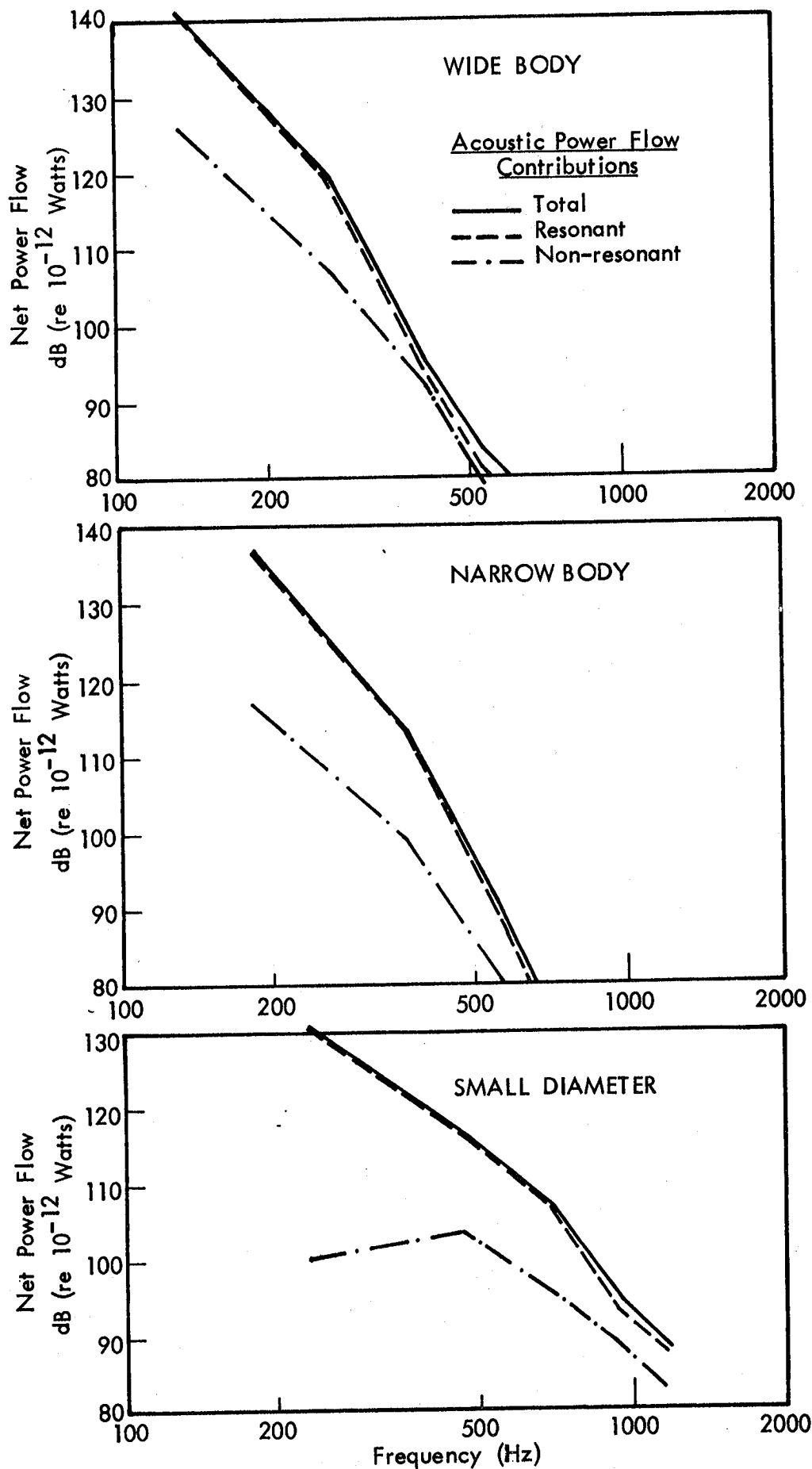


FIGURE 41. CALCULATED POWER FLOW THROUGH FUSELAGE STRUCTURES. (BASELINE STRUCTURE, SIDEWALL AND ABSORPTION)

indicate however, that over the frequency range of interest, resonant transmission controls the acoustic power flow.

6.1.2 Interior Noise Levels

Having calculated the power inflow, through each of the fuselage sections, it is now possible, by means of the imaging procedure outlined in Section 3.10 to calculate the variation of sound level along the length of the cabin.

Prior to considering each particular study airplane, the effect of variations in interior absorption coefficient on the axial variation in interior sound levels is examined. Figure 42 shows, for the narrow-body airplane, the axial sound level variation for two different values of absorption coefficient for the case where a single panel element (number 4) is radiating into the cabin interior. $\alpha = 0.05$ corresponds essentially to a bare fuselage structure while $\alpha = 0.75$ would be considered the maximum achievable value in the study airplanes. The smaller the value of α , the more diffuse the internal sound field. Some unpublished empirical data is available to support these calculations. For example, Figure 43 presents a comparison of calculated and measured variations in cabin sound levels for a small diameter propeller-driven aircraft: good agreement is found between measured data and calculations using the image source array model.

Figure 44 shows the calculated axial variation of cabin A-weighted interior noise levels for the study airplanes, where the baseline fuselage structures have been used. Results for the bare fuselage and baseline add-on sidewall treatment for the Hamilton Standard excitation spectra [6] are presented. Maximum noise levels of the treated baseline fuselage are between 5 and 10 dB

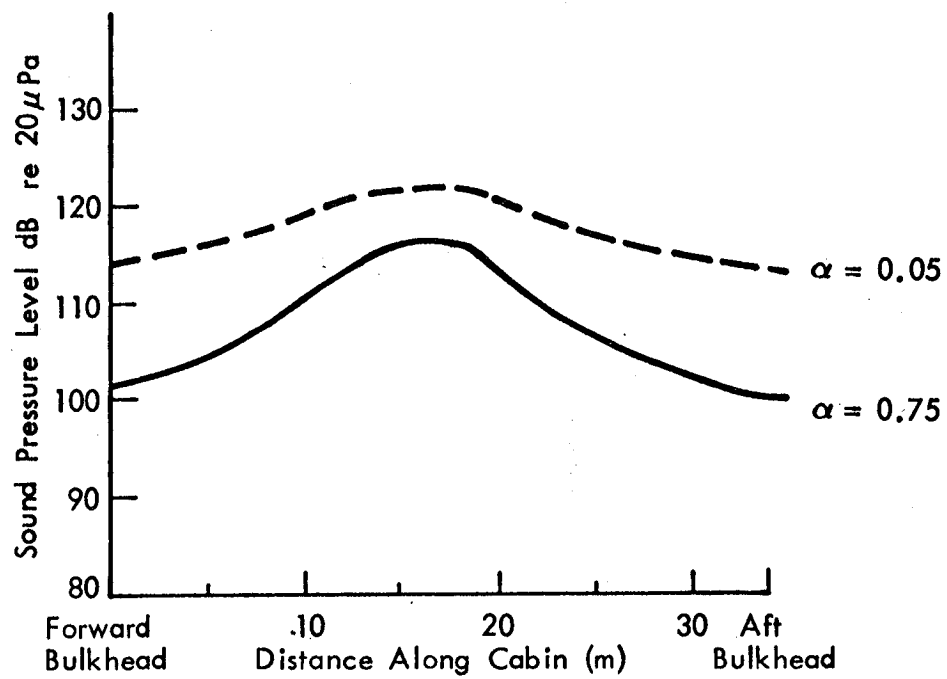
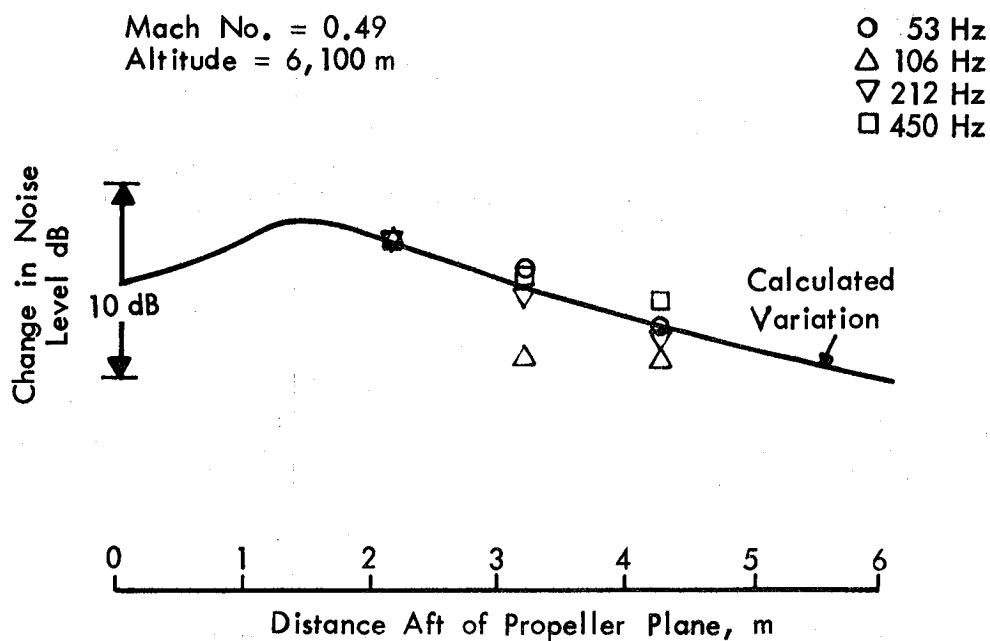


FIGURE 42. AXIAL VARIATION IN SOUND LEVEL FOR DIFFERENT INTERIOR ABSORPTION COEFFICIENTS (NARROW BODY)



Data Points are the Average for 5 Microphone Positions at Each Longitudinal Location.

FIGURE 43. COMPARISON OF CALCULATED AND MEASURED VARIATION OF SOUND LEVEL ALONG CABIN OF A SMALL DIAMETER PROPELLER-DRIVEN AIRCRAFT (Data From BBN Files)

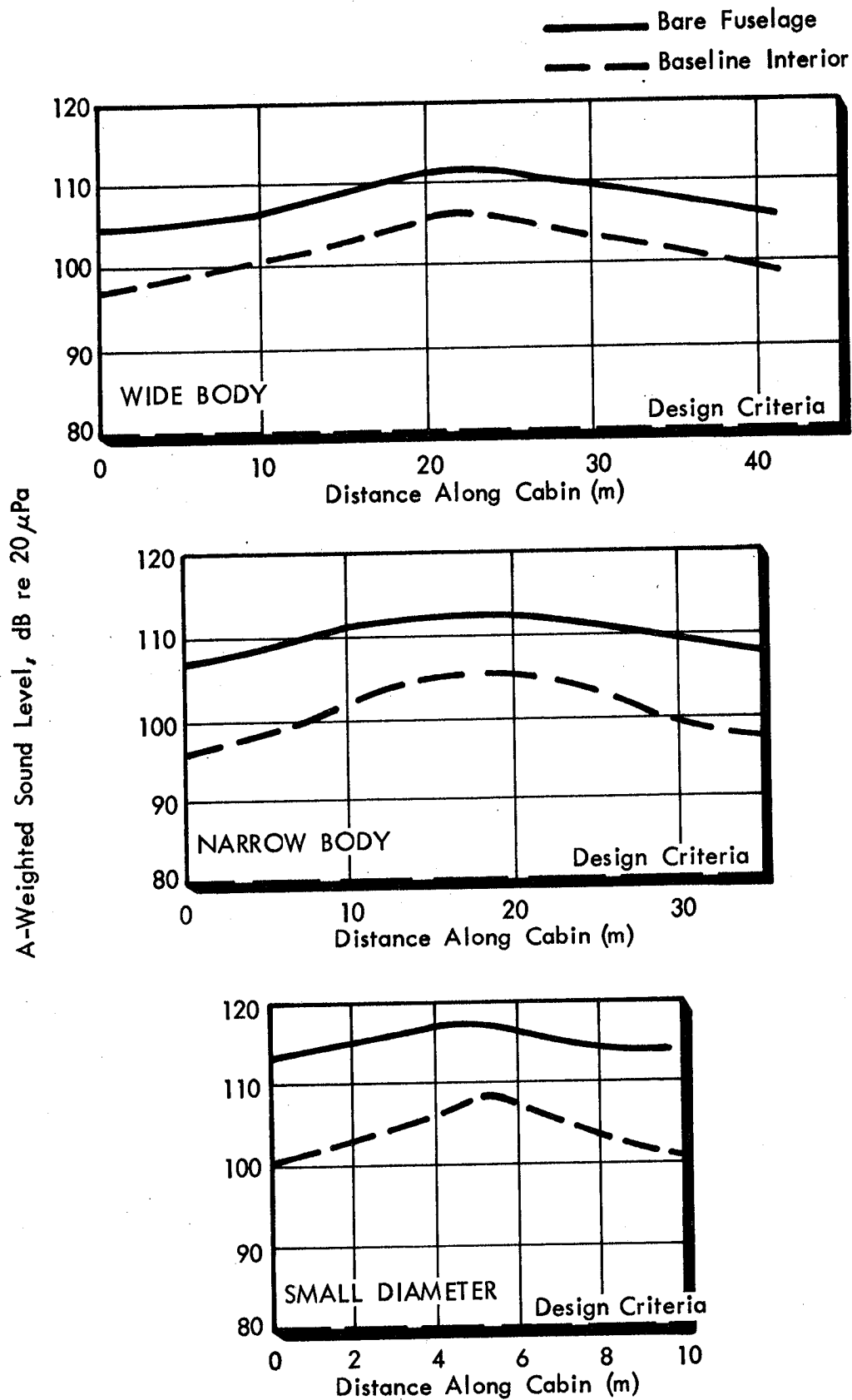


FIGURE 44. AXIAL VARIATION OF CABIN A-WEIGHTED SOUND LEVEL FOR DIFFERENT SIDEWALL TREATMENTS (HAMILTON STANDARD EXCITATION [6])

lower than for the bare fuselage. That the effect of the baseline sidewall and associated increased interior absorption is so small results because the A-weighted interior noise levels are in general controlled by the excitation level at the propeller blade passage frequency, where the transmission loss provided by the baseline sidewall is small, particularly for the larger diameter fuselage. The axial variation for the bare fuselage is notably less than that for the baseline treated fuselage, a result of the decreased absorption present in the bare fuselage.

It is clear that conventional airplane sidewall and fuselage designs are inadequate to achieve the design criteria (i.e., 80 dB(A) maximum internal noise level) in the study airplanes. Therefore substantial improvement will be required in the fuselage/sidewall noise reduction.

Cabin noise spectra at the location of maximum calculated dB(A) levels for each study airplane for bare and baseline fuselages, and for the Hamilton Standard excitation spectra [6] are presented in Figure 45. For each airplane, the propeller fundamental dominates the internal A-weighted noise level, as well as the interior noise spectra. Baseline sidewall treatments provide minimal noise reduction for these low-frequency excitations, but are increasingly effective as harmonic order increases.

Table 8 presents a summary of the minimum noise reductions required for the baseline structures to achieve the design goal of 80 dB(A): these minima have been assessed at the propeller fundamental frequencies since it is at these low frequencies that it is most difficult to achieve high noise reductions.

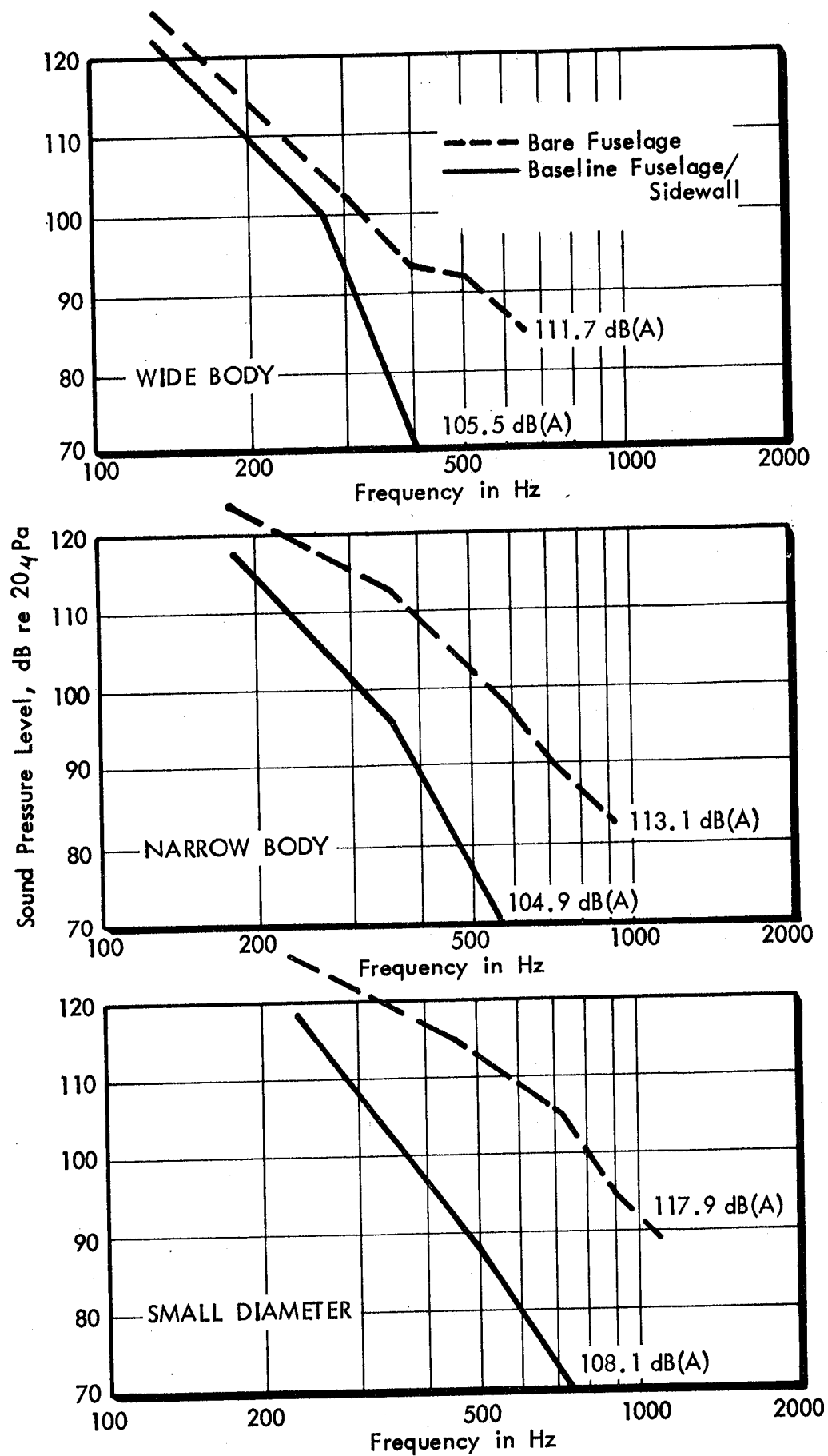


FIGURE 45. CABIN SPECTRA AT LOCATION OF MAXIMUM dBA LEVELS FOR BARE AND BASELINE TREATED FUSELAGES

TABLE 8.
MINIMUM ADDITIONAL NOISE REDUCTION REQUIRED FOR BASELINE STRUCTURE

Baseline Structure	Wide-Body	Narrow-Body	Small Diameter
Maximum Cabin dBA level	105.5	104.9	108.1
Frequency of Fundamental, Hz	133	183	231
Sound pressure level at fundamental frequency, dB	120.8	116.5	117.4
Sound pressure level at fundamental frequency to meet 80 dBA goal, dB	95.5	91.8	89.5
Minimum Noise Reduction required at Fundamental Frequency, dB	25.3	24.7	27.9

Limited experimental evidence from current commercial aviation airplanes exists to support the above conclusions. In Figure 46 are shown comparisons between calculated baseline noise reductions for each of the study airplanes with empirical data for narrow-body fuselages, where noise reduction is taken to be the difference between peak excitation levels and the maximum internal noise levels. The current predictions agree well with the range of data, lending some confidence to the analytical predictions.

6.1.3 Error Analysis

For the study airplanes of interest, Table 9 and Figure 47 show the expected error limits involved in the computation; these estimates result only from modeling of the fuselage structures and the coupling with the cabin volume, and do not include such errors as may result from inaccuracies in the description of the excitation pressure field.

Following the approach outlined in Section 3.5.3, the normalized standard error in calculations of the net acoustic power flow can be derived as

$$\epsilon_r = \left[2\pi \bar{\eta}_r n_r(\omega_b) \omega_b \right]^{-1/2} + \left[2\pi \eta_n n_n(\omega_b) \omega_b \right]^{-1/2}$$

The upper and lower bound 2σ limits for 95% confidence in power flow calculations are calculated as $10 \log_{10} (1+2\epsilon_r)$ and $10 \log_{10} (1-2\epsilon_r)$ above and below the expected value of the power flow. These error limits should be interpreted as follows: at any time, the actual value of the acoustic power flow is expected to fall within the noted limits 95% of the time such a check is made.

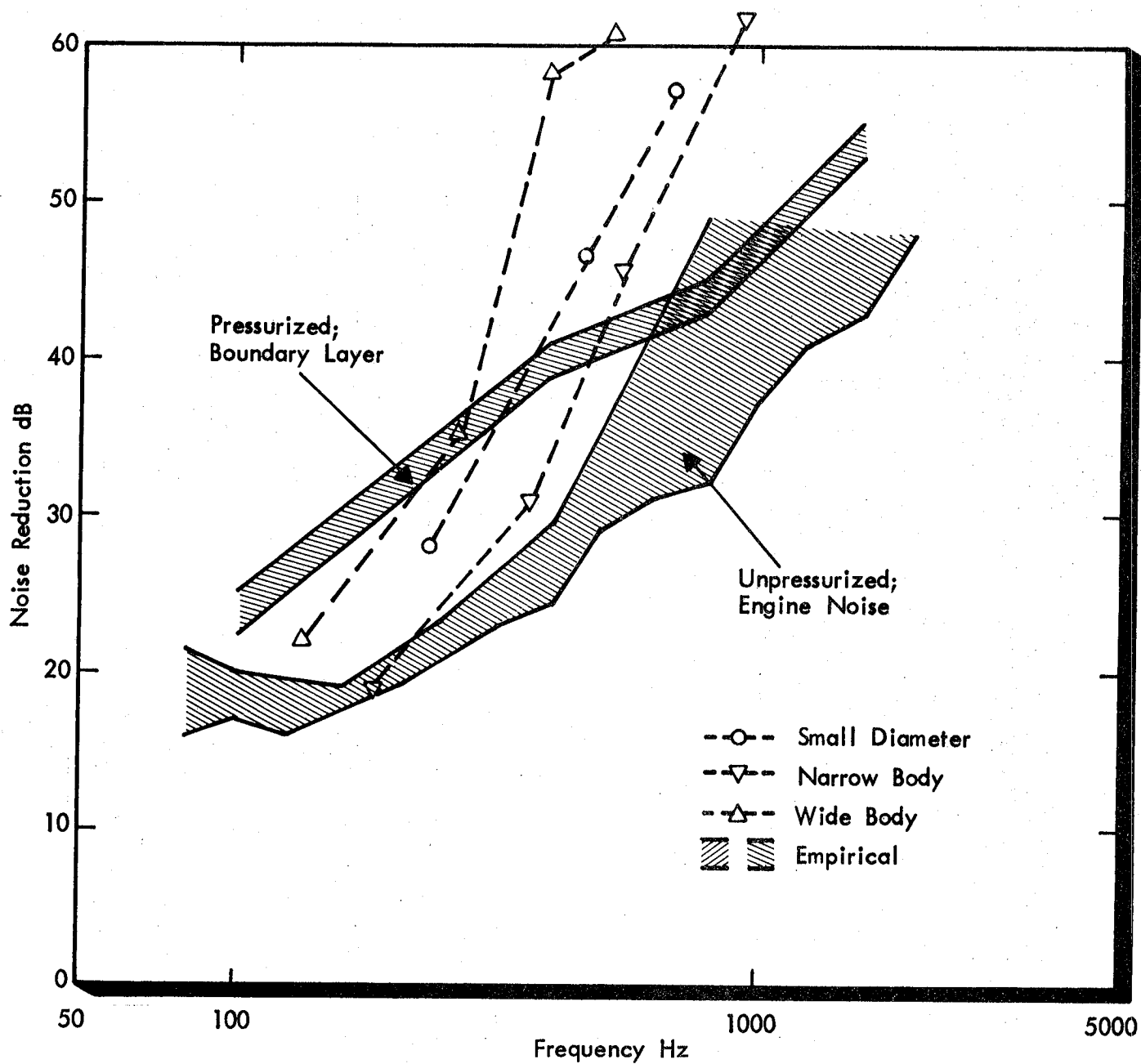


FIGURE 46. COMPARISON OF CALCULATED BASELINE NOISE REDUCTIONS WITH EMPIRICAL DATA FOR NARROW-BODIED FUSELAGES

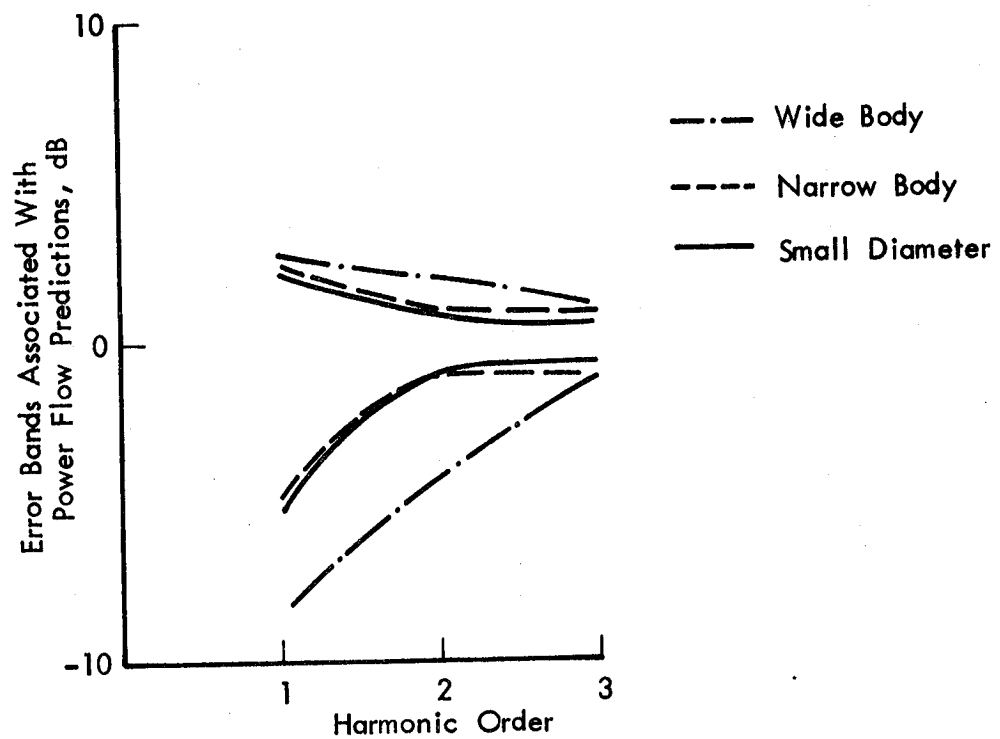


FIGURE 47. EXPECTED ERROR LIMITS FOR THE ACOUSTIC POWER FLOW INTO THE AIRPLANE CABINS

Table 9.

Calculated error limits for the
acoustic power flow into airplane cabins

Harmonic Order	Upper Limit (10 log(1+2ε)) * dB			Lower Limit (10 log (1-2ε)) dB		
	1	2	3	1	2	3
Wide-Body	+2.7	+2.1	+1.1	-8.5	-4.2	-1.5
Narrow-Body	+2.3	+0.9	+0.9	-4.9	-1.1	-1.2
Small-Diameter	+2.3	+0.8	+0.6	-5.2	-1.0	-0.7

*2ε corresponds to 2σ limits on the acoustic power flow.

6.2 Alternative Excitation Spectra

The calculated axial variation in cabin A-weighted interior noise levels for the study airplanes, with baseline fuselage and sidewall structures, but with alternative excitation spectra, are presented in Figure 48, and the corresponding cabin noise spectra at the location of maximum dB(A) level are shown in Figure 49. The differences in maximum dB(A) noise level between different spectra for each of the airplanes (Figure 48) result from changes in the level of the fundamental relative to the SPL5 baseline excitation, as shown directly in Figure 49. Errors in estimation of the fundamental of the excitation spectrum are directly reflected as errors in the A-weighted interior noise levels.

Since the Hamilton Standard spectrum represents the state-of-the-art prediction and also leads to the most conservative

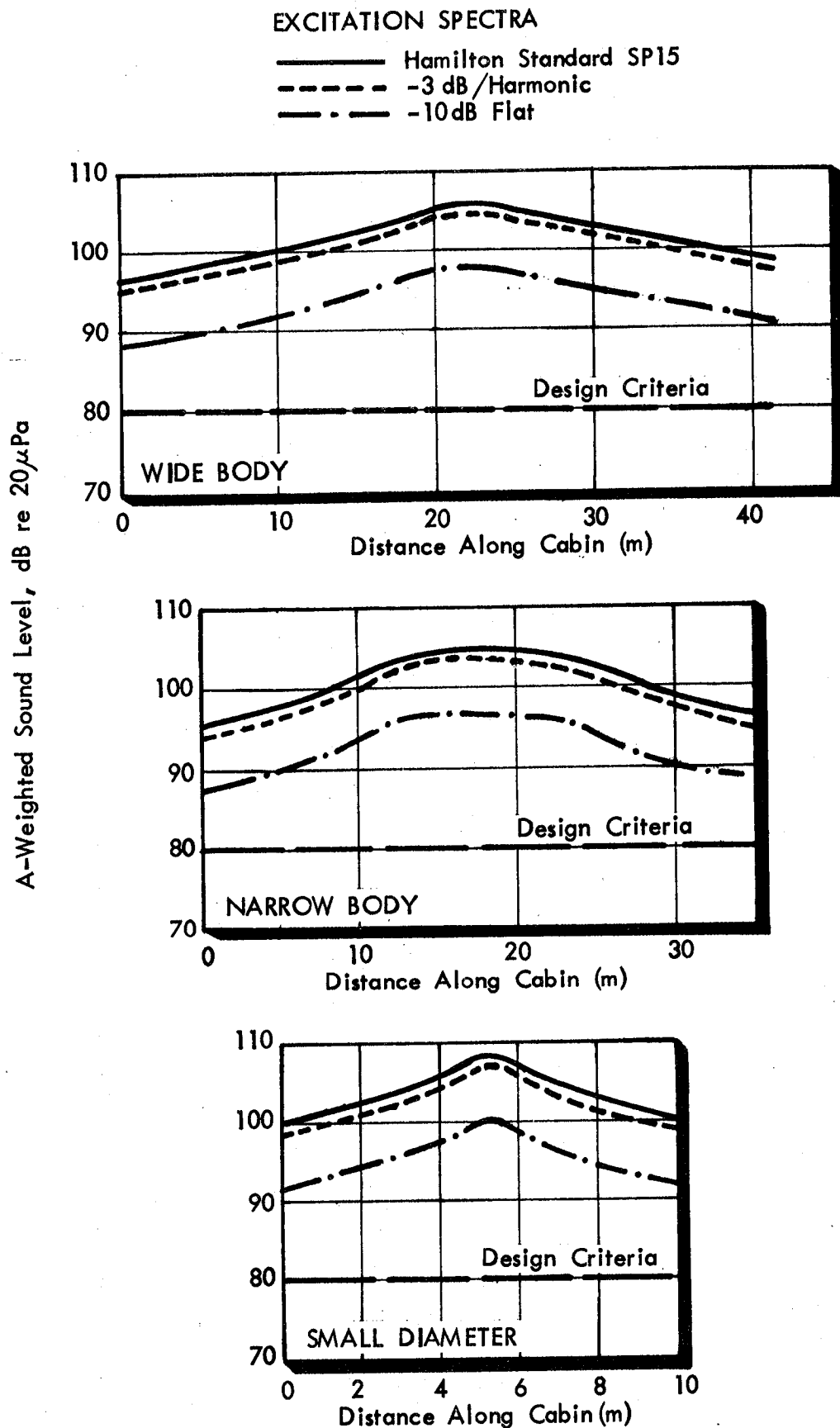


FIGURE 48. AXIAL VARIATION OF CABIN A-WEIGHTED SOUND LEVEL FOR DIFFERENT EXCITATION SPECTRA (BASELINE STRUCTURE, TRANSMISSION LOSS AND ABSORPTION)

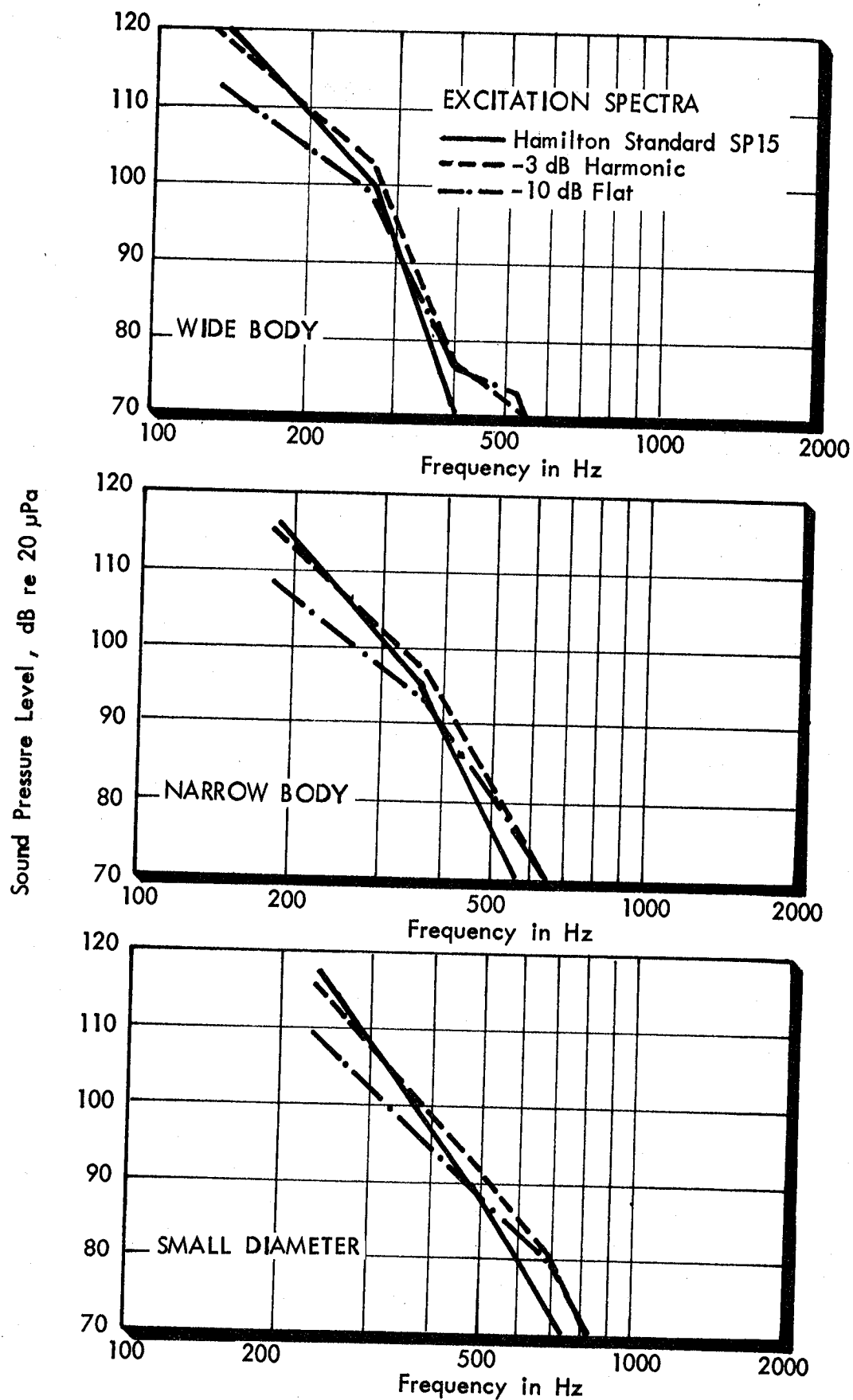


FIGURE 49. CABIN SPECTRA AT LOCATION OF MAXIMUM SOUND LEVEL FOR DIFFERENT EXCITATION SPECTRA

(i.e., highest) interior noise estimates, all subsequent calculations will be performed using this spectrum model for the excitation.

6.3 Conclusions

Clearly, substantial increases in the transmission loss of fuselage/sidewall structure are required for each of the study airplanes to achieve the design A-weighted noise level of 80 dB maximum anywhere within the airplane cabin. The required increases in airplane sidewall noise reduction vary between 24 and 28 dB at the fundamental excitation frequency, significantly greater than the noise reductions provided by the baseline sidewall fuselage structures, typical of conventional airplanes, particularly for the larger diameter aircraft which are driven by slower, larger diameter propellers.

7. ADD-ON NOISE REDUCTION METHODS

7.1 General

The range of add-on noise control treatments available for consideration in the analytical model includes variations of the sidewall transmission coefficient, variations to the internal absorption coefficient, increased damping and stiffness of the primary structure by add-on means, and optimizing the location of interior furnishings such as galleys and lavatories. Following a series of preliminary calculations of the structural characteristics and of the baseline interior noise levels, it is apparent that certain approaches would not provide significant increases in the fuselage noise reduction. For example, at low frequency, the "smeared" properties of the fuselage structure are dominated by the major stiffeners (frames, stringers) so that the adhesion of honeycomb panels to subpanel elements would produce little change in "smeared" stiffness and mass characteristics of the structure. Consequently, the associated changes in fuselage noise reduction would be small. Partitioning of the cabin volume and, similarly, placement of galleys, lavatories, etc. at particular fuselage locations close to the areas of peak excitation pressure levels, are also of little benefit for noise control because of the large extent of the fuselage structural area aft of forward propeller plane that transmits significant levels of acoustic power into the cabin interior.

Thus, efforts have been concentrated on those add-on methods of noise control for which it is clear that substantial increases in fuselage noise reduction would be possible. These include

1. optimizing the low-frequency absorption coefficients;
2. increasing the structural loss factor of the fuselage at low frequencies by the addition of patches of damping material to the skin and stiffeners; and
3. upgrading the noise reduction of add-on sidewall treatment by construction of a limp-mass double wall system.

The results of computations for these add-on treatments are now presented.

7.2 Maximizing the Interior Absorption Coefficients

Baseline absorption coefficients for the various study airframes are discussed in Section 4.5. At low frequencies, the absorption coefficients are generally less than 0.3 so that there is some potential for increasing the absorption at these frequencies. The improvements would be practical only on sidewall and ceiling surfaces where significant cavity depth exists, although the use of relatively massive trim panels in a double-wall configuration will tend to limit the increases in sidewall absorption coefficients.

For modeling purposes, however, changes in interior absorption are assumed to occur only on the sidewall surfaces. The maximum absorption considered practical is shown in Figure 50 together with baseline data. The effects of this change in cabin absorption on cabin A-weighted sound levels are shown in Figure 51 for each of the study aircraft. At the location of maximum internal sound level, reductions of only 1 to 2 dB are produced, while away from this location the benefits of increased sidewall absorption are somewhat greater with changes in space-average A-weighted

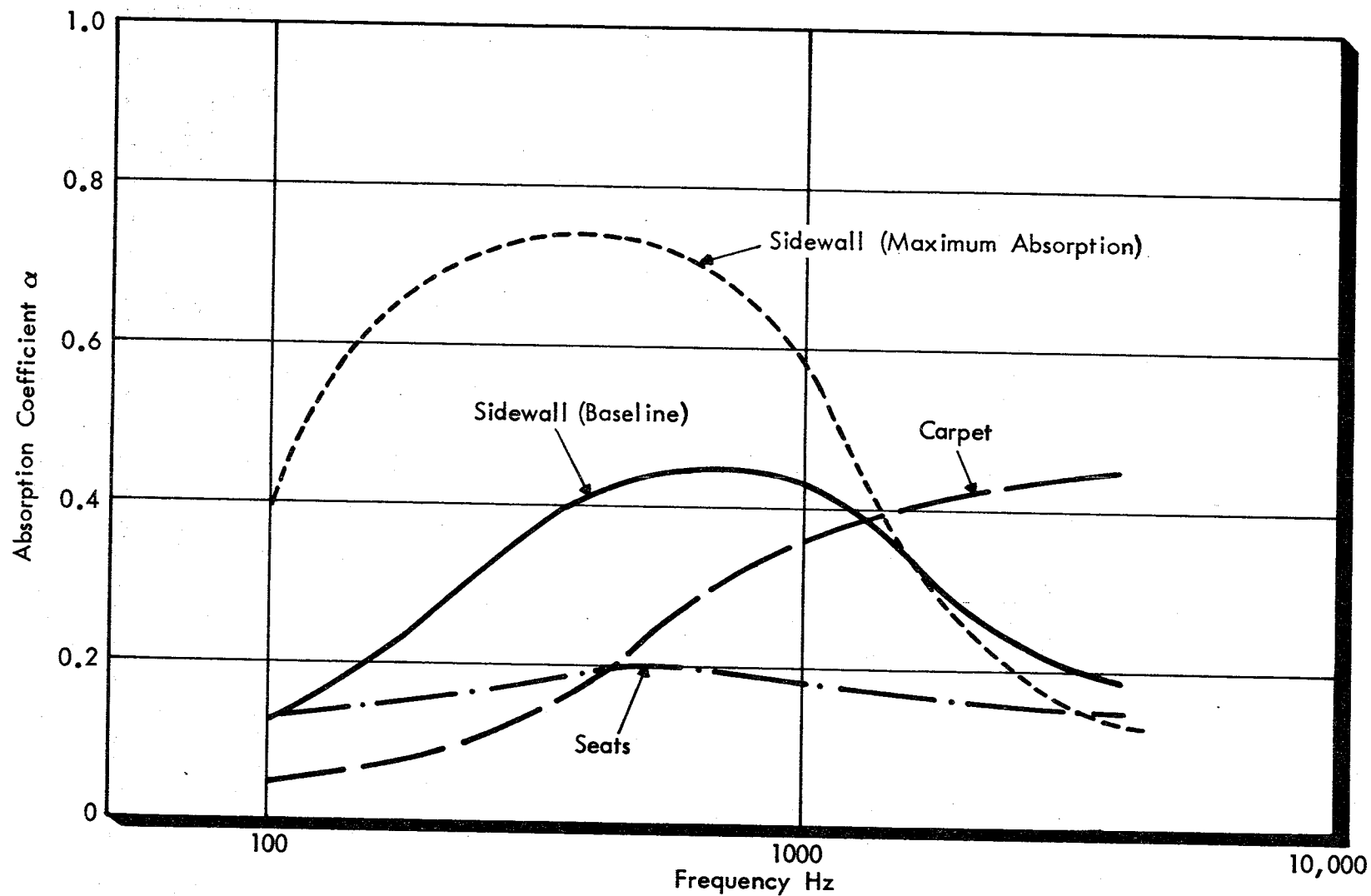
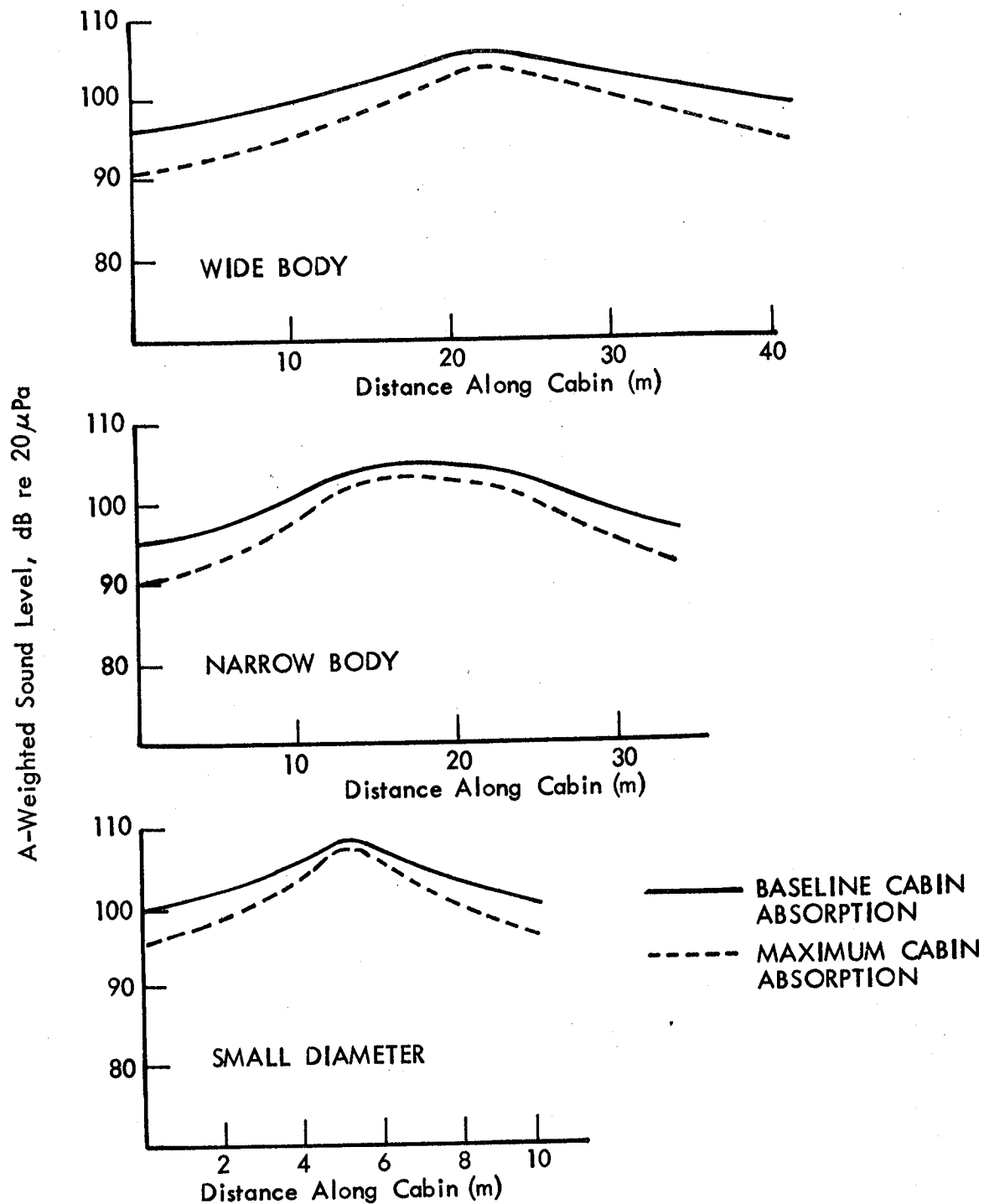


FIGURE 50. SOUND ABSORPTION SPECTRA ASSUMED FOR FURNISHING COMPONENTS



Cabin Absorption	Maximum Sound Levels in Cabin, dB(A)		
	Wide Body	Narrow Body	Small Diam.
Baseline	105.5	104.9	108.1
Maximum	103.5	103.3	107.1

FIGURE 51. EFFECT OF CABIN ABSORPTION ON CABIN A-WEIGHTED SOUND LEVELS

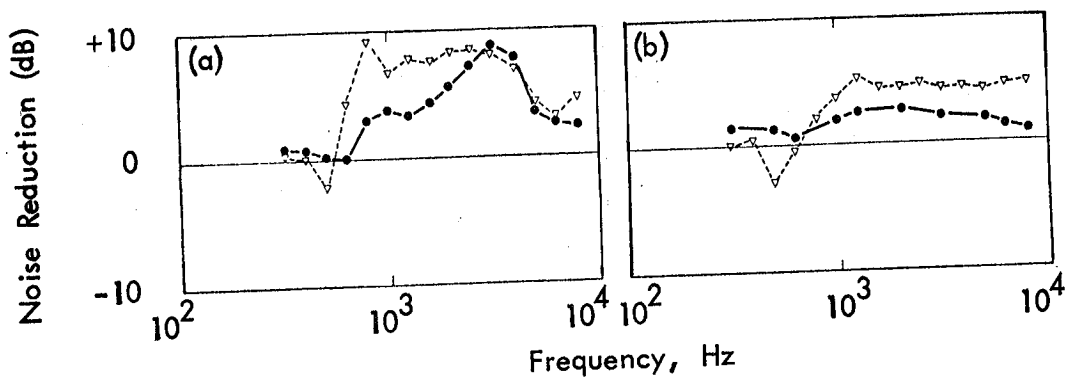
noise levels varying between 2 and 4 dB. The reason that the peak levels change by such small amounts is due to the dominance of the direct contribution of sidewall radiation. The reverberant level contributions to local A-weighted sound levels lie some 3 to 4 dB below the direct field levels.

It is concluded that maximizing interior absorption coefficients will lead to only small decreases in interior noise levels, insufficient to achieve the 80 dB A-weighted interior sound level criterion.

7.3 Increased Structural Damping

It has been shown, in Section 5.6 and, in particular, Figure 36, that the low frequency structural total loss factors for the baseline aircraft are mainly determined by radiation losses. The application of damping treatments to the fuselage structure must therefore be quite extensive to be at all effective in increasing the total low frequency structural loss factors. In practice this is not an easily accomplished task, particularly since at low frequencies the add-on treatment must be applied to stiffening members rather than to the skin alone. When damping treatments are applied to the fuselage skin, increased structural loss factors and increased fuselage noise reduction are produced only at frequencies of the order of, and above, the fundamental resonance frequencies of the sub-panel elements (bounded by frames and stringers), as shown in Figure 52 taken from [35].

When damping treatments are applied to stringers in stringer-panel structures, using constrained layer techniques, the structure component, η_{struc} , of the total loss factor can be



Noise Reduction Survey. (a) Mach 0.85; (b) Mach 0.55.

● — — — ● Bare Skin, Damping Tape
 ▼ - - - - - ▼ Bare Skin, Rubber Wedges

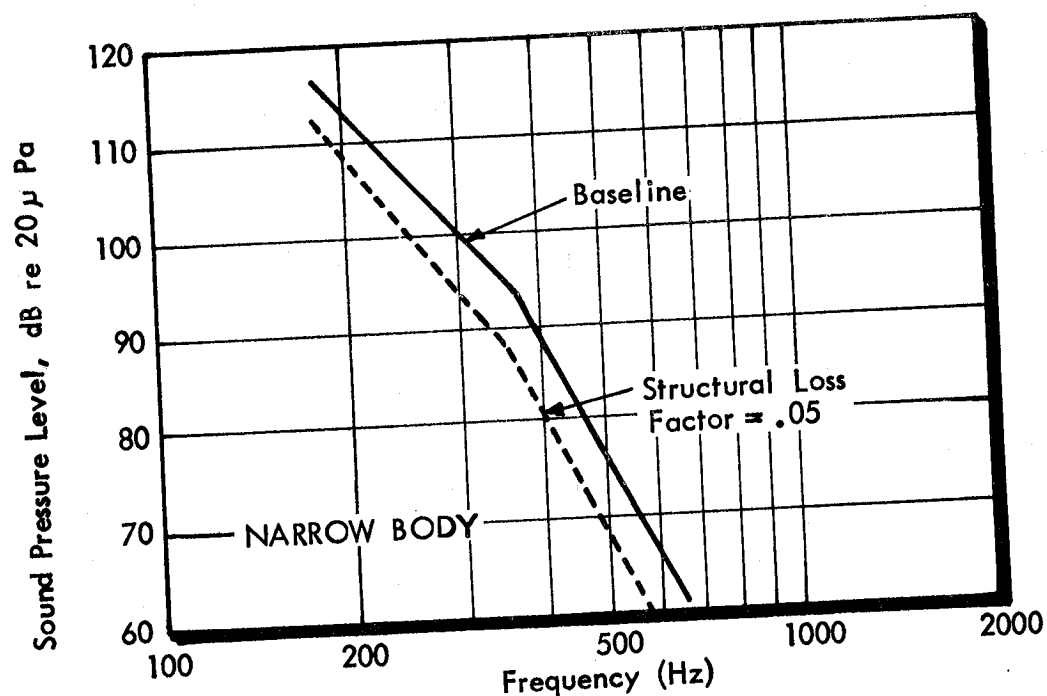
FIGURE 52. AIRPLANE TEST DATA ON THE EFFECT OF DAMPING TREATMENTS ON AIRPLANE INTERIOR NOISE LEVELS [35]

increased, by conventional techniques, to values in the range 0.05 to 0.10 [42]. If similar treatments are applied to the fuselage frames as well, it is probable that values of η_{struc} of 0.05 will be possible at low frequencies, where the frame stiffness influences the fuselage response and acoustic power flow. Taking this value $\eta_{\text{struc}} = 0.05$ for all frequencies, the total loss factor for the fuselage structure has been calculated for the three study airplanes and the resulting values are given by the upper curves in Figure 36.

These values of total structural loss factor were then used to estimate the probable maximum effect of add-on damping treatment on interior sound levels for each of the study airplanes. A typical spectral result is shown in Figure 53 for the narrow-body airplane, where results are compared for the baseline airplane and the airplane with anticipated maximum structural loss factor. Results showing the effect of increased structural damping on the maximum A-weighted levels for each of the study airplanes are also shown in Figure 53. It is clear that, at best, add-on damping treatments will provide only small noise reductions (3 to 5 dB) relative to baseline levels, and that add-on damping treatments of themselves will not provide the noise reduction required to achieve the design interior sound level criterion. Further, the combination of add-on damping treatments and tuned interior absorption, whose effects are essentially additive, will achieve interior sound levels only 5 to 7 dB lower than those of the baseline airplanes.

7.4 Double-Wall Sidewall Configurations

A preliminary investigation of add-on sidewall treatments by use of the analytical model indicated that large decreases in cabin sound level can be achieved by means of double-wall structures



CABIN SPECTRA FOR NARROW BODY AIRPLANE

Structural Damping	Airplane		
	Wide Body	Narrow Body	Small Diam.
Baseline	105.5	104.9	108.1
$\eta_s = .05$	102.1	100.6	104.7
Noise Reduction (dBA)	3.4	4.3	3.4

TABLE OF MAXIMUM SOUND LEVELS IN CABIN (dBA)

FIGURE 53. EFFECT OF STRUCTURAL DAMPING AT LOCATION OF MAXIMUM A-WEIGHTED SOUND LEVELS

which have fundamental resonance frequencies well below the fundamental excitation frequency. The lowering of the double-wall resonance frequency can be accomplished either by increasing the cavity depth ℓ or by increasing the trim panel surface density μ_2 (see Section 3.9 for nomenclature definitions). The presence of porous material within the cavity of the double wall is important to damp both the double-wall resonance and the airgap resonances which occur at frequencies where the airgap depth is approximately equal to an acoustic half-wavelength. On the other hand, the use of a single layer of glass fibers, either alone or in combination with light-weight septa were shown in [5] to provide insignificant increases in sidewall transmission loss at the low frequencies characteristic of the prop-fan fundamental blade passage frequencies.

Sample calculations, using the model presented in Section 3.9, have been performed to show the estimated transmission losses associated with different double wall systems where a limp trim panel was added to each of the baseline fuselage structures. The calculations were performed both for an empty air space between the two walls and for a space filled with porous material. The depth of the airgap was taken to be 127mm (5 in), a value which is typical of the maximum depth acceptable in current day commercial aircraft. Resulting transmission loss spectra for the wide-body fuselage are compared in Figure 54 for two values of the trim panel surface density μ_2 (2.0 and 8.0 kg/m², or 0.41 and 1.64 lb/ft²) and with porous material having characteristics similar to those of PF105AA glass fibers and a bulk density of 9.6 kg/m³. The results for other study airplane fuselage structures are essentially identical with those presented. The curves in Figure 54 show that the effect of increasing μ_2 from 2.0 to 8.0 kg/m² is to increase the sidewall transmission

Porous Material: Owens-Corning Fibreglas
 PF - 105 AA 9.6 kg/m³
 $R_1 = 4.3 \times 10^4$ mks rays/m

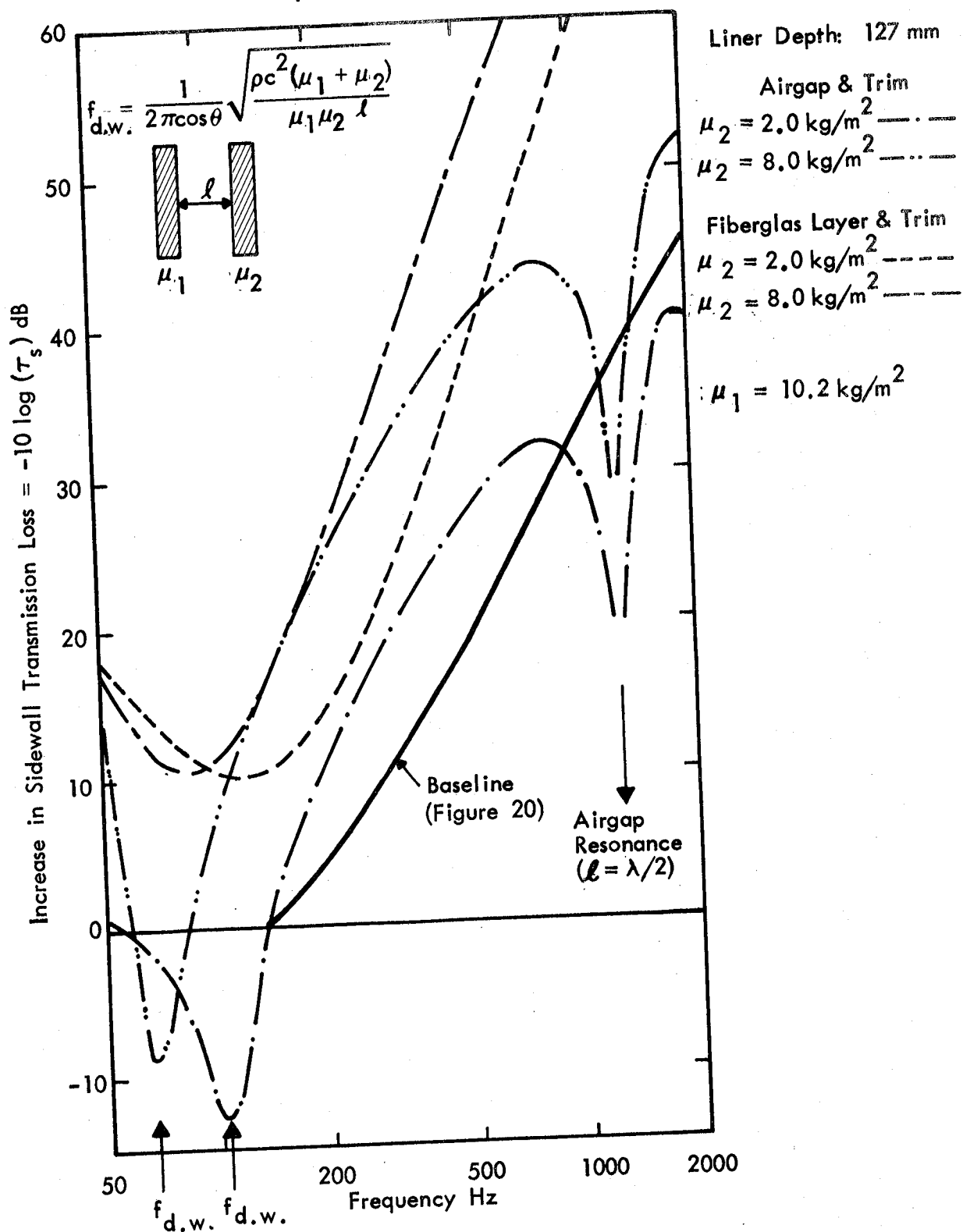


FIGURE 54. ADDITIONAL SIDEWALL TRANSMISSION LOSS
 (DOUBLE WALL CONFIGURATION WITHOUT
 FLANKING)

loss by about 12 dB, or by 6 dB per doubling of μ_2 . The double-wall resonance frequency decreases in accordance with the frequency equation given in Figure 54. At frequencies just above the double-wall resonance frequency, the effect of the porous material in the air space is small, at least for moderate values of flow resistance R_1 . As R_1 increases, the analysis predicts substantial increases in sidewall transmission loss, even at the double-wall resonance frequency. However, it is possible that at these high values of R_1 the assumption that there is no structureborne transmission through the material fibers is no longer valid. In all cases the calculations assume that the trim panel is highly damped, or limp, and that there is no mechanical flanking path through the trim panel supports.

Figure 54 also contains the sidewall empirical transmission loss spectrum (Figure 20) assumed for the baseline treatment. The baseline properties ($\ell = 102$ mm, $\mu_2 = 1.76$ kg/m²) are similar to those for the lighter weight of the two analytical model sidewalls, yet the transmission losses are significantly lower. This difference between laboratory data and analytical predictions has been attributed [5] to the effects of flanking paths but there is, as yet, no confirmatory evidence. Little information is available on the vibration transmission through presently-used trim panel mounts, but, on the basis of [34], mounts with very low transmissibility will be required if the 80 dB(A) goal is to be achieved.

It has been shown in Section 6 that, in order to achieve the 80 dB(A) criteria, noise reductions of about 25 dB relative to the baseline sidewall treatment will be required at the fundamental blade passage frequency for each airplane. This increase in transmission loss is greater than the values shown in Figure 54 at corresponding frequencies. In fact, calculated

values of μ_2 , required to achieve the extra noise reduction, range from 15 to 35 kg/m², depending on airplane type. Figure 55 shows a representative set of transmission loss curves calculated for the range of values of μ_2 required to satisfy the design criterion.

Since the acoustic power inflow varies along the length of the fuselage (see Figure 40), the additional noise reduction required to meet the interior noise criterion will also vary. This will result in a sidewall installation whose weight varies along the length of the cabin. Figure 56 shows the predicted variation in sidewall treatment surface weight, calculated for the structural element idealization described in Section 5.7. In practice the variation in treatment weight will follow a smoother distribution along the cabin length but the total weight penalties will be similar. The data in Figure 56 show that well forward and well aft of the propeller planes, the sidewall treatment weights are similar to those of the baseline aircraft although, as indicated in Figure 54, the analytical model sidewall is more effective in reducing noise transmission. The main weight increases occur near the propeller plane of rotation.

Total weight penalties associated with the additional sidewall treatments are listed in Table 10. It is assumed that the sidewall treatments are applied only to the region above the floor line, although in practice some acoustic treatment will be required below the floor, and are applied uniformly in the circumferential direction above the floor. Since there is some circumferential variation in the external pressure field it is possible that some reduction in treatment weight might be achievable. However, the effect on total weight penalty will be small, and will be counteracted by the omission of under-floor treatment in the calculations.

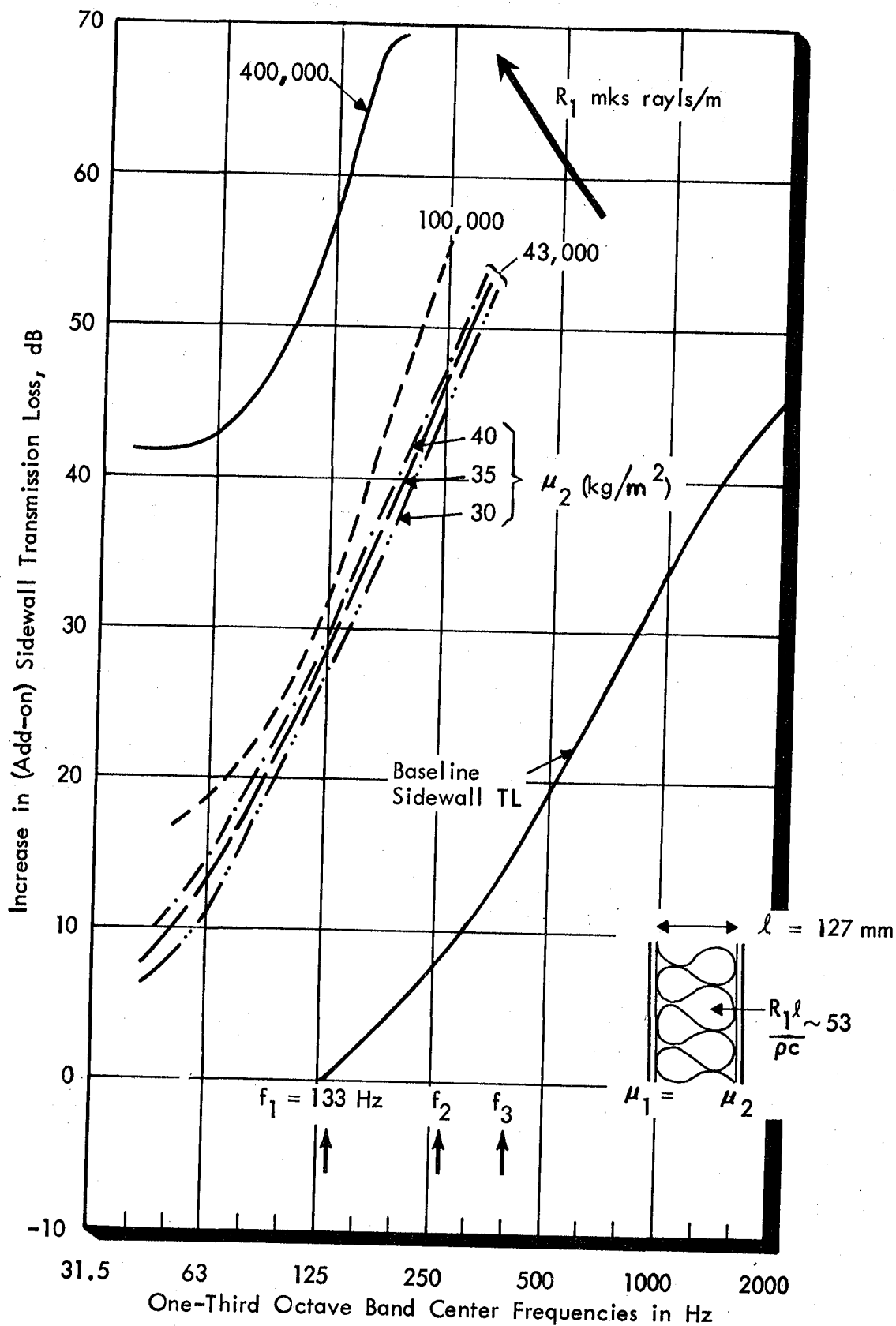


FIGURE 55. EFFECT OF FLOW RESISTANCE AND TRIM SURFACE DENSITY ON ADD-ON SIDEWALL TRANSMISSION LOSS FOR DOUBLE WALL SIDEWALL (NO FLANKING)
 $(\mu_1 = 10.2 \text{ kg/m}^2)$
 $(\mu_2 = 30.0 \text{ kg/m}^2 \text{ for } R_1 = 100,000 \text{ \& } 400,000 \text{ mks rays/m})$

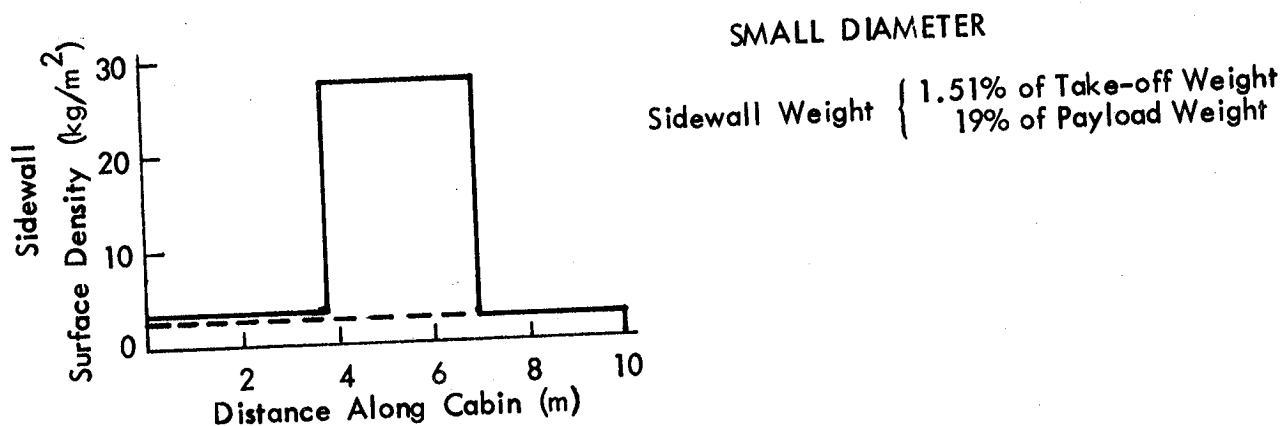
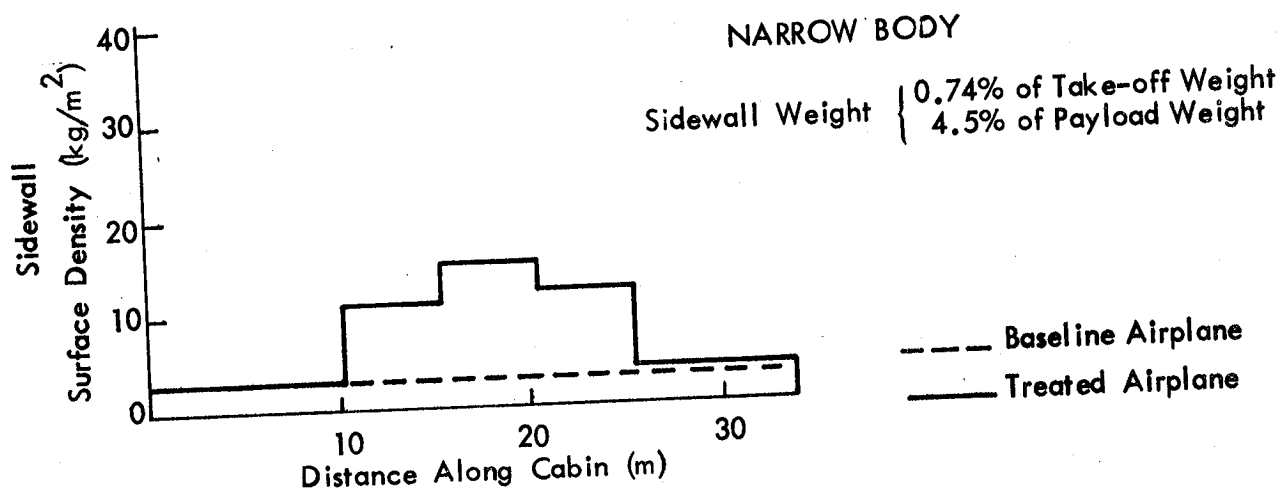
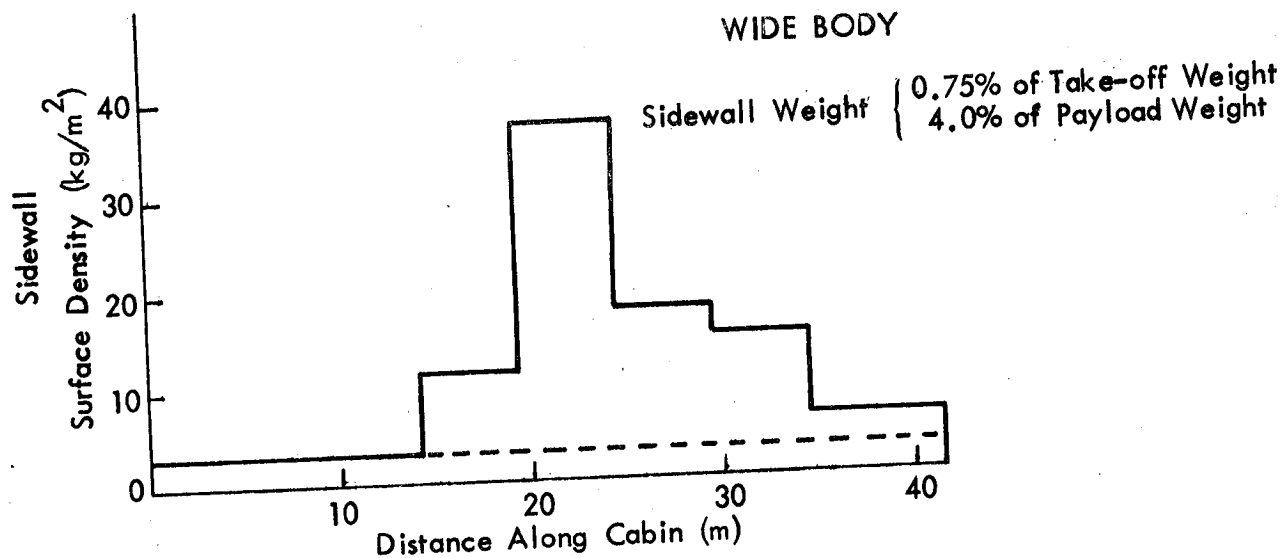


FIGURE 56. VARIATION OF SIDEWALL TREATMENT SURFACE DENSITY ALONG CABIN LENGTH TO ACHIEVE 80dB(A) MAXIMUM CABIN SOUND LEVEL

TABLE 10
 Predicted Weight Increase, relative to Baseline
 Aircraft, to achieve 80 dB A-Weighted Sound Level Criterion

Airplane	Airplane Weight (kg)	Payload Weight (kg)	Additional Sidewall Weight		
			(kg)	% Take-Off Weight	% Payload Weight
Wide-Body	252,000	47,500	1,890	0.75	4.0
Narrow-Body	148,000	24,500	1,090	0.74	4.5
Small-Diameter	30,000	2,350	450	1.51	19.0

From this analysis it is apparent that, at least for the idealized double-wall system, the required reductions in cabin noise level can be achieved. However, in order to achieve these exceptionally high transmission losses at low frequencies it is imperative that there be no structural flanking paths across the trim panel mounts or through the porous material in the cavity. The practicality of achieving this vibration-isolated double-wall system in an airplane environment has to be proven.

7.5 Summary

Add-on treatments considered in this study included double walls (with and without glass fiber batts), damping, skin panel stiffness, absorption in the cabin, and cabin partitions. Only the double wall with batts can provide the required noise reductions at low frequencies. Cabin partitions have no benefit because of the spatial extent of the power inflow, and add-on stiffness to the panel has little effect at low frequencies because the power inflow is determined by stringer and frame characteristics.

Large increases in cabin absorption or structural damping result in only small reductions in peak cabin noise level. Furthermore the damping material has to be applied to the frames and stringers, and practical methods of accomplishing this have yet to be developed.

The add-on sidewall treatments developed for the three study airplanes are summarized in Appendix D. Detailed optimization studies to minimize weight were not performed because the weights associated with increased damping treatments would be speculative and the predicted noise reductions are small. However, when practical methods of increasing the structural damping and cabin absorption at low frequencies have been developed, optimization studies can be performed, combining double walls, add-on damping and increased absorption techniques. The predicted noise reduction and weight penalties will, of course, depend on the external pressure field characteristics, the results presented in Section 7 and Appendix D referring to the pressure spectrum shape (SP15 Spectrum of Figure 26) given by current prediction procedures. For a given overall level, this spectrum shape resulted in higher interior noise levels, and larger weight penalties, than did the other two study spectra.

8.0 ADVANCED NOISE REDUCTION METHODS

In the present context, advanced noise reduction methods are those methods which involve modification to the fuselage primary structure. It is unlikely that such changes could be made as retrofit modifications to existing structures. Instead, they would be incorporated in new fuselage designs, and, as such, they would have to undergo the usual pre-certification testing before being placed in passenger service. The testing could be extensive if the new structures are significantly different from present-day aluminum skin-stringer-frame configurations. Because of the anticipated long lead time associated with the introduction of advanced noise reduction methods, they have been given less emphasis in the present study than have the add-on noise reduction methods.

Since the fuselage frames determine the fuselage stiffness at low frequencies, modification to the frames was one of the important advanced noise reduction methods explored in the study. Also changes were made to the skin thickness. Variations to the stringer stiffness were not considered in this phase of the study as the effects would lie between those due to the frames and the skin. However, some indication of the effect of stringer stiffness can be seen in Figure 86 in Section 9.5. Factors considered in the study of advanced noise control included frame spacing and stiffness, skin thickness, and the use of honeycomb panels. The calculations were performed using the baseline acoustic sidewall system as presented in Section 4.5.4.

8.1 Variations in Frame Parameters

8.1.1 Frame Stiffness

The effects of doubling the frame bending stiffness parameter, $E_r I_r / Eh$, are shown in Figure 57. (This parameter gives the frame stiffness normalized with respect to the skin parameters.) The figure compares harmonic levels for the cabin sound levels at the location of maximum A-weighted level, using baseline calculations as reference. Data for each study airplane show that the increased frame stiffness results in reductions in cabin sound level, but the changes are small (0 to 3 dB).

The structural changes represented by this doubling of frame stiffness could be achieved either by the use of composite materials in the frame construction or by redesign of the conventional frame cross-section to increase the frame modulus of inertia I_r , while keeping the radius of gyration \bar{z}_r and cross-sectional area A_r constant.

Structural dimensions and fuselage parameters associated with the doubling of frame stiffness are listed in Tables 11 through 13 for each of the study airplanes.

8.1.2 Frame Spacing

A second approach considered was that of maintaining the frame stiffness equal to that of the baseline configuration, but doubling the number of frames by halving the frame spacing. Structural dimensions and fuselage parameters associated with this modification are given in Tables 11 through 13 for the three study airplanes, and the changes in harmonic sound level are plotted in Figure 57 for the three lowest order harmonics.

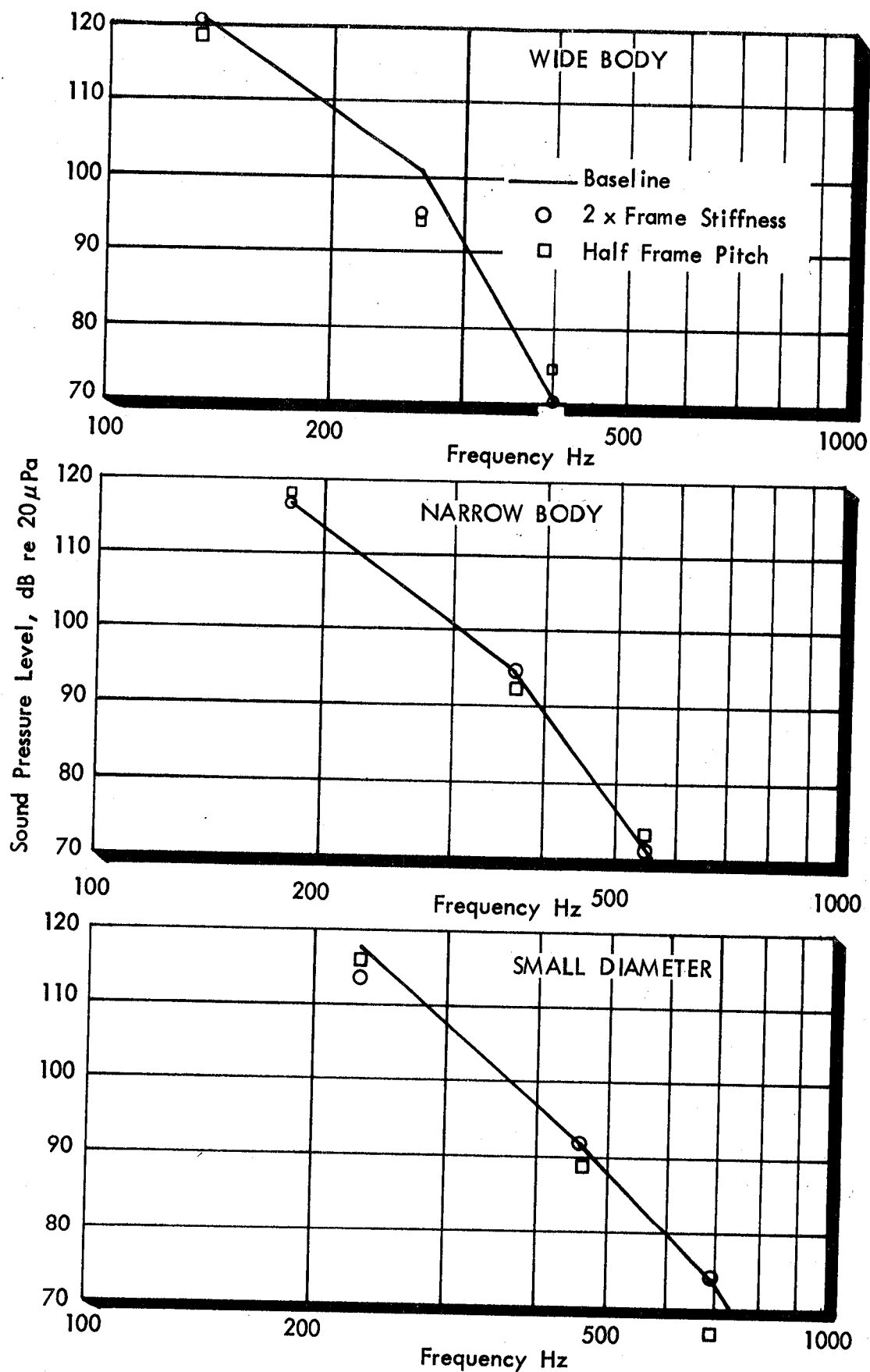


FIGURE 57. CABIN SPECTRA AT LOCATION OF MAXIMUM SOUND LEVELS, FOR CHANGES IN FRAMES

Table 11
FUSELAGE DETAILS FOR ADVANCED NOISE CONTROL STRUCTURES: WIDE BODY

Description	Baseline	2x Frame E	1/2 Frame Pitch	2x Skin Thickness	4x Skin Thickness	Honeycomb Skin
Element Number	4	4	4	4	4	4
Frame Spacing ℓ_x (m)	0.5080	0.5080	0.2540	0.5080	0.5080	0.5080
Stringer Spacing ℓ_y (m)	0.1829	0.1829	0.1829	0.1829	0.1829	-
<u>Skin</u>						
Thickness (mm)	1.778	1.778	1.778	3.556	7.112	34.408*
Mass/Unit Area (kg/m ²)	4.8006	4.8006	4.8006	9.6012	19.202	5.7472
Bending Stiffness D (N-m)	38.133	38.133	38.133	305.06	2440.5	13.012
Torsional Stiffness D_k (N-m)	12.584	12.584	12.584	100.67	805.36	17.474
<u>Stringer</u>						
Mass/Unit Area $\rho A_s / \ell_y$ (kg/m ²)	2.6680	2.6680	2.6680	2.6680	2.6680	-
Bending Parameter $E_s I_s / D \ell_y$	170.72	170.72	170.72	21.340	2.6675	-
Membrane Parameter $E_s A_s / E h \ell_y$	0.5558	0.5558	0.5558	0.2779	0.1389	-
Torsional Parameter $G_s J_s / D \ell_y$	0.5084	0.5084	0.5084	0.06355	0.007944	-
Centroid \bar{Z}_s (m)	-0.01583	-0.01583	-0.01583	-0.01672	-0.01850	-
<u>Frame</u>						
Mass/Unit Area $\rho A_r / \ell_x$ (kg/m ²)	2.8209	2.8209	5.6417	2.8209	2.8209	1.3807
Bending Parameter $E_r I_r / D \ell_x$	4585.9	9171.7	9171.7	573.23	71.654	4.1835
Membrane Parameter $E_r A_r / E h \ell_x$	0.5876	1.1752	1.1752	0.2938	0.1469	0.3157
Torsional Parameter $G_r J_r / D \ell_x$	0.6427	1.2855	1.2855	0.08034	0.010043	0.000673
Centroid \bar{Z}_r (m)	-0.05468	-0.005468	-0.05468	-0.05557	-0.05735	-0.03817
$A_{rib} \times 10^3$ (m ²)	0.2734	0.2734	0.3273	0.2734	0.2734	-

*Equivalent skin thickness based on radius of gyration.

Table 12

FUSELAGE DETAILS FOR ADVANCED NOISE CONTROL STRUCTURES: NARROW BODY

Description	Baseline	2x Frame E	1/2 Frame Pitch	2x Skin Thickness	4x Skin Thickness	Honeycomb Skin
Element Number	4	4	4	4	4	4
Frame Spacing ℓ_x (m)	0.5080	0.5080	0.2540	0.5080	0.5080	0.5080
Stringer Spacing ℓ_y (m)	0.2286	0.2286	0.2286	0.2286	0.2286	-
<u>Skin</u>						
Thickness (mm)	3.0	3.0	3.0	6.0	12.0	23.326*
Mass/Unit Area (kg/m^2)	8.100	8.100	8.100	16.200	32.400	5.0195
Bending Stiffness D (N-m)	183.18	183.18	183.18	1465.4	11,723	5610.7
Torsional Stiffness D_k (N-m)	60.45	60.45	60.45	483.6	3868.7	6.4379
<u>Stringer</u>						
Mass/Unit Area $\rho A_s / \ell_y$ (kg/m^2)	1.0817	1.0817	1.0817	1.0817	1.0817	-
Bending Parameter $E_s I_s / D \ell_y$	23.687	23.687	23.687	2.9608	0.3701	-
Membrane Parameter $E_s A_s / E h \ell_y$	0.1335	0.1335	0.1335	0.06677	0.03338	-
Torsional Parameter $G_s J_s / D \ell_y$	0.01264	0.01264	0.01264	0.001581	0.000198	-
Centroid \bar{Z}_s (m)	-0.01855	-0.01855	-0.01855	-0.02005	-0.02305	-
<u>Frame</u>						
Mass/Unit Area $\rho A_r / \ell_x$ (kg/m^2)	1.6233	1.6233	3.2467	1.6233	1.6233	1.2389
Bending Parameter $E_r I_r / D \ell_x$	294.55	589.10	589.10	36.819	4.6023	6.6599
Membrane Parameter $E_r A_r / E h \ell_x$	0.2004	0.4008	0.4008	0.1002	0.05010	0.3019
Torsional Parameter $G_r J_r / D \ell_x$	0.04455	0.08910	0.8910	0.005569	0.000696	0.001397
Centroid \bar{Z}_r (m)	-0.03921	-0.03921	-0.03921	-0.04071	-0.04371	-0.03698
$A_{rib} \times 10^3$ (m^2)	0.1579	0.1579	0.1929	0.1579	0.1579	-

*Equivalent skin thickness based on radius of gyration.

Table 13
FUSELAGE DETAILS FOR ADVANCED NOISE CONTROL STRUCTURES: SMALL DIAMETER

Description	Baseline	2x Frame E	1/2 Frame Pitch	2x Skin Thickness	4x Skin Thickness	Honeycomb Skin
Element Number	2					
Frame Spacing ℓ_x (m)	0.3302	0.3302	0.1651	0.3302	0.3302	0.3302
Stringer Spacing ℓ_y (m)	0.1270	0.1270	0.1270	0.1270	0.1270	-
<u>Skin</u> Thickness (mm)	1.016	1.016	1.016	2.032	4.064	22.886*
Mass/Unit Area (kg/m ²)	2.7432	2.7432	2.7432	5.4864	10.9728	3.6695
Bending Stiffness D (N-m)	7.1151	7.1151	7.1151	56.921	455.37	3624.5
Torsional Stiffness D_k (N-m)	2.3480	2.3480	2.3480	18.784	150.27	5.0663
<u>Stringer</u> Mass/Unit Area $\rho A_s/l_y$ (kg/m ²)	1.0973	1.0973	1.0973	1.0973	1.0973	-
Bending Parameter $E_s I_s/Dl_y$	96.588	96.588	96.588	12.074	1.5092	-
Membrane Parameter $E_s A_s/Eh l_y$	0.4000	0.4000	0.4000	0.2000	0.1000	-
Torsional Parameter $G_s J_s/Dl_y$	0.4947	0.4947	0.4947	0.06184	0.007730	-
Centroid \bar{Z}_s (m)	-0.00744	-0.00744	-0.00744	-0.00795	-0.00897	-
<u>Frame</u> Mass/Unit Area $\rho A_r/l_x$ (kg/m ²)	1.0034	1.0034	2.0068	1.0034	1.0034	1.0889
Bending Parameter $E_r I_r/Dl_x$	2840.9	5681.7	5681.7	355.11	44.388	4.5981
Membrane Parameter $E_r A_r/Eh l_x$	0.3658	0.7315	0.7315	0.1829	0.09144	0.3954
Torsional Parameter $G_r J_r/Dl_x$	0.4066	0.8132	0.8132	0.05083	0.006353	0.001011
Centroid \bar{Z}_r (m)	-0.03911	-0.03911	0.03911	-0.03962	-0.04064	-0.02500
$A_{rib} \times 10^3$ (m ²)	0.07136	0.07136	0.08252	0.07136	0.07136	-

*Equivalent skin thickness based on radius of gyration.

It is seen that this method produces only small changes in harmonic level, and in some cases the sound level increases rather than decreases.

8.2 Variation in Fuselage Skin Thickness

Two situations were considered with regard to skin thickness. First, the skin thickness was doubled with respect to the baseline configuration. Then the thickness was doubled again so that it was four times the baseline value. The resulting fuselage details for the three study airplanes are tabulated in Tables 11 through 13.

Changes in harmonic sound level associated with the doubled and quadrupled skin thicknesses are shown in Figure 58 for the three lowest-order harmonics and the three study airplanes. The spectra correspond to the location in the cabin with the highest A-weighted sound level.

In general an increase in skin thickness results in a decrease in harmonic level for the cabin sound spectra. However, only in the case of the narrow-bodied airplane, which has a relatively thick skin in the baseline configuration, does the noise reduction exceed 3 dB for either the first order (fundamental) harmonic or the A-weighted sound level. As the skin thickness increases within the range considered, it is found that the structural modal density at low frequencies increases but, at the same time, the band-averaged joint acceptance decreases. The increase in modal density occurs because, at these frequencies, the fuselage stiffness is dominated by the frame characteristics and the increase in skin thickness is observed mainly as an increase in structural mass.

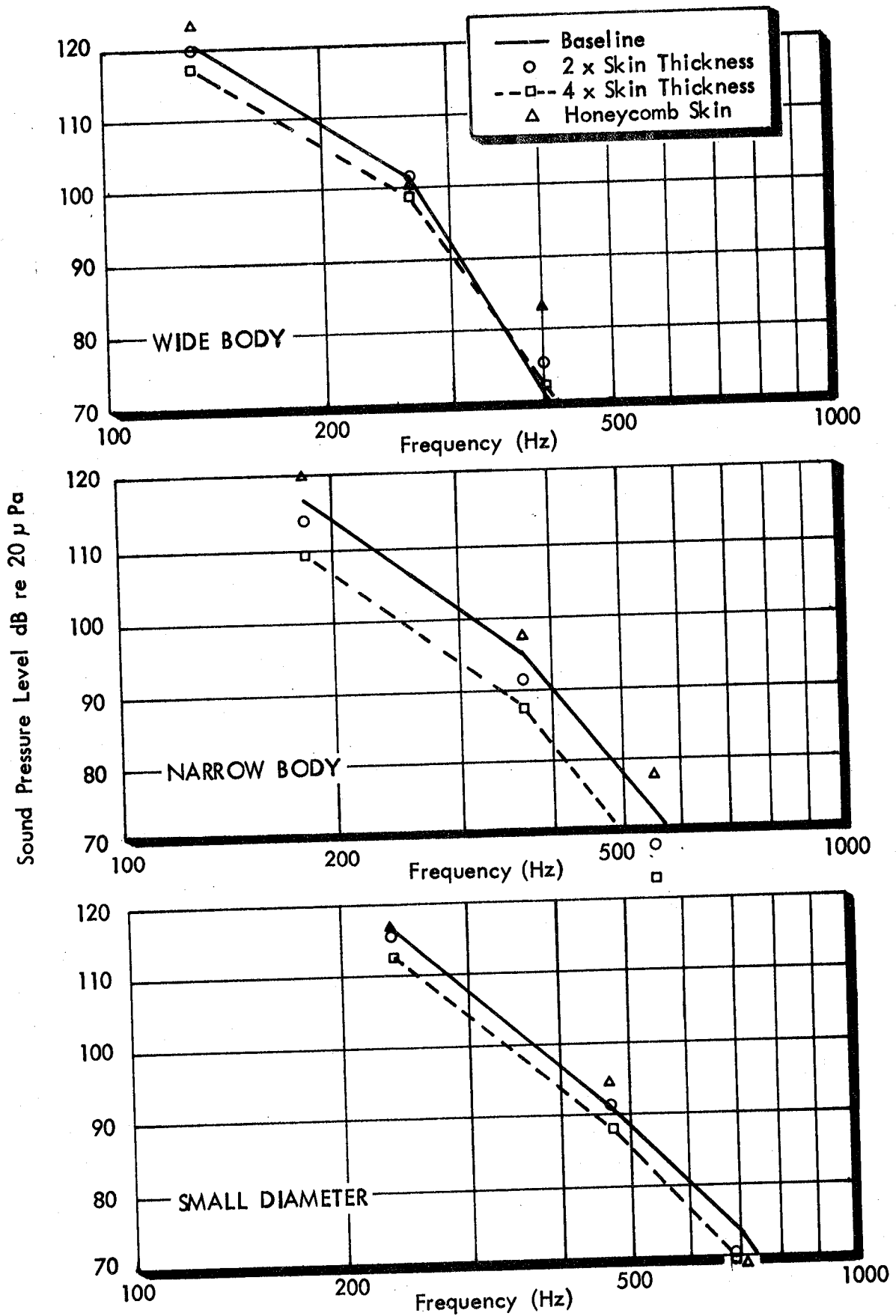


FIGURE 58. CABIN SPECTRA AT LOCATION OF MAXIMUM SOUND LEVELS, FOR CHANGES IN SKIN

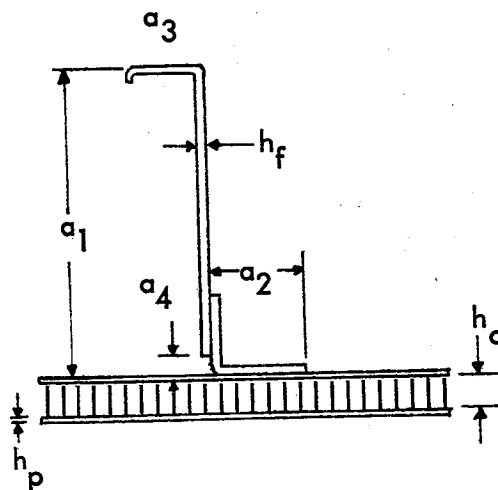
These changes in modal density and joint acceptance essentially cancel each other for the wide-body and small diameter cases and the resulting noise reduction is small. For the narrow-body airplane, however, the baseline skin mass is relatively large so that the cabin noise levels are more sensitive to further increases in skin thickness.

8.3 Honeycomb Skin Panels

During recent years there have been several investigations concerned with the use of honeycomb panels for fuselage primary structures, although no such structures have yet been introduced for passenger-carrying aircraft. One advantage of honeycomb construction is that fuselage stiffness characteristics can be maintained whilst reducing the total weight of the fuselage. However, the noise transmission characteristics of the honeycomb panels, when exposed to typical fuselage exterior pressure fields, have not been explored. Consequently honeycomb skin panels were included in this analysis of advanced noise control methods.

It was not possible, within the scope of this program to develop an analytical model for noise transmission, to derive general design characteristics for honeycomb fuselage structures. Thus, reference was made to available structural investigations. In particular honeycomb structures were designed on the basis of fuselage configurations presented in [29]. The honeycomb structures have ring frames with the same pitch as for the corresponding baseline study aircraft, but no stringers are used. A typical panel configuration is shown in Figure 59, and dimensions are listed in Table 14. Structural characteristics are presented in Tables 11 through 13.

TABLE 14: DIMENSIONS FOR HONEYCOMB STRUCTURES



			WIDE-BODY FUSELAGE	NARROW-BODY FUSELAGE	SMALL-DIAMETER FUSELAGE
CORE THICKNESS	h_c	(mm)	19.05	12.70	12.70
FACE PLATE THICKNESS	h_p	(mm)	0.81	0.76	0.51
FRAME THICKNESS	h_f	(mm)	1.40	1.40	1.02
FRAME DEPTH	a_1	(mm)	101.6	88.9	63.5
FLANGE LENGTH	a_2	(mm)	31.75	25.40	20.32
FLANGE LENGTH	a_3	(mm)	25.4	25.4	20.32
WEB-HONEYCOMB SEPARATION	a_4	(mm)	6.35	6.35	6.35
FRAME SPACING		(m)	0.508	0.508	0.330

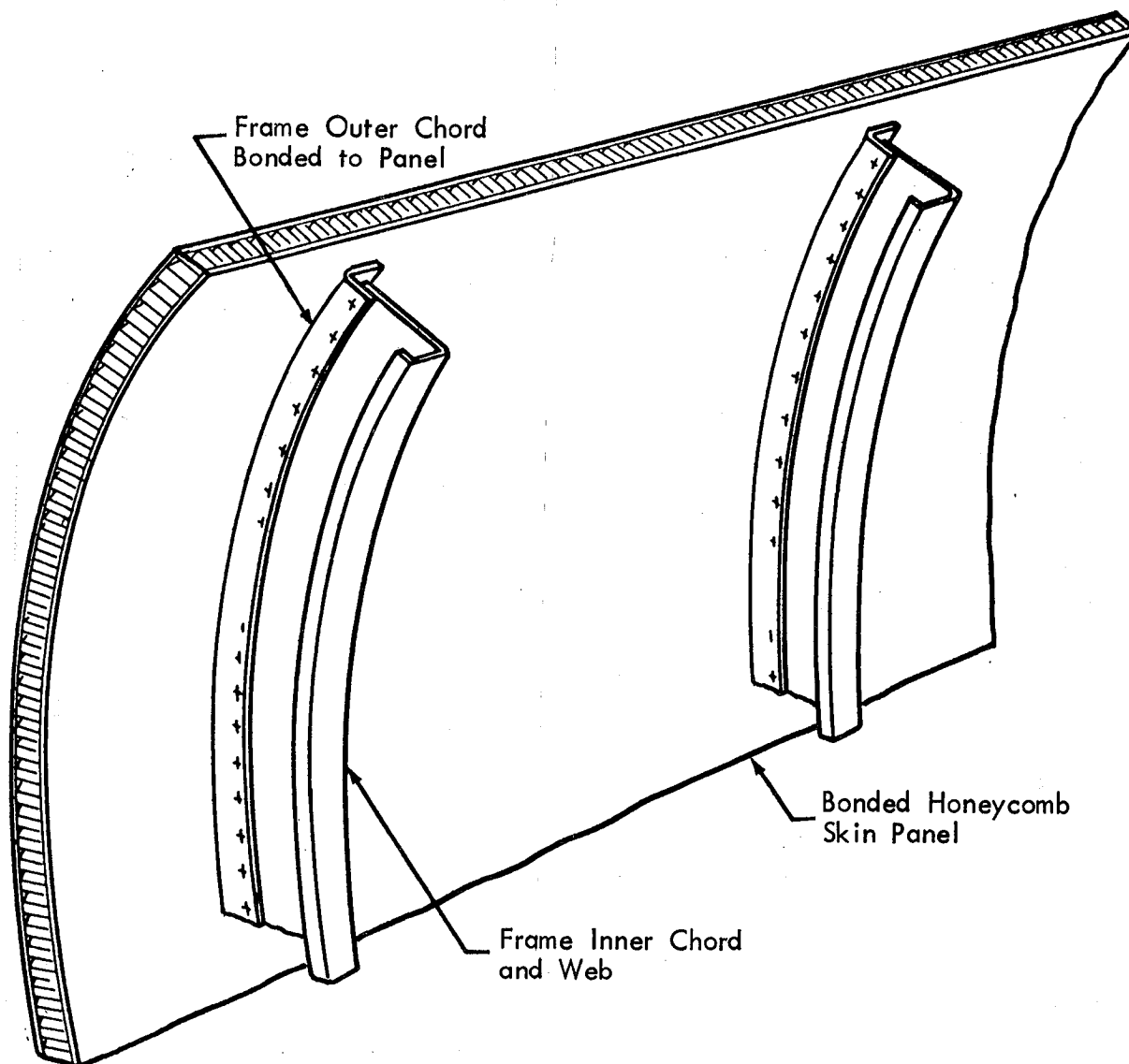


FIGURE 59. REPRESENTATION OF FRAME-STIFFENED HONEYCOMB FUSELAGE SHELL

Predicted spectra associated with the cabin maximum A-weighted sound levels for each study airplane with honeycomb structure are presented in Figure 58. It is seen that, for the selected structures, there is a general, although small, increase in sound level relative to the baseline configuration. Inspection of the analysis indicates that the noise increase is due to the decrease in smeared-out mass of the structure. Thus, the use of light-weight fuselage structures with bending and membrane stiffness parameters equivalent to those of conventional structures, and with similar fuselage loss factors will lead in general to increases in interior sound levels. Optimization of honeycomb structures with respect to noise transmission will require extensive use of the analytical model and development of dynamic models more suitable for honeycomb structures.

8.4 Summary

The results of the study of advanced noise control methods presented in this section are summarized in Table 15 and Figure 60 in terms of changes in A-weighted sound level and the surface mass density of the structural element which transmits the major fraction of the acoustic power inflow. The total mass per unit area is quoted in the table, and the change in surface density, relative to the baseline structure, is shown in the figure. In all cases it is assumed that the sidewall treatment is the same as that for the corresponding baseline study airplane.

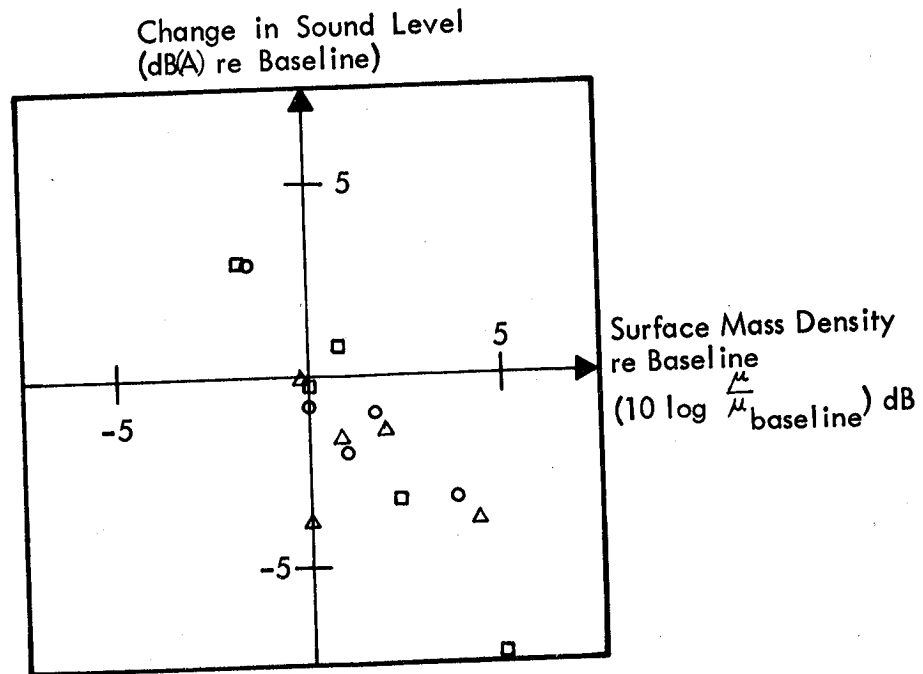
In general the decrease in the A-weighted interior noise level is proportional to the increase in the mass surface density of the structure. A 3 dB decrease in noise level is produced approximately by a 3 dB (doubling) increase in mass density of the fuselage structure independent of whether the mass addition

TABLE 15
SUMMARY OF NOISE REDUCTIONS ACHIEVED WITH
ADVANCED CONCEPTS

Structure	Wide Body		Narrow Body		Small Diam.	
	Mass/ Unit Area	Max.Cabin dBA	Mass/ Unit Area	Max.Cabin dBA	Mass/ Unit Area	Max.Cabin dBA
Baseline	9.46	105.5	10.29	104.9	4.84	108.1
2 x Frame Stiffness	9.46	104.1	10.29	104.7	4.84	104.2
Half Frame Pitch	11.05	102.9	13.11	106.0	5.85	106.4
2 x Skin Thickness	16.2	104.4	15.09	102.2	7.59	106.6
4 x Skin Thickness	29.7	101.9	24.69	97.6	13.07	104.2
Honeycomb Skin	6.26	108.1	7.13	108.8	4.76	107.8

Mass/Unit Area (kg/m^2) Includes Skin, Stringers and Frames For the Structural Elements For Which the Input Power is a Maximum.

- Wide Body
- Narrow Body
- △ Small Diameter



occurs as a result of increasing the number of stiffening ring frames, or as a result of increasing the skin thickness. There are, of course, some exceptions to this general trend. For example, a 4 dB reduction in noise level is predicted for the small diameter airplane when the frame stiffness is doubled, yet this method does not increase the structural mass.

From this analysis of advanced noise control concepts it is apparent that it will be difficult to achieve the required noise reductions by means of these methods alone. Whilst a more extensive parametric analysis is required than was possible under this study, it is anticipated that add-on noise reduction methods will have to be used with the advanced concepts in order to meet the 80 dB(A) goal for interior noise levels. An optimization procedure will be required to perform the analysis.

9.0 REQUIREMENTS FOR EXPERIMENTAL VERIFICATION OF ANALYTICAL MODEL

9.1 Introduction

The analytical model developed in Section 3 has been used to evaluate the various add-on and advanced noise control methods described in Sections 7 and 8. However, it is advisable that the analytical model undergo some form of experimental validation just as was done for a similar analytical model of the acoustic environment in the Space Shuttle orbiter payload bay [10, 4]. The key questions to be answered in the validation of the present analytical model are:

- (i) Does the analytical model adequately predict the response of the fuselage structure to a convected pressure field with a rapidly decaying amplitude?
- (ii) Does the analytical model adequately predict the sound levels in the interior of a fuselage with a sidewall treatment typical of present-day turbofan aircraft?
- (iii) Can the add-on sidewall treatments provide the high noise reductions predicted by the analytical model at low frequencies?
and
- (iv) Does the analytical model adequately predict the noise reductions provided by different fuselage structure designs?

Practical questions concerned with the design of validation tests revolve around several key steps: construction of a model fuselage which adequately simulates the full-scale propfan airplane; simulation of the propfan excitation;

and definition of the experimental measurements and procedures to be followed to answer the above questions.

In this section, criteria for adequate simulation of typical propfan airplane configurations are discussed in detail. In Section 9.2, sensitivity studies are conducted to demonstrate the importance of excitation, structural, and cabin variables on the measured noise reduction. Alternative excitation simulation methods are reviewed in Section 9.3, bearing in mind the criteria developed in Section 9.2 for achieving the above test program objectives. Section 9.4 presents detailed recommendations, resulting from the preceding discussion, for the proposed test program. Excitation and fuselage models, and measurement and data analysis procedures are outlined. The relationship between experimenter and analyst is discussed in detail. Validation using flight tests with an existing propeller-driven airplane is discussed in Section 9.5.

9.2 Sensitivity Studies

The planning of a model test study requires the selection of an appropriately constructed and scaled test model. Fundamental to correct model selection is an understanding of the sensitivity of the calculated noise reduction (and the parameters such as $\langle j_r^2 \rangle_p$, σ , n_r , \bar{n}_r , τ_s) to variations of the characteristics of the excitation and the structural and sidewall configurations from the prototype propfan airplane designs. In this section, scaling laws are presented which show how the characteristics of the excitation, structure, sidewall acoustic treatment, and interior acoustics depend on the size and material selection in the model fuselage relative to the propfan prototype. Approximate limits within which critical parameters must be maintained, are presented for guidance in the practical selection of a scale model experiment.

9.2.1 Model Scaling

The Mikulas resonance-frequency equation (Section 3.8.1), which smears out the mass and stiffness characteristics of frames and stringers over the skin surface, has been used to predict the wavenumber-frequency distribution for the structures of the various study airplanes. The equations were modified to include the effects of cabin pressurization. The contributions of the skin and stiffener masses and stiffness are clearly represented in the equations (Figure 5) in a series of non-dimensional groups which can be readily varied independently to quantify the influence of each component in the prediction of fuselage wavenumber-frequency distributions. Correct scaling implies that the test model fuselage has the same non-dimensional wavenumber-frequency distribution as the prototype fuselage. The resonance frequencies v_{mn} of the model fuselage, when non-dimensionalized by the theoretical cylindrical fuselage ring frequency, must remain constant for all vibration modes. The Mikulas equation (Figure 5), both sides of which are non-dimensional, can be written in abbreviated form, as

$$\frac{v_{mn}^2}{\pi^4} \frac{h_e^4}{h^3 R^2} = \text{function} \left[\frac{E_r I_r}{D l_x}, \frac{E_r A_r}{E l_x h}, \frac{\bar{z}_r}{R}, \dots \right] \quad (84)$$

(all non-dimensional groups are listed in Figure 5). Here h is the skin thickness, h_e is the thickness of the equivalent orthotropic panel (i.e. skin plus smeared-out stiffeners) and $v_{mn} = \omega_{mn}/\omega_r$ where $\omega_r = c_L/R$ and c_L is the longitudinal wavespeed in the skin. It is assumed in the following sections that the skin and stiffeners are of the same material.

For v_{mn} to be constant for model and full-scale fuselages requires a dimensionally-scaled model where h/ℓ , h/R and h_e/R are maintained constant. Then the non-dimensional groups on the right hand side of Eq.(84) must be maintained constant, which requires that all dimensions are scaled to maintain the same ratio with the fuselage radius. Dimensionally-scaled models, in which all dimensions are changed in the same ratio, will maintain the same non-dimensional wavenumber-frequency distribution according as

$$\omega_{mns}/\omega_{mnf} = R_f/R_s$$

using the same material or, more generally, a material with the same compressional wavespeed c_L for both model and full-scale fuselages, and where ω_{mns} is the (m,n)th resonance frequency of the model cylindrical fuselage of radius R_s ; subscript f refers to the full-scale fuselage. Thus, for example, use of a half-scale test model requires that measurements be carried out at twice the excitation frequency of the full-scale fuselage.

By analogy with uniform axisymmetric circular cylinders, the non-dimensional modal density $N(v)$ is given by $N(v) = n(\omega_b)\omega_r/(L_x/\kappa)$, when κ is the effective radius of gyration of the stiffened cylindrical fuselage. L_x/κ is constant for a dimensionally-scaled model fuselage so that $n(\omega)\omega_r$ must also be constant for model and full-scale fuselages when evaluated at the scaled excitation frequency if $N(v)$ is to be constant. Figure 61 shows that $n(\omega_b)/R$ is constant for model and full-scale structures when correctly scaled dimensionally; minor variations occur due to band-width computation procedures at low frequencies. In performing this analysis, it is assumed that the model and full-scale fuselage structures are constructed of the same material, more particularly, materials with the same value of c_L . Detailed examination of the

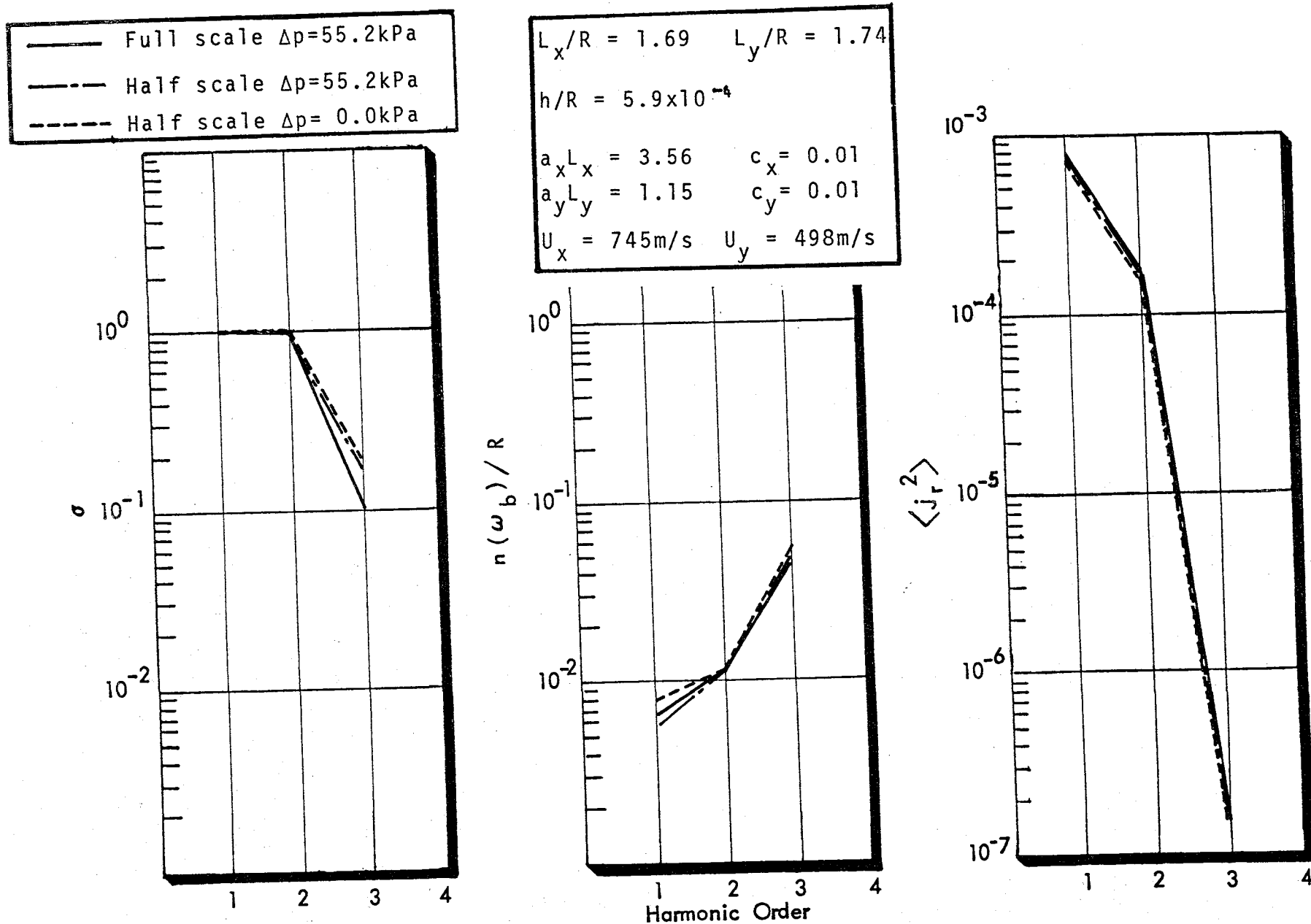


FIGURE 61. EFFECT OF STRUCTURAL SCALING ON $\langle j_r^2 \rangle$, $n(\omega_b)/R$, and $\langle \sigma \rangle$

Wide Body Airplane: Full scale $f_r = 290 \text{ Hz}$; Half-scale $f_r = 580 \text{ Hz}$

resonant modes used in computations show that an essentially identical wavenumber-frequency distribution is produced for a correctly scaled model fuselage when evaluated at frequency (ω_b/ω_r) .

9.2.2 Noise Reduction Scaling

The high frequency formulation (Section 3.5.4) is used exclusively for all study airplanes. For baseline aircraft where $W_{out}(\omega)$ can be neglected in comparison with $W_{abs}(\omega)$, the fuselage noise reduction can be calculated, from Eqs. (26) and (54), as

$$NR(\omega_b) = 10 \log_{10} \frac{\langle p_{Xo}^2(\omega_b) \rangle}{\langle p_i^2(\omega_b) \rangle} \quad (85)$$

where

$$\frac{\langle p_{Xo}^2(\omega_b) \rangle}{\langle p_i^2(\omega_b) \rangle} = \left[\frac{8\pi(\rho_i c_i)^2}{\omega_b} \frac{A}{\omega_r \mu^2 \bar{\alpha} S} \left\{ \frac{[n_r(\omega_b)\omega_r] \langle j_r^2(\omega_b) \rangle_P \langle \sigma_{rad} \rangle \tau_s}{\bar{n}_r} \right\} \right]^{-1} \quad (86)$$

The excitation frequency is denoted in Eq.(86) by ω_b , where it is implicitly assumed, from Section 9.2.1, that the ratio (ω_b/ω_r) is the same for model and full-scale conditions. Thus, when it is stated that some function, say $\phi(\omega_b)$, is the same for model and full-scale conditions, what is really implied is that $\phi(\omega_b/\omega_r)$ remains constant. An equivalent approach is to specify that $\phi(\omega_b)$ is constant for constant harmonic order b.

As will be shown, parameters contained within the { } brackets are all non-dimensional, depending only on non-dimensional groups which are, or can be, maintained constant in scale model testing. The terms preceding the { } brackets determine the dependence of the noise reduction on dimensional, material, and frequency changes: these, if any, must be clearly defined if model acoustic tests are to be properly interpreted and used for full-scale noise reduction predictions. The variables on which the important parameters determining the structural response of, and acoustic radiation from, the fuselage depend, are briefly reviewed.

For simplicity, the following discussion will present numerical examples based only on the wide-body fuselage structure, but similar conclusions can be drawn for other aircraft. Also, the discussion is limited to the three lowest order harmonics since these dominate the interior noise levels.

9.2.2.1 Scaling of the external acoustic excitation

The excitation is described by its cross spectral density function which depends on the pressure amplitude decay rate parameters ($a_x L_x, a_y L_y$), the excitation coherence parameters (c_x, c_y) and the non-dimensional excitation trace wavenumber (k_{xR}, k_{yR}). Each must be maintained constant between model and full-scale fuselage to maintain correct excitation scaling. For example, for a half-scale model fuselage, the pressure amplitude decay (in dB/m) for the fuselage model will be twice that for the full-scale fuselage since the model is half as long as the full-scale fuselage: i.e. $a_{xs} = a_{xf} L_{xf} / L_{xs}$. The coherence decay parameters (c_x, c_y) can be written as $c_x = c'_x (\frac{\omega \xi}{U_x})$ where c'_x is a constant. The Strouhal number $\omega \xi / U_x$ will be constant if the trace velocity U_x is constant,

since, as determined earlier, length scales (such as ξ) vary inversely with frequency. (The selection of c_x is somewhat arbitrary on account of a lack of experimental data.) Further, as will be shown, the sensitivity of the joint acceptance to variations in (c_x, c_y) is weak when (c_x, c_y) are small. For constant trace velocities (U_x, U_y) in the axial and circumferential directions respectively, $(k_x R, k_y R)$ will be constant for a scale model since $\omega_b R$ will be maintained constant. Furthermore it is imperative from the point-of-view of excitation source directivity, that the acoustic wavenumber $\omega_b R/c_e$ be maintained constant. These various requirements are consistent with each other and with the structural scaling requirements.

9.2.2.2 Band-averaged joint acceptance $\langle j_r^2(\omega_b) \rangle_p$:

The band-averaged joint acceptance for a progressive wave excitation is calculated for a group of resonant structural modes by summing the individual joint acceptance functions at the analysis-band center frequency and then dividing by the number of modes. The variables, on which the modal joint acceptances depend, are given by

$$j_{mm}^2(\omega_b) = \text{function} \left[\left(\frac{k_x R}{k_m R}, \frac{k_y R}{k_n R} \right), (m, n), (a_x L_x, a_y L_y), (c_x, c_y) \right]$$

where $\frac{k_x R}{k_m R} = \frac{\omega_b L_x}{m \pi U_x}$, $\frac{k_y R}{k_n R} = \frac{\omega_b L_y}{n \pi U_y}$, (m, n) is the structural mode order, (k_m, k_n) the structural modal wave numbers, and (k_x, k_y) the excitation wavenumbers. If $(a_x L_x, a_y L_y)$, (c_x, c_y) and (U_x, U_y) remain constant, as required to correctly simulate the excitation characteristics on a test model, and the model is also dimensionally scaled, (m, n) , $(k_x R/k_m R)$ and

$(k_y R / k_n R)$ will also be maintained constant at the scaled excitation frequencies and correct simulation of the joint acceptances of the full-scale propfan will be achieved. Figure 61 presents calculations of the band-averaged joint acceptance for full-scale and half-scale fuselage elements for the wide body study airplane for in-flight pressurization conditions. The model and excitation have been scaled in accordance with the previous discussion: it is clear that $\langle j_r^2(\omega_b) \rangle_p$ is constant for constant harmonic order b .

9.2.2.3 Band-averaged radiation efficiency $\langle \sigma_{rad} \rangle$:

The band-averaged radiation efficiency (or radiation ratio) $\langle \sigma_{rad} \rangle$ depends on the individual modal radiation efficiencies, which themselves are functions of mode order, relative structural and acoustic wavespeeds, and structure dimensions; i.e.,

$$\langle \sigma_{rad} \rangle = \text{function} [(m,n), (k_{ci} R / k_{mn} R), k_{ci} L, k_{ci} R]$$

where $k_{ci} R = \omega_b R / c_i$. A correctly scaled model will preserve the same non-dimensional wavenumber-frequency distribution for model and full-scale structures while $k_{ci} L$ and $k_{ci} R$ will also be constant at the new model-scale test frequencies. Thus $\langle \sigma_{rad} \rangle$ will remain constant for correctly-scaled model fuselage structures. This is also shown in Figure 61.

9.2.2.4 Band-Averaged Structural Loss Factor $\bar{\eta}_r$:

The band-averaged structural loss factor $\bar{\eta}_r$ depends on structural dissipation associated with factors such as joint friction, gas pumping, and applied damping treatments, as well as on radiation damping forces. Thus

$$\bar{\eta}_r = \bar{\eta}_{struc} + \bar{\eta}_{rad}$$

where, as discussed in Section 5.6, $\bar{\eta}_{\text{struc}}$ depends essentially on the structural mode order, provided the joint details are similar and the frequency change is not too great, while the acoustic radiation loss factor $\bar{\eta}_{\text{rad}}$ depends on both structural surface density and radiation ratio: i.e.,

$$\bar{\eta}_{\text{rad}} = \rho_i c_i \langle \sigma_{\text{rad}} \rangle / \omega_b \mu$$

where μ is the surface density of the fuselage structure. Since dimensionally-scaled models will maintain (m,n) , $\omega_b b$, v_{mn} and $\langle \sigma_{\text{rad}} \rangle$ constant at the new modal test frequency then $\bar{\eta}_{\text{rad}}$, $\bar{\eta}_{\text{struc}}$, and consequently $\bar{\eta}_r$, will all be maintained constant.

9.2.2.5 Sidewall Transmission Coefficient τ_s :

The sidewall transmission coefficient τ_s of a double-wall structure, is essentially a function of the acoustic and double-wall resonance wavenumbers, non-dimensionalized with respect to cavity depth l , as well as the attenuation and wavenumber parameters for the medium in the double-wall cavity. Thus,

$$\tau_s = \text{function} \left[k_{ci} l = \frac{\omega l}{c_i}, k_{dw} l, \alpha l, \beta l \right]$$

If each of these non-dimensional parameters is maintained constant between model and full-scale fuselages, τ_s will be constant.

The non-dimensional acoustic wavenumber $k_{ci} l$ will be held constant for constant c_i since ωl is constant for a dimensionally-scaled model fuselage.

The double-wall, non-dimensional resonance wavenumber $k_{dw} \ell$ is given, approximately, by

$$k_{dw} \ell = \left(\frac{\rho \ell (\mu_1 + \mu_2)}{\mu_1 \mu_2} \right)^{1/2} \quad (87)$$

$$= \left(\frac{\rho \ell}{\rho_1 h_1} + \frac{\rho \ell}{\rho_2 h_2} \right)^{1/2}$$

where μ_1, μ_2 are the material densities for the fuselage and trim panels respectively: h_1, h_2 are the corresponding panel thicknesses, ρ is the density of the cavity medium. Then if the materials are the same for model and fullscale panels, the model and fullscale values of $k_{dw} \ell$ will be the same when ℓ, h_1 , and h_2 are all scaled in proportion to radius R . The attenuation parameter $\alpha \ell$ where α is attenuation per unit distance (dB/m) in the porous medium (see Section 3.9.2), may be written non-dimensionally as

$$\alpha \ell = k \ell \left\{ 0.564 \left[k \ell / \left(\frac{R_1 \ell}{\rho c} \right) \right]^{-0.595} \right\} \quad (88)$$

while the porous material wavenumber parameter $\beta \ell$, where $\beta = 2\pi / (\text{acoustic wavelength in the material})$, can be written non-dimensionally as

$$\beta \ell = k \ell \left\{ 1 + 0.35 \left[k \ell / \left(\frac{R_1 \ell}{\rho c} \right) \right]^{-0.700} \right\}. \quad (89)$$

Maintaining the acoustic wavenumber $k \ell$ and the non-dimensional flow resistance ($R_1 \ell / \rho c$) constant will ensure $\alpha \ell$ and $\beta \ell$ are properly scaled and maintained constant.

Consequently the double-wall sidewall transmission coefficient and the add-on sidewall transmission loss will be the same for

model and full-scale fuselage configurations. The requirement that the flow resistance $R_1 \ell$ remain constant for the model sidewall implies a change in flow resistivity R_1 : this can be achieved by changing either the material density ρ_m or the material fiber diameter d since $R_1 \propto \rho_m^{1.53}/d^2$ [26]. Changes in ρ_m are most easily arranged by compressing standard porous material samples, although there will be a small increase in the total weight of the material. Such an increase will be small compared with the double-wall mass, and will not cause a significant change in the noise reduction provided by the wall panels, provided that the mechanical stiffness of the layer is not so high that it invalidates the acoustic modeling. Detailed calculations, as seen in Figure 62 for full-(curve (a)) and half-scale (curve (b)) models where $\tau_s(k\ell)$ remains constant for $k_{dw}\ell$ and $R_1\ell$ constant, verify the scaling arguments. If $R_1\ell$ is not scaled correctly, $\tau_s(k\ell)$ will not be correctly scaled as shown by curve (c) in Figure 62.

9.2.2.6 Interior Acoustics:

The acoustic modal overlap of the cabin volume, expressed by

$$\begin{aligned} \psi_n(\omega_b) &= \bar{n}_n n_n(\omega_b) \omega_b \\ &= \frac{\bar{\alpha}(\omega_b) S k_b^2}{8\pi} \end{aligned}$$

must be kept constant to ensure correct scaling of the side-wall radiation characteristics. In a dimensionally-scaled model, $k_b^2 S \propto (k_b R)(k_b L)$ will remain constant. Then, to keep the modal overlap unchanged, the absorption coefficient of the various surfaces must be the same for the model and prototype fuselages. In the above equation, $k_b = \omega_b/c_1$.

	Trim, μ_2 kg/m ²	Porous Layer, R_1 mks rays/m	Sidewall Comments
—	2.0	43,000	Full-scale (a)
- . -	1.0	86,000	Half-scale (b)
- - -	1.0	43,000	R_1 Incorrectly (c) Scaled; Otherwise Half-scale

$$\mu_1 = 10.2 \text{ kg/m}^2$$

$$\lambda = 127 \text{ mm}$$

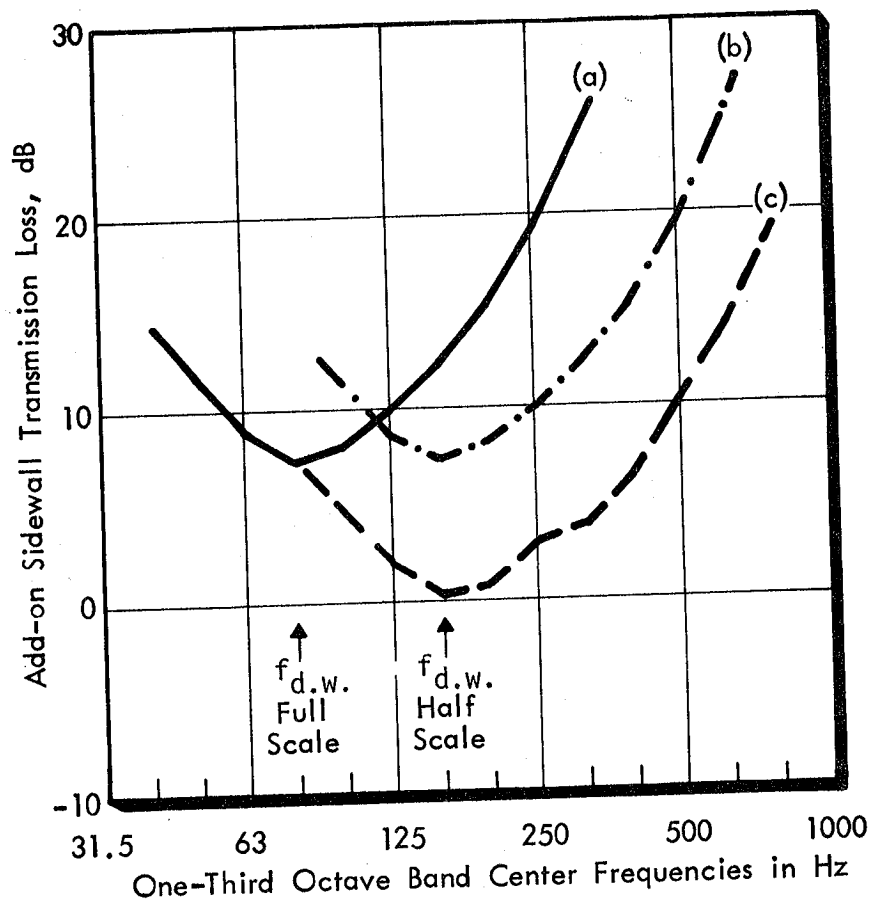


FIGURE 62. PREDICTED ADDITIONAL SIDEWALL TRANSMISSION LOSS, FULL AND HALF-SCALE FUSELAGE MODELS

The absorption coefficient depends essentially on sidewall characteristics since the bulk of the cabin absorption is provided by the bounding surfaces: for example,

$$\bar{\alpha}(\omega_b) = \text{function} \left[k_b L, \frac{R_1 L}{\rho_i c_i}, \frac{\omega_b \mu_2}{\rho_i c_i} \right],$$

all terms of which are non-dimensional and remain constant for a dimensionally-scaled model (μ_2 is the interior trim-panel surface density). Thus $\bar{\alpha}$ will be constant if τ_s remains constant, since the same non-dimensional parameters are involved in both cases.

In practice, the cabin length L may be shorter than dimensional scaling would allow: additional absorption can then be added to non-radiating surfaces so that $\Psi_n(\omega_b)$ remains constant.

9.2.2.7 Summary:

Referring to Eq. (86) for the fuselage noise reduction, it has been shown that, for a dimensionally-scaled model and excitation, the terms inside the { } brackets will be equal to those for the full-scale fuselage. The change in noise reduction from full-scale to model-scale then reduces to

$$\begin{aligned} NR_{\text{full}} - NR_{\text{scale}} &= 10 \log_{10} \left[\frac{(\rho_i c_i)_s^2}{(\rho_i c_i)_f^2} \cdot \frac{A_s}{A_f} \cdot \frac{\omega_{bf}}{\omega_{bs}} \cdot \frac{\omega_{rf}}{\omega_{rs}} \left(\frac{\mu_f}{\mu_s} \right)^2 \frac{S_f}{S_s} \right] \\ &= 10 \log_{10} \left[\frac{(\rho_i c_i)_s^2}{(\rho_i c_i)_f^2} \left(\frac{\rho_f}{\rho_s} \right)^2 \right] \quad (90) \end{aligned}$$

for a dimensionally-scaled model, where, according to the

analytical model, subscripts s and f refer to model-scale and fullscale conditions, respectively.

Thus, the measured noise reduction on a dimensionally-scaled test model will be essentially equal to that measured on a full-scale fuselage at the same non-dimensional frequency provided the excitation has been properly scaled.

9.2.3 Effects of variations in excitation and structural characteristics.

In a practical model test situation it may not be feasible and/or economic to construct a fully-scaled test model: for example, exact simulation of stiffener details would be a relatively expensive task. Thus it is necessary to know the magnitude of the errors produced in noise reduction calculations or, more directly, in the parameters shown in Eq. (86) on which the noise reduction depends, when other than complete simulation exists. The most important of these parameters are the band-averaged joint acceptance, the structural modal density and radiation resistance, and the sidewall transmission coefficient.

Consider first the effects of pressurization loads. Figures 61 and 63 show that for the wide body fuselage and for frequencies below the subpanel resonance frequency, $\langle j_r^2(\omega_b) \rangle_P$, $n(\omega_b)/R$ and $\langle \sigma_{rad} \rangle$ do not depend significantly on whether full-scale pressurization loads are simulated in the model scale test. This is true because the frames and stringers have high bending stiffness relative to the induced in-plane (pressurization) membrane stiffness. Similar results are found for the other study aircraft, as seen in Figures 64 and 65.

$L_x = 5.080 \text{ m}; L_y = 5.227 \text{ m}$
 $h = 1.78 \text{ mm}$
 $R = 3.010 \text{ m}$
 $a_x = 0.70; c_x = 0.010; U_x = 745 \text{ m/s}$
 $a_y = 0.22; c_y = 0.010; U_y = 498 \text{ m/s}$

$\Delta p \text{ (k Pa)}$

————	Baseline	55.2
-----	Baseline	0.0
- - - - -	4 x Skin Th.	55.2
- - - - -	4 x Skin Th.	0.0
.....	2 x Frame St.	55.2
.....	2 x Frame St.	0.0

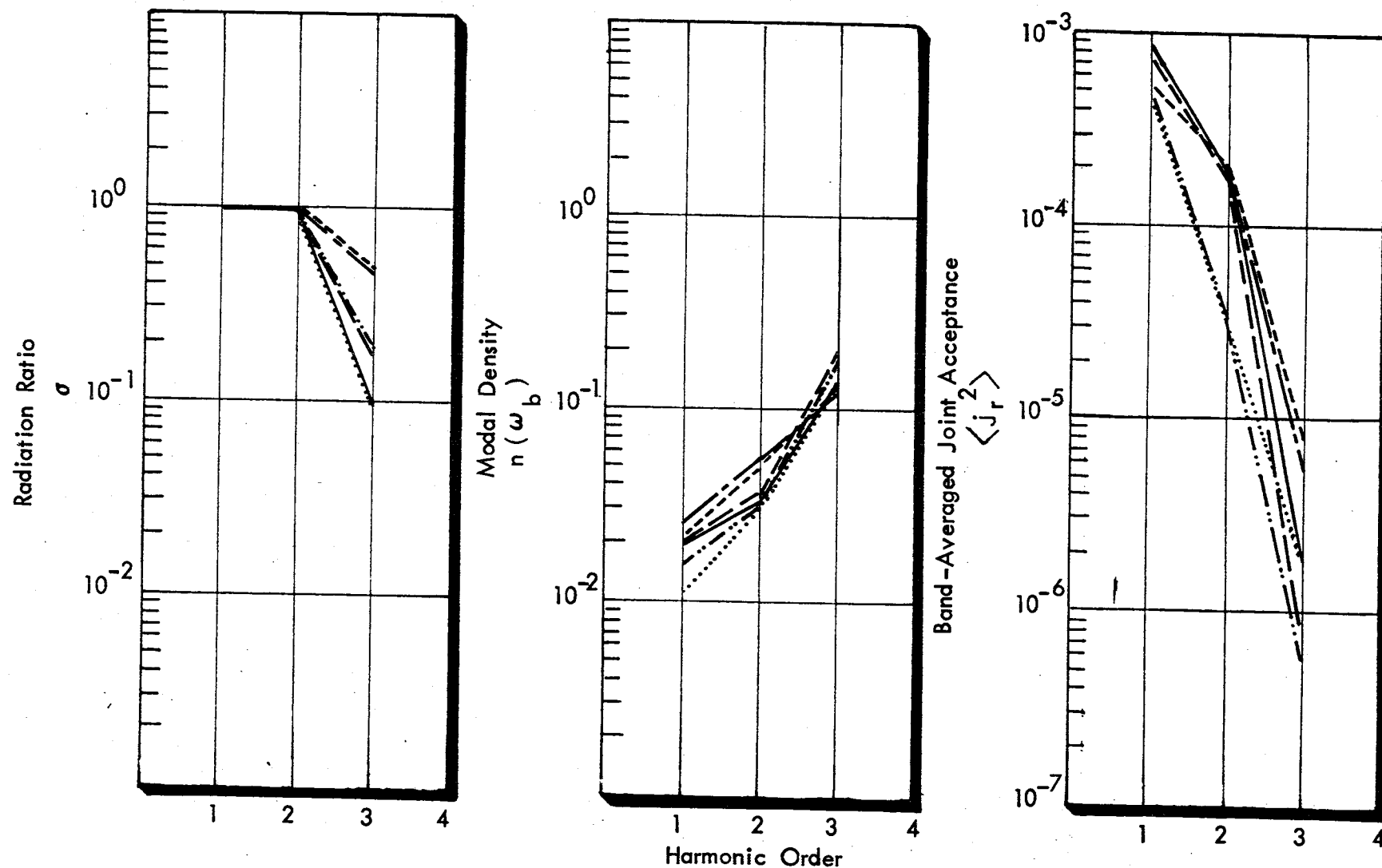


FIGURE 63. EFFECT OF CHANGES IN FRAME STIFFNESS AND SKIN THICKNESS AND OF PRESSURE DIFFERENCE ON $\langle j_r^2 \rangle$, $n(\omega)$, AND σ FOR WIDE BODY AIRCRAFT (Element 4)

$R = 1.88 \text{ m}$ $L_x = 5.08 \text{ m}$ $L_y = 7.00 \text{ m}$ $h = 3.00 \text{ mm}$ $U_x = 1038 \text{ m/s}$ $U_y = 926 \text{ m/s}$				$\Delta p (\text{kPa})$
$\left. \begin{array}{l} \\ \\ \\ \\ \end{array} \right\} \text{Baseline}$			———— Baseline	55.2
			———— Baseline	0.0
			----- 4 x Skin Thickness	55.2
			----- 4 x Skin Thickness	0.0
			----- 2 x Frame Stiffness	55.2
			----- 2 x Frame Stiffness	0.0

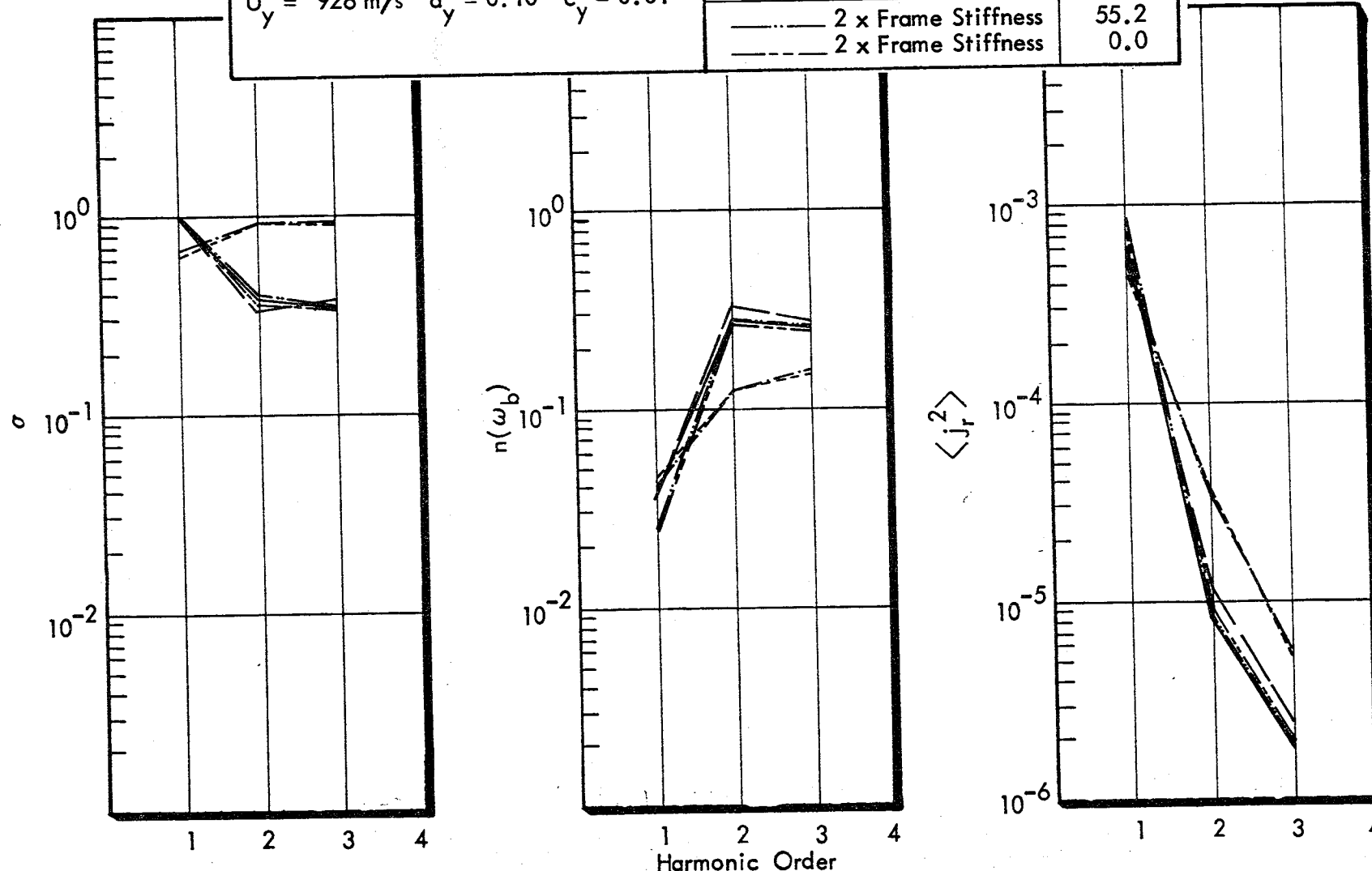


FIGURE 64. EFFECT OF CHANGES IN FRAME STIFFNESS AND SKIN THICKNESS AND OF PRESSURE DIFFERENCE ON $\langle j_r^2 \rangle$, $n(\omega_b)$ AND σ FOR NARROW-BODY AIRPLANE (ELEMENT 4)

$R = 1.22 \text{ m}$ $L_x = 3.65 \text{ m}$ $L_y = 5.66 \text{ m}$ $h = 1.02 \text{ mm}$ $U_x = 658 \text{ m/s}$ $U_y = 451 \text{ m/s}$				$\Delta p (\text{kPa})$
$\left. \begin{array}{l} a_x = 1.422 \\ a_y = 0.317 \end{array} \right\} \text{Baseline}$ $c_x = 0.01$ $c_y = 0.01$			———— Baseline	55.2
			———— Baseline	0.0
		 4 x Skin Thickness	55.2
			----- 4 x Skin Thickness	0.0
		 2 x Frame Stiffness	55.2
			----- 2 x Frame Stiffness	0.0

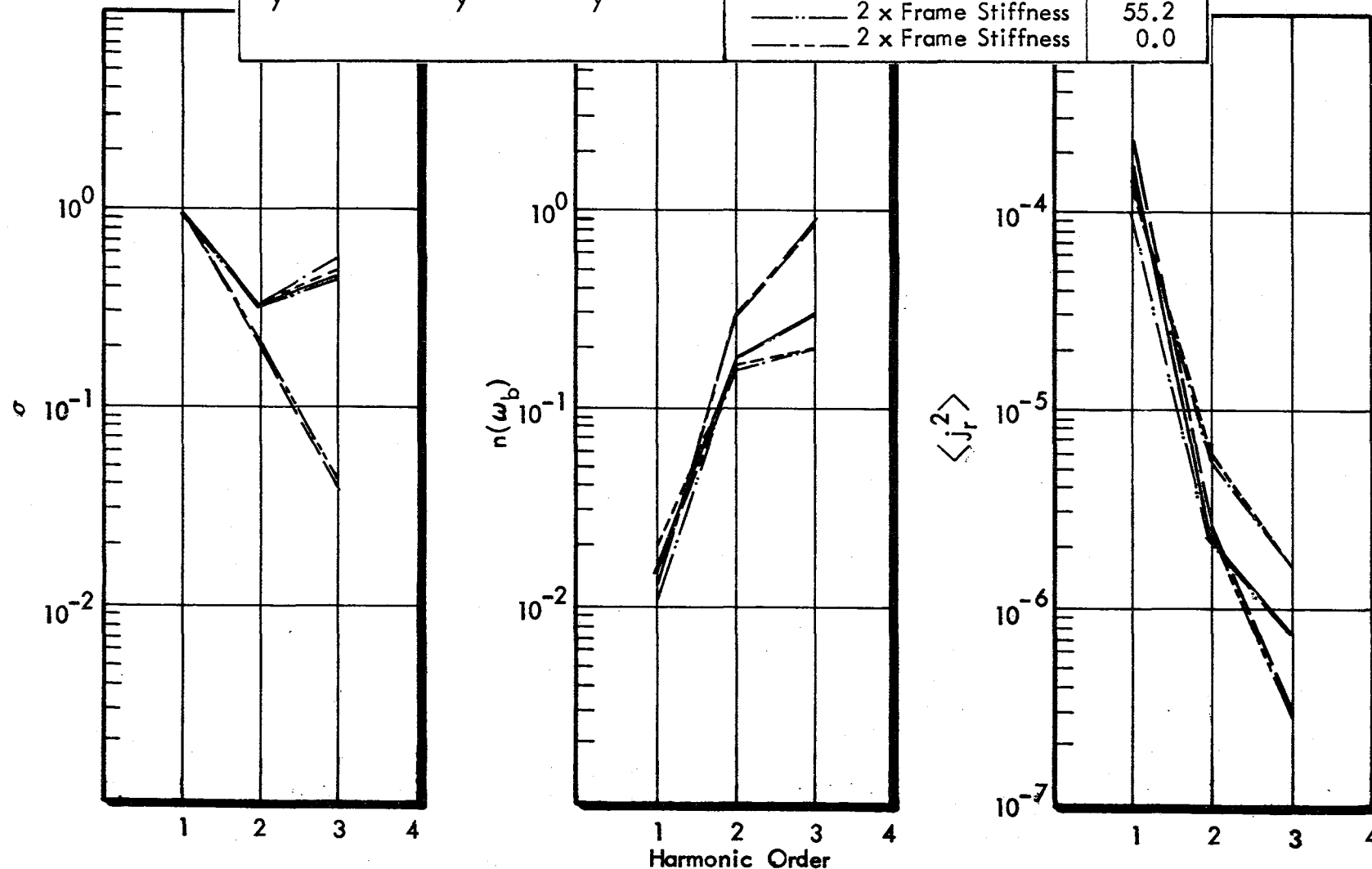


FIGURE 65. EFFECT OF CHANGES IN FRAME STIFFNESS AND SKIN THICKNESS AND OF PRESSURE DIFFERENCE ON $\langle j_r^2 \rangle$, $n(\omega_b)$ AND σ FOR SMALL DIAMETER AIRPLANE

Thus there is little need to pressurize a test model fuselage if one is concerned only with low frequency noise reduction, for example, at the lower three harmonics which are of present concern.

Of interest now is the accuracy with which the excitation characteristics, (a_x, a_y) , (U_x, U_y) and (c_x, c_y) must be modeled. Consider the dependence of the band-averaged joint acceptance on the amplitude decay rate parameter (a_x, a_y) . Figure 66 shows, for the wide-body airplane (baseline structure, element 4), the dependence of $\langle j_r^2 \rangle_P$ on variations in (a_x, a_y) for a range of harmonic order, (U_x, U_y) and (c_x, c_y) being kept constant. The dependence is marked, as predicted by Eq. (A.9) of Appendix A. The values of $\langle j_r^2 \rangle_P$ relative to the baseline estimate are shown in Figure 67 for different values of (a_x, a_y) . It is clear that close simulation of (a_x, a_y) is most important; for an accuracy of ± 1 dB in $\langle j_r^2 \rangle_P$ and, hence, in structural response and noise reduction simulation, (a_x, a_y) must be modeled with an accuracy of $\pm 10\%$. However, as shown in Figure 66 for situations involving strong decay in the pressure amplitude, simulation of (c_x, c_y) need not be very precise.

Figure 68 shows the dependence of $\langle j_r^2 \rangle_P$ on variations in trace velocities (U_x, U_y) for the wide body aircraft: it is clear that close simulation of U_x , and U_y is imperative, and limits of $\pm 10\%$ are suggested as reasonable. A similar strong dependence on the variation in U_x, U_y is found for the other study aircraft, although the errors do not follow any general pattern since basic structural differences exist between different study aircraft.

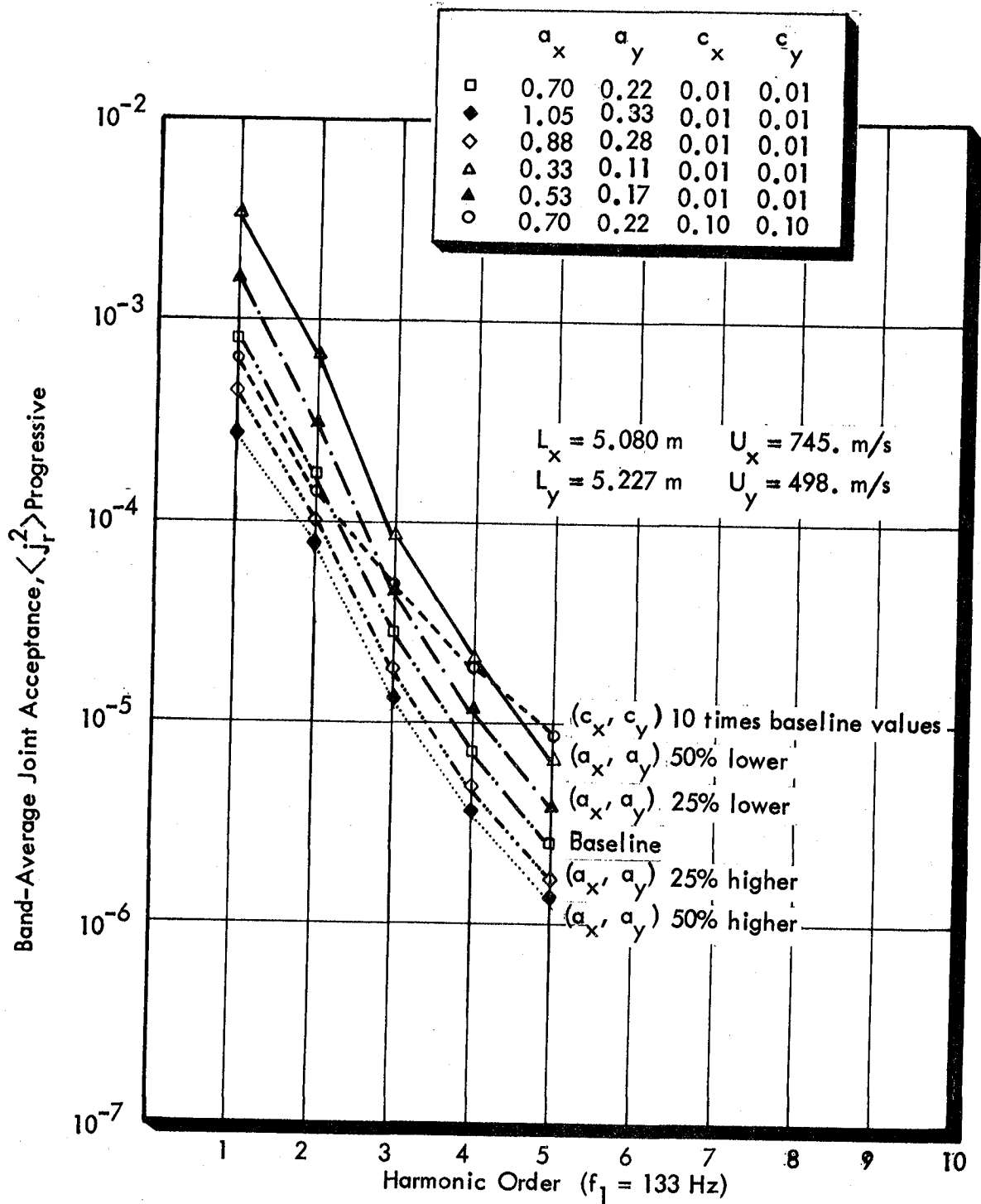


FIGURE 66. EFFECT OF VARIATIONS IN AMPLITUDE DECAY RATE AND COHERENCE ON BAND-AVERAGED JOINT ACCEPTANCE: WIDE BODY AIRPLANE-ELEMENT 4: LOW FREQUENCY STRUCTURAL MODEL

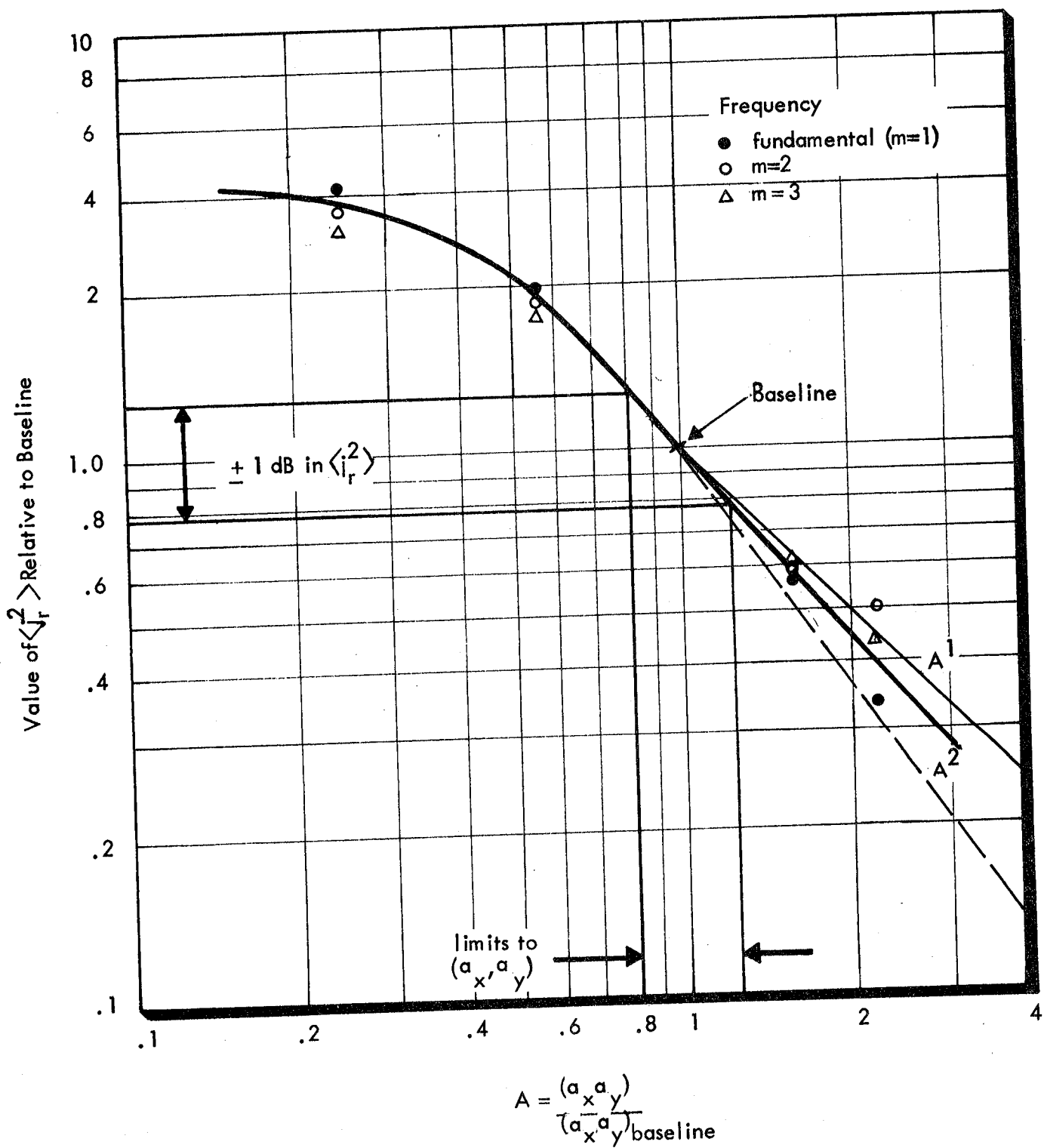


FIGURE 67. DEPENDENCE OF $\langle j_r^2 \rangle$ ON CHANGES IN $(a_x a_y)$, SHOWING CONSTRAINTS ON $(a_x a_y)$ AS DETERMINED BY REQUIRED ACCURACY IN $\langle j_r^2 \rangle$

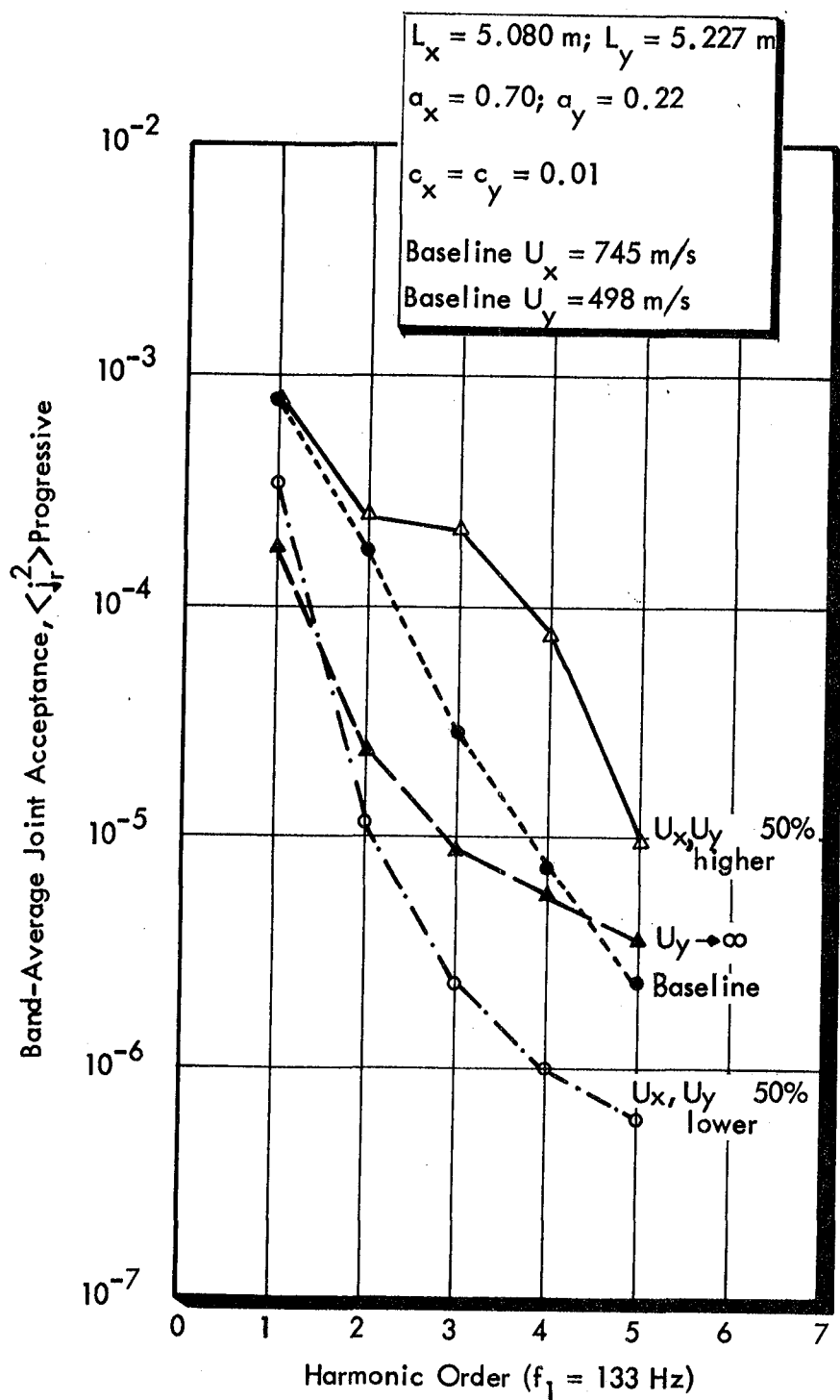


FIGURE 68. EFFECT OF VARIATIONS IN TRACE WAVE SPEED ON BAND-AVERAGED JOINT ACCEPTANCE: WIDE BODY AIRPLANE - ELEMENT 4: LOW FREQUENCY STRUCTURAL MODEL

The effects of incorrectly scaling frame, stringer, and skin parameters are now discussed. Consider first the situation where the frame bending stiffness, expressed by the term $(E_r I_r / D l_x)$ (see Figure 5), is not simulated correctly, while all other parameters remain constant. Figure 69 shows the variations in $\langle \sigma_{rad} \rangle$, $n(\omega_b)$ and $\langle j_r^2 \rangle_p$ for the widebody airplane which result from variations in the baseline frame bending stiffness. Small variations in $\langle \sigma_{rad} \rangle$ occur since the modes are still supersonic for all cases tested. The effects of the modal density and joint acceptance are important only for the case where the baseline frame bending stiffness is doubled. It seems that the frame stiffness and spacing should be fairly closely scaled, within $\pm 20\%$ of the dimensionally scaled values. On the other hand, as seen in Figure 70 the errors introduced by improperly modeling the frame membrane stiffness are small even for changes in $(E_r A_r / E h l_x)$ to 50% of baseline values. Likewise, the radius of gyration of the frame about the skin and the combined frame and stringer torsional stiffness parameter both appear to have only minor influences on either parameter.

Variations in stringer stiffnesses for the widebody airplane are shown in Figures 71 and 72. The stringer bending stiffness, membrane stiffness and radius of gyration are most important in the intermediate or mid-frequency structural regime (where only the stringers and skin properties are considered). However, from Figure 72, it is clear that stringers must be included in the test model for good simulation of $n(\omega_b)$, even at low frequencies, although it appears that precise dimensional scaling is not necessary.

Variations in the wide-body skin thickness produce substantial changes in response parameters in the mid- and high frequency

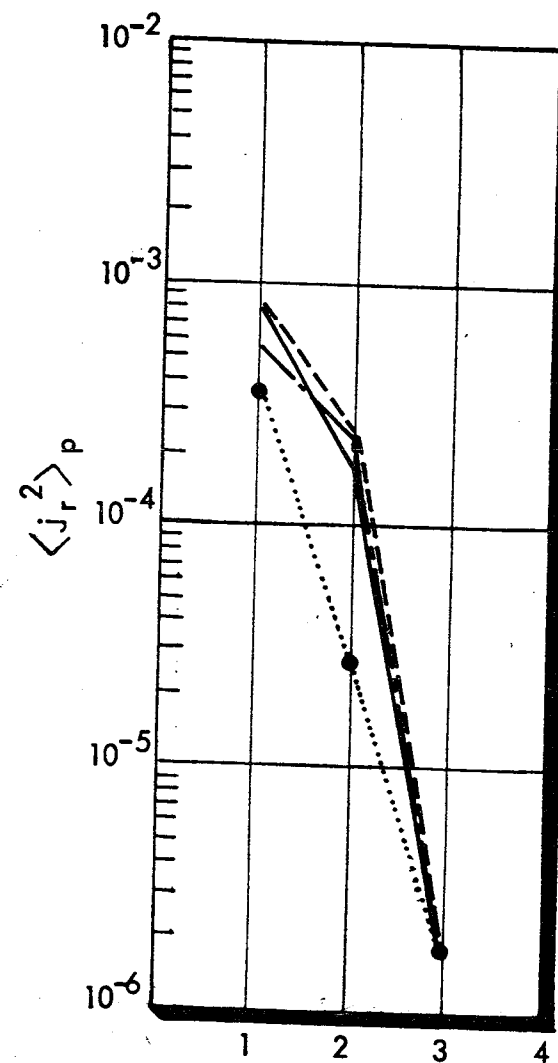
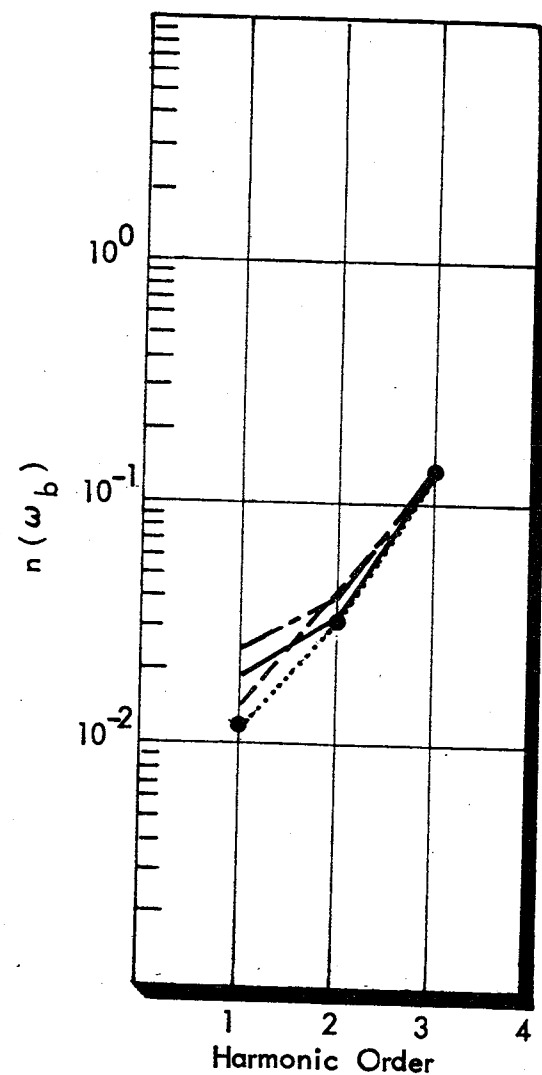
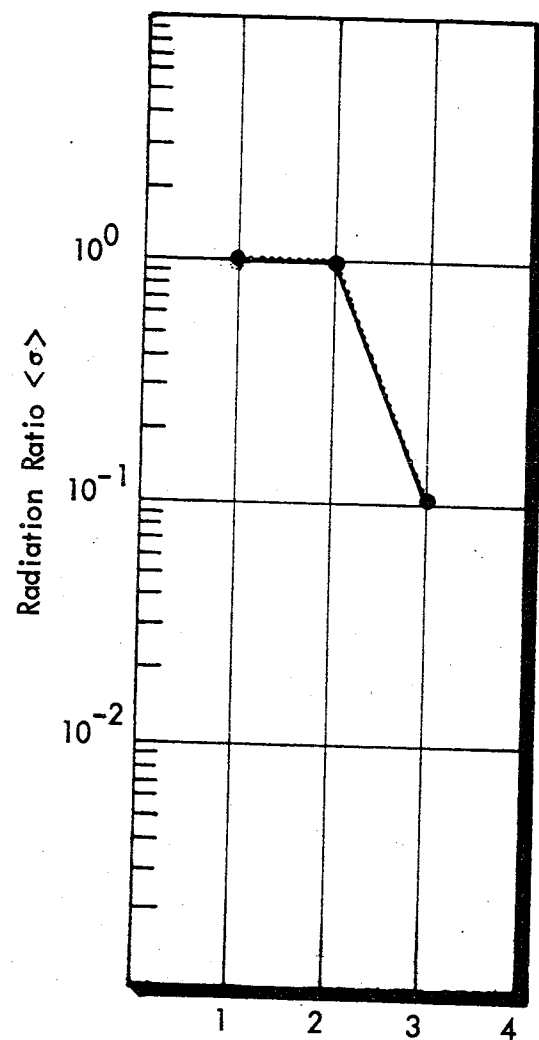
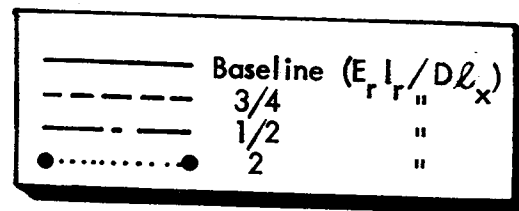


FIGURE 69. EFFECT OF VARIATIONS IN FRAME PROPERTIES FOR WIDE BODY AIRPLANE - VARIATION IN FRAME BENDING STIFFNESS

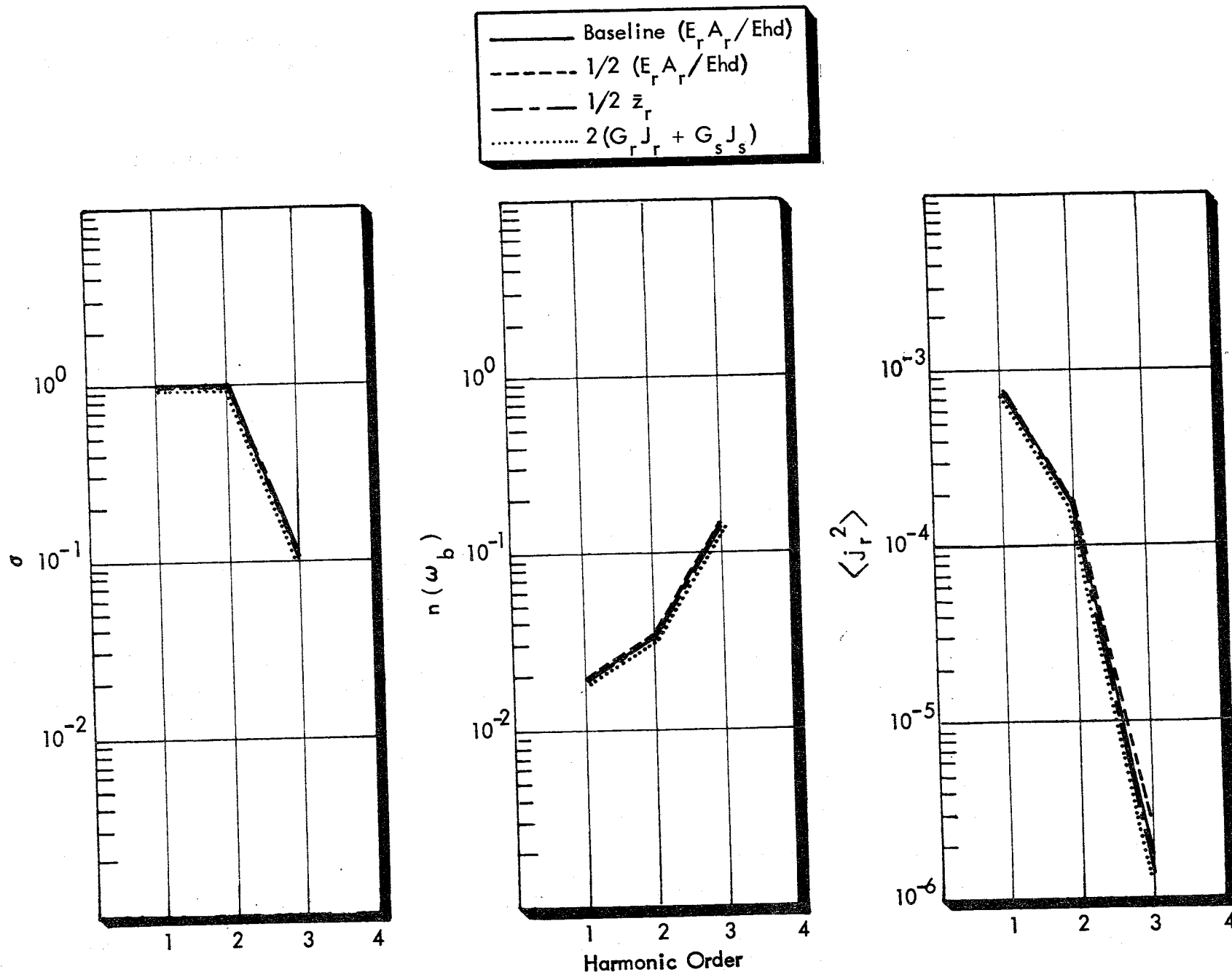


FIGURE 70. EFFECT OF VARIATIONS IN FRAME PROPERTIES FOR WIDE BODY AIRPLANE - VARIATION IN FRAME MEMBRANE STIFFNESS

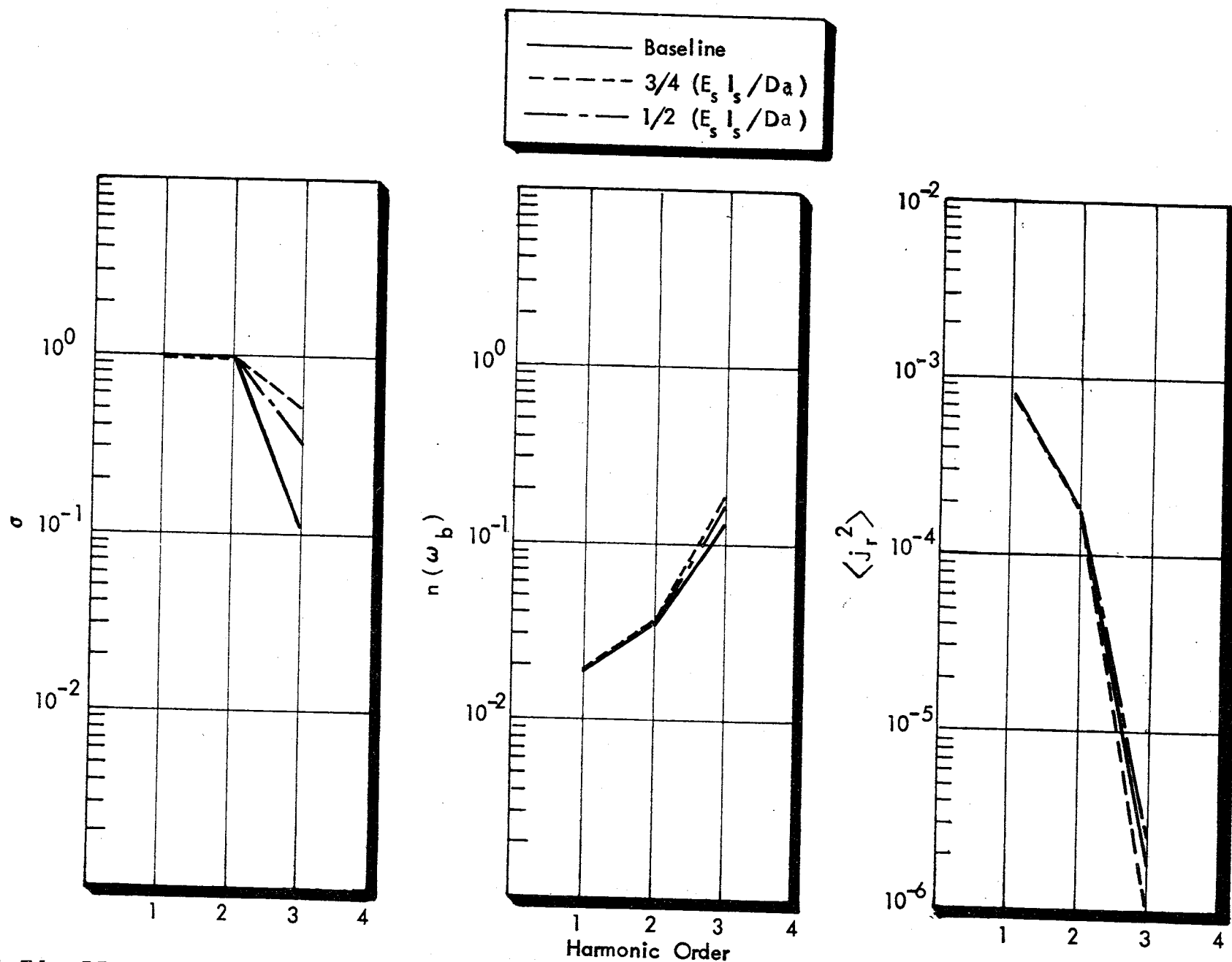


FIGURE 71. EFFECT OF VARIATIONS IN STRINGER PROPERTIES FOR WIDE BODY AIRPLANE - IN STRINGER BENDING STIFFNESS

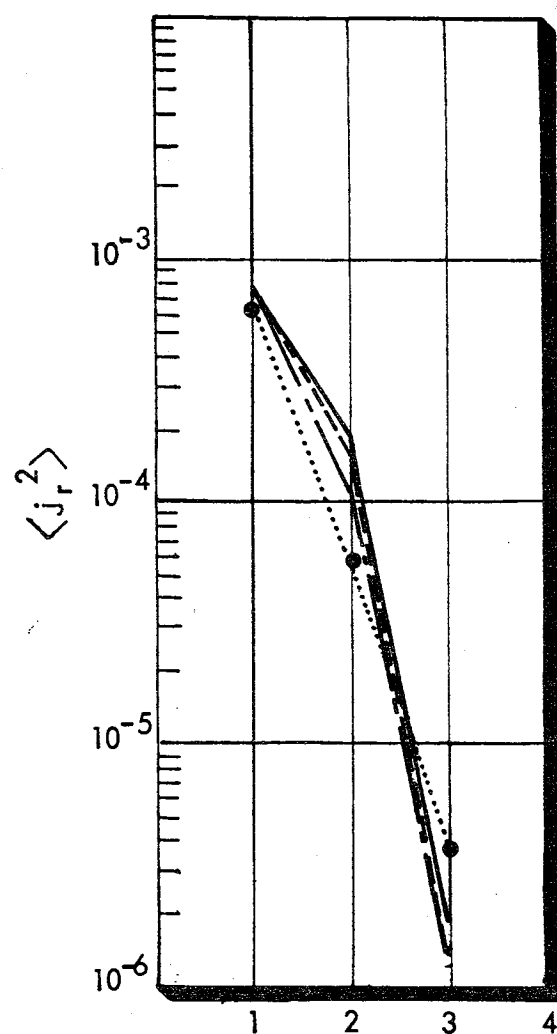
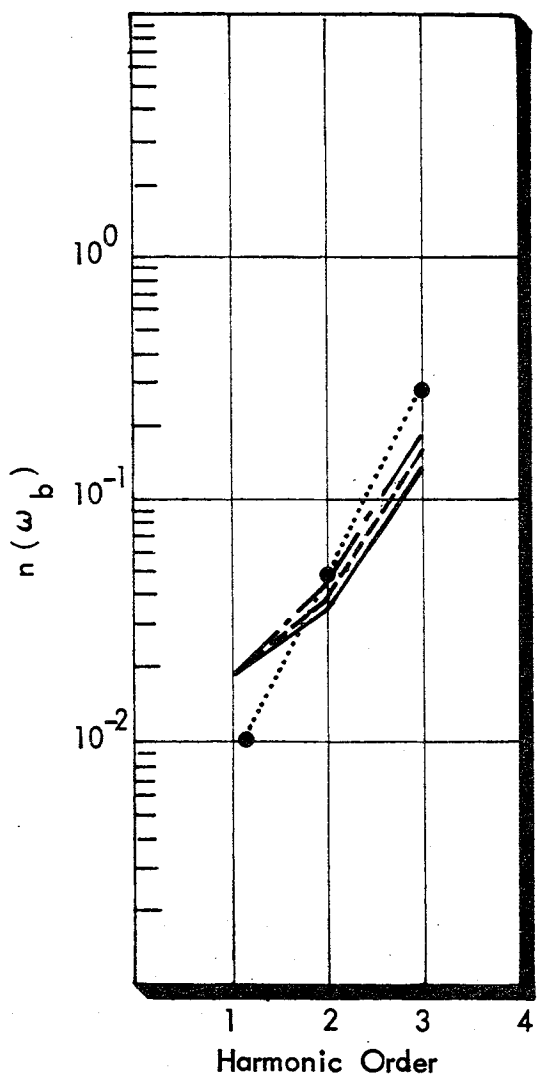
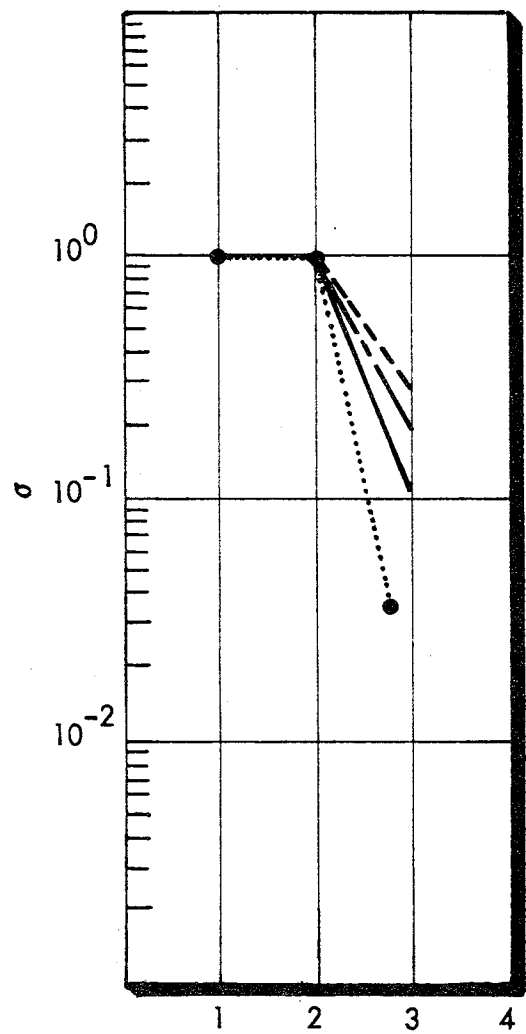
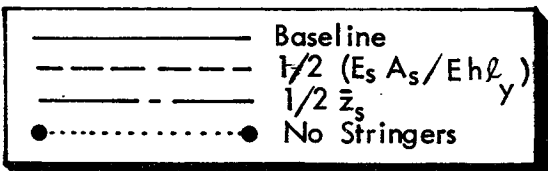


FIGURE 72. EFFECT OF VARIATIONS IN STRINGER PROPERTIES FOR WIDE BODY AIRPLANE - IN STRINGER MEMBRANE STIFFNESS

-222-

regimes where only stringer and skin properties are included in the fuselage model. Increases in $\langle \sigma_{\text{rad}} \rangle$, $n(\omega_b)$ and $\langle j_r^2 \rangle_P$ occur due to increases in skin thickness, as seen in Figure 73. Similar trends occur for the other study aircraft. These increases are counterbalanced to some extent by increases in the 'smeared out' fuselage surface density, but increases in skin thickness can lead to decreases in the fuselage noise reduction (see Figures 58 and 60). Since the fuselage noise reduction, at least for the excitation spectrum given by the Hamilton Standard prediction procedure [6], depends on the lower order harmonics and since at these frequencies the noise reduction of the study airplanes is controlled to a large extent by stiffener properties, precise simulation of the full-scale skin thickness is not necessary: variations of $\pm 25\%$ from dimensionally-scaled values would seem to be acceptable.

The discussion in Section 5.1 shows that panel curvature controls the wavenumber-frequency distribution of the fuselage structure at low frequencies. Figure 74 shows the effect on the various parameters of interest of using a flat panel to simulate a curved panel. Thus, it is clear that flat test panels are not appropriate as model structures at low frequencies.

The area of the test fuselage should be large enough that strong decay in the pressure amplitude occurs between the peak location and the panel boundaries. As shown in Figures 30 and 33, and as discussed in Section 5.2, significant underestimates of the panel modal density parameter, $n(\omega_m)/A$ and joint acceptance parameter, $A^2 \langle j_r^2 \rangle_P$, result from using too small a panel area. The criterion suggested by Eq. (A.9)

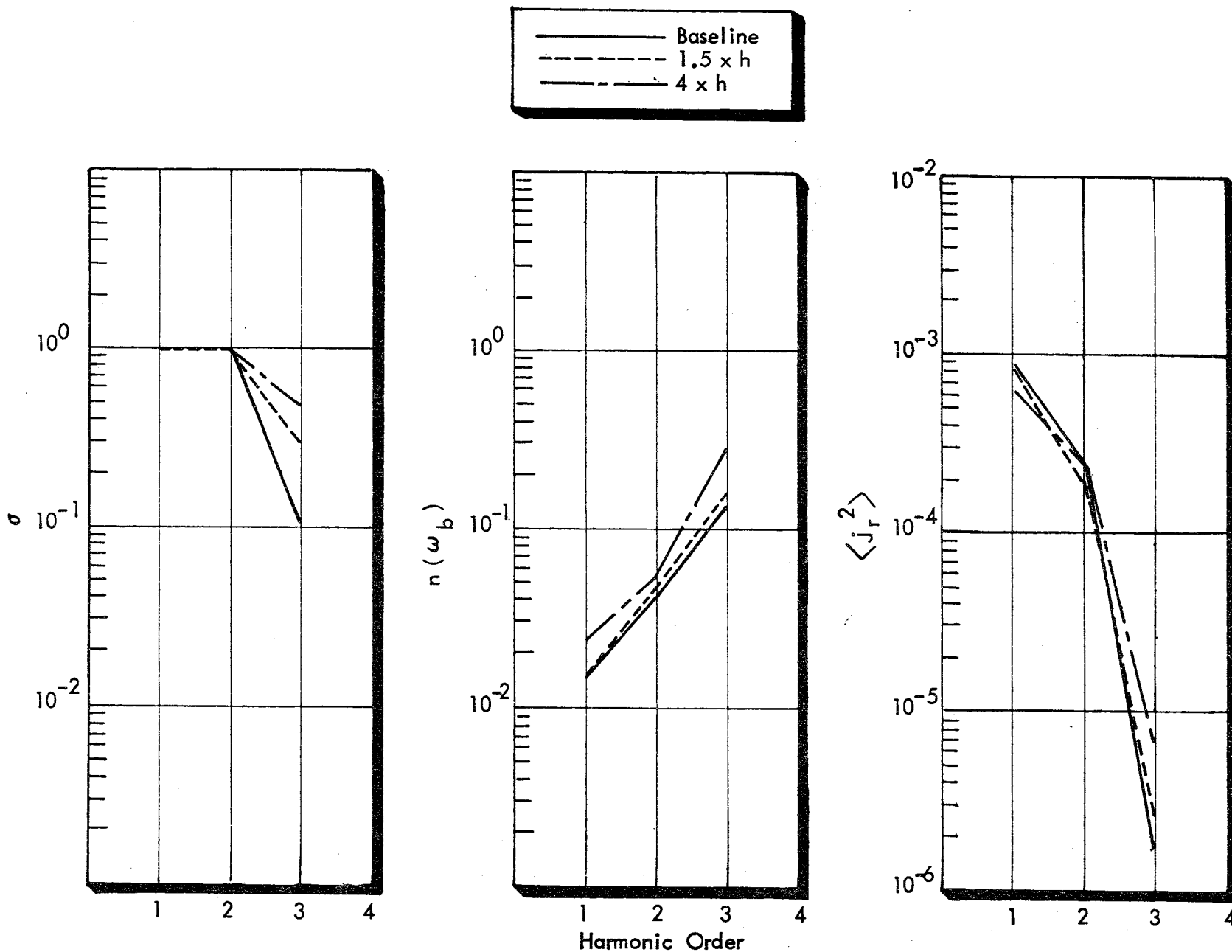


FIGURE 73. EFFECT OF VARIATIONS IN SKIN THICKNESS FOR WIDE BODY AIRPLANE

$L_x = 5.08 \text{ m}; L_y = 5.227 \text{ m}$
 $h = 1.78 \text{ mm}$
 $a_x = 0.70; c_x = 0.01; u_x = 745 \text{ m/s}$
 $a_y = 0.22; c_y = 0.01; u_y = 498 \text{ m/s}$

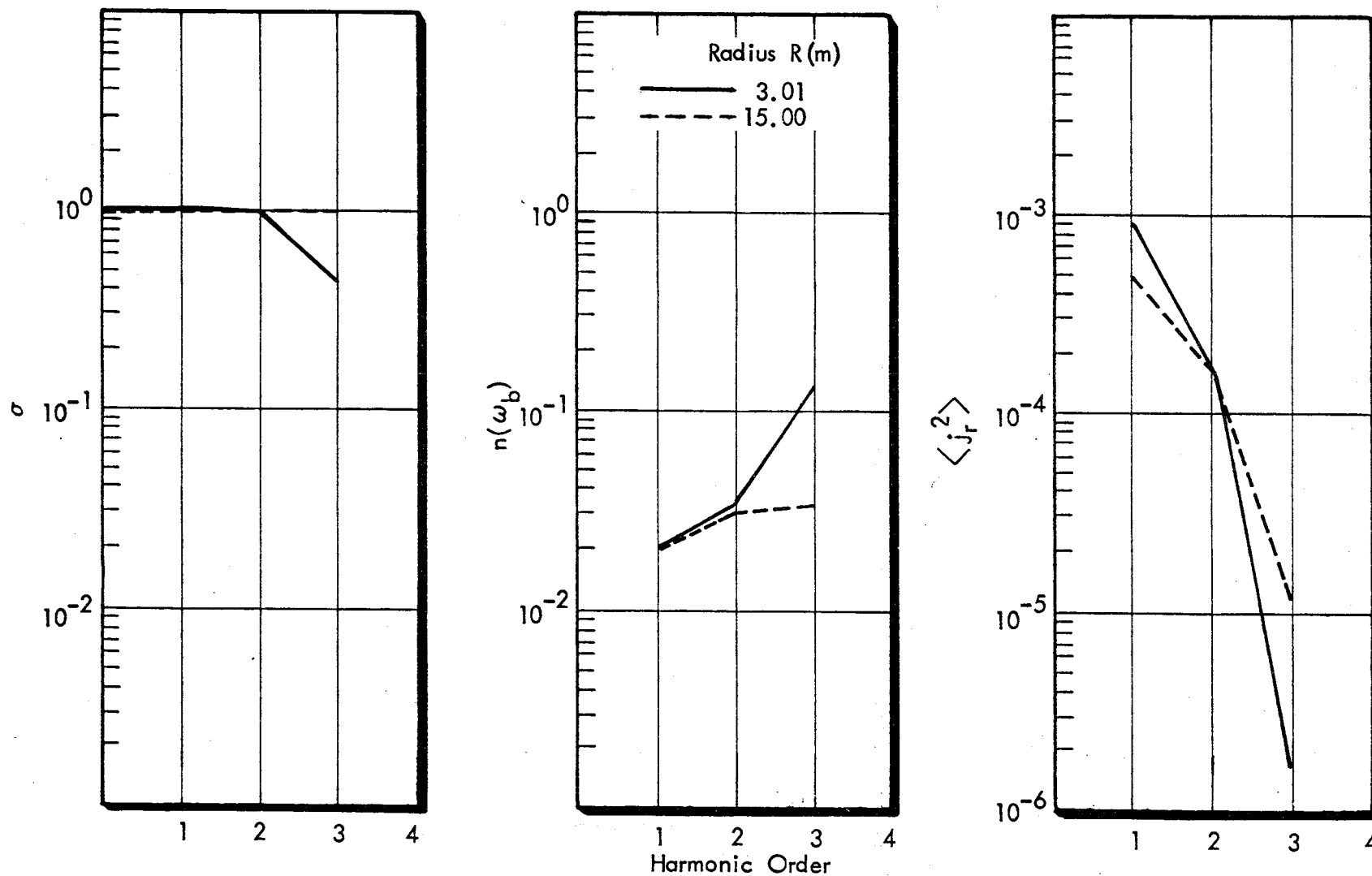


FIGURE 74. EFFECT OF PANEL CURVATIVE ON $\langle j_r^2 \rangle$, $n(\omega_b)$ AND σ FOR WIDE BODY AIRCRAFT (ELEMENT 4)

of Appendix A, that $L_x > a_x^{-1}$ and $L_y > a_y^{-1}$, must be used in selecting appropriate panel dimensions both circumferentially and axially over the fuselage surface. Thus, while the analytical model does not of itself require a cylindrical test section, it does require that the panel elements have the correct curvature and have dimensions which satisfy the decay rate criterion. Correct simulation of the fuselage structural response and associated noise reduction will require in general a model fuselage which extends circumferentially from floor to floor.

9.2.4 Summary of Practical Model Simulation Requirements

The parametric studies in Sections 9.2.2 and 9.2.3 have produced requirements for the design of validation tests for the analytical model. These requirements can now be summarized for easy reference. It is also important at the same time to reiterate the assumptions which formed the basis for the requirements.

Firstly, it was assumed that the tests will attempt to model as closely as possible a fullscale baseline fuselage structure and sidewall treatment, so that it will not be necessary to perform extensive analytical work to complement the measurements. Secondly, since the noise control problems are most severe for the low order harmonics, emphasis is given to the simulation of the fullscale conditions at the model scale frequencies associated with the low order harmonics.

Requirements for the model are as follows:-

Excitation: Trace velocities and amplitude decay rates should be simulated closely (within an accuracy of $\pm 10\%$). Coherence decay can be simulated less

accurately. (Note that, without superimposing a mean airflow, the trace velocity will be supersonic, i.e. it will represent only that portion of the pressure field which is in the plane of rotation or downstream of the propeller. This is the region of high acoustic transmission).

- Structure: The structure should be curved and have frames and stringers. The structure should extend from floor to floor, and be at least two fuselage diameters long. The stiffness, mass and spacing of the frames and stringers should be simulated closely, (within an accuracy of $\pm 20\%$). Simulation of skin mass is less important (an accuracy of $\pm 25\%$). In-plane loads due to fuselage pressurization need not be simulated.
- Sidewall Treatment: Simulation of the add-on sidewall treatment is most important. Structural flanking must be avoided.
- Cabin Spaces: The model overlap of the acoustic space should be simulated closely. However, details of the cabin space, such as location of absorption, and shape of furnishings and passengers, are of low importance: the length need not be scaled provided that the absorption is scaled.

9.3 Candidate Noise Sources

The analysis performed in Section 9.2 indicated that the noise transmission through the fuselage structure was strongly dependent on the trace velocity and spatial decay of the excitation field. Thus the selected model sound source should be capable

of representing these properties fairly accurately. It should be noted that the analytical model does not distinguish between a trace velocity associated with the propagation of acoustic waves and a trace velocity associated with forward motion of the fuselage. Thus it is not necessary to introduce mean flow over the model structure, although if the mean flow is zero it will not be possible to model the subsonic trace velocities which occur over the forward regions of the baseline airplanes. These regions are, however, of lesser importance in terms of noise transmission.

Several alternative noise sources have potential for use in simulation of the excitation. Propeller noise sources include the various model propfans, and full or model-scale propellers, either operated statically or in the presence of air flow, such as provided by a wind-tunnel or by in-flight conditions. Electro-acoustic sources, such as a single or an array of suitable loudspeakers, have found application as simulation devices in some verification programs [10]. The arguments for candidate sources are reviewed herein.

9.3.1 Model Propfan

A model propfan has been used in NASA Lewis/Hamilton Standard test programs. The model has the correct geometry and number of blades (at least as far as the current state of technology is concerned) and would be operated at scaled rpm to maintain correct tip Mach number. It could be operated alongside a small model fuselage in a wind tunnel, although to reach a flow Mach number of 0.8 it is probable that a test section without acoustic treatment (and with attendant data interpretation problems) would have to be used. Tunnels with

acoustically treated test sections generally operate at Mach numbers no greater than 0.35. It should be noted that the simulation of propfan performance by overspeeding the model propfan to achieve the helical tip Mach number associated with cruise conditions does not necessarily simulate propfan acoustics correctly. It has been claimed that such a situation does not correctly simulate pressure amplitude, and that it will not simulate directivity and trace velocities either.

Firstly, the main disadvantage of the model propfan is that, to maintain the correct ratio of fuselage diameter to propeller diameter, the model fuselage would be very small thereby making it very difficult to scale the fuselage structure and acoustic treatment. For example, considering the narrow-body airplane, ($D/\phi = 1.13$ and $r/D = 1.8$) use of the SR-3 model propfan [43] with $D = 0.622\text{m}$ requires that the model fuselage be 0.55m or 21.5 inches in diameter. Then, maintaining the ratio of add-on sidewall treatment depth ℓ to fuselage diameter, $\ell/\phi = 0.042$, the model fuselage would require a sidewall depth of 6.3mm and an associated flow resistance for the porous infill in excess of 10^6 mks rayls/m. Such scaling of the sidewall is impractical. Furthermore, effects of the measurement processes, such as the presence of a microphone array in the cabin volume, or (light-weight) accelerometers on the model skin, might lead to erroneous results.

Secondly, even though the propeller and fuselage would be small, it would still be difficult to install both of them in a wind tunnel test section (open or closed) with a representative distance between propeller tip and fuselage, and with adequate clearance between tunnel wall (or shear layer) on one hand, and

propeller tip and fuselage wall on the other. For example, using the above example with $D/\phi = 1.13$, $r/D = 1.8$ and $D = 0.622\text{m}$, and assuming a shear-layer thickness of 150mm, it is clear that only half the model fuselage can be immersed within the open jet flow of the anechoic flow facility at NSRDC, Carderock [44], as shown in Figure 75. (The maximum flow Mach Number of the tunnel is $M_0 \sim 0.2$). Larger fuselage models compound the problem. A similar situation exists with the United Technologies facility [45], where $M_0 = 0.35$ can be achieved.

9.3.2 General Aviation Propeller

Use of a general aviation propeller in conjunction with a model fuselage has the advantage that the noise mechanisms show certain similarities with those of the propfan. However, it is anticipated that there will be several problems associated with a test configuration of this type, one problem being the general inflexibility in matching the model characteristics with those for the baseline airplanes.

If a fullscale propeller is used with a model fuselage, the combination of propeller and fuselage would be too large for any wind tunnel test section except the large, low speed tunnels which could not reproduce a forward Mach number of 0.8. Consequently, the tests would have to be performed under static conditions.

The longitudinal spatial variations of external sound pressure level predicted for the three study aircraft can be compared with measured variations for general aviation aircraft, as shown in Figure 76. It is seen that for a given tip clearance, r/D , the rate of change of sound level predicted for the propfan

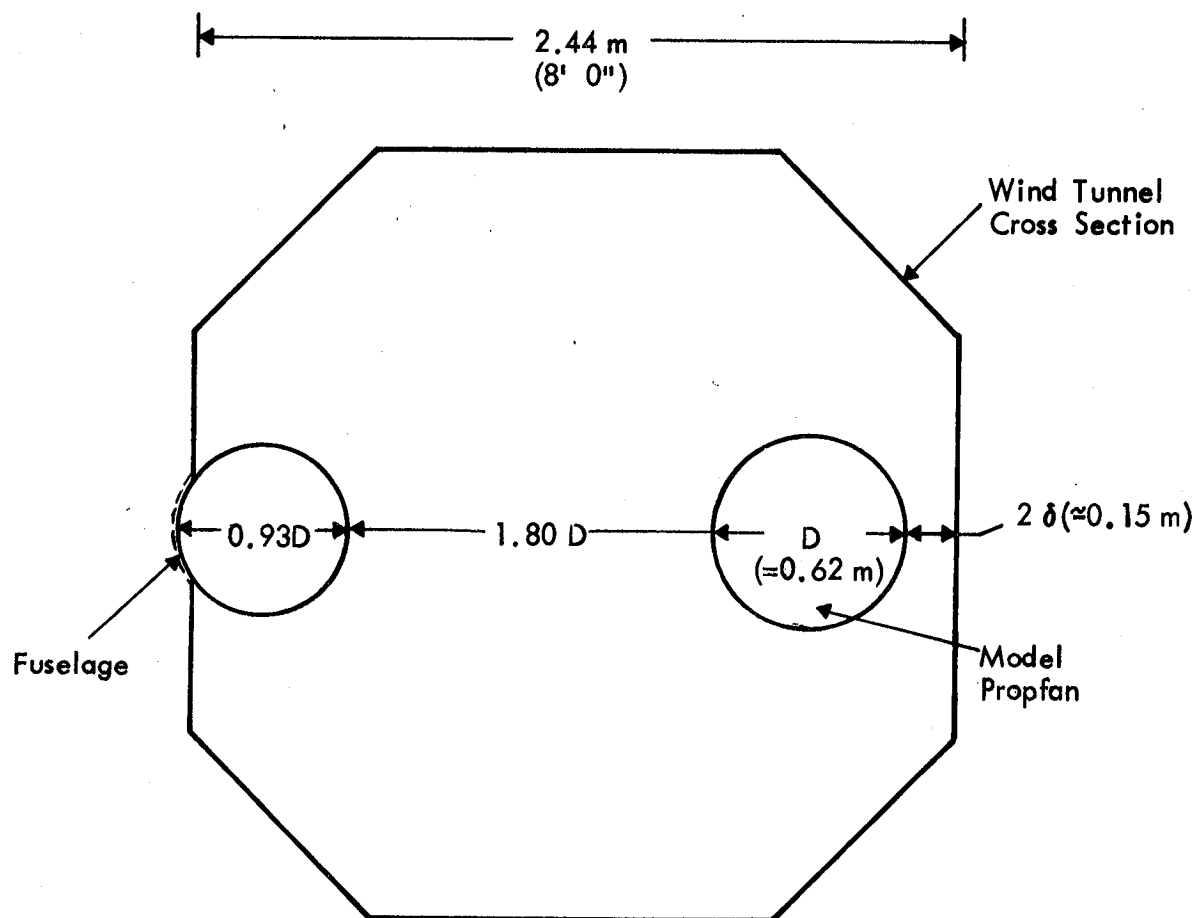
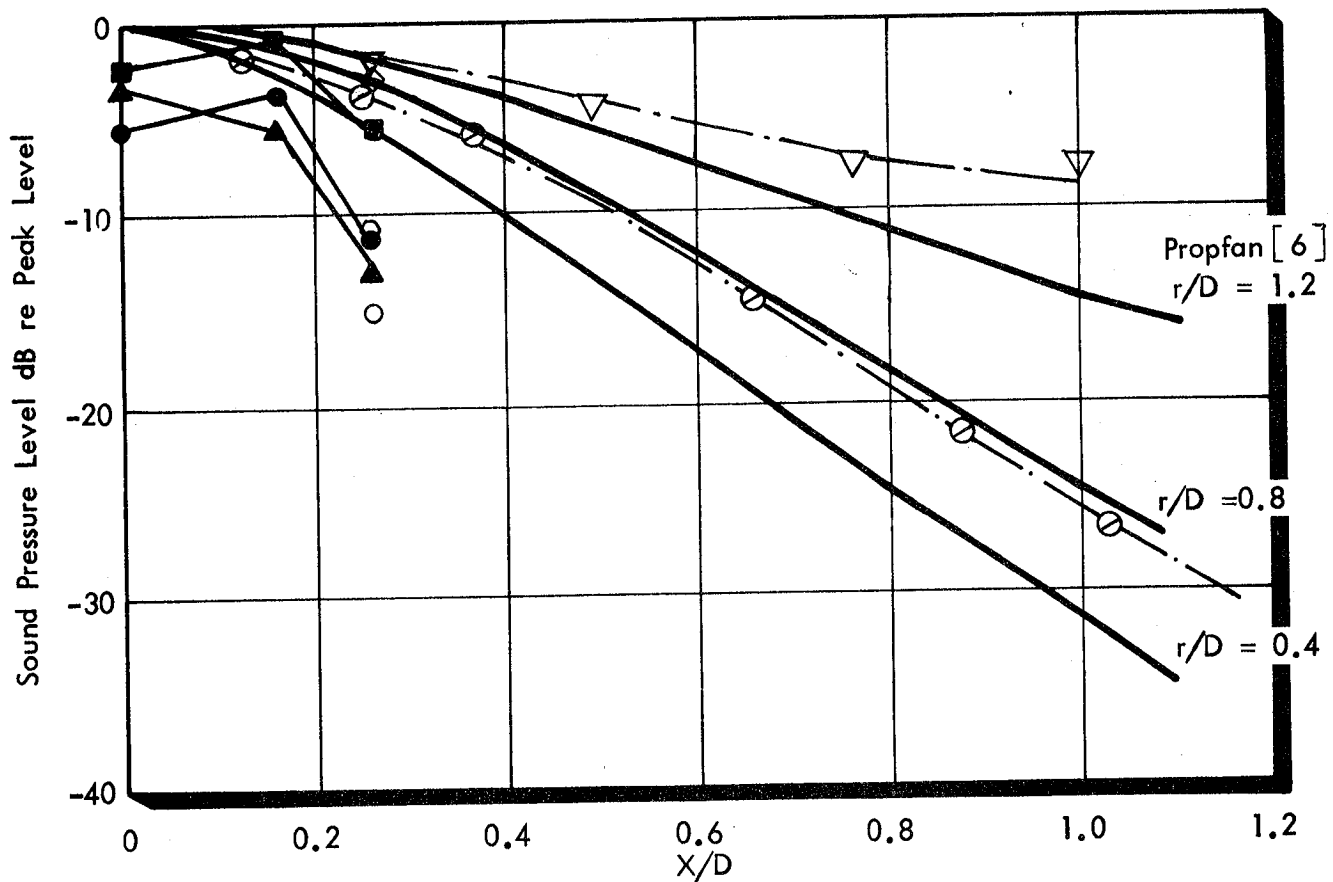


FIGURE 75. SKETCH OF POSSIBLE ARRANGEMENT OF MODEL PROPFAN AND FUSELAGE WITHIN THE ANECHOIC FLOW FACILITY, NSRDC, CARDEROCK [44]



Propfan Calculations

Harmonic	1	2	3	
Static	■	●	▲	$M_t = 0.6$ $r/D = 0.051$
30 Knots	◇	◇	○	

Model Tests [46]

- $M_t \approx 0.75$ $r/D = 0.083$
- ▽— $M_t = 0.60$ $r/D = 0.333$

FIGURE 76. SPATIAL VARIATION OF PROPELLER OVERALL SOUND LEVEL IN LONGITUDINAL DIRECTION: COMPARISON OF PROPFAN PREDICTIONS AND GENERAL AVIATION MEASUREMENTS

under cruise conditions is much greater than that for the (model test) general aviation propeller under static conditions.

A comparison of pressure field trace velocities also shows significant differences between the propfan predictions and general aviation measurements (Figure 77), although in this case only one set of data is available for general aviation propellers. At large separation distances the differences between trace velocities for propfan and general aviation propellers are associated mainly with the contribution from forward motion, whereas at small separation distances the controlling parameter is tip clearance. The circumferential trace velocity is also a function of tip clearance.

From this brief comparison it is seen that a general aviation propeller under static conditions cannot reproduce simultaneously both sound level spatial decay and pressure field trace velocity -- two parameters which are considered to be important in the analytical model.

Another problem is associated with the values of the blade passage frequencies. If the rotational tip Mach number is maintained at 0.8 for the general aviation propeller then the blade passage frequency will be too low (because of the small number of blades). Consequently the required scaled frequencies for the propfan blade harmonics will have to be modeled by higher-order harmonics of the general aviation propeller. Since harmonic level decreases as harmonic order increases, the higher order harmonics will be lower in level and could create a signal-to-noise ratio problem for the high transmission loss tests. The higher order harmonics may also have different directivity patterns.

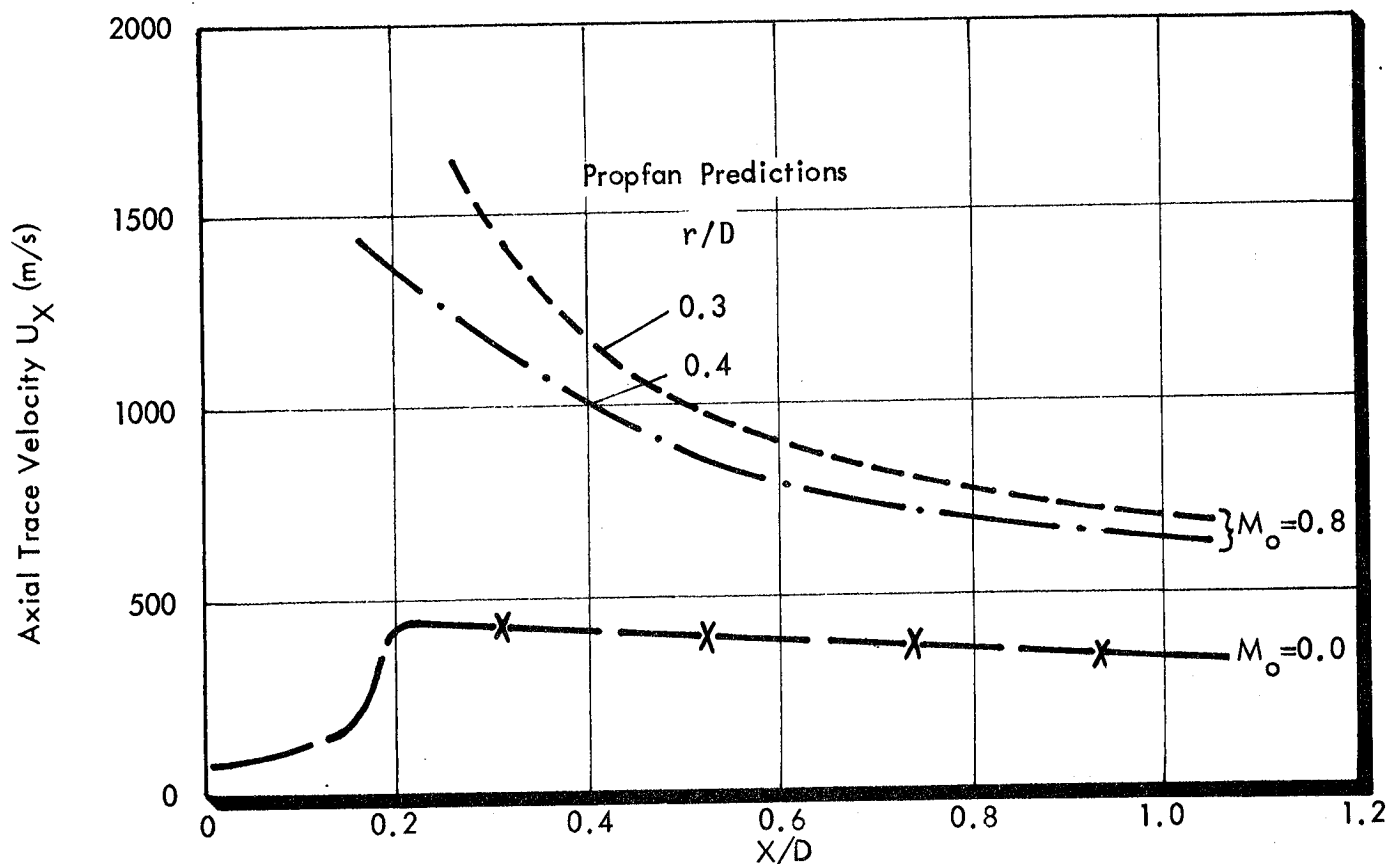


FIGURE 77(a). VARIATION OF AXIAL TRACE VELOCITY WITH X/D FOR 3 STUDY AIRPLANES (RAY ACOUSTICS MODEL WITH SOURCE LOCATION AT 0.7 PROPELLER RADIUS)
 — X — AERO COMMANDER DATA [8]

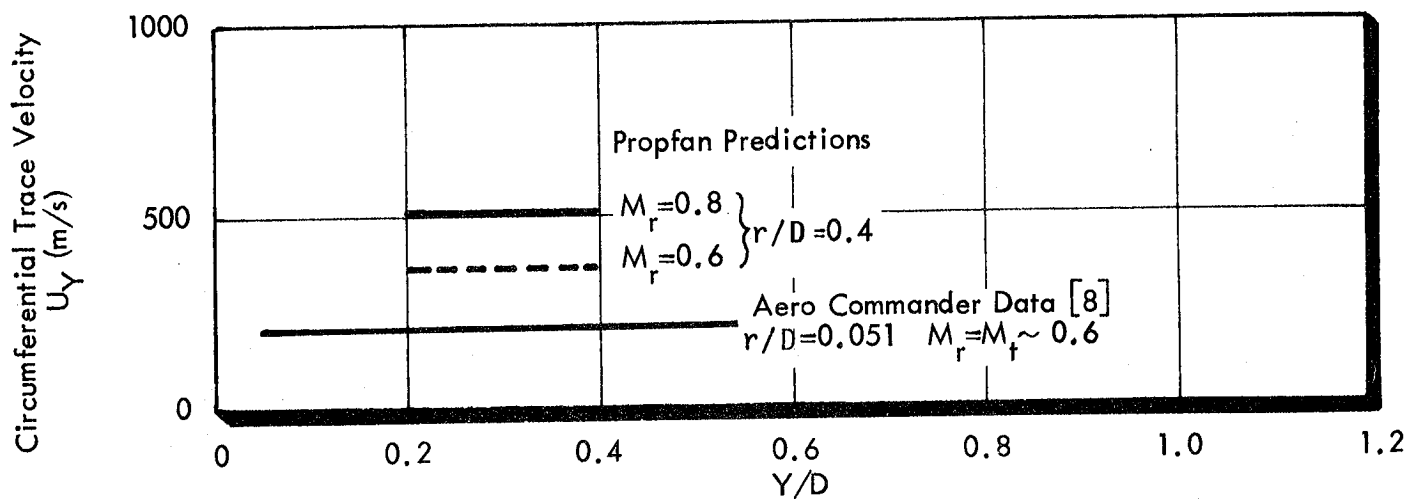


FIGURE 77(b). VARIATION OF CIRCUMFERENTIAL TRACE VELOCITY. PROPFAN PREDICTIONS BASED ON 'RIGID BODY' ROTATION OF HYDRODYNAMIC PROPELLER PRESSURE FIELD.

This brief discussion has identified several important differences between the pressure field of a fullscale general aviation propeller and the desired field for the model propfan. These differences are sufficiently important that the general aviation propeller is not recommended as a model source for direct modeling of the baseline aircraft conditions. It could be used, however, as a noise source in a test to validate the analytical model for general aviation conditions.

9.3.3 Electro-acoustic source

An electro-acoustic source, such as an electro-magnetic driver coupled to an acoustic horn offers great flexibility in frequency content of the excitation. Also, by suitable choice of horn characteristics and orientation, the source can be used to represent pressure field trace velocities in longitudinal and circumferential directions, and sound level spatial variation over the model surface.

Figure 78 presents the directivity required of an electro-acoustic source used to simulate the propfan directivity, for each of the study airplanes. The Hamilton Standard method [6] was used to construct the curve. Comparison with the directivity of a point source, located to develop the required pressure field trace velocities of the model fuselage surface shows that an omni-directional source is not adequate. Strong longitudinal directivity is required.

Ray acoustics has been used to determine the propfan trace wavenumbers (see Section 4.6) and is also used to determine the position of the electro-acoustic source. Figure 79 presents a polar plot of the required directivity for the

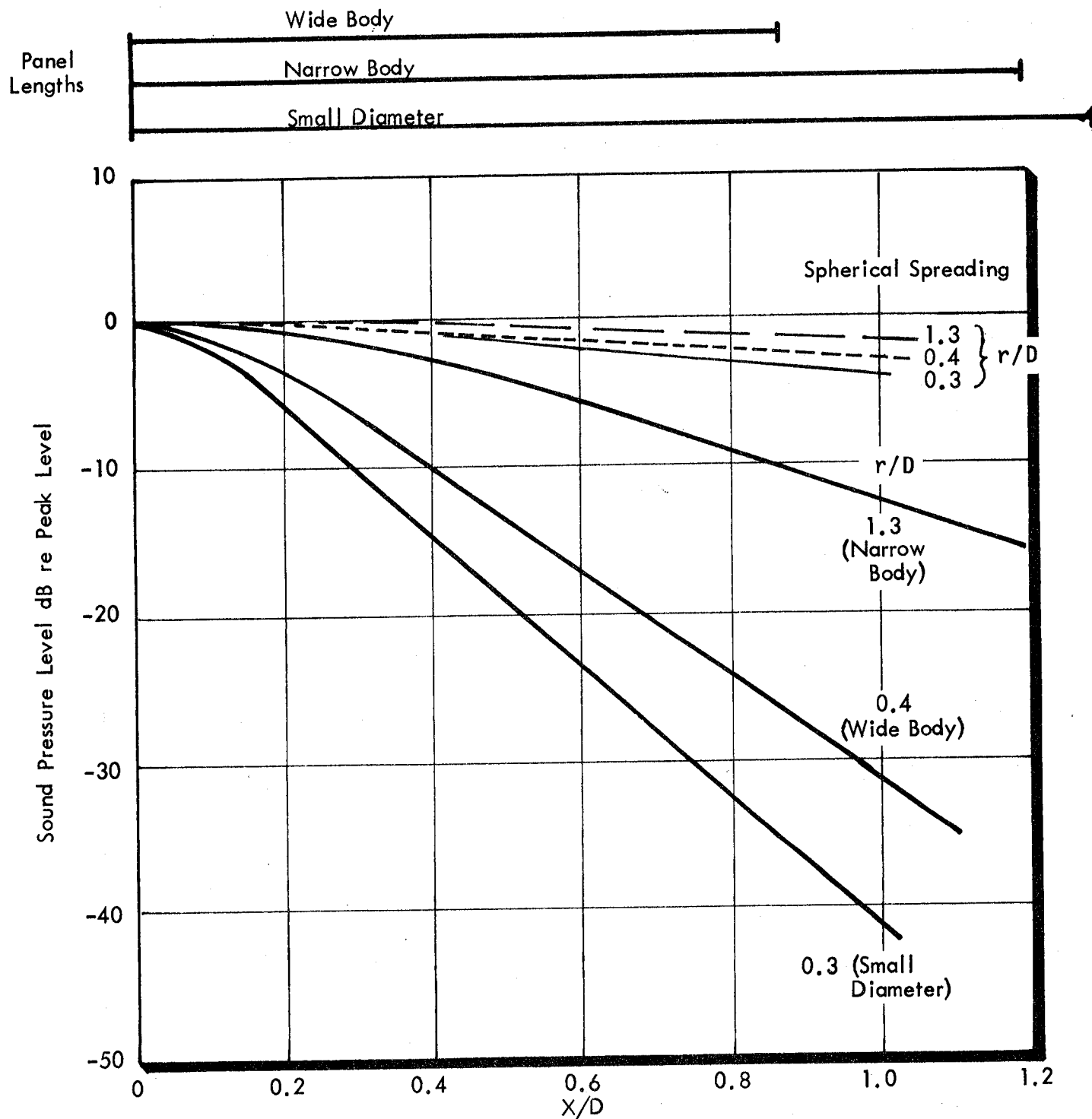


FIGURE 78. REQUIRED AXIAL DIRECTIVITY & SPHERICAL SPREADING LOSSES FOR EACH STUDY AIRCRAFT (INBOARD PROPELLER)

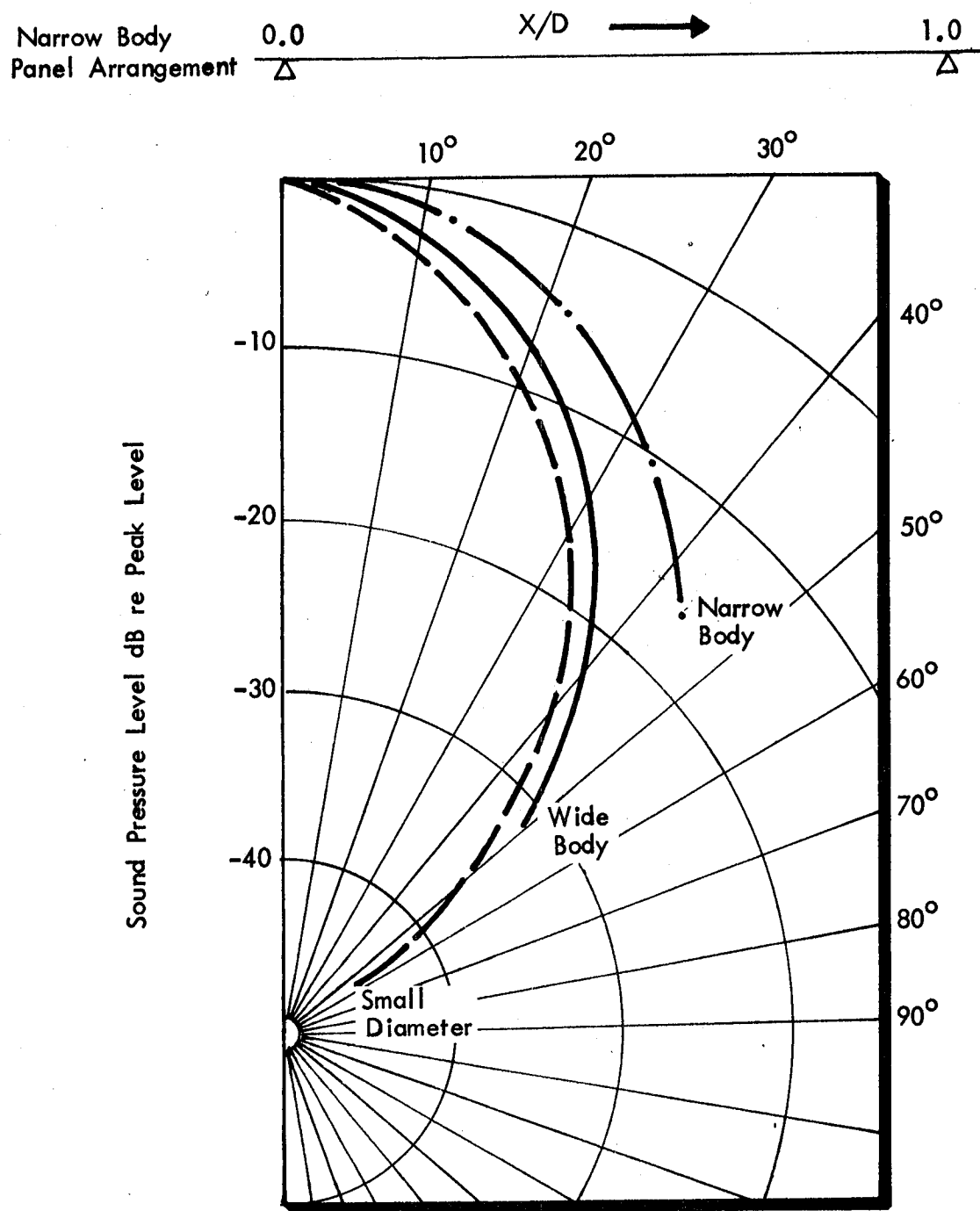


FIGURE 79. REQUIRED DIRECTIVITY FOR ACOUSTIC SOURCE (INBOARD PROPELLER) SHOWING PANEL LOCATION FOR NARROW BODY AIRCRAFT

electro-acoustic source for inboard-propeller simulation for each study airplane. In order to provide representative dimensions, the figure also shows the location of a narrow-body panel. It is clear that the electro-acoustic source must have pronounced longitudinal directivity.

Figure 80 shows the predicted variation in circumferential levels for an electro-acoustic source, assumed to have point-source radiation characteristics in the circumferential direction, (X is the center of the electro-acoustic source). The propfan acoustic decay rate is much smaller in the circumferential direction than in the longitudinal direction, and is well approximated by a point source. Thus the electro-acoustic source should have little circumferential directivity.

A long, flat horn, aligned so that the horn axis is perpendicular to the model surface, will produce such a pressure field spatial variation. The horn width will be approximately two acoustic wavelengths long at the lowest model test frequency, and the depth will be quite narrow. Possibly two horns will be required depending on the frequency range to be tested. An alternative configuration would involve a line array of several closely-spaced point sources, aligned parallel to the model fuselage axis. An electro-acoustic source (or, for that matter a general aviation propeller) under conditions of zero forward motion could not model the subsonic trace velocity predicted for the fuselage region well forward of the propeller plane of rotation. However, calculations using the analytical model indicate that this forward region is of low importance in terms of noise transmission and can be omitted from the validation process for the analytical model.

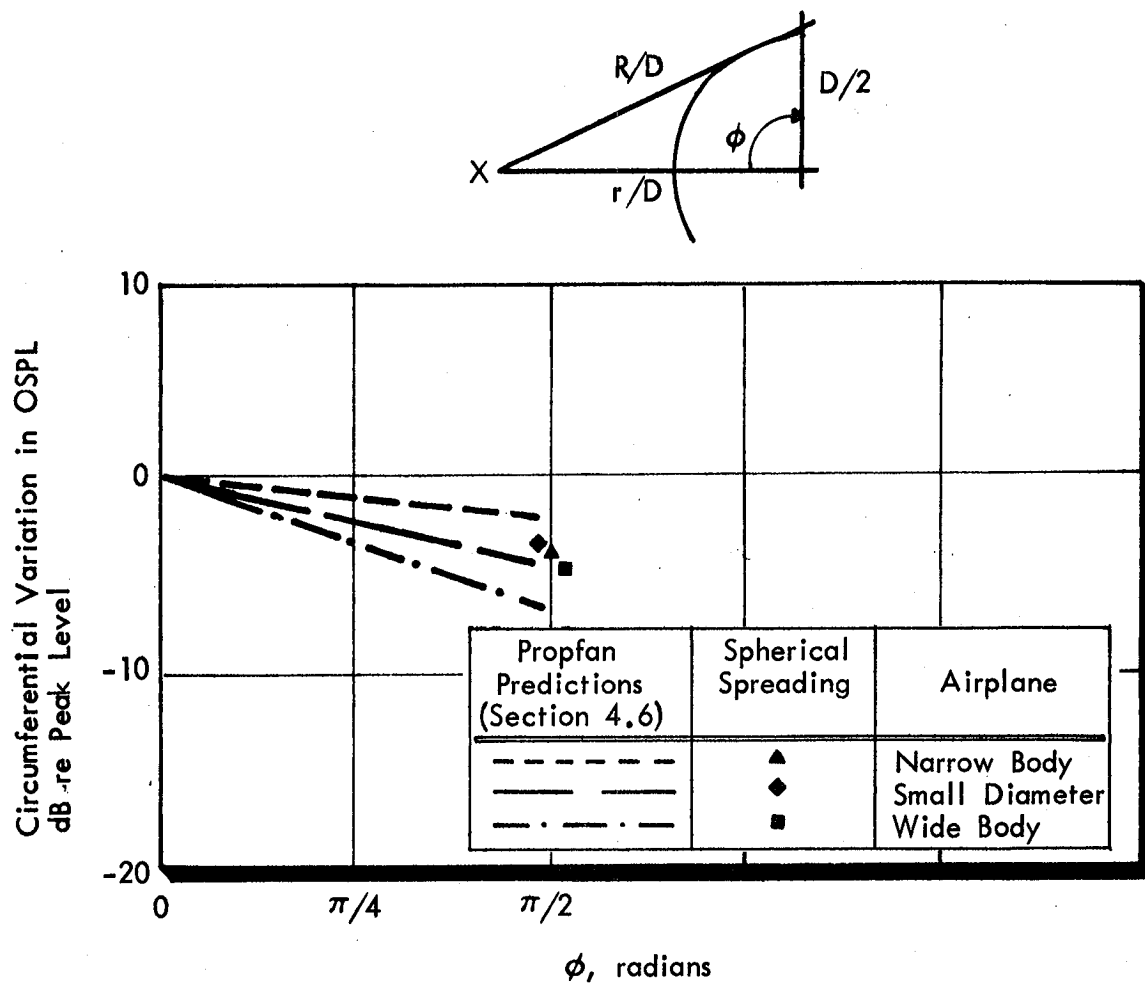


FIGURE 80. COMPARISON OF ACOUSTIC SOURCE SPHERICAL SPREADING LOSSES WITH PROPFAN AIRPLANE PREDICTIONS - CIRCUMFERENTIAL DIRECTION

9.4 Validation Experiments with a Model Fuselage

9.4.1 General

Sections 9.2 and 9.3 presented an investigation of the excitation, structure and cabin parameters affecting the design of experiments for validation of the analytical model and associated noise control predictions. It was assumed in the investigation that the performer of the validation tests would not have ready access to the computer program developed for the analytical model. Thus, the design of the model and experiment would be carried out in a manner such that the prop-fan airplane conditions could be adequately simulated. Analytical results available from the present study could then be used directly for comparison with the experimental data.

It is recognized that the separation of experimenter and analyst imposes severe constraints on the validation process. In contrast, verification of a similar model for the payload bay acoustic environment of the Space Shuttle orbiter vehicle [4,10] was achieved by close collaboration between the experimenter and analyst. With the Space Shuttle experience in mind, care has been taken in the planning of the proposed test program to minimize problems associated with a possible lack of access to the computer program for the analytical model.

In this section a detailed description is presented for a model test program that would provide experimental validation of the analytical model and its use in the prediction of prop-fan interior noise control. Problems discussed include the test configuration (size and number of test models, test environment), excitation details (frequency content, orientation,

spectrum shape), error assessment as it relates to comparisons between experiment and predictions, required measurements, and data acquisition methods.

9.4.2 Model Test Configurations

The most straight forward test program would be the validation of the analytical model only for the case of add-on noise control treatments. This could probably be accomplished with the use of only one structural model. On the other hand, if the predictions are to be validated for both add-on and advanced noise control methods, several structural models will be required, with at least two incorporating the advanced noise control concepts.

The requirements for accurate simulation of the noise transmission into a prop-fan airplane under cruise conditions have been identified in section 9.2.4 and in section 9.3. While practical experimental design will force various compromises to be made, it is argued that good simulation of full-scale fuselages representative of the baseline airplanes is feasible and that the use of an electro-acoustic loudspeaker source would enable adequate simulation of the major characteristics of prop-fan acoustics in the region of maximum transmission of acoustic power through the airplane fuselage.

Figure 81 shows a sketch of the end view of the recommended test configuration for the evaluation of the analytical model for the baseline structure and the add-on noise control treatments. The model consists of a complete cylinder which is lined with appropriate sidewall treatment. The cylinder is elevated on supports and located in an essentially anechoic

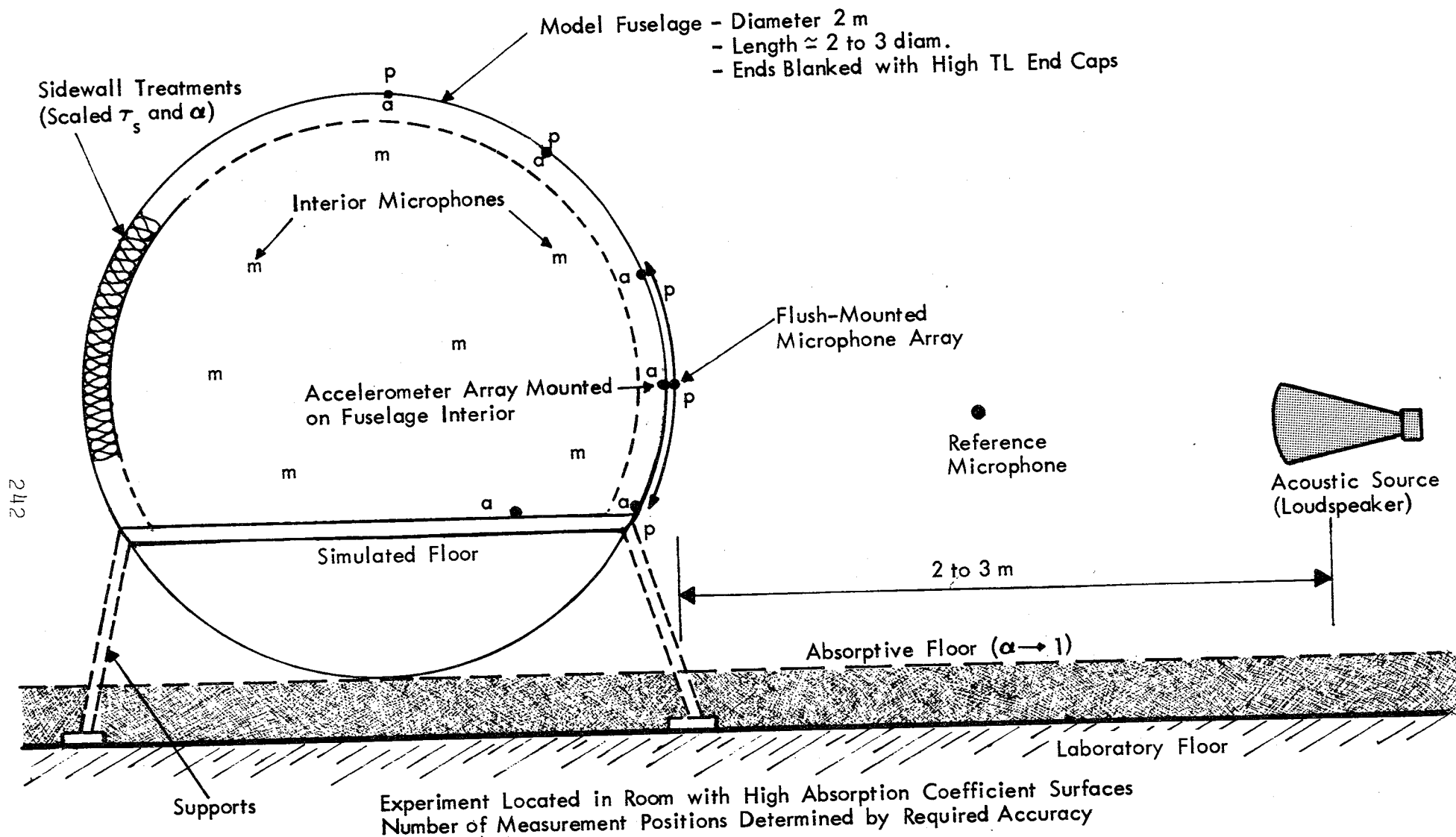


FIGURE 81. SCHEMATIC END VIEW OF TEST CONFIGURATION

environment. The acoustic source, a loudspeaker, is located approximately 1.5 model fuselage diameters from the skin surface and part way between the cylinder ends. The structure of the cylinder would be of skin-stringer-frame construction using aluminum material. The dimensions of the structural items would be scaled with respect to cylinder diameter as indicated in sections 9.2 and 9.3.

The diameter of the model fuselage is approximately half that for the narrow-body study airplane, i.e. 2m. Such a scaling allows for convenient measurement of the various important physical quantities and does not introduce significant construction difficulties which, if the test model is built to too small a scale, might change the physics of the noise transmission. The length of the model fuselage is selected to be between 2 and 3 model diameters, to ensure adequate decay of the pressure amplitude over the model length and to allow the peak excitation amplitude to be located away from the model boundaries. The model length, while not scaled in proportion to the fuselage radius, is also required to give sufficient modal overlap for the acoustic modes. Care is required to position the interior absorptive material to simulate a longer cabin volume: additional absorption will be required on the test model forward and aft bulkheads. End caps will be required on the test model and the caps will have to have high transmission loss characteristics so that there are no flanking paths when the high transmission loss treatments are tested on the sidewall. The tests proposed will not require pressurization of the model. Thus the end caps will not have to withstand pressurization loads. The caps should be removable to allow for introduction of the various noise control treatments to the model cabin space. No simulation of the cabin furnishings is considered necessary.

In order to achieve the correct spatial variation for the exterior pressure field, the noise source will be located at some position between the two planes defined by the end caps, and the directivity of the source will be such that there is a propagating pressure field over the model. It should not be necessary to provide extension sections to the test cylinder to correct for diffraction at the ends of the structure. However, the test chamber should be treated with absorptive material so that the propagating pressure field over the model surface is not contaminated unduly by any reverberant field in the chamber.

Add-on treatments tested in the model cylinder would concentrate on double-wall systems with porous material in the space between the walls. All the parameters of interest would be scaled as required from the analysis in Sections 9.2 and 9.3. Special consideration should be given to the identification and elimination of flanking paths. Other noise control treatments could be tested although only the double-wall was found, analytically, to achieve the noise reductions required to meet the 80 dB goal for A-weighted interior sound level.

It is possible, in principle, to construct scale models for any of the advanced noise control methods although, in practice, there may be difficulties in achieving the correct scaling for the more exotic designs. Structures which involve modifications to conventional aluminum skin-stringer-frame construction should follow the same scaling laws as for the baseline structure. Composite structures will probably need some additional analysis to determine the most appropriate scaling procedure.

The specific choice of test hardware for the advanced concepts is less well defined than in the case of add-on treatments. However, potential candidates include those discussed in Section 8:

- a) Additional ring frames on the baseline model
- b) Frames with increased stiffness achieved by redesign of the frame cross-section
- c) Increased skin thickness
- d) Extensive damping treatment
- e) Composite (honeycomb) skin with ring frames, (with and without additional damping).

It should be noted that the noise control concepts listed above have been investigated using the analytical model and in no case did the predicted noise reduction approach the required reduction of 25 dB for the A-weighted level. Thus validation of the analytical model in this case has the somewhat negative result of confirming that the noise control approach is not very effective.

The model test structure recommended for validation of the analytical model predictions for the baseline structures and the add-on noise control treatments is in the form of a cylinder with end plates. However, this type of model could be extremely expensive for tests of advanced type structures, unless these structures could be formed as modifications to the basic skin-stringer-frame cylinder. An alternative approach would be the use of large curved panels rather than complete cylinders. These panels would be placed in one wall of an enclosure, which could be constructed as a wooden double-wall with high transmission loss material in the space between the walls. The cost of construction for the advanced structures would then be reduced.

The use of test items should not have a large impact on the validation of the analytical model since it is assumed when making the noise transmission predictions in Sections 6 through 8 that the fuselage structures can be represented as curved panels rather than a complete cylinder. The use of curved panels in the test program would mean that the above assumption could not be verified, but all other assumptions in the analytical model could be validated.

9.4.3 Basic Measurements

Two sets of measurements should be made for the validation tests. One set, basic measurements, represents the minimum requirements for validation. The second set, diagnostic measurements, will provide the additional information required to fully understand the reliability and accuracy of the analytical model.

The basic measurements involve the exterior and interior sound levels. The exterior measurements ensure that the correct excitation is being used and the interior measurements indicate whether or not the 80 dB(A) goal is achieved. Exterior data required to describe the excitation field will include the variation of sound level in the longitudinal and circumferential directions, and the coherence and phase of the pressure field in the two directions.

In the case of the interior sound levels, the following measurement procedure is recommended:

- a) Determine space average sound levels from a series of fixed microphones or from microphone traverses. Microphone locations can be associated with equal volumes for ease in space averaging.

- b) Measure sound level gradients in radial and axial directions to obtain estimates of spatial variation.
- c) For given microphone locations, measure sound levels as excitation frequency changes by small amounts. Calculate deviation for sound levels.

The recommendation to measure both space-average and spatial gradients for the interior sound levels is based on experience from other validation programs. Factors to be considered include:

- a) the model test cavity may not be fully representative of the airplane cabin shape and contents;
- b) a detailed analytical representation of the cavity is not possible within the accuracy of the present analytical model; and
- c) the analytical model predicts space-averaged levels and then estimates the distribution along the cabin using imaging methods.

Space-averaging has the advantage that inaccuracies in predictions of the detailed modal response of the cavity are smeared-out. However, even space-averaging has to be performed keeping in mind that the measured value has, for practical reasons, to be based on a finite number of measurement locations. Statistical analysis has to be performed to relate the measured value to the expected value. This can be done, for example, by means of standard deviation and confidence limits.

9.4.4 Diagnostic Measurements

It frequently happens that, when experimental data are compared with an analytical model, deficiencies are found in the model. Improvements will then be required to improve the accuracy of the model, but usually these improvements can be made only if there are adequate diagnostic measurements to supplement the basic data. It is recommended that diagnostic measurements be made during the validation tests. These additional measurements will relate directly to various outputs of the analytical model so that appropriate corrections can be made to the model.

Measurements recommended for this diagnostic phase of the validation tests include the following items, which describe the structural response, and structural and acoustic damping.

- Structural response:

- Spatial variation of model vibration
 - Flexural wavelengths (by means of coherence measurements)
 - Modal density (by means of point force excitation)
 - Standard deviation of response as excitation frequency is varied slightly

- Structural Damping:

- Total loss factors for the structure (by means of vibration decay measurements)
 - Radiation loss factors (by relating vibration response to radiated acoustic power)

- Acoustic Damping:

- Acoustic loss factors (from acoustic decay measurements)

9.4.5 Performance of the Validation Tests

In terms of the basic validation tests, the experimenter could simulate an exterior spectrum shape and then measure the A-weighted sound level in the model cabin. However, the resulting overall noise reduction would depend on the selected spectrum shape, and a coarse test of this type is not recommended for the validation of the analytical model. Instead, it is recommended that the tests be conducted on an individual frequency (harmonic) basis. The noise levels or noise reductions would be measured, and compared with the analytical predictions on a frequency by frequency basis. Only then can the analytical model be subjected to an appropriate validation process.

This individual harmonic approach has several other advantages. Firstly, the tests can be performed and the model validated without concern as to the spectrum shape which will be generated by the final propfan design in actual cruise conditions. Secondly, if a noise source is used which enables the sound level to be adjusted at a given frequency, then signal-to-noise ratio problems at higher frequencies will be minimized. The proposed electro-acoustic source provides this control of the excitation characteristics.

The proposed tests include the following excitation conditions:

- (i) Perform the tests at the model frequencies of interest for the three baseline aircraft used in the analysis.
- (ii) Repeat at several frequencies either side of each frequency used in (i) in order to obtain a measure of the statistical variation about the mean. The number of

frequencies used will be determined by the measured standard deviation and the desired confidence limits. (Various tests on airplane fuselages have shown that the noise reduction characteristics can change rapidly as frequency changes.) The statistical analysis is discussed briefly in Section 9.4.7.

(iii) Narrow-band noise, centered at given harmonic frequencies to be used for comparison with (i) and (ii).

The first step in the validation tests will be to ensure that the excitation pressure field satisfies the model requirements in terms of spatial variation in sound level, coherence and phase (or trace) velocity. Subsequent steps in the test program would then be concerned with measurement of interior sound levels or structural response -- with adequate care being taken to ensure that the excitation pressure field characteristics remain unchanged.

9.4.6 Instrumentation Requirements

The instrumentation requirements for signal generation, data acquisition and data reduction are associated with the use of discrete frequency and narrowband noise. Typical schematic diagrams are shown in Figures 82 and 83, where both on-line and recorded data options are included. The use of on-line data acquisition and reduction will probably be the selected approach for many of the tests performed for the validation.

Figure 82 shows potential signal generation and data acquisition systems. The excitation signal is generated as a discrete frequency or narrowband noise and used as input to a loudspeaker. The signal can also be recorded for future

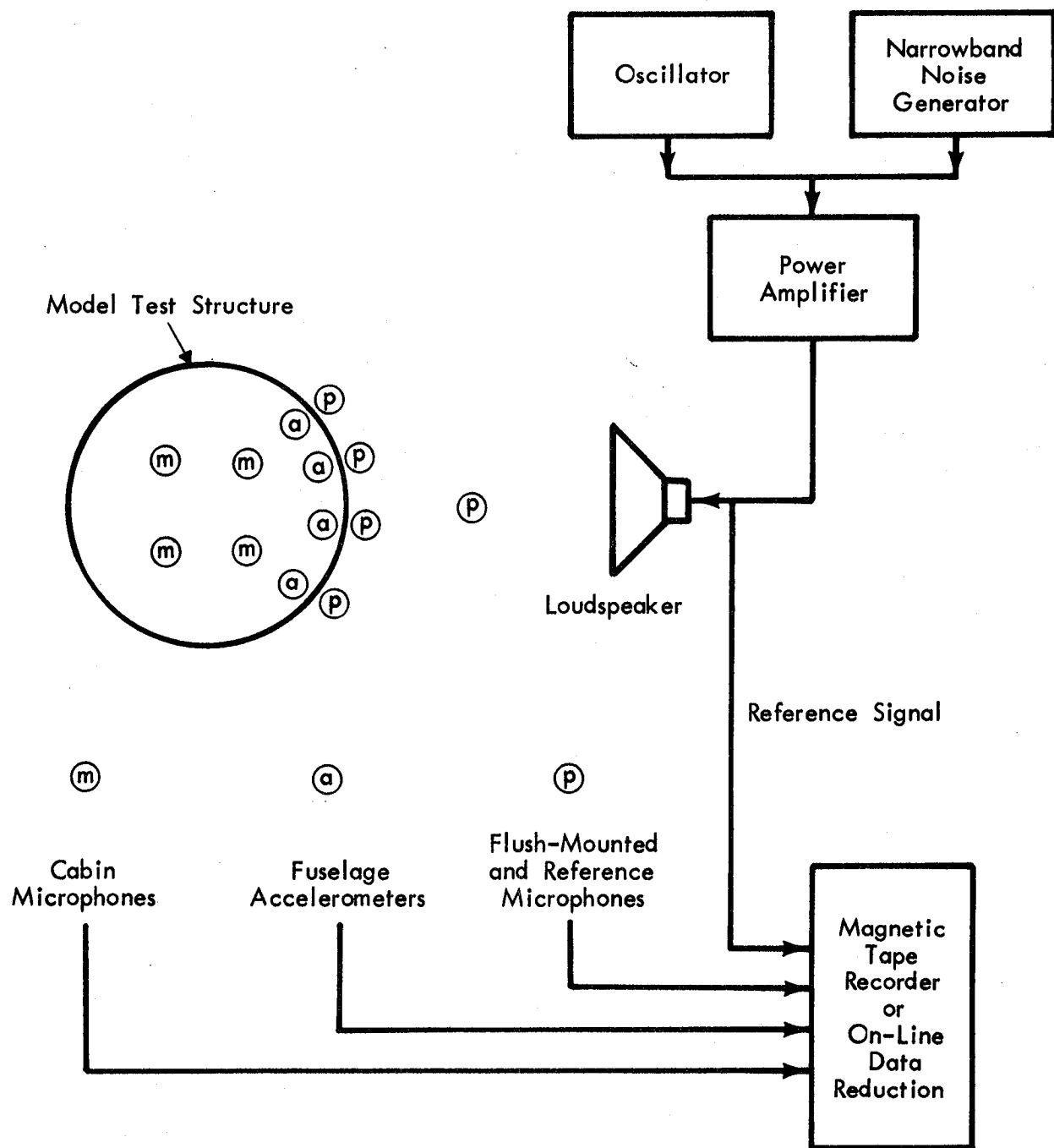


FIGURE 82. SCHEMATIC DIAGRAM OF SIGNAL GENERATION AND DATA ACQUISITION SYSTEMS

reference. In the initial set-up tests, when the loudspeaker is being located so that it generates the required noise field, flush-mounted microphones would be placed on the test structure to measure pressure amplitude and cross-spectral density. The microphones would be arranged in a cruciform array, with 12 to 20 locations selected to adequately define the pressure field characteristics. A reference microphone would be used to monitor sound levels from test to test. These microphones would be, typically, 6mm (0.25 inch) in diameter.

The microphone array inside the model fuselage would consist of 8 to 12 microphones positioned, for example, at fixed positions in the model cross-section, but capable of being moved in the longitudinal direction. The number of measured axes would be determined from an initial examination of the measured data and from the required measurement accuracy. Locations in the cross-sectional plane would be selected so that the areas associated with each microphone were equal.

The structural response would be measured by an array of accelerometers attached to the interior surface of the model fuselage shell. These accelerometers would measure the spatial characteristics of the fuselage vibration.

A typical schematic for data reduction is shown in Figure 83. Spectral analysis is straightforward since the basic filtering is performed by the signal generation system. The analysis consists of measuring the level of the discrete frequency or narrowband acoustic signal for the excitation of the interior pressure fields. Cross-spectral data reduction requires, for example, a multi-function digital signal processor. Signal

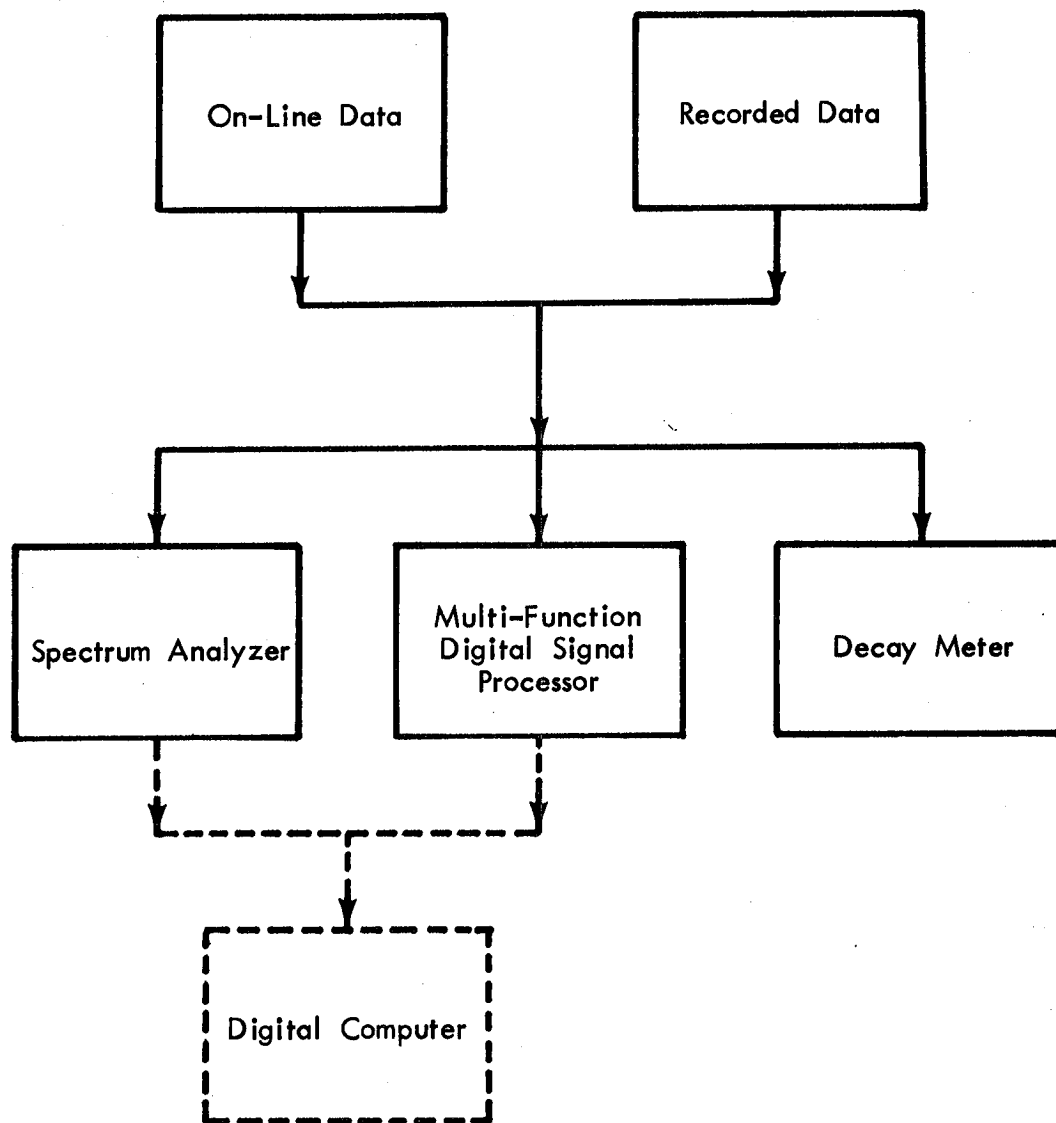


FIGURE 83. SCHEMATIC DIAGRAM OF DATA REDUCTION SYSTEM

decay measurements, to be used in the estimation of structural and acoustic loss factors, requires the use of a decay meter (or a level recorder if the decay is not too rapid).

9.4.7 Data Reliability

Two factors have to be considered under the heading of data reliability. One factor, data repeatability, is important because of the use of discrete frequency excitation. The second factor, data accuracy, is concerned with the comparison between measured and predicted results.

Because of the use of discrete frequency excitation, microphone location may be critical in achieving data repeatability when there is a small number of modes. This problem is alleviated by performing space-averaging of the measured sound levels in the cabin and by the fact that, in the frequency range of interest, there is high modal overlap for the acoustic modes. The situation will become somewhat more severe when spatial gradients are measured for the interior sound field at a given frequency of excitation. Thus, repeat measurements should be made for a given test condition, and allowances made when comparing spatial gradients for different sidewall configurations.

The proposed tests include discrete frequency excitation at several frequencies on either side of a given frequency of interest. One purpose of this variation in frequency is to allow for uncertainties in the prediction of structural and cavity resonance frequencies. By the same token, the data, when averaged over frequency, will show improved repeatability from test to test.

The comparison between measured and predicted sound levels or noise reductions will have to be made on a statistical basis. The importance of such an approach was evident in the validation of the Space Shuttle payload bay acoustic model [11], a situation for which the excitation was broadband in nature and fairly uniform in level. Instead of comparing only the average measured and calculated noise levels, consideration was also given to the variability of the measurement used to make the comparison. Since both the exterior and interior average sound levels were based on a finite number of sample measurements, it followed that the computed estimates would be subject to random errors. These errors were taken into consideration by computing the variances for the measured levels and then constructing confidence limits such as those shown in Figure 84. A similar approach should be followed for the propfan validation tests.

9.5 Aircraft Tests

9.5.1 Applicability of Aircraft Tests

The discussion in Sections 9.2 and 9.3 has concentrated on the design of scale model tests which could be used to validate results from the analytical model. The tests were envisaged as providing answers to the questions posed in Section 9.1. An alternative approach is that of using an existing airplane and performing either ground or flight tests to measure the noise transmission into the fuselage. The question now arises - can the use of an existing propeller-driven airplane provide data which will validate the analytical predictions for the propfan-powered study airplanes? If the answer to the question is negative, then airplane tests can be discarded unless it can be shown that they would serve an alternative, but still useful, evaluation of the analytical model.

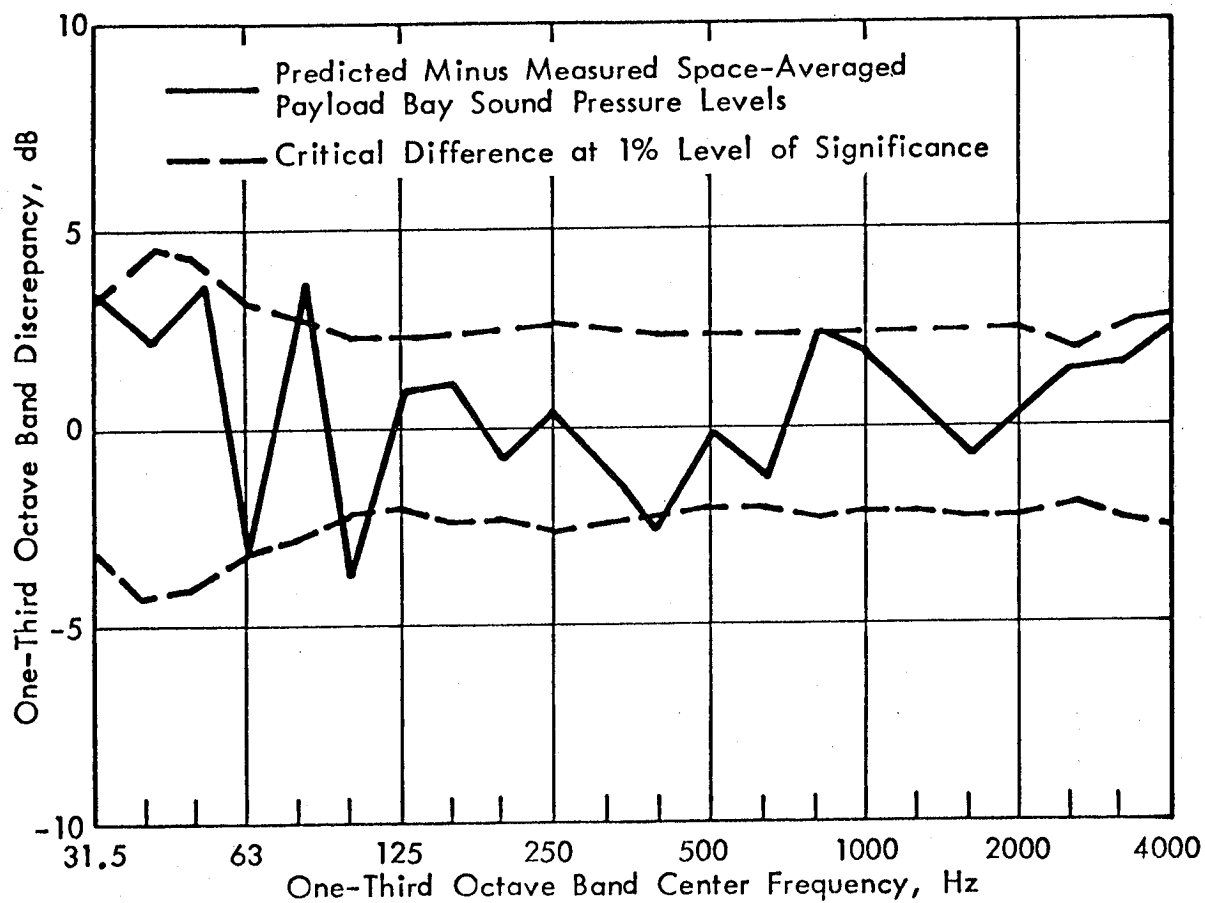


FIGURE 84. DIFFERENCES BETWEEN PREDICTED AND MEASURED PAYLOAD BAY LEVELS FOR SPACE SHUTTLE VALIDATION TESTS [II]

In order to answer the above question regarding the direct applicability of airplane tests, consider first the relevant characteristics of the three aircraft considered in the analytical model development. The aircraft are low-winged and have two or four propellers, with the plane of rotation for all the propellers intersecting the passenger cabin sidewall. The propeller diameter is equal to, or greater than the corresponding fuselage diameter, the propeller has 10 blades and a tip rotational Mach number of 0.8, the separation distance between propeller tip and fuselage structure is greater than $0.3D$ where D is the propeller diameter, the fuselage diameter is greater than 2.44m (8 feet), and the airplane Mach number is 0.8.

Obviously there is no airplane at the present time which meets all these requirements, although there are some aircraft which meet some of the requirements. Two such airplanes are the Lockheed Electra/P3 and the Swearingen Metroliner. They are both low-wing, turboprop aircraft; other typical characteristics are listed in Table 16.

Table 16. Comparison of Study and Existing Aircraft

Aircraft	Propfan Baselines	Lockheed Electra/P3	Swearingen Metroliner
Number of Propellers	2-4	4	2
Number of Blades	10	4	3
Propeller diameter D (m)	3.37-5.83	4.11	2.49
Fuselage diameter ϕ (m)	2.44-6.02	3.45	1.73
Tip Clearance (Inbd.Prop.)	$0.3D-1.3D$	$0.2D$	$0.12D$
D/ϕ	0.97-1.38	1.20	1.44
Tip Rotational Mach No.	0.8	0.7	0.8
Airplane Mach No.	0.8	0.6	0.4
Typical Cruise Alt. (m)	9140	7620	6100
Blade Passage Freq. (Hz)	133-231	68	96

The main differences between the baseline aircraft and the Electra and Metroliner occur in the number of blades, tip clearance and airplane Mach number. The number of blades (and propeller rpm) influences the blade passage frequency, tip clearance influences the spatial decay and trace velocities of the external pressure field, and airplane Mach numbers influence the pressure field longitudinal velocity. All these parameters have been shown to be important in the analytical model in determining the noise reduction from exterior to interior of the fuselage.

Differences in blade passage frequency can be off-set to some extent by considering the higher order harmonics for the Electra or Metroliner. For example, if one selects as a criterion, a constant value of $k\phi$ where k is the acoustic wave number of the pressure field and ϕ is the fuselage diameter, then the blade passage frequency for a propfan airplane is represented approximately by the third order harmonic of the Electra or Metroliner propeller. However, the use of higher order harmonics runs into the problem of signal-to-noise ratio for the tests on high-transmission loss sidewalls, since the external levels of the higher order harmonics for the subsonic propellers in the Electra and Metroliner will be relatively low.

Trace velocities in the longitudinal direction are influenced by tip clearance and airplane velocity. The effects of decreased tip clearance and decreased airplane velocity both act to reduce the trace velocity in the region aft of the plane of rotation of the propeller. In addition, using Aero Commander data [9] as a basis, the decreased tip clearance also reduces the circumferential trace velocity. This velocity may be

subsonic for the Electra and Metroliner whereas the analytical model predicts a supersonic circumferential trace velocity.

Finally, as tip clearance decreases, the longitudinal decay of the pressure field becomes more rapid. Thus, if one takes the directivity patterns to be those predicted by Hamilton Standard the longitudinal decay factors associated with the tip clearance of the Electra and Metroliner aircraft will be at least twice as large as those for the corresponding propfan designs. It is also reasonable to expect that the small tip clearances will increase the spatial decay in the circumferential direction. Typical calculations for propfan aircraft indicate that a 50% increase in the spatial decay factors can produce about a 5dB change in joint acceptance. Thus the decay parameters are important in determining noise transmission and, hence, the spatial extent of noise control treatment.

From the above discussion it is apparent that significant acoustic differences exist between the baseline propfan aircraft on one hand and present day propeller aircraft such as the Electra and Metroliner on the other hand. Consequently, flight tests in current aircraft would have to be viewed as validating the model for the specific test airplane, rather than verifying the predictions for the study aircraft. Corresponding calculations would have to be performed to apply the analytical model to the particular test airplane.

Some comment is also appropriate with regard to the structure of the airplane fuselage, particularly that of a small-diameter airplane such as the Metroliner. Analysis of the three study airplanes indicates that the small-diameter fuselage skin is

thicker than it would be for a similar diameter scale model of the wide or narrowbody fuselage. Consequently a small-diameter fuselage does not form a completely representative scale model of a larger diameter fuselage. Differences in calculated radiation efficiency, modal density and band-averaged joint acceptance are shown in Figures 85 and 86. The situation becomes worse if the smeared-out mass of the small diameter fuselage is reduced to that of the scale model by removal of the stringers. Thus, if a small-diameter fuselage is used as the test hardware, the validation cannot be considered as a direct verification of the analytical model predictions for the narrow or wide body fuselages. Some adjustments will be necessary, for example, by use of figures such as Figure 86.

There are other disadvantages in using a current airplane as a means of validating the analytical model. The airplane provides little or no flexibility in varying excitation frequency, pressure decay rate or trace velocity. It would be highly desirable to have such flexibility in order to check the analytical model over a range of conditions. Also, while a test program in an actual airplane is highly desirable as a means of reducing interior noise levels which are transmitted by a variety of paths from a variety of sources, it is not desirable as a means of validating an analytical model directed to a particular noise source and a particular noise transmission path. It is recognized that the propfan airplane may well have numerous transmission paths, to which noise control methods must be applied, but such noise control approaches should be the subject of separate programs, or await testing on a prototype propfan aircraft.

Wide Body $f_1 = 133 \text{ Hz}$, $k_1 R = 8.30$

Small Diam. $f_1 = 328 \text{ Hz}$, $k_1 R = 8.30$

— Wide Body
 - - - Small Diameter, as Model
 Small Diameter, as Model,
 but no Stringers

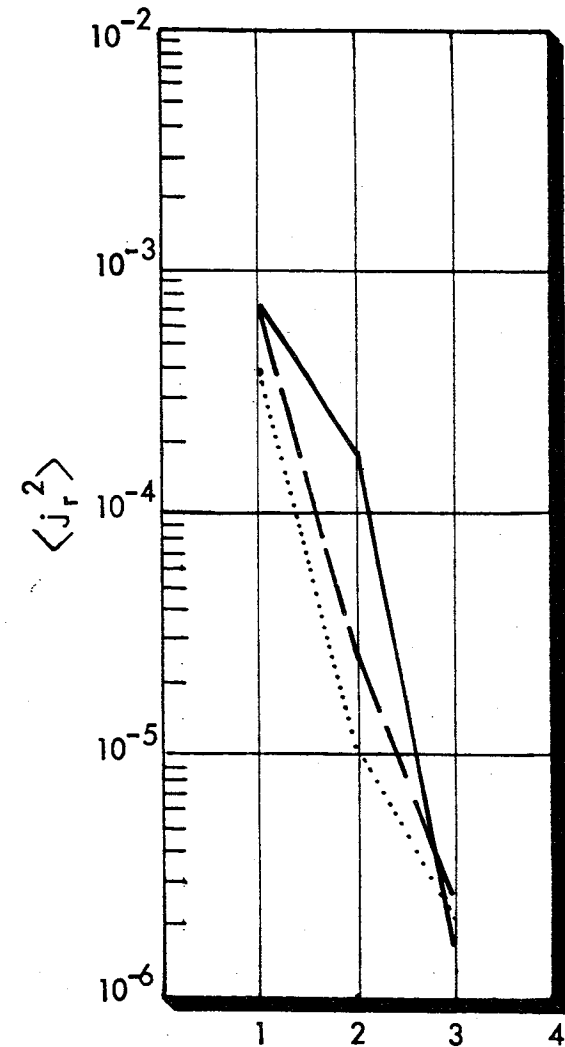
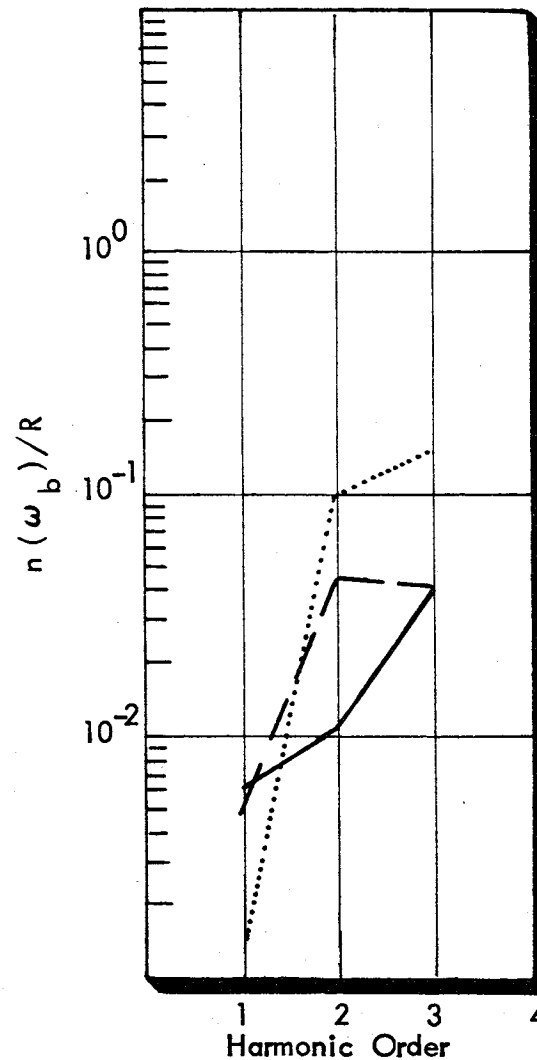
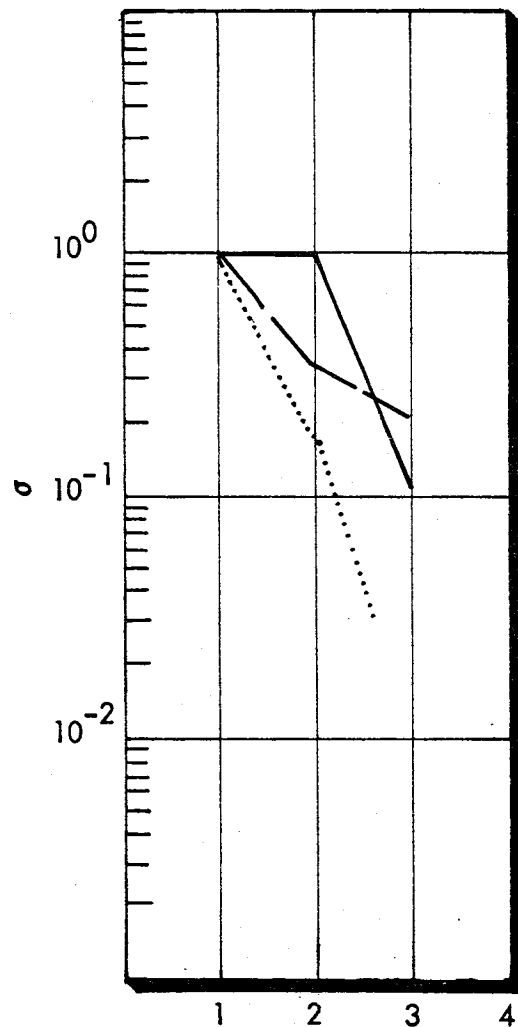


FIGURE 85. USE OF SMALL DIAMETER FUSELAGE TO SCALE MODEL WIDE BODY FUSELAGE

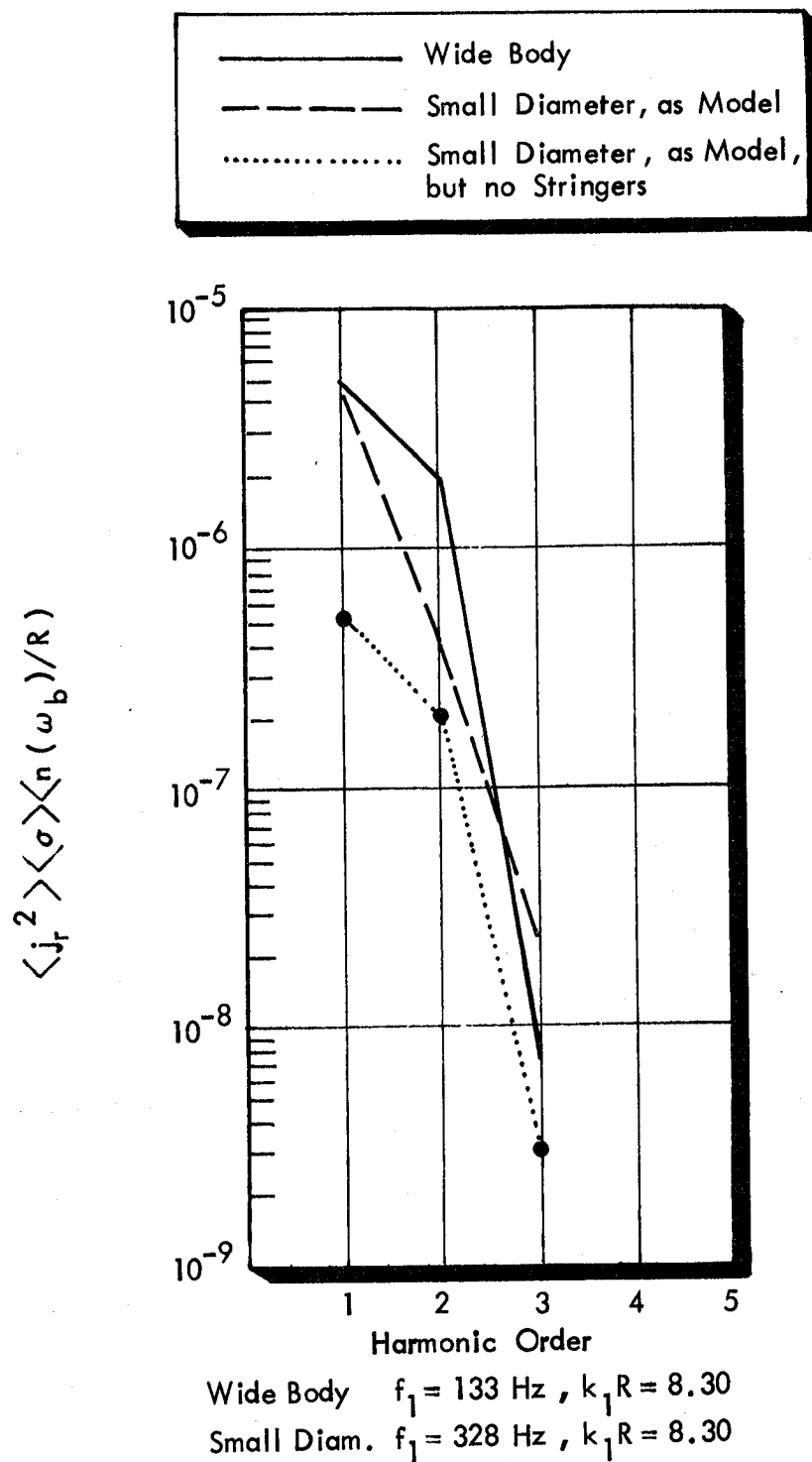


FIGURE 86. USE OF SMALL DIAMETER FUSELAGE TO SCALE MODEL WIDE BODY FUSELAGE

9.5.2 Airplane Tests

Although it is concluded above that airplane tests would not validate the analytical predictions for the study aircraft, some useful information could be obtained from such tests. Thus it is appropriate to review briefly the type of tests which could be performed and the measurement procedures which should be followed.

The simplest test would be one in which several noise control treatments were installed in a propeller-driven airplane and the noise reduction measured for each treatment. Such a test gives very little information on the validity of the present analytical model. A more useful experimental program would provide information on the exterior pressure field, structural response, and cabin noise levels for a test airplane, and the noise reductions due to add-on treatments. Data appropriate to these test conditions would be used in the analytical model to predict the structural vibration and cabin noise levels. Then the experimental and analytical results would be compared and necessary modifications, if any, made to the analytical model.

As the tests are concerned with propeller noise only, the test airplane should be powered by turboprop engines, and the plane of rotation of the propellers should intersect the passenger cabin. It might at first seem appropriate to install bulkheads in the cabin so that the noise transmission region can be controlled to a specific region of the fuselage structure. There are, however, restrictions on this approach because the analytical model assumes high modal overlap for the acoustic modes for all frequency bands of interest. Consequently the size of

the receiving cavity cannot be made too small. This assumption of high modal overlap also influences the choice of propeller harmonics for the noise tests. It is probable that the lowest order harmonics of the propeller will occur at frequencies which do not satisfy the condition of high acoustic modal overlap. The measurements will then have to be performed for the higher order harmonics. High transmission loss treatments should be applied to the floor.

It is known that the effect of forward motion on the noise of subsonic propellers is to reduce the levels of the higher order harmonics, a trend which may have an adverse effect on the signal-to-noise ratio when treatments with a high transmission loss are tested. One possible way of alleviating the problem is to perform the tests under static conditions. This has the added advantage that the tests are more convenient to perform but there is the disadvantage that forward motion is not simulated in the trace velocity of the exterior pressure field. Resolution of these arguments would probably need an evaluation of the specific airplane proposed for the tests.

Assuming that the objective of the test program is a validation of the analytical model as applied to the specific test airplane, the following measurements should be made.

- (i) Exterior pressure field:
Use a cruciform array of flush-mounted pressure transducers to measure the spatial decay, coherence, and phase angle parameters for the pressure field in the longitudinal and circumferential directions. The array would be similar to that used in the Aero Commander tests [8], but more extensive in terms of

number of transducers and spatial extent. The results of these measurements would be used as a basis for the representation of the exterior pressure field in the analytical model;

(ii) Structural vibration:

Analysis of the study airplanes indicates that the acoustic power flow is dominated by resonant response. Thus vibration measurements -- which give the response -- can be used for diagnostic purposes. The vibration measurements would be made using light-weight accelerometers mounted mainly on fuselage skin panels in the neighborhood of high exterior noise levels.

(iii) Cabin Noise Levels:

Noise levels would be measured in the cabin in the region of high exterior sound levels. The measurements would be repeated for a) bare interior (with some absorption), b) baseline sidewall treatment and, c) one or more high-transmission-loss treatments.

The measurement locations would be chosen such that space-averaged levels could be calculated for an appropriate cabin volume, and such that longitudinal and radial gradients could be determined.

The test conditions would be limited by the performance of the selected airplane. Assuming that flight tests were performed, the airplane would be operated at high speed with high propeller rpm. Tests would be repeated at different engine rpm, provided that rpm variations can be accomplished. To avoid beat effects, the right and left hand propellers should be operated at different rpm. Measurements could be performed

with and without cabin pressure differential although the analysis indicates that pressure differential is not very important for the frequency range which dominates the noise transmission through the sidewall. Consideration could be given to performing certain ground, static tests for comparison with the flight results.

10.0 CONCLUSIONS

An analytical model has been developed to predict the sound levels in the interior of high-speed propeller-driven aircraft. Although the assumptions contained in the model have not yet been validated experimentally, the analytical model has been used to predict the sound levels in three study aircraft and to explore potential noise control concepts.

The analytical study indicates that, if the high-speed propeller-driven aircraft have fuselage structures and cabin sidewall treatments similar to those in current-day turbofan-powered aircraft, the cabin noise levels will reach a maximum of about 105 dB(A). These levels are about 25 dB higher than the goal of 80 dB(A). Consequently, a significant increase in cabin sidewall transmission loss is required, and this increase has to be achieved at relatively low frequencies (130-230 Hz) since the cabin A-weighted sound levels are dominated by contributions at the propeller blade passage frequency.

The noise control methods investigated in the analytical study include add-on and advanced concepts. The add-on treatments do not involve changes to the fuselage primary structure whereas the advanced concepts usually do require structural changes. Of the concepts studied, only one shows the capability of achieving the required reductions in transmission loss. This treatment involves the use of a double-wall system with a heavy, limp trim panel which is isolated from fuselage vibrations. All the other concepts studied provided relatively small noise reductions. The weight penalties associated with the double-wall system are significant, ranging from 0.75% to 1.5 % of take-off

gross weight, depending on fuselage diameters. In terms of passenger payload, the penalties lie in the range of 4 to 19% of payload weight. In both cases the highest penalties are associated with the smallest airplane.

It should be noted that an extensive weight-optimization study was not performed and that, by suitable combination of different noise control treatments, the weight penalties could be reduced. On the other hand, it should be noted that the achievement of the required large transmission losses in a practical situation has yet to be proven, and the effects of windows and other potential flanking paths have been excluded from the present analytical model.

Experimental validation of the analytical model and the predicted noise reductions is an essential part of the overall development of the model. Such validation should be possible with laboratory tests, and experimental procedures for performing these tests are presented in this report.

REFERENCES

1. Anon, "Energy Consumption Characteristics of Transports under the Prop-Fan Concept", NASA CR-137937, October 1976.
2. Hopkins, J. P., Wharton, M.E., "Study of the Cost/Benefit Trade-offs for Reducing the Energy Consumption of the Commercial Air Transport System:", NASA CR-137927, August 1976.
3. Anon, "Assessment of Fuel Conservation Merits and Operating Cost Benefits of Advanced Turboprop Transport Aircraft", Final Oral Review, Contract NAS2-8612, October 1977.
4. Pope, L. D., Wilby, J.F., "Space Shuttle Payload Bay Acoustics Prediction Study, Volume II Analytical Model", NASA CR-159956, Vol. II March 1980.
5. Rennison, D. C., Wilby, J. F., "A Review of Analytical Models for Sound Transmission through Fuselage Sidewalls with Application to General Aviation Aircraft", BBN Report 3851, September 1978.
6. Anon, "Prop-fan and Gearbox Near Field Noise Predictions", Hamilton Standard Report SP15A77, Revision A, February 1978.
7. Anon, (a) "Prop-Fan Performance Estimation for the Six Blade Prop-Fan Configuration", SP12A77; (b) "Prop-Fan Performance Estimation for the Eight-Blade Prop-Fan Configuration:", SP13A77; (c) "Prop-Fan Performance Estimation for the Ten Blade Prop-Fan Configuration", SP14A77, Hamilton Standard Reports, October 1977.
8. Piersol, A. G., Wilby, E. G., Wilby, J. F., "Evaluation of Aero Commander Propeller Acoustic Data: Static Operations", NASA CR-158919, May 1978.
9. Piersol, A. G., Wilby, E. G., Wilby, J.F., "Evaluation of Aero Commander Propeller Acoustic Data: Taxi Operations" NASA CR-159124, July 1979.
10. Piersol, A. G., Rentz, P. E., "Experimental Studies of the Space Shuttle Payload Acoustic Environment", *SAE Transactions*, 86, Sec. 4, 3345-3362, 1977.

11. Wilby, J. F., Pope, L. D., "The Development of a Method for Predicting the Noise Exposure of Payloads in the Space Shuttle Orbiter Vehicle", *The Shock and Vibration Bulletin*, No. 49 Part 1, 5-30, September 1979.
12. Pope, L. D., "On the Transmission of Sound through Finite, Closed Shells: Statistical Energy Analysis, Modal Coupling, and Nonresonant Transmission", *J. Acoust. Soc. Am.*, 50, 1004-1018 (1971).
13. Morse, P. M., Ingard, K. U., "Theoretical Acoustics", p. 580, McGraw-Hill, New York, 1968.
14. White, P. H., "Response of Structures to Non-Homogeneous Random Pressure Fields", ASME 70-WA/DE-11, 1970.
15. Cockburn, J. A., Jolly, A. C., "Structural-Acoustic Response, Noise Transmission Losses and Interior Noise Levels of an Aircraft Fuselage Excited by Random Pressure Fields", AFFDL-TR-68-2, 1968.
16. Ungar, E. E., Wilby, J. F., Bliss, D. B., et al., "A Review of Methods for Estimation of Aeroacoustic Loads on Flight Vehicle Surfaces", AFFDL-TR-76-91, Vol. II, September, 1976.
17. Wilby, J. F., "The Response of Simple Panels to Turbulent Boundary Layer Excitation", AFFDL-TR-67-70, 1967.
18. Liessa, A. W., "Vibration of Shells", NASA SP-288, 1973, pp. 207-220.
19. Bozich, D. J., "Spatial Correlation in Acoustic-Structural Coupling", *J. Acoust. Soc. Am.* 36, 52 (1964).
20. Chyu, W. J., Au-Yang, M. K., "Random Response of Rectangular Panels to the Pressure Field Beneath a Turbulent Boundary Layer in Subsonic Flows", NASA TN D-6970, 1972.
21. Scharton, T. D., "Random Vibration of Coupled Oscillators and Coupled Structures", Sc.D. Thesis, MIT Dept. of Mechanical Engineering, 1965.
22. White, R. W., "Predicted Vibration Response of Apollo Structure and Effects of Pressure Correlation Lengths on Response", Wyle Laboratories Report WR67-4, 1967 (Revised March 1968).

23. Abramowitz, M., Stegun, I. A., "Handbook of Mathematical Functions", Dover (1965).
24. Pope, L. D., "Energetics of Resonant Structures and Reverberant Acoustic Fields", Shock and Vibration Digest 6, 7, 3-13 (1974).
25. Mikulas, M. M., McElman, J. A., "On Free Vibrations of Eccentrically Stiffened Cylindrical Shells and Flat Plates", NASA TN D-3010, 1965.
26. Bies, D. A., Hansen, C. H., "Flow Resistance Information for Acoustical Design", Submitted for publication in *Applied Acoustics*.
27. Koval, L. R., "Effect of Airflow, Panel Curvature, and Internal Pressurization on Field Incidence Transmission Loss, *J. Acoust. Soc. Am.*, 59, 6, June 1976.
28. Teriyi Yamamoto, "On the Distribution of Sound Energy Along a Corridor", *J. Acoust. Soc. Japan* 17, 4, pp. 286-292, Dec. 1961.
29. McCarty, J. E., et al, "Advanced Metallic Structure: Cargo Fuselage Design for Improved Cost, Weight, and Integrity", AFFDL-TR-73-53, June 1973.
30. Goss, R. P., "Acoustics Program for the Grumman Gulfstream II", AIAA Paper 71-783, July 1971.
31. Gebhardt, G. T., "Acoustical Design Features of Boeing Model 727", *J. Aircraft*, 2, 4, 272-277, July 1965.
32. Marsh, A. H., "Noise Control Features of the DC-10", *Noise Control Engineering*, 4, 3, 130-139, May 1975.
33. Taniguchi, H. H., "Acoustic Properties of Various Sound Proofing Materials", Boeing Airplane Co., Document D-15853, July 1955.
34. Wilby, J. F., Scharton, T. D., "Acoustic Transmission through a Fuselage Sidewall", NASA CR-132602, July 1974.
35. Bhat, W. V., Wilby, J. F., "Interior Noise Radiated by an Airplane Fuselage Subjected to Turbulent Boundary Layer Excitation and Evaluation of Noise Reduction Treatments", *J. Sound Vib.* 18, 4, 449-464, 1971.

36. Hu, W. C. L., Gormley, J. F., Lindholm, U. S., "An Analytical and Experimental Study of Vibrations of Ring-Stiffened Cylindrical Shells", Southwest Research Institute Technical Report 9, June 1967.
37. Szechenyi, E., "Approximate Methods for the Determination of the Natural Frequencies of Stiffened and Curved Plates", *J. Sound Vib.*, 14, 3, 401-418, 1971.
38. Wilby, J. F., Gloyna, F. L., "Vibration Measurements of an Airplane Fuselage Structure", *J. Sound Vib.*, 23, 4, 467-486, 1972.
39. Maidanik, G., "Response of Ribbed Panels to Reverberant Acoustic Fields", *J. Acoust. Soc. Amer.*, 34, 6, 809-826, 1962.
40. Barger, J. E., Spencer, J. A., Wagner, R. A., "Simulated Full-Scale Hull Vibration Noise in Flush-Mounted Hydrophones", BBN Report 1725, March 1969.
41. Ungar, E. E., Carbonell, J. R., "On Panel Vibration Damping due to Structural Joints", *AIAA Journal*, 4, 1385-1390, 1966.
42. Sen Gupta, G., "Low Frequency Cabin Noise Reduction Based on the Intrinsic Structural Tuning Concept", NASA CR-145262, March 1978.
43. Dugan, J. F., Jr., Gatzen, B. S., and Adamson, W. M., "Prop-Fan Propulsion - It's Status and Potential", S.A.E. Paper 780995, San Diego, November 1978.
44. Bowers, B. E., "The Anechoic Flow Facility - Aerodynamic Calibration and Evaluation", N.S.R.D.C., Ship Acoustics Department, SAD-48E-1942, May 1973.
45. Patterson, R. W., Vogt, P.G., and Foley, W. M., "Design and Development of the United Aircraft Research Laboratories Acoustic Research Tunnel", *J. Aircraft*, 10, 7, 427-433, July 1973.
46. Hubbard, H. H., and Rieger, A. A., "Free-Space Oscillating Pressures near the Tips of Rotating Propellers", NACA Report 996, 1950.

47. Bies, D. A. Chapter 10, "*Noise and Vibration Control*"
Editor, L. L. Beranek, 1971, McGraw-Hill, New York.
48. Jane's Pocket Book of Commercial Transport Aircraft,
Editor J. W. R. Taylor, Collier Books, 1974.
49. Anon. "The Gulfstream 2 - A long range executive aircraft"
Interavia No. 3, pp. 297-299, 1968.

APPENDIX A

JOINT ACCEPTANCE EXPRESSIONS FOR NON-HOMOGENEOUS PRESSURE FIELDS

The joint acceptance function describes the coupling between the excitation field and the structure and can be defined for an excitation tonal frequency as

$$j_r^2(\omega) = \frac{1}{A^2 \langle p_{X_0}^2(\omega) \rangle} \iint_{\bar{x} \bar{x}'} C_p(\bar{x}, \bar{x}'; \omega) \psi^r(\bar{x}) \psi^r(\bar{x}') d\bar{x} d\bar{x}' \quad (A.1)$$

where A is the panel area, $\langle p_{X_0}^2(\omega) \rangle$ is the mean square pressure at X_0 attributable to the b^{th} harmonic, $C_p(\bar{x}, \bar{x}'; \omega)$ is the co-spectrum of the non-homogeneous pressure field (defined relative to X_0), and $\psi^r(\bar{x})$ is the shape of the r^{th} mode. To evaluate this joint acceptance function, expressions are required for the mode shapes of the structure and for the excitation pressure field.

The excitation is represented as a convecting pressure field with pressure amplitude decaying with distance from the location of peak levels X_0 and with spatially-decaying coherence. Exponential forms for both amplitude and coherence decays have been modeled to enable convenient mathematical manipulation. Then

$$C_p(\bar{x}, \bar{x}'; \omega) = e^{-a|\bar{x}-\bar{X}_0|} e^{-a|\bar{x}'-\bar{X}_0|} e^{-c|\bar{x}'-\bar{x}|} \cos[k(\omega)(\bar{x}' - \bar{x})] \langle p_{X_0}^2(\omega) \rangle \quad (A.2)$$

where a is the amplitude decay rate, c is the coherence decay rate, and k is the excitation wavenumber at frequency ω .

Consider the example of a one-dimensional system in which a beam of length L is driven to vibrate in its m^{th} mode shape by a non-homogeneous pressure field. In general, X_0 , the location of peak

pressure levels, will lie at some arbitrary point along the beam. The expression for the joint acceptance function has been evaluated for such a case; but for present demonstration purposes a simpler case will be considered, where the maximum intensity is located at $X_0 = 0$. Figure A.1 describes this situation.

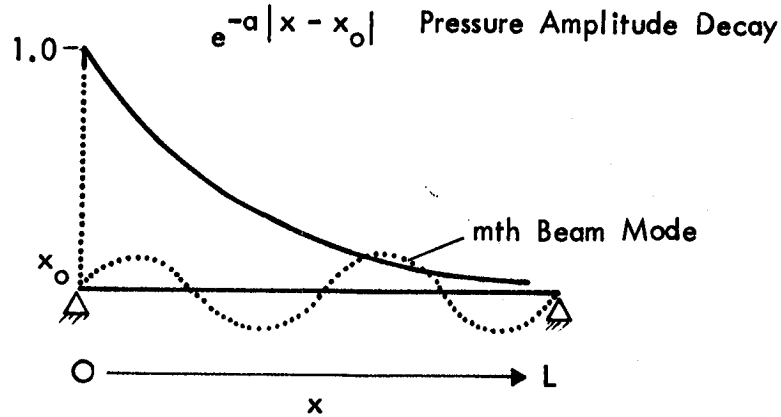


FIGURE A.1 EXCITATION OF BEAM MODE BY NON-HOMOGENEOUS PRESSURE FIELD

With $X_0 = 0$, the joint acceptance (one-dimensional) becomes

$$j_{mm}^2(\omega) = \frac{1}{L^2} \int_0^L \int_0^L e^{-ax'} e^{-ax} e^{-c|\xi|} \cos[k(\omega)\xi] \psi^m(x) \psi^m(x') dx dx' \quad (A.3)$$

where $\xi = x' - x$.

Using sinusoidal mode shapes, $j_{mm}^2(\omega)$ becomes

$$j_{mm}^2(\omega) = \frac{1}{L^2} \int_0^L e^{-ax} \sin k_m x dx \int_0^L e^{-ax'} e^{-c|\xi|} \cos(k\xi) \sin k_m x' dx' \quad (A.4)$$

where k_m is the wavenumber of the structural mode.

Evaluation of $j_{mm}^2(\omega)$ leads to the result:

$$\begin{aligned}
j_{mm}^2(\omega) = & \frac{A'}{4L^2} \left\{ (-1)^m e^{-bL} \left[\frac{-b \sin kL - (k_m + k) \cos kL}{b^+} + \frac{b \sin kL - (k_m - k) \cos kL}{b^-} \right] \right. \\
& \left. + (k_m + k)/b^+ + (k_m - k)/b^- \right\} \\
& + \frac{B'}{4L^2} \left\{ (-1)^m e^{-bL} \left[\frac{-b \cos kL - (k_m - k) \sin kL}{b^-} + \frac{b \cos kL - (k_m + k) \sin kL}{b^+} \right] \right. \\
& \left. + b/b^- - b/b^+ \right\} \\
& + \frac{C'}{4L^2} \left\{ \left(\frac{1 - e^{-2aL}}{2a} \right) - \frac{a}{2} \left(\frac{1 - e^{-2aL}}{a^2 + k_m^2} \right) \right\} + A' \left\{ \frac{k_m (1 - e^{-2aL})}{2(a^2 + k_m^2)} \right\} \\
& + \frac{D'}{4L^2} \left\{ (-1)^m e^{-dL} \left[\frac{-d \sin kL - (k_m + k) \cos kL}{d^+} + \frac{d \sin kL - (k_m - k) \cos kL}{d^-} \right] \right. \\
& \left. + (k_m + k)/d^+ + (k_m - k)/d^- \right\} \\
& + \frac{E'}{4L^2} \left\{ (-1)^m e^{-dL} \left[\frac{-d \cos kL - (k_m - k) \sin kL}{d^-} + \frac{d \cos kL - (k_m + k) \sin kL}{d^+} \right] \right. \\
& \left. + d/d^- - d/d^+ \right\} \\
& + \frac{F'}{4L^2} \left\{ \left(\frac{1 - e^{-2aL}}{2a} \right) - \frac{a}{2} \left(\frac{1 - e^{-2aL}}{a^2 + k_m^2} \right) \right\} + G' \left\{ \frac{k_m (1 - e^{-2aL})}{2(a^2 + k_m^2)} \right\}
\end{aligned}$$

where:

$$b = a + c$$

$$d = a - c$$

$$b^+ = b^2 + (k_m + k)^2$$

$$b^- = b^2 + (k_m - k)^2$$

$$d^+ = d^2 + (k_m + k)^2$$

$$d^- = d^2 + (k_m - k)^2$$

$$A' = \left[\frac{k_m + k}{d^+} + \frac{k_m - k}{d^-} \right]$$

$$B' = \left[\frac{d}{d^-} - \frac{d}{d^+} \right]$$

$$C' = \left[\frac{d}{d^-} + \frac{d}{d^+} \right]$$

$$D' = \left[\frac{\alpha'}{b^+} - \frac{\gamma'}{b^-} \right]$$

$$E' = \left[\frac{\delta'}{b^-} - \frac{\beta'}{b^+} \right]$$

$$F' = \left[\frac{b}{b^+} + \frac{b}{b^-} \right]$$

$$G' = \left[\frac{(k_m + k)}{b^+} + \frac{(k_m - k)}{b^-} \right]$$

$$\alpha' = (-1)^{m+1} e^{-bL} [b \sin kL + (k_m + k) \cos kL]$$

$$\beta' = (-1)^{m+1} e^{-bL} [b \cos kL - (k_m + k) \sin kL]$$

$$\gamma' = (-1)^{m+1} e^{-bL} [b \sin kL - (k_m - k) \cos kL]$$

$$\delta' = (-1)^{m+1} e^{-bL} [b \cos kL + (k_m - k) \sin kL]$$

Special cases:

a) Zero amplitude and correlation decay rates: $a = c = 0$

$$j_{mm}^2(\omega) = \frac{2}{k_m^2 L^2} \frac{[1 - (-1)^m \cos kL]}{[1 - (k/k_m)^2]^2} \quad (A.5)$$

which is the well-known result, corresponding to plane acoustic waves propagating with zero spatial decay along a beam of length L [A.1].

At coincidence where $k = k_m$,

$$j_{mm}^2(\omega) = 1/4 \quad \text{for all modes.}$$

b) Zero correlation decay, but a is finite: $c = 0, a \neq 0$.

$$j_{mm}^2(\omega) = [A''^2 + B''^2]/4L^2 \quad (A.6)$$

where:

$$A'' = \left[\frac{k_m + k}{a^+} + \frac{k_m - k}{a^-} - (-1)^m e^{-aL} \left\{ \frac{a \sin kL + (k_m + k) \cos kL}{a^+} - \frac{a \sin kL - (k_m - k) \cos kL}{a^-} \right\} \right]$$

$$B'' = \left[\frac{a}{a^-} - \frac{a}{a^+} - (-1)^m e^{-aL} \left\{ \frac{a \cos kL + (k_m - k) \sin kL}{a^-} - \frac{a \cos kL - (k_m + k) \sin kL}{a^+} \right\} \right]$$

$$a^+ = a^2 + (k_m + k)^2$$

$$a^- = a^2 + (k_m - k)^2.$$

The action of strong amplitude decay is to dampen the oscillation of $j_{mm}^2(\omega)$ as k/k_m varies through coincident conditions (see Fig. 2).

Asymptotic limits can be developed for the case where strong amplitude decay occurs, i.e. when $e^{-aL} \ll 1$. Three examples are given below:

For $k_m \gg k$ and $k_m L > aL$,

$$j_{mm}^2(\omega) \approx \frac{1}{(m\pi)^2}. \quad (A.7)$$

For $k_m \ll k$ and $k_m L > aL$,

$$j_{mm}^2(\omega) \approx \frac{1}{(m\pi)^2} \left(\frac{k_m}{k} \right)^4. \quad (A.8)$$

For $k_m \approx k$ (i.e. close to coincidence) and $kL \gg aL$,

$$j_{mm}^2(\omega) \approx \frac{1}{4a^2L^2} = \frac{\ell^2}{4L^2} \quad (A.9)$$

where ℓ is that equivalent length over which the excitation may be considered to be of equivalent constant amplitude. ℓ is analogous to a correlation length for homogeneous excitations in which the coherence decay is rapid relative to the beam length.

REFERENCE

- A.1 A. Powell, "On the Response of Structures to Random Pressures and to Jet Noise in Particular," Chap. 8 in *Random Vibration*, Vol. 1, ed. S. H. Crandall. Cambridge, Mass., The M.I.T. Press, 1959.

APPENDIX B

EXPECTED VALUE OF THE MODAL ADMITTANCE FUNCTION $g(\omega_b, \omega_n)$

It is required to solve for the expected value of $g(\omega_b, \omega_n)$, which is the expected value that $g(\omega_b, \omega_n)$ takes in the frequency band $\Delta\omega$ as, for example, ω_b varies within $\Delta\omega$.

By definition [B.1],

$$E[g(\omega_b, \omega_n)] = \int_{\Delta\omega} \int_{\Delta\omega} g(\omega_b, \omega_n) p(\omega_b, \omega_n) d\omega_b d\omega_n \quad (B.1)$$

where ω_b and ω_n are statistically independent processes, in which case Eq. (B.1) reduces to

$$E[g(\omega_b, \omega_n)] = \int_{\Delta\omega} \int_{\Delta\omega} g(\omega_b, \omega_n) p(\omega_b) p(\omega_n) d\omega_b d\omega_n. \quad (B.2)$$

The probability density function $p(\omega_b)$ describing ω_b in $\Delta\omega$ is $(\Delta\omega)^{-1}$ [B.2]. The number of acoustic modes with frequencies ω_n below the band $\Delta\omega$ for a rectangular volume is approximately

$$N_{n < \Delta\omega} \approx K\omega_c^3$$

where ω_c is the band center frequency and K is a constant of proportionality.

The probability distribution function $P(\omega_n)$ for acoustic modes located in the frequency band $\Delta\omega$ may be calculated as [B.2]

$$P(\omega_n) = \frac{N_u - N_l}{N_u - N_l} = \frac{K\omega_n^3 - K\omega_c^3(1 - \epsilon)^3}{K\omega_c^3(1 + \epsilon)^3 - K\omega_c^3(1 - \epsilon)^3}$$

$$= \frac{\omega_n^3 - \omega_c^3(1 - \epsilon)^3}{\omega_c^3[(1 + \epsilon)^3 - (1 - \epsilon)^3]}$$

where $\Delta\omega = 2\epsilon\omega_c$ and $\epsilon \ll 1$. Subscripts u and l refer to the upper and lower limits of the frequency band $\Delta\omega$.

By definition, the probability density of ω_n [B.2] is

$$p(\omega_n) = \frac{dP(\omega_n)}{d\omega_n} = \frac{1}{\Delta\omega} \left(\frac{\omega_n}{\omega_c} \right)^2.$$

Hence,

$$E[g(\omega_b, \omega_n)] = \int_{\Delta\omega} \int_{\Delta\omega} \left[\left(1 - \frac{\omega_b^2}{\omega_n^2} \right)^2 + \eta_n^2 \right]^{-1} \left(\frac{1}{\Delta\omega} \right)^2 \left(\frac{\omega_n}{\omega_c} \right)^2 d\omega_b d\omega_n.$$

Consider integration with respect to ω_b :

$$\int_{\omega_c(1-\epsilon)}^{\omega_c(1+\epsilon)} \left[\left(1 - \frac{\omega_b^2}{\omega_n^2} \right)^2 + \eta_n^2 \right]^{-1} d\omega_b$$

$$= \int_{\omega_c(1-\epsilon)}^{\omega_c(1+\epsilon)} \left[1 + \eta_n^2 + \left(\frac{\omega_b}{\omega_n} \right)^4 - 2 \left(\frac{\omega_b}{\omega_n} \right)^2 \right]^{-1} d\omega_b$$

$$= \frac{\omega_n}{2\eta_n} \left\{ \tan^{-1} \left[\frac{\left(\frac{\omega_c}{\omega_n} \right)^2 (1 + \epsilon)^2 - 1}{\left(\frac{\omega_c}{\omega_n} \right) (1 + \epsilon) \eta_n} \right] - \tan^{-1} \left[\frac{\left(\frac{\omega_c}{\omega_n} \right)^2 (1 - \epsilon)^2 - 1}{\left(\frac{\omega_c}{\omega_n} \right) (1 - \epsilon) \eta_n} \right] \right\} \text{ for } \eta_n \ll 1.$$

The function contained in { } brackets varies between $\pi/2$ and π , as ω_n varies between $\omega_c(1 - \epsilon)$ and $\omega_c(1 + \epsilon)$, with values generally close to π . Consequently,

$$\begin{aligned} E[g(\omega_b, \omega_n)] &= \left(\frac{1}{\Delta\omega}\right)^2 \left(\frac{1}{\omega_c}\right)^2 \int_{\omega_c(1-\epsilon)}^{\omega_c(1+\epsilon)} \frac{\omega_n}{2\bar{\eta}_n}(\pi) \omega_n^2 d\omega_n^2 \\ &= \frac{\pi}{2\bar{\eta}_n(\Delta\omega)^2 \omega_c^2} \int_{\omega_c(1-\epsilon)}^{\omega_c(1+\epsilon)} \omega_n^3 d\omega_n \\ &\approx \frac{\pi}{8\bar{\eta}_n} \left(\frac{\omega_c}{\Delta\omega}\right)^2 8\epsilon, \text{ on ignoring terms of order } \epsilon^2 \text{ and above.} \end{aligned}$$

and so,

$$E[g(\omega_b, \omega_n)] = \frac{\pi\omega_b}{2\bar{\eta}_n\Delta\omega}.$$

Further, since

$$\begin{aligned} E[G(\omega_b, \omega_n)] &= N_{n<\Delta\omega} E[g(\omega_b, \omega_n)] \\ &= N_{n<\Delta\omega} \frac{\pi\omega_c}{2\bar{\eta}_n\Delta\omega} \\ &= n_n(\omega_b) \frac{\pi\omega_b}{2\bar{\eta}_n} \quad \text{as } \omega_b = \omega_c. \end{aligned}$$

REFERENCES

- B.1 J. S. Bendat and A. G. Piersol, *Random Data: Analysis and Measurement Procedures*. Wiley-Interscience, 1971.
- B.2 Ibid, p. 58.

APPENDIX C

RELATIONSHIP BETWEEN $\text{Im}[I^{rr}(\omega)]$ AND $f^2(n,r)$, $j_r^{\text{rev}}(\omega)$

The expected value of the joint intermodal coefficient, which expresses the coupling between structural modes and modes of the cavity, is defined by Eq. (20) as

$$E[I^{rr}(\omega)] = E\left[\frac{A^2}{V} \sum_n \frac{\epsilon_n}{(\bar{k}_n^2 - k^2)} f^2(n,r)\right] \quad (\text{C.1})$$

where $f(n,r) = \frac{1}{A} \int \phi_n(\bar{x}) \psi^r(\bar{x}) d\bar{x}$ is the coupling factor between the structure and the cavity.

The imaginary part of $E[I^{rr}(\omega)]$ is required for calculation of the real power flowing inwardly [see Eq. (17)]; then

$$\begin{aligned} \text{Im}\{E[I^{rr}(\omega)]\} &= E\{\text{Im}[I^{rr}(\omega)]\} = E\left[\frac{2A^2}{V} \sum_n \frac{\epsilon_n k_n \kappa_n}{|\bar{k}_n^2 - k^2|^2} f^2(n,r)\right] \\ &= E\left[\frac{A^2 c_1^2}{V} \sum_n \frac{\epsilon_n \eta_n f^2(n,r)}{\omega_n^2 \left[\left(1 - \frac{\omega^2}{\omega_n^2}\right)^2 + \eta_n^2\right]}\right] \end{aligned} \quad (\text{C.2})$$

using Eqs. (22) and (23).

$$= \frac{A^2 c_1^2}{V \omega^2} \langle \epsilon_n f^2(n,r) \rangle \bar{\eta}_n E[G(\omega, \omega_n)] \quad (\text{C.3})$$

where $E[G(\omega, \omega_n)]$ is defined and derived in Section (3.5.1) [Eqs. (39) and (40)]: then

$$E\{\text{Im}[I^{rr}(\omega)]\} = \frac{\pi A^2 c_1^2}{2V\omega} \langle \epsilon_n f^2(n,r) \rangle n_n(\omega). \quad (C.4)$$

Alternatively, an approximation for $\text{Im}[I^{rr}(\omega)]$ can be obtained in terms of $j_r^{\text{rev}}(\omega)$, the joint acceptance function for a reverberant pressure field. This approximation is obtained by analogy with results from [C.1] and [C.2], as discussed in [C.3] to give

$$E\{\text{Im}[I^{rr}(\omega)]\} = \frac{1}{2\pi} \frac{\omega}{c_1} A^2 j_r^{\text{rev}}(\omega). \quad (C.5)$$

Then, comparing Eqs. (C.4) and (C.5), one finds that

$$\frac{1}{2\pi} \frac{\omega}{c_1} A^2 j_r^{\text{rev}}(\omega) = \frac{\pi A^2 c_1^2}{2V\omega} \langle \epsilon_n f^2(n,r) \rangle n_n(\omega)$$

and so

$$n_n(\omega) \langle \epsilon_n f^2(n,r) \rangle = \frac{\omega^2 V}{\pi^2 c_1^3} j_r^{\text{rev}}(\omega). \quad (C.6)$$

REFERENCES

- C.1 L. D. Pope and R. C. Leibowitz. "Intermodal Coupling Coefficients for a Fluid-Loaded Rectangular Plate," *J. Acoust. Soc. Am.* 56, p. 414, Section III, 1974.
- C.2 L. D. Pope. "Energetics of Resonant Structures and Reverberant Acoustic Fields," *Shock and Vibration Digest* 6(7), 3-13, 1974.
- C.3 L. D. Pope and J. F. Wilby. "Space Shuttle Payload Bay Acoustics Prediction Study, Vol. II, Analytical Model." BBN Report 3286R Vol. II, March 1980.

APPENDIX D

FINAL SIDEWALL DESIGN UTILIZING ADD-ON TREATMENTS

It is demonstrated in Section 7 that the only add-on treatment capable of providing the noise reductions required to achieve the goal of an A-weighted sound level less than 80 dB is a double-wall system with a limp-mass inner wall. In addition, the calculations in Section 8 do not identify any advanced concept which can achieve the noise reduction predicted for the double wall. Thus it is appropriate to summarize the final double-wall designs that are predicted to provide cabin noise levels which do not exceed 80 dB(A) in the three study airplanes.

For the purposes of the investigation, three baseline aircraft were chosen on the basis of existing technology and conventional fuselage construction. To some extent the choice of airplane influences the amount of treatment required on the sidewall, and this influence will be reflected in the details of the three double-wall systems described in this Appendix. Furthermore, certain simplifying assumptions were made, with the result that noise transmission through the floor and windows was neglected, as was structureborne transmission through the sidewall itself. It is probable that, in practice, these paths will require some noise control treatment, or the performance of the double-wall sidewall will be compromised.

The construction of the three sidewall systems is described below in terms of the different components. The sidewall is shown schematically in Figure D.1.

Fuselage Structure:-

In all the study aircraft the fuselage structure is conventional aluminum skin-stringer-frame construction. For two of the study aircraft (wide-body and small-diameter) the skin thickness is constant along the cabin length, while for the narrow-body design the skin thickness is allowed to vary. Details of the fuselage structure are given in Sections 4.5 and 5.7, Figures 17 to 19, and Tables 3 and 7. The structures have no additional damping treatment although it might be advisable to treat the frames and stringers in order to minimize structure-borne noise transmission through flanking paths such as the floor and the trim panel mounts.

Add-On Insulation:-

The add-on insulation consists of a limp-mass trim panel, which forms the second wall of the double wall system, and acoustic insulating material which fills the cavity between the fuselage skin and the trim panel.

The trim panel is installed at a distance of at least 12.7mm from the fuselage skin panel, has limp-mass characteristics such as those of lead-impregnated vinyl, and has high internal damping, with a loss factor of about 0.1. The damping could be provided by the use of visco-elastic material. A framework may be necessary to support the trim panels, but the framework should be isolated from the fuselage structure so that there is negligible structureborne noise transmission.

The acoustic insulation in the cavity is a light-weight, porous material such as glass fiber wool. The flow resistivity should be approximately 50,000 mks rayls/m and the bulk density about

9.6 kg/m³. For a thickness of 127 mm, the surface density is 1.2 kg/m².

The variation in surface density of the trim panel plus porous material along the length of the cabin is shown in Figure 56. Since there is a uniform distribution (1.2 kg/m²) of the porous material, the longitudinal variation is due solely to changes in trim panel surface density. There is a uniform circumferential distribution of porous material and trim panel surface densities. The maximum values of the trim panel surface density are approximately 36 kg/m² for the wide-body airplane, 14 kg/m² for the narrow-body airplane, and 26 kg/m² for the small-diameter airplane. The maximum trim panel weight for the narrow-body airplane is lower than those for the other two aircraft because of the heavier skin panel weight in the region of maximum exterior sound pressure level.

Good isolation of the trim panel from the fuselage structure (skin, stringers, frames and floor) is essential if the acoustic performance of the add-on sidewall is not to be degraded. The design of vibration isolation mounts was not included in the present study and work is required on this topic. It is possible that the low transmissibilities required at the fundamental blade passage frequencies will require the use of constrained damping material on the frames and stringers, to increase the total damping loss factor to lie in the range 0.05 to 0.1.

Interior Furnishings:-

The acoustic absorption coefficients for the interior surfaces and furnishings should be equal to, or greater than, the values

shown in Figure 22. To achieve these values, the carpets, seats and the surface of the trim panels will have to be at least as acoustically absorptive as are the furnishings in current turbofan aircraft.

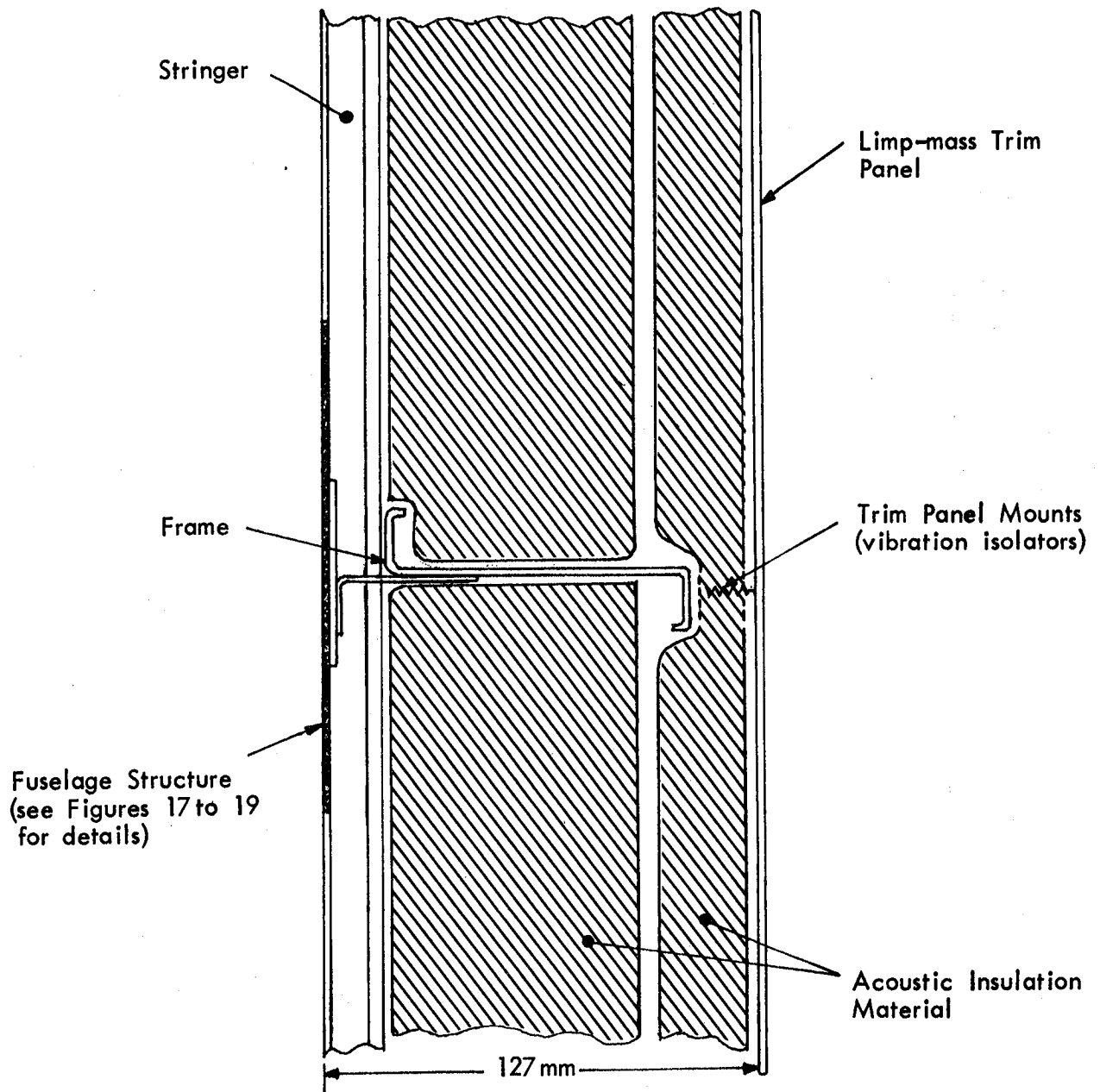


FIGURE D.1 SCHEMATIC OF PROPOSED SIDEWALL TREATMENT

APPENDIX E LIST OF SYMBOLS

A	Structural area
A_r, A_s	Cross-sectional area of ring frames and stringers, respectively
A_j, A_x, A_y, A_z	Areas of absorbing walls
a, a_x, a_y	Pressure amplitude decay rate parameter
a, b, c	Cavity dimensions in x,y,z directions (Figure 4(a))
b	Propagation constant in porous material $b = \alpha + j\beta$
$C_p(\bar{x}, \bar{x}'; \omega)$	Co-spectral density of exterior blocked pressure
c, c_x, c_y	Correlation decay parameters for exterior pressure field
c_i, c_e	Speed of sound in air in the interior and exterior media
c_L	Compressional wavespeed in material
D	Propeller diameter; or bending rigidity of structure
D_x, D_y	Bending rigidities of structure and skin
D_{xy}	Cross rigidity of structure
D_k	$= Gh^3/12$
E_r, E_s, E	Elastic modulus for ring frame, stringer and skin, respectively
$E[g(\omega_b, \omega_n)]$	Expected value of function $g(\omega_b, \omega_n)$
$E[W_{in}(\omega_b)]_{\Delta\omega}$	Expected value of the acoustic power flow into cavity at frequency ω_b centered in band $\Delta\omega$
$f(n, r)$	Internal coupling factor for structure and cavity

G	Modulus of rigidity for shear stresses of structure
$G_p(\bar{x} \bar{x}';\omega)$	Green's function for the airplane cabin interior
$G_p^o(\bar{x} \bar{x}';\omega)$	Green's function for the exterior field
G_r, G_s	Torsion modulus of ring frames and stringer, respectively
$g(\omega_b, \omega_n)$	Modal admittance function at frequency ω_b
H	Cabin height
h, h_e	Skin thickness and effective thickness respectively
I_o	Acoustic intensity at observer position, $= \langle p_o^2 \rangle / \rho_i c_i$
I_r, I_s	Moment of inertia of ring frame and stringer, respectively
I^{rs}, I^{rr}	Internal acoustic coupling factors for structural modes (Section 3.2.1)
j^{rs}, j^{rr}	External acoustic coupling factors for structural modes (Section 3.2.1)
J_r, J_s	Polar moment of inertia of ring frames and stringers respectively
$j_r^2(\omega)$	$= j_m^2(\omega) j_n^2(\omega)$ Structural joint acceptance in longitudinal and lateral directions for progressive wave excitation
$j_r^{2, rev}(\omega)$	Joint acceptance for reverberant field excitation
K	Complex compressibility of the porous material
k	Wavenumber $= \omega/c_o (k=k_x, k_y)$
$k_p (= k_m, k_n)$	Structural wavenumber, where $k_m = m\pi/L_x$
\bar{k}_n	Complex eigenvalue for cavity
k_n	Real part of \bar{k}_n
L_x, L_y	Dimensions of rectangular curved structural element

ℓ	Sidewall cavity depth
ℓ_x, ℓ_y	Subpanel element dimensions
ℓ_x	Frame Pitch
ℓ_y	Stringer Pitch
M_r	Modal mass of structure
m, n	Number of axial halfwaves and number of circumferential full waves in structure
N_n	Number of modes in band
NR	Noise reduction = $10 \log (\langle p_e^2 \rangle / \langle p_i^2 \rangle)$
n_r, n_n	Structural and acoustic modal densities, respectively
$P_T^o, P_T^i, P_{b T}$	Fourier transform of external, interior and blocked pressures of truncated signal of length T, respectively
$\langle p_i^2 \rangle$	Space-averaged, band-limited, mean square pressure in cabin volume
$\langle p_n^2 \rangle$	Space-averaged band limited mean square pressure in volume V, for n th mode
p, q, r	Mode orders; also indices in image array formulation
$q_1(\bar{x}, \bar{x}')$	Spatial distribution function for power spectral density of the exterior blocked pressure field
R	Radius of curvature; or distance between source and observer in cabin
\bar{R}, \bar{S}	Ring frame and stringer bending parameters, respectively
R_{rad}	Radiation resistance
R_{rad}^{int}	Internally-looking radiation resistance
R_{rad}^{ext}	Externally-looking radiation resistance

R_l	Flow resistivity of the porous material
$R_p(\bar{x}, \bar{x}'; \tau)$	Average cross-correlation of the blocked pressure over the exterior
r	Distance between propeller tip and fuselage sidewall
$(S\bar{\alpha})$	Absorption, in cabin interior, of absorbing area S
$S_p(\omega)$	Power spectral density of exterior blocked pressure
$S_p(\bar{x}, \bar{x}'; \omega)$	Cross power spectral density of exterior blocked pressure
$S_{p_{Xo}}(\omega)$	One-sided power spectral density of exterior blocked pressure at reference location X_o
$S_w(\bar{x}, \bar{x}'; \omega)$	Cross-power spectral density of panel displacement
$Sp_1 v(\bar{x}, \bar{x}'; \omega)$	Cross-power spectral density of pressure at \bar{x} and velocity at \bar{x}'
U_x, U_y	Average trace wavespeed of exterior pressure field
V	Volume of airplane cabin
W	Net power flowing through structure; or cabin width
W_T	Fourier transform of displacement truncated signal of length T
$W_{rad}^{in}(\omega)$	Spectral density of power radiated into cabin
$[W_{in}(\omega)]_{\Delta\omega}$	Power inflow to acoustic structural modes resonant in band $\Delta\omega$
W_j	Power radiated from j th structural element
W_{abs}^{int}	Power absorbed on cabin surfaces

\bar{X}_0	= X_0, Y_0 , is the location of peak pressure on the structural element
Y	Porosity of porous material
Y_r	Structural receptance for mode r
Z_0	Characteristic impedance of porous material, $Z_0 = -jKb/\omega y$, see Eq. (65), Section 3.9.2
z	Surface specific acoustic impedance ($= p/v$)
z_p	Infinite panel impedance, Eq. (68)
\bar{z}_r, \bar{z}_s	Distance from skin middle surface to centroids of ring frame and stringer
$\alpha_j, \alpha_x, \alpha_y, \alpha_z, \alpha_w, \alpha_c, \alpha_f$	Absorption coefficients of surfaces
β	Surface admittances, $\beta = \xi - i\sigma$. Also complex wavenumber in porous material
Γ_{plb_T}	Generalized blocked force
Γ_ϵ^x	Defined in Eq. (26)
$\Delta\omega$	Frequency bandwidth
Δp	Pressure differential across cabin fuselage
δ	$= nL_x/m\pi R$
$\epsilon_p, \epsilon_q, \epsilon_r$	Mode participation factors, ($= 1; p, q, r=0: =2; p, q, r>0$)
ϵ_n	$= \epsilon_p \epsilon_q \epsilon_r$
ϵ_r	Also relative error - Eq. (46)
ζ	Separation distance in y direction ($\zeta = y' - y$)
η_r	Structural mode loss factor
$\bar{\eta}_r$	Average value of η_r over band $\Delta\omega$

η_n	Acoustic mode loss factor
$\bar{\eta}_n$	Average value of η_n over band
η_{rad}	Radiation loss factor, $= \rho c \sigma_{rad} / \omega \mu$
η_{struc}	Loss factor associated with structural dissipation mechanisms
κ, κ_p	Radius of gyration of panel, structure
κ_n	Imaginary part of \bar{k}_n
$\Lambda_s, \Lambda_r, \Lambda, \Lambda_{rs}$	Parameters used in frequency equation for simply-supported cylinder
λ_c	Skin critical wavelength
μ	Average mass surface density of structure
μ_1, μ_2	Average mass surface densities for two walls of a double wall structure
ν_{mn}	Structural resonance frequency, non-dimensionalized by the ring frequency
ν_x, ν_y	Poisson's ratio of structure, for x,y axes
ξ	Separation distance in x direction, $\xi = x' - x$
ξ, ξ_x, ξ_y, ξ_z	Normalized surface conductances for surfaces of cavity
ρ_i, ρ_e	Ambient densities in the interior and exterior media
$\sigma^2[G]$	Variance of function G
$\sigma, \sigma_x, \sigma_y, \sigma_z$	Normalized susceptances of surfaces of cavity
σ_{rad}	Radiation efficiency, $\sigma_{rad} = R_{rad}^{int} / \rho_i c_i A$
τ_p	Bare fuselage transmission coefficient
τ_s	Transmission coefficient of add-on sidewall treatment
$\bar{\phi}_n(\bar{x})$	Complex mode shape for cavity

$\phi_n(\bar{x})$	Real part of complex mode shape $\bar{\phi}_n(x)$ of cavity
$\psi^r(\bar{x})$	Mode shape, or eigenfunction, of the r th mode of the structure
ω	Angular frequency
ω_b	$= b\omega_0$, b th harmonic of the blade passage frequency ω_0
ω_c	Center frequency in band $\Delta\omega$
ω_0	Angular blade passage frequency, $2\pi f_0$
ω_r	Structural mode resonance frequency; also fuselage ring frequency
ω_n	Acoustic mode resonance frequency
$\langle \rangle_r$	indicate averages over modes in band

1. Report No. NASA CR-159200		2. Government Accession No.		3. Recipient's Catalog No.	
4. Title and Subtitle Interior Noise Control Prediction Study for High-Speed Propeller-Driven Aircraft				5. Report Date September 1979	
				6. Performing Organization Code	
7. Author(s) D. C. Rennison, J. F. Wilby, A. H. Marsh, E. G. Wilby				8. Performing Organization Report No. 4026	
9. Performing Organization Name and Address Bolt Beranek and Newman Inc. 21120 Vanowen Street Canoga Park, CA 91303				10. Work Unit No.	
				11. Contract or Grant No. NAS1-15426	
12. Sponsoring Agency Name and Address National Aeronautics and Space Administration Langley Research Center Hampton, VA 23665				13. Type of Report and Period Covered Contractor Report	
				14. Sponsoring Agency Code	
15. Supplementary Notes Contract Monitor: Dr. John S. Mixson, NASA Langley Research Center					
16. Abstract An analytical model has been developed to predict the noise levels inside propeller-driven aircraft during cruise at $M=0.8$. The model has been applied to three study aircraft with fuselages of different size (wide-body, narrow-body and small diameter) in order to determine the noise reductions required to achieve the goal of an A-weighted sound level which does not exceed 80 dB. The model was then used to determine noise control methods which could achieve the required noise reductions. Two classes of noise control treatments were investigated -- add-on treatments which can be added to existing structures, and advanced concepts which would require changes to the fuselage primary structure. Only one treatment, a double wall with limp panel, provided the required noise reductions. Weight penalties associated with the treatment were estimated for the three study aircraft.					
17. Key Words (Suggested by Author(s)) Aircraft interior noise Propeller noise High-speed subsonic cruise Noise control			18. Distribution Statement Unclassified - Unlimited		
19. Security Classif. (of this report) Unclassified	20. Security Classif. (of this page) Unclassified		21. No. of Pages 296	22. Price*	

DO NOT REMOVE SLIP FROM MATERIAL

Delete your name from this slip when returning material to the library.

NAME	MS
Al. McEaster	149
W	
Ray-Singh	6/95
J. Betts 9/00	903